D 2021

U.PORTO
FEUP FACULDADE DE ENGENHARIA
UNIVERSIDADE DO PORTO

CONTROL OF THE CONTINUOUS CRYSTALLIZATION OF ACTIVE PHARMACEUTICAL INGREDIENTS (APIS) IN AN OSCILLATORY FLOW CRYSTALLIZER

PATRÍCIA DA CONCEIÇÃO FERREIRA DIAS CRUZ

TESE DE DOUTORAMENTO APRESENTADA
À FACULDADE DE ENGENHARIA DA UNIVERSIDADE DO PORTO EM
PROGRAMA DOUTORAL EM ENGENHARIA QUÍMICA E BIOLÓGICA

U.PORTO
FEUP FACULDADE DE ENGENHARIA
UNIVERSIDADE DO PORTO

Control of the continuous crystallization of active pharmaceutical ingredients (APIs) in an oscillatory flow crystallizer

by

Patrícia Cruz

A dissertation submitted in partial fulfilment of the requirements for the degree of Doctor of Philosophy in Chemical and Biological Engineering

Supervisors

António Manuel Azevedo Ferreira
Fernando Alberto Nogueira da Rocha
Laboratory for Process Engineering, Environment, Biotechnology and Energy (LEPABE)

Carlos Manuel Alvarez Perez
Hovione FarmaCiencia SA

Porto, July 2021

lepabe
Laboratory for Process Engineering, Environment, Biotechnology and Energy

Hovione

Patrícia Cruz gratefully acknowledges doctoral scholarship [SFRH/BD/119391/2016] from Fundação para a Ciência e Tecnologia (FCT), co-financed by the European Social Fund (ESF) through North Portugal Regional Operational Programme (NORTE 2020), and by national funds from the Ministry of Science, Technology and Higher Education (MCTES).













This work was financially supported by:

I) Project PTDC/QEQ-PRS/3787/2014 – POCI-01-0145-FEDER-016816 – funded by the European Regional Development Fund (ERDF) through COMPETE2020 – Programa Operacional Competitividade e Internacionalização (POCI) and by national funds through Fundação para a Ciência e a Tecnologia, I.P. (FCT) – Project 9471 – Reforçar a Investigação, o Desenvolvimento Tecnológico e a Inovação;

II) IF exploratory project [IF/01087/2014] funded by FCT;

III) POCI-01-0145-FEDER-006939 (Laboratory for Process Engineering, Environment, Biotechnology and Energy – UID/EQU/00511/2013) funded by ERDF, through COMPETE2020 – Programa Operacional Competitividade e Internacionalização (POCI), and by national funds, through FCT;

IV) NORTE-01-0145-FEDER-000005 – LEPABE-2-ECO-INNOVATION, supported by North Portugal Regional Operational Programme (NORTE 2020), under the Portugal 2020 Partnership Agreement, through ERDF;

V) Base Funding [UIDB/00511/2020] and Programmatic Funding [UIDP/00511/2020] of the Laboratory for Process Engineering, Environment, Biotechnology and Energy – LEPABE – funded by national funds through the FCT/MCTES (PIDDAC).













This page was intentionally left in blank

Acknowledgments

First of all, I would like to thank my supervisors at LEPABE, Professor António Ferreira and Professor Fernando Rocha. Thank you for your guidance and encouragement over the last four years. Thank you for trusting me and giving me the opportunity to pursue my ideas and learn from my mistakes. Thank you for your kindness. This thesis is as much mine as it is yours.

I would also like to thank my supervisor at Hovione, Eng. Carlos Alvarez. I am truly thankful for your invaluable collaboration and support. Thank you for giving me the opportunity to learn from your immense knowledge and experience.

I am also sincerely grateful to all my colleagues and dear friends at LEPABE, Anabela Veiga, Antónia Gonçalves, Berta Estevinho, Carolina Silva, Cecília Rodrigues, Filipa Freitas, Filipe Almeida, Ioana Carlan, Joana Ferreira, Marisa Ribeiro and Sílvia Coelho. Thank you for all the laughs and tears we shared. This would have been a lot harder without you.

I would also like to thank all the scientists and laboratory technicians at Hovione, especially Elsa Gonçalves, Filipe Estanislau, Nuno Lousa, Pedro Carvalho and Rómulo Oliveira. Thank you for always being available to help me in any way you could.

I am also deeply indebted to all my wonderful friends, Ameessa Tulcidas, Ana Leal, Andreia Sousa, André Silva, Bárbara Teixeira, Bruno Sousa, Joana Rocha, Juliana Silva, Luís Rocha, Ana Luísa Coelho, Maria do Carmo Oliveira, Rui Churro and Sara Severo. Thank you for being there for me no matter what. Your friendship means the world to me.

I would also like to express my gratitude to all my family, especially my parents, for their endless support and love. Thank you for always encouraging me to follow my dreams.

Last but not least, I would also like to thank Tiago, the love of my life and my best friend. Thank you for making me smile every day.

This page was intentionally left in blank

Abstract

The advent of continuous manufacturing in the pharmaceutical industry has encouraged the development of new crystallizers specifically designed for continuous crystallization. One of the examples is the planar oscillatory flow crystallizer (planar-OFC), a new variant of OFCs specifically designed to improve the suspension and flowability of solids during continuous crystallization. In this work, three sets of experiments were performed in planar-OFCs.

In the first set of experiments, an aqueous solution of indigo carmine was used as a liquid tracer, and a suspension of polyvinyl chloride (PVC) particles was used as a solid tracer to investigate the impact of operating and geometric parameters on the state of mixing in a planar-OFC. First, the minimum mixing intensity required to keep solids in suspension was determined, then, the mixing time was determined for the liquid phase and for the solid phase, and finally, the axial dispersion was determined for both phases.

In the second set of experiments, the isothermal crystallization of paracetamol was used as a case study to investigate the impact of the frequency and amplitude of oscillation on the nucleation and crystal growth kinetics in a planar-OFC. First, the nucleation rate was calculated from the probability distribution of detection times, and the nucleation kinetic and thermodynamic parameters were estimated from the classical nucleation theory. Then, an empirical power-law equation was used to describe the influence of supersaturation on the crystal growth rate and the crystal growth kinetic parameters were estimated by fitting a mass balance equation to the experimental data.

In the third set of experiments, the continuous cooling crystallization of paracetamol and the continuous antisolvent crystallization of a commercial active pharmaceutical ingredient were used as case studies. In each case study, the operating parameters were manipulated so as to adjust the crystal size distribution of the final product in accordance with different specifications. In the first case study, temperature cycling was employed to reduce the percentage of fines and agglomerates and, therefore, improve the uniformity of the crystal size distribution in the final product. In the second case study, the planar-OFC was divided into two spatially independent sections and the residence time in each section was manipulated so as to promote the formation of aggregates with a narrow crystal size distribution.

The previous approaches allowed to demonstrate the potentialities of the planar-OFC in the continuous crystallization of active pharmaceutical ingredients, namely in the control of the crystal size distribution, by adjusting the operating and geometric parameters in the planar-OFC.

This page was intentionally left in blank

Resumo

O advento da produção em contínuo na indústria farmacêutica tem incentivado o desenvolvimento de novos cristalizadores especificamente adaptados para cristalização em contínuo. Um dos exemplos é o cristalizador de fluxo oscilatório planar (planar-OFC), uma nova variante de OFCs especialmente desenvolvida para melhorar a suspensão e a fluidez de sólidos durante a cristalização em contínuo. Neste trabalho, realizaram-se três conjuntos de experiências em planar-OFCs.

No primeiro conjunto de experiências, uma solução aquosa de índigo carmim foi usada como marcador líquido e uma suspensão de partículas de policloreto de vinilo (PVC) foi usada como marcador sólido para investigar o impacto de parâmetros operacionais e geométricos no estado de mistura num planar-OFC. Primeiro, a intensidade de mistura mínima necessária para manter sólidos em suspensão foi determinada, depois o tempo de mistura foi determinado para a fase líquida e para a fase sólida, e finalmente, a dispersão axial foi determinada para ambas as fases.

No segundo conjunto de experiências, a cristalização isotérmica de paracetamol foi usada como caso de estudo para investigar o impacto da frequência e da amplitude de oscilação nas cinéticas de nucleação e crescimento num planar-OFC. Primeiro, a velocidade de nucleação foi calculada a partir da distribuição de probabilidades do tempo de deteção, e os parâmetros cinético e termodinâmico de nucleação foram estimados a partir da teoria clássica de nucleação. Depois, uma equação de potência empírica foi usada para descrever a influência da sobressaturação na velocidade de crescimento, e os parâmetros cinéticos de crescimento foram estimados ajustando uma equação de balanço de massa aos dados experimentais.

No terceiro conjunto de experiências, a cristalização em contínuo por arrefecimento de paracetamol e a cristalização em contínuo por adição de antisolvente de um princípio ativo comercial foram usadas como casos de estudo. Em cada caso de estudo, os parâmetros operacionais foram manipulados de forma a ajustar a distribuição de tamanhos de cristal do produto final de acordo com diferentes especificações. No primeiro caso de estudo, usaram-se ciclos de temperatura para reduzir a percentagem de finos e aglomerados e assim melhorar a uniformidade da distribuição de tamanhos de cristal no produto final. No segundo caso de estudo, o planar-OFC foi dividido em duas secções espacialmente independentes e o tempo de residência em cada secção foi manipulado de forma a promover a formação de agregados com uma distribuição de tamanhos de cristal apertada.

As abordagens anteriores permitiram demonstrar as potencialidades do planar-OFC na cristalização em contínuo de princípios ativos, nomeadamente no controlo da distribuição de tamanhos de cristal, atuando, para isso, nos parâmetros operacionais e geométricos do planar-OFC.

This page was intentionally left in blank

List of Contributions

Publications

- Cruz, P. C.; Silva, C. R.; Rocha, F. A.; Ferreira, A. M. Mixing Performance of Planar Oscillatory Flow Reactors with Liquid Solutions and Solid Suspensions. Ind. Eng. Chem. Res. 2021, 60 (6), 2663–2676.
- Cruz, P. C.; Silva, C. R.; Rocha, F. A.; Ferreira, A. M. The Axial Dispersion of Liquid Solutions and Solid Suspensions in Planar Oscillatory Flow Crystallizers. AIChE J. 2019, 65 (9), e16683.
- Cruz, P. C.; Rocha, F. A.; Ferreira, A. M. Crystallization of Paracetamol from Aqueous Solutions in a Planar Oscillatory Flow Crystallizer: Effect of the Oscillation Conditions on the Nucleation Kinetics. CrystEngComm 2021, 23 (39), 6930-6941.
- Cruz, P. C.; Rocha, F. A.; Ferreira, A. M. Crystallization of Paracetamol from Mixtures of Ethanol and Water in a Planar Oscillatory Flow Crystallizer: Effect of the Oscillation Conditions on the Crystal Growth Kinetics. CrystEngComm 2021, Advance Article, DOI: 10.1039/D1CE00858G.
- Cruz, P. C.; Rocha, F. A.; Ferreira, A. M. Tailoring the Crystal Size Distribution of an Active Pharmaceutical Ingredient by Continuous Antisolvent Crystallization in a Planar Oscillatory Flow Crystallizer. Chem. Eng. Res. Des. 2021, 175, 115-123.

Provisional patent application

- Alvarez, C.; Ferreira, A.; Cruz, P. A Continuous Crystallization Method for Tetracyclines. PT117016. January 2021.

Oral Communications

- Cruz, P.; Rocha. F.; Ferreira, A. The Axial Dispersion Performance of a Novel Oscillatory Flow Reactor – a Design of Experiments Approach. 2nd Doctoral Congress in Engineering, Porto, Portugal, June 2017.
- Cruz, P.; Silva, C.; Rocha, F.; Ferreira, A. The Axial Dispersion Performance of a Novel Oscillatory Flow Reactor with Liquid Solutions and Solids Suspensions – a Design of Experiments Approach. 8th World Congress on Particle Technology, Orlando, Florida, United States of America, April 2018.

Poster communications

- Cruz, P.; Silva, C.; Rocha, F.; Ferreira, A. Planar Oscillatory Flow Crystallizers: a New Generation of Crystallizers with Relevance for Continuous Crystallization. 3rd International Symposium on Continuous Manufacturing of Pharmaceuticals, London, United Kingdom, October 2018.

List of Figures

Figure 1.1 – Oscillatory flow crystallizer. 3
Figure 1.2 – (a) Tubular-OFC with SPC. (b) Planar-OFC with SPC. *D* is the tube diameter in the straight section, D_0 is the tube diameter in the constriction, L_1 is the constriction length, L_2 is the straight section length, *W* is the channel width in the straight section, W_0 is the channel width in the constriction, and *H* is the channel height. 4
Figure 2.1 – Ostwald-Miers diagram. Adapted from reference 4. 12
Figure 2.2 – Free energy diagram. Adapted from reference 8. 14
Figure 2.3 – Surface energy diagram. Adapted from reference 8. 16
Figure 2.4 – Heterogeneous nucleation when θ=180 ° (on the left), 0 °<θ<180 ° (on the middle) and θ=0 ° (on the right). 17
Figure 2.5 – Stages of crystal growth. Adapted from reference 8. 19
Figure 2.6 – Concentration driving forces. Adapted from reference 8. 20
Figure 2.7 – Particle strength against particle size. Adapted from reference 29. 22
Figure 2.8 – Formation of a solid bridge after collision. Adapted from reference 29. 23
Figure 2.9 – Number of particles per unit volume against specific power input. Adapted from reference 29. 23
Figure 3.1 – OFC with moving fluid (on the top) and OFC with moving baffles (on the bottom). *D* is the tube diameter in the straight section; D_0 is the tube diameter in the constriction; *L* is the distance between constrictions. 27
Figure 3.2 – Mechanism of oscillatory flow mixing. (a) start of up stroke; (b) maximum velocity in up stroke; (c) start of down stroke; (d) maximum velocity in down stroke. Reprinted from Chemical Engineering Journal, 112, Fitch, A. W., Jian, H., Ni, X., An investigation of the effect of viscosity on mixing in an oscillatory baffled column using digital particle image velocimetry and computational fluid dynamics simulation, 197–210, Copyright 2005, with permission from Elsevier B.V. 28
Figure 3.3 – Baffle geometries. (a) Integral baffles; (b) Central axial baffles; (c) Round-edged helical baffles; (d) Sharp-edged helical baffles; (e) Sharp-edged helical baffles with a central insert; (f) Wire wool baffle. Reprinted from Chemical Engineering Journal, 265, McDonough, J. R., Phan, A. N., Harvey, A. P., Rapid Process Development Using Oscillatory Baffled Mesoreactors – A State-of-the-Art Review, 110–121, Copyright 2014, with permission from Elsevier B.V. 29
Figure 4.1 – Plate-like planar-OFC. 58
Figure 4.2 – Experimental set-up for the determination of the critical amplitude for total suspension of solids. A – planar-OFC; B – video camera; C – light source. 60
Figure 4.3 – Image processing steps. Crystallizer 1 with a 10% (w/w) suspension. (a) Original image. (b) Reduction of color depth from 256 to 2 levels of gray. (c) Elimination of objects that contact the boarder of the image and the identification of the particles. (d) Determination of the number and total area of the particles. 61

Figure 4.4 – Percentage of particles and total area as a function of the amplitude in Crystallizer 1 operating at f=1 Hz with a 10% (w/w) suspension. The error bars represent the standard deviation of 5 frames. 62
Figure 4.5 – Critical amplitude of oscillation for total suspension of solids as a function of the frequency of oscillation in three planar-OFCs operating with (a) 10% (w/w), (b) 20% (w/w), and (c) 30% (w/w) suspensions. 64
Figure 4.6 – Velocity ratio at the critical amplitude of oscillation for total suspension of solids as a function of the frequency of oscillation in three planar-OFCs operating with (a) 10% (w/w), (b) 20% (w/w), and (c) 30% (w/w) suspensions. 64
Figure 4.7 – Power input per unit volume at the critical amplitude of oscillation for total suspension of solids as a function of the frequency of oscillation in three planar-OFCs operating with (a) 10% (w/w), (b) 20% (w/w), and (c) 30% (w/w) suspensions. 64
Figure 4.8 – Typical top and side views of a particle suspension in a planar-OFC operating below $x_{0,crit}$ with f>5Hz. The deposit of particles is identified with an arrow. 65
Figure 5.1 – Experimental set-up for the determination of the mixing time. 73
Figure 5.2 – (a) Coefficient of determination as a function of the wavelength for the calibration curve of indigo carmine. (b) Calibration curve for the concentration of indigo carmine at λ=581 nm. *Abs* is the absorbance. 74
Figure 5.3 – (a) Coefficient of determination as a function of the wavelength for the calibration curve of PVC particles. (b) Calibration curve for the concentration of PVC particles at λ=655 nm. *Abs* is the absorbance. . 74
Figure 5.4 – Factor space for the determination of the mixing time. 75
Figure 5.5 – (a) Concentration curve of indigo carmine. (b) Application of F test. (f=3 Hz and V_d/V_{cell}=1.1 in Crystallizer 3). 76
Figure 5.6 – t_m^L as a function of the oscillation conditions in (a) Crystallizer 1, (b) Crystallizer 2, and (c) Crystallizer 3. 78
Figure 5.7 – t_m^S as a function of the oscillation conditions in (a) Crystallizer 1, (b) Crystallizer 2, and (c) Crystallizer 3. 78
Figure 5.8 – t_m^L and t_m^S as a function of Re_o in (a) Crystallizer 1, (b) Crystallizer 2, and (c) Crystallizer 3. .. 78
Figure 5.9 – t_m^L and t_m^S as a function of St (f=2 Hz) in (a) Crystallizer 1, (b) Crystallizer 2, and (c) Crystallizer 3. 79
Figure 5.10 – Comparison of t_m^L and t_m^S obtained from the model, $(t_m^L)^m$ and $(t_m^S)^m$, and obtained experimentally, $(t_m^L)^e$ and $(t_m^S)^e$ in each crystallizer. L stands for liquid tracer and S stands for solid tracer. . 82
Figure 5.11 – Main effects plot for t_m^L and t_m^S in (a) Crystallizer 1, (b) Crystallizer 2, and (c) Crystallizer 3.83
Figure 6.1 – Experimental set-up for the determination of the axial dispersion..... 89
Figure 6.2 – Factor space for the determination of the axial dispersion. 90
Figure 6.3 – Normalized RTD profile with liquid tracer in Crystallizer 1 for (a) Run 1 and (b) Run 2. 92
Figure 6.4 – Normalized RTD profile with solid tracer in Crystallizer 1 for (a) Run 1 and (b) Run 2. 93

Figure 6.5 – D_{ax}^{L} as a function of the operating conditions for the factorial and center points in (a) Crystallizer 1, (b) Crystallizer 2 and (c) Crystallizer 3. 95
Figure 6.6 – D_{ax}^{S} as a function of the operating conditions for the factorial and center points in (a) Crystallizer 1, (b) Crystallizer 2 and (c) Crystallizer 3. 95
Figure 6.7 – Comparison of D_{ax}^{L} and D_{ax}^{S} obtained from the model, $(D_{ax}^{L})^{m}$ and $(D_{ax}^{S})^{m}$, and obtained experimentally, $(D_{ax}^{L})^{e}$ and $(D_{ax}^{S})^{e}$ in each crystallizer. L stands for liquid tracer and S stands for solid tracer. 99
Figure 6.8 – Main effects plot for D_{ax}^{L} and D_{ax}^{S} in (a) Crystallizer 1, (b) Crystallizer 2, and (c) Crystallizer 3. 100
Figure 6.9 – Interaction plot between Q and V_d/V_{cell} for D_{ax}^{L} in Crystallizer 1. 101
Figure 6.10 – Volume-based CSD of the seeds and final products obtained in each crystallizer (Q=100 mL min^{-1}, f=6 Hz, and V_d/V_{cell}=1). 102
Figure 7.1 – Plate-like planar-OFC. (a) Three stacked plates. (b) Dimensions of each inter-constriction cell. 111
Figure 7.2 – Experimental set-up for the determination of the nucleation kinetics. A – aqueous solution of paracetamol; B – hotplate stirrer; C – peristaltic pump; D – planar-OFC; E – linear motor; F – heating bath; G – cooling bath; H – ATR-UV/Vis immersion probe; I – Pt100 thermometer. 112
Figure 7.3 – Evolution of the temperature and absorbance over time. t_0 is the moment when the temperature reaches 20.0±0.5 °C, and t_d is the moment when the ATR-UV/Vis probe detects a sudden drop in the concentration of paracetamol, corresponding to the onset of nucleation. 114
Figure 7.4 – Mean detection time as a function of supersaturation for each experimental condition. 114
Figure 7.5 – Probability distribution of detection times at (a) f=3 Hz and x_0=6 mm; (b) f=6 Hz and x_0=6 mm; (c) f=3 Hz and x_0=12 mm; (d) f=6 Hz and x_0=12 mm. 115
Figure 7.6 – Growth time as a function of supersaturation for each experimental condition. 116
Figure 7.7 – (a) J as a function of S and (b) ln(J/S) as a function of 1/Ln^2 S for each experimental condition. 117
Figure 7.8 – Comparison of A obtained from the model, A^m, and obtained experimentally, A^e. 121
Figure 7.9 – Main effects plot for A. 121
Figure 7.10 – Interaction plot between f and x_0 for A. 122
Figure 7.11 – Contour plot. 123
Figure 8.1 – Calibration curve for the absorbance as a function of the concentration of paracetamol in a 40% (v/v) mixture of ethanol and water at different temperatures. The error bars represent the interval between the minimum and maximum values of the three replicates. 135
Figure 8.2 – Plate-like planar-OFC. (a) Three stacked plates. (b) Dimensions of each inter-constriction cell. 137

Figure 8.3 – Experimental set-up for the determination of the crystal growth kinetics. A – suspension with seeds; B – hotplate stirrer; C – peristaltic pump; D – planar-OFC; E – linear motor; F – cooling bath; G – ATR-UV/Vis immersion probe; H – thermocouple..... 138
Figure 8.4 – Volume-based CSD of the seeds and final products. The inset shows the CSD for the smaller sizes. 142
Figure 8.5 – Coefficient of variation of the CSD for the seeds and final products of each run..... 142
Figure 8.6 – Microscope images of the seeds and final products. The scale bar represents 200 µm. 143
Figure 8.7 – Evolution of supersaturation ratio and temperature in Runs 1-7..... 144
Figure 8.8 – Overall linear growth rate as a function of the concentration driving force for Runs 1-7. 145
Figure 8.9 – Parity plots for Runs 1-7. 146
Figure 8.10 – (a) Overall coefficient of crystal growth and (b) growth rate order as a function of the frequency and amplitude of oscillation. The error bars represent the interval between the minimum and maximum values of the three replicates..... 146
Figure 8.11 – Evolution of supersaturation ratio and temperature in Runs 1, 8 and 9. 148
Figure 8.12 – Parity plots for Runs 1, 8 and 9..... 149
Figure 8.13 – Inverse of the diffusion control index for Runs 1-7 (S=1.2). 151
Figure 9.1 – Plate-like planar-OFC. (a) Three stacked plates. (b) Dimensions of each inter-constriction cell. 161
Figure 9.2 – Experimental set-up for continuous crystallization without seeding with two planar-OFCs in series. A – jacketed glass vessel; B – magnetic stirrer; C – cooling/heating bath; D – peristaltic pump; E – linear motor; F1 and F2 – planar-OFCs; G – cooling/heating bath; H – thermocouple; I – ATR-UV/Vis immersion probe. 162
Figure 9.3 – Experimental setup for the preparation of the seeds. A – STC; B – magnetic stirrer; C – cooling/heating bath; D – thermocouple; E – ATR-UV/Vis immersion probe. 164
Figure 9.4 – Protocol 1 and Protocol 2 for the preparation of the seeds. 165
Figure 9.5 – Experimental set-up for continuous crystallization with seeding and temperature cycling with two (a) and three (b) planar-OFCs in series. A – STC; B – magnetic stirrer; C – cooling/heating bath; D – peristaltic pump; E – linear motor; F – hot planar-OFC; F1 – first hot planar-OFC; F2 – second hot planar-OFC; G – cooling/heating bath; H – cold planar-OFC; I – cooling/heating bath; J – thermocouple; K – ATR-UV/Vis immersion probe..... 166
Figure 9.6 – Continuous crystallization without seeding: evolution of absorbance and temperature for each run. 170
Figure 9.7 – Continuous crystallization without seeding: evolution of the volume-based CSD for each run.171
Figure 9.8 – (a) Evolution of temperature and (b) evolution of absorbance during Protocol 1. (c) Evolution of temperature and (d) evolution of absorbance during Protocol 2. 172
Figure 9.9 – (a) Mean diameter and (b) volume-based CSD of the seeds produced via Protocol 1. (c) Mean diameter and (d) volume-based CSD of the seeds produced via Protocol 2..... 173

Figure 9.10 – Run 1. (a) Evolution of supersaturation and temperature at the outlet of the continuous crystallizer. (b) Evolution of the volume-based CSD along the continuous crystallizer. (c) Images of the seeds. (d) Images of the crystals after T_h. (e) Images of the crystals after T_c. 175
Figure 9.11 – Run 2. (a) Evolution of supersaturation and temperature at the outlet of the continuous crystallizer. (b) Evolution of the volume-based CSD along the continuous crystallizer. (c) Images of the seeds. (d) Images of the crystals after T_h. (e) Images of the crystals after T_c. 176
Figure 9.12 – Run 3. (a) Evolution of supersaturation and temperature at the outlet of the continuous crystallizer. (b) Evolution of the volume-based CSD along the continuous crystallizer. (c) Images of the seeds. (d) Images of the crystals after T_h. (e) Images of the crystals after T_c. 177
Figure 9.13 – Run 4. (a) Evolution of supersaturation and temperature at the outlet of the continuous crystallizer. (b) Evolution of the volume-based CSD along the continuous crystallizer. (c) Images of the seeds. (d) Images of the crystals after T_h. (e) Images of the crystals after T_c. 178
Figure 9.14 – Run 5. (a) Evolution of supersaturation and temperature at the outlet of the continuous crystallizer. (b) Evolution of the volume-based CSD along the continuous crystallizer. (c) Images of the seeds. (d) Images of the crystals after T_h. (e) Images of the crystals after T_c. 179
Figure 9.15 – Run 6. (a) Evolution of supersaturation and temperature at the outlet of the continuous crystallizer. (b) Evolution of the volume-based CSD along the continuous crystallizer. (c) Images of the seeds. (d) Images of the crystals after T_h. (e) Images of the crystals after T_c. 180
Figure 9.16 – Run 7. (a) Evolution of supersaturation and temperature at the outlet of the continuous crystallizer. (b) Evolution of the volume-based CSD along the continuous crystallizer. (c) Images of the seeds. (d) Images of the crystals after T_h. (e) Images of the crystals after T_c. 181
Figure 9.17 – Run 8. (a) Evolution of supersaturation and temperature at the outlet of the continuous crystallizer. (b) Evolution of the volume-based CSD along the continuous crystallizer. (c) Images of the seeds. (d) Images of the crystals after T_h. (e) Images of the crystals after T_c. 182
Figure 9.18 – Run 9. (a) Evolution of supersaturation and temperature at the outlet of the continuous crystallizer. (b) Evolution of the volume-based CSD along the continuous crystallizer. (c) Images of the seeds. (d) Images of the crystals after T_h. (e) Images of the crystals after T_c. 183
Figure 9.19 – Run 10. (a) Evolution of supersaturation and temperature at the outlet of the continuous crystallizer. (b) Evolution of the volume-based CSD along the continuous crystallizer. (c) Images of the seeds. (d) Images of the crystals after T_h. (e) Images of the crystals after T_c. 184
Figure 9.20 – Run 11. (a) Evolution of supersaturation and temperature at the outlet of the continuous crystallizer. (b) Evolution of the volume-based CSD along the continuous crystallizer. (c) Images of the seeds. (d) Images of the crystals after T_h. (e) Images of the crystals after T_c. 185
Figure 9.21 – Run 12. (a) Evolution of supersaturation and temperature at the outlet of the continuous crystallizer. (b) Evolution of the volume-based CSD along the continuous crystallizer. (c) Images of the seeds. (d) Images of the crystals after T_h. (e) Images of the crystals after T_c. 186

Figure 9.22 – Run 13. (a) Evolution of supersaturation and temperature at the outlet of the continuous crystallizer. (b) Evolution of the volume-based CSD along the continuous crystallizer. (c) Images of the seeds. (d) Images of the crystals after T_h. (e) Images of the crystals after T_c. 187
Figure 9.23 – Mean diameter of the seeds, after T_h and after T_c for Runs 2-5 (T_c=6 °C). 188
Figure 9.24 – Mean diameter of the seeds, after T_h and after T_c for Runs 6-9 (T_c=16 °C). 189
Figure 9.25 – Mean diameter of the seeds, after T_h and after T_c for Runs 2, 6, 10 and 12 (S_{max}=1.3). 190
Figure 9.26 – Mean diameter of the seeds, after T_h and after T_c for Runs 3, 7, 11 and 13 (S_{max}=1.4). 190
Figure 10.1 – Calibration curve for the absorbance as a function of the concentration of API in the mother liquor at room temperature (~23 °C). The error bars represent the interval between the minimum and maximum values of the three replicates..... 200
Figure 10.2 – Plate-like planar-OFC. (a) Three stacked plates. (b) Dimensions of each inter-constriction cell. 201
Figure 10.3 – Experimental set-up for batch crystallization in a planar-OFC. 202
Figure 10.4 – Experimental set-up for continuous crystallization in a planar-OFC. 203
Figure 10.5 – (a) Initial concentration, C_i, and final concentration, C_f, as a function of V_A/V_B. (b) Experimental and expected mass of crystallized API as a function of V_A/V_B. (c) Yield as a function of V_A/V_B. (d) Mass of crystallized API per volume of solution as a function of V_A/V_B. The error bars represent the standard deviation of the three replicates..... 205
Figure 10.6. Effect of f, T, x_0 and V_A/V_B on the CSD after 2 h of residence time (from the top to the bottom). 207
Figure 10.7 – SEM images of the product obtained from Run B2. 208
Figure 10.8 – Schematic representation of Runs C1-C4. 210
Figure 10.9 – Concentration of API in the mother liquor at the outlet of the planar-OFC over (a) Run C1, (b) Run C2, (c) Run C3, and (d) Run C4. Steady state volume-based CSDs obtained from (e) Run C1, (f) Run C2, (g) Run C3, and (h) Run C4. 211
Figure 10.10 – SEM images of the product obtained at steady state from (a) Run 1, (b) Run 2, (c) Run 3, and (d) Run 4. 212
Figure 10.11 – Volume-based CSDs obtained from a traditional batch and from Run C4. 214

List of Tables

Table 3.1 – Summary of published studies on suspension of solids in baffled tubes. 30
Table 3.2 – Summary of published studies on mixing efficiency in baffled tubes. 30
Table 3.3 – Summary of published studies on axial dispersion in baffled tubes. 31
Table 3.4 – Summary of published studies on batch crystallization in tubular-OFCs. 36
Table 3.5 – Summary of published studies on continuous crystallization in tubular-OFCs. 45
Table 4.1 – Dimensions of each planar-OFC. 59
Table 5.1 – Optimal values/ranges for L/D and α reported in different works. 72
Table 5.2 – Experimental conditions and respective dimensionless numbers in each run. 75
Table 5.3 – t_m^L and t_m^S obtained in Crystallizer 1 in each run. 77
Table 5.4 – t_m^L and t_m^S obtained in Crystallizer 2 in each run. 77
Table 5.5 – t_m^L and t_m^S obtained in Crystallizer 3 in each run. 77
Table 5.6 – Coded coefficients for the transformed response and coefficient of determination of each model. 82
Table 6.1 – Experimental conditions and respective dimensionless numbers in each run. 90
Table 6.2 – Minimum and maximum coefficients of determination of Model 1, and maximum deviation of mean residence time to hydraulic time for each crystallizer. 93
Table 6.3 – Experimental conditions and results obtained in Crystallizer 1 with the liquid and the solid tracers. 94
Table 6.4 – Experimental conditions and results obtained in Crystallizer 2 with the liquid and the solid tracers. 94
Table 6.5 – Experimental conditions and results obtained in Crystallizer 3 with the liquid and the solid tracers. 95
Table 6.6 – Coded coefficients and coefficient of determination of each model. 98
Table 6.7 –Volume-based CSD parameters of the seeds and final products obtained in each crystallizer. ... 101
Table 7.1 – Results obtained from the experimental data for each experimental condition. 117
Table 7.2 – Coefficients and coefficient of determination. 120
Table 7.3 – Prediction, prediction interval and experimental result for the test point. 123
Table 8.1 – Published studies on paracetamol crystal growth kinetics. 133
Table 8.2 – Solubility data. 136
Table 8.3 – Experimental conditions of each run. 139
Table 8.4 – Crystal growth kinetic parameters obtained in Runs 1-7. 145
Table 8.5 – p-values for the two models. 147
Table 8.6 – Crystal growth kinetic parameters obtained in Runs 1, 8 and 9. 148

Table 8.7 – Parameters obtained from fitting equation (8.2) to the experimental data..... 149
Table 8.8 – Average power input and mass transfer coefficient for Runs 1-7..... 151
Table 9.1 – Continuous crystallization without seeding: experimental conditions of each run..... 163
Table 9.2 – Continuous crystallization with seeding and temperature cycling: experimental conditions of each run..... 167
Table 10.1 – Batch crystallization in a planar-OFC: experimental conditions and results obtained in each run. 206
Table 10.2 – Continuous crystallization in a planar-OFC: experimental conditions of each run. 209
Table A.1 – Linear regression: equation, variables and parameters. 223
Table A.2 – Methodology used to assess each validation parameter..... 223
Table A.3 – Result for each validation parameter. 224
Table B.1 – Linear regression: equation, variables and parameters. 225
Table B.2 – Methodology used to assess each validation parameter and respective result. 225

Table of Contents

Chapter 1 - Introduction **1**
1.1 Thesis Scope 1
1.2 Thesis Motivation 3
1.3 Thesis Goals 4
1.4 Thesis Outline 5
Notation 7
References 7
Chapter 2 - Crystallization Theory **11**
2.1 Nucleation 12
2.1.1 Methods to Create Supersaturation 13
2.1.2 Primary Nucleation 13
2.1.3 Secondary Nucleation 17
2.2 Crystal Growth 19
2.3 Agglomeration 22
Notation 24
References 24
Chapter 3 - Literature Review **27**
3.1 Hydrodynamic Conditions in Tubular-OFCs 29
3.1.1 Suspension of Solids 32
3.1.2 Mixing Efficiency 32
3.1.3 Axial Dispersion 33
3.2 Batch Crystallization in Tubular-OFCs 35
3.2.1 Crystallization Kinetics 38
3.2.2 Control of Final Properties 40
3.3 Continuous Crystallization in Tubular-OFCs 44
3.3.1 Crystallization Kinetics 46
3.3.2 Control of Final Properties 47
Notation 49
References 49
Chapter 4 - Suspension of Solids in Planar Oscillatory Flow Crystallizers **57**
4.1 Introduction 57
4.2 Materials and Methods 58
4.2.1 Crystallizers 58

4.2.2 Experimental Procedure 59
4.3 Results and Discussion 61
4.4 Conclusion 67
Notation 67
References 68
Chapter 5 - Mixing Times in Planar Oscillatory Flow Crystallizers 71
5.1 Introduction 71
5.2 Materials and Methods 72
5.2.1 Crystallizers 72
5.2.2 Experimental Procedure 72
5.2.3 Calibration Curves 73
5.2.4 Design of Experiments 74
5.3 Results and Discussion 76
5.3.1 Determination of the Mixing Time 76
5.3.2 Comparison of Mixing Times for the Liquid and Solid Tracers 79
5.3.3 Effect of the Oscillation Conditions on the Mixing Time 79
5.3.4 Effect of the Geometric Parameters on the Mixing Time 80
5.3.5 Model Development 81
5.4 Conclusion 84
Notation 84
References 85
Chapter 6 - Axial Dispersion in Planar Oscillatory Flow Crystallizers 87
6.1 Introduction 87
6.2 Materials and Methods 88
6.2.1 Crystallizers 88
6.2.2 Experimental Procedure 88
6.2.3 Design of Experiments 89
6.2.4 Continuous Crystallization Experiments 91
6.3 Results and Discussion 91
6.3.1 Determination of the Axial Dispersion 91
6.3.2 Comparison of Axial Dispersion for the Liquid and Solid Tracers 96
6.3.3 Effect of the Operating Conditions on the Axial Dispersion 96
6.3.4 Effect of the Geometric Parameters on the Axial Dispersion 97
6.3.5 Model Development 97
6.3.6 Continuous Crystallization Experiments 101
6.4 Conclusion 102
Notation 103

References 104
Chapter 7 - Nucleation Kinetics in a Planar Oscillatory Flow Crystallizer 107
7.1 Introduction 107
7.1.1 Theoretical Background 108
7.2 Materials and Methods 110
7.2.1 Material 110
7.2.2 Crystallizer 110
7.2.3 Experimental Procedure 111
7.2.4 Design of Experiments 113
7.3 Results and Discussion 113
7.3.1 Determination of the Detection Time 113
7.3.2 Effect of the Oscillation Conditions on the Detection Time 114
7.3.3 Effect of the Oscillation Conditions on the Growth Time 116
7.3.4 Effect of the Oscillation Conditions on the Nucleation Rate 116
7.3.5 Effect of the Oscillation Conditions on the Kinetic Parameter 118
7.3.6 Effect of the Oscillation Conditions on the Thermodynamic Parameter 119
7.3.7 Model development 120
7.4 Conclusion 123
Notation 124
References 125
Chapter 8 - Crystal Growth Kinetics in a Planar Oscillatory Flow Crystallizer 129
8.1 Introduction 129
8.2 Materials and Methods 135
8.2.1 Material 135
8.2.2 Calibration Curves 135
8.2.3 Solubility 136
8.2.4 Preparation of the Seeds 136
8.2.5 Crystallizer 137
8.2.6 Crystal Growth Experiments 137
8.2.7 Design of experiments 139
8.3 Results and Discussion 139
8.3.1 Estimation of crystal growth kinetic parameters 140
8.3.2 Effect of the Oscillation Conditions on the Crystal Growth Kinetic Parameters 141
8.3.3 Effect of Temperature on the Crystal Growth Kinetic Parameters 147
8.3.4 Rate controlling step of crystal growth 149
8.3.5 Comparison with other works 152
8.4 Conclusion 152

Notation 153
References 154
Chapter 9 - Continuous Cooling Crystallization in a Planar Oscillatory Flow Crystallizer 159
9.1 Introduction 159
9.2 Materials and Methods 161
9.2.1 Material 161
9.2.2 Crystallizer 161
9.2.3 Continuous Crystallization without Seeding 162
9.2.4 Preparation of the Seeds 164
9.2.5 Continuous Crystallization with Seeding and Temperature Cycling 165
9.3 Results and Discussion 167
9.3.1 Continuous Crystallization without Seeding 167
9.3.2 Preparation of the Seeds 172
9.3.3 Continuous Crystallization with Seeding and Temperature Cycling 174
9.4 Conclusion 191
Notation 192
References 192
Chapter 10 - Continuous Antisolvent Crystallization in a Planar Oscillatory Flow Crystallizer 197
10.1 Introduction 197
10.2 Materials and Methods 199
10.2.1 Calibration Curve 199
10.2.2 Batch Crystallization in a STC 200
10.2.3 Crystallizer 200
10.2.4 Batch Crystallization in a Planar-OFC 201
10.2.5 Continuous Crystallization in a Planar-OFC 203
10.3 Results and Discussion 204
10.3.1 Batch crystallization in a STC 204
10.3.2 Batch crystallization in a planar-OFC 205
10.3.3 Continuous crystallization in a planar-OFC 208
10.4 Conclusion 214
Notation 215
References 216
Chapter 11 - Final Remarks 219
11.1 Conclusions 219
11.2 Recommendations for Future work 220
Appendix A - Calibration Curves for the Concentration of Paracetamol in a 40% (v/v) Mixture of Ethanol and Water 223

Appendix B - Calibration Curve for the Concentration of API in the Mother Liquor 225

This page was intentionally left in blank

Chapter 1 - Introduction

1.1 Thesis Scope

The concept of continuous manufacturing is not new. It has been widely adopted in the oil, gas, petrochemicals, polymers and food industries. However, the pharmaceutical industry still relies on batch manufacturing to produce the vast majority of their active pharmaceutical ingredients (APIs).[1,2] This dependence on batch manufacturing is such that processes naturally continuous or semi-continuous, like in-line milling, spray drying, and tablet compression, are often adapted for batch operation.[3]

There are several reasons why batch manufacturing has been the preference of the pharmaceutical industry for so many years. First of all, the multipurpose equipment that is typically used in batch manufacturing offers the versatility required to deliver a wide range of products with limited lifetimes. Batch manufacturing is also the easiest way to segregate the product in lots, facilitating the elimination of off-spec material to comply with quality requirements and regulations. In addition, the first development stages that are performed in the laboratory, where operations are predominantly batch, are naturally translated into the industrial scale. Moreover, the regulatory agencies tend to discourage any attempt to change the processes once the products are licensed.[3,4] However, there are also several disadvantages associated with batch manufacturing. The production costs are usually inflated by high labor costs, excess inventories and significant downtime between batches; there are also serious issues with batch-to-batch variability and scale-up.[1,3,5] Moreover, batch manufacturing lacks flexibility to respond to market growth or shortages.[2]

The pharmaceutical industry has benefited from high-profit margins, overall market control and a highly regulated environment that constrains competition for many years. This generated a competitive business that relies almost exclusively on the development of new drugs, while the investment in innovative technologies remains practically overlooked.[1,5] However, over the past few decades, the entry of generics products after patent expiration, the opening of new markets, and the socioeconomic pressure to reduce prices, has been forcing manufacturers to increase the efficiency of their processes.[6] This new stimulus for innovation has highlighted the benefits of continuous manufacturing to produce APIs. Increased safety is one of the main advantages of continuous manufacturing, mainly because it requires smaller volumes of equipment than batch manufacturing, which reduces the severity in case of an accident. In addition, it does not require batch handling, which reduces the number of operators on site and increases the operator safety.[7] Operation in continuous flow also provides enhanced heat and mass transfer, and precise control of the temperature and residence time, which minimizes the formation of impurities, enhances the selectivity, and maximizes the yield. Ultimately, the generation of waste and the consumption of energy can also be minimized.[7] Furthermore, continuous laboratory-scale

operations can be linearly scaled up with minimal re-optimization, thus reducing the time required to implement new processes at manufacturing-scale and accelerating the release of new products.[1,7] In addition, the production capacity can be more easily controlled to reduce costs associated with transportation, overproduction and long-term storage of APIs prior to formulation.[7]

The manufacture of APIs typically involves a series of reaction steps, followed by several postreaction operations, such as crystallization, filtration, drying and crystal size reduction operations. The benefits of continuous manufacturing are particularly relevant in the crystallization step, which defines the final properties of the product, including purity, crystal size and crystal size distribution (CSD), crystal shape, polymorphism and chirality. However, continuous crystallization is still one of the most challenging and undeveloped postreaction operations in the manufacture of APIs.

Most APIs are crystallized in simple batch processes. These processes are reasonably well understood and offer considerable advantages: the equipment is rather simple and flexible and requires a low level of maintenance; they are suitable for toxic or viscous substances, which are particularly difficult to process; their design and development often require reduced time and investment; they are suitable to produce larger crystals for systems that exhibit slow crystal growth; and also show reduced encrustation on heat-exchanger surfaces.[8,9] However, batch crystallization processes also suffer from low capacity, high requirements of human intervention and significant down time between batches. There are also significant issues with batch-to-batch variability that can have a significant impact on downstream processes, such as filtration and drying, and lead to corrective processes, such as granulation, milling and recrystallization. In addition, there are also many challenges associated with scaling-up the agitation from the laboratory- to the manufacturing-scale, particularly the impossibility of keeping the same tip speed (which influences peak shear, and, therefore, particle breakage) and power per unit volume (which influences the blending time and the particle suspension) at the same time.[10–13] In contrast, continuous crystallization offers several advantages in each of these challenges. Continuous crystallization processes require small equipment and space, which makes them efficient and high throughput, and reduces safety hazards. Also, they have short supply chains, which allow fast response to market shortage and eliminates (or at least reduces) the storage/shipping costs for intermediates. In addition, continuous crystallization processes are simpler to develop, monitor and control because their key characteristics are roughly constant at all times, which reduces batch-to-batch variations and eliminates some downstream corrective operations. Therefore, continuous crystallization has been attracting the interest of more and more pharmaceutical companies.[11,14–17]

1.2 Thesis Motivation

The advent of continuous manufacturing in the pharmaceutical industry has encouraged the development of new crystallizers specifically designed for continuous crystallization. There are basically two ideal models of continuous crystallizers: the mixed suspension mixed product removal (MSMPR) crystallizer and the plug flow crystallizer (PFC), which are analogous to the continuous stirred tank reactor and the plug flow reactor in the chemical reaction engineering. On the basis of these two models, many other continuous crystallizers have been developed. The oscillatory flow crystallizer (OFC), a relatively recent variant of the PFC, is one of the examples.

A conventional OFC consists of a tubular crystallizer containing evenly spaced orifice baffles where a periodically oscillating motion is superimposed on the net flow – **Figure 1.1**. The interaction between the oscillating fluid and the baffles results in the generation and cessation of vortices, which provides both axial and radial mixing in the tube. This creates zones of uniform mixing in each inter-baffle cell, and the OFC itself can be regarded as a series of well mixed cells with an overall plug flow behavior.

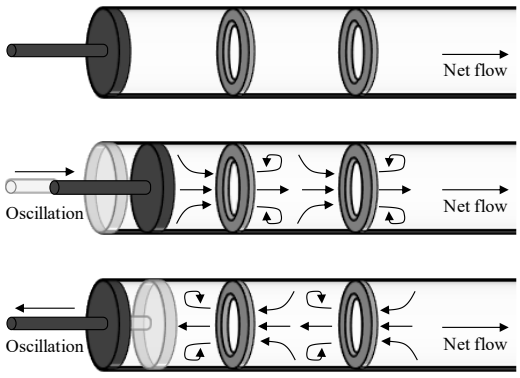


Figure 1.1 – Oscillatory flow crystallizer.

OFCs have been used for the continuous crystallization of a variety of products, including aspirin,[18] L-glutamic acid,[19] lactose,[20,21] paracetamol,[22,23] salicylic acid,[24] benzoic acid,[25] α-lipoic acid:nicotinamide[26] and an unspecified API.[12] One of the major benefits provided by OFCs is their close to plug flow behavior, which allows to produce crystals with narrow CSDs. This is important for pharmaceutical crystallization because the CSD determines the API dissolution profile and, consequently, its bioavailability, and plays a key role in the efficiency of downstream operations, such as filtration, drying and formulation.[10,13]

Besides the conventional orifice baffles, several other baffle types have been developed, including integral, central axial, round-edged helical, sharp-edged helical, sharp-edged helical with a central insert and wire wool baffles. Integral baffles are particularly useful for continuous crystallization, especially when they are designed with smooth periodic constrictions (SPC) instead of sharp edge periodic constrictions (SEPC). This is because OFCs with SPC generally require a lower amplitude of oscillation to fully suspend solids than OFCs with SEPC

of the same size ratio,[27] presumably due to the formation of stagnant zones close to the SEPC.[28] Additionally, OFCs with SPC also display more uniform mixing and less extent of backmixing than OFCs with SEPC.[27]

Despite their mixing efficiency, some problems related to the suspension and flowability of solids in tubular-OFCs have been reported lately.[27] In some cases, the formation of encrustations on the surfaces of the tubes has even lead to loss of control, blockages and, ultimately, process shut-down.[19,22,25] To overcome these limitations, a new variant of OFCs, known as planar-OFCs, was recently developed.[29] The main difference between a planar-OFC and a conventional tubular-OFC lies in its cross-section, which is rectangular rather than circular – **Figure 1.2**. Therefore, while in a tubular-OFC the constriction section is more elevated than the straight section, which restrains the flow of solids along the tube due to the accumulation of solids close to the constrictions, in a planar-OFC the constriction section and the straight section are at the same level, which facilitates the flow of solids along the channel. Another important feature of a planar-OFC is its design with SPC, which also facilitates the suspension of solids. However, despite their great potential, planar-OFCs have not yet been used for the continuous crystallization of APIs. This will be the main subject of this thesis.

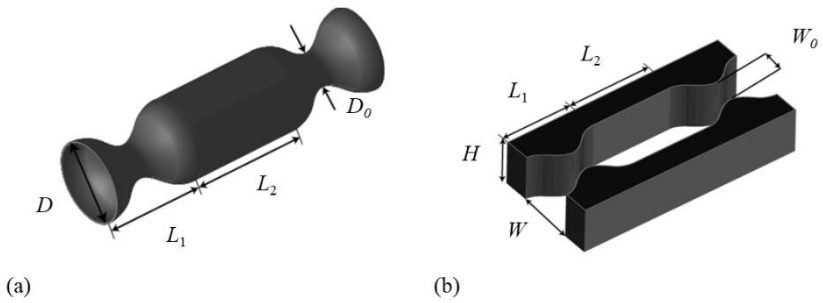


Figure 1.2 – (a) Tubular-OFC with SPC. (b) Planar-OFC with SPC. D is the tube diameter in the straight section, D_0 is the tube diameter in the constriction, L_1 is the constriction length, L_2 is the straight section length, W is the channel width in the straight section, W_0 is the channel width in the constriction, and H is the channel height.

1.3 Thesis Goals

The main goal of this thesis was to investigate how continuous crystallization processes can be implemented in planar-OFCs to produce APIs with narrow CSDs. To accomplish this goal, the geometry of the planar-OFC was optimized to facilitate the suspension of solids, maximize the mixing efficiency, and minimize the axial dispersion during continuous crystallization, and the operating conditions in the planar-OFC were manipulated to control the nucleation and crystal growth kinetics during continuous crystallization.

1.4 Thesis Outline

This thesis is divided into eleven chapters.

Chapter 1 – Introduction

Chapter 1 introduces the thesis scope, motivation and goals, and describes the thesis outline.

Chapter 2 – Crystallization Theory

Chapter 2 presents basic concepts related to the crystallization theory, including supersaturation, homogeneous and heterogeneous primary nucleation, secondary nucleation, crystal growth and agglomeration.

Chapter 3 – Literature Review

Chapter 3 presents the basic operating principles of an OFC, and reviews the relevant literature on the hydrodynamic characterization of tubular-OFCs, with a special focus on suspension of solids, mixing efficiency and axial dispersion, and on the batch and continuous crystallization in tubular-OFCs, with a special focus on crystallization kinetics, including nucleation and crystal growth kinetics, and control of final properties, including purity, crystal size, crystal shape, polymorphism, and enantiomorphism.

Chapter 4 – Suspension of Solids in Planar Oscillatory Flow Crystallizers

Chapter 4 explains how the suspension of solids is affected by the oscillation conditions and the geometric parameters in a planar-OFC. The minimum mixing intensity required to fully suspend different concentrations of polyvinyl chloride (PVC) particles in water was determined in three planar-OFCs with different geometries. The experimental conditions were chosen to simulate typical conditions during pharmaceutical crystallization: diameter of the particles between 100 and 200 μm, density of the fluid close to 1 g cm^{-3} and concentration of solids between 10 and 30% (w/w). In this chapter, the experiments were performed in batch.

Chapter 5 – Mixing Time in Planar Oscillatory Flow Crystallizers

Chapter 5 explains how the mixing time is affected by the oscillation conditions and the geometric parameters in a planar-OFC. The time required to reach a specific degree of concentration uniformity after an injection of a tracer was determined in three planar-OFCs with different geometries. The mixing time was determined for a

homogeneous system using indigo carmine as a liquid tracer, and for a heterogeneous system using particles of PVC as a solid tracer. In this chapter, the experiments were performed in batch.

Chapter 6 – Axial Dispersion in Planar Oscillatory Flow Crystallizers

Chapter 6 explains how the axial dispersion is affected by the oscillation conditions and the geometric parameters in a planar-OFC. The residence time distribution was determined in three planar-OFCs with different geometries. The axial dispersion was determined for a homogeneous system using indigo carmine as a liquid tracer, and for a heterogeneous system using particles of PVC as a solid tracer. In this chapter, the experiments were performed in continuous.

Chapter 7 – Nucleation Kinetics in a Planar Oscillatory Flow Crystallizer

Chapter 7 explains how the nucleation kinetics are affected by the oscillation conditions in a planar-OFC. In this chapter, the batch isothermal crystallization of paracetamol from aqueous solutions was used as a case study. The nucleation rate was calculated from the probability distribution of detection times, and the kinetic and thermodynamic parameters were estimated from the classical nucleation theory

Chapter 8 – Crystal Growth Kinetics in a Planar Oscillatory Flow Crystallizer

Chapter 8 explains how the crystal growth kinetics are affected by the oscillation conditions in a planar-OFC. In this chapter, the batch isothermal crystallization of paracetamol from mixtures of ethanol and water was used as a case study. An empirical power-law equation was used to describe the influence of supersaturation on the crystal growth rate, and the crystal growth kinetic parameters were estimated by fitting a mass balance equation to the experimental desupersaturation data.

Chapter 9 – Continuous Cooling Crystallization in a Planar Oscillatory Flow Crystallizer

Chapter 9 describes how a continuous cooling crystallization process can be implemented in a planar-OFC. In this chapter, the continuous cooling crystallization of paracetamol from mixtures of ethanol and water was used as a case study. The main goal was to produce crystals with a narrow CSD.

Chapter 10 – Continuous Antisolvent Crystallization in a Planar Oscillatory Flow Crystallizer

Chapter 10 describes how a continuous antisolvent crystallization process can be implemented in a planar-OFC. In this chapter, the continuous antisolvent crystallization of a model API was used as a case study. The main goal was to produce small crystals to meet very specific formulation requirements and, simultaneously, promote the aggregation of these small particles to optimize the filtration operation.

Chapter 11 – Final Remarks

Chapter 11 presents the main conclusions of this thesis and proposes future work.

Notation

Acronyms		**Latin Symbols**	
API	Active pharmaceutical ingredient	D	Tube diameter in the straight section
CSD	Crystal size distribution	D_0	Tube diameter in the constriction
MSMPR	Mixed suspension mixed product removal	H	Channel height
OFC	Oscillatory flow crystallizer	L_1	Constriction length
PFC	Plug flow crystallizer	L_2	Straight section length
PVC	Polyvinyl chloride	W	Channel width in the straight section
SEPC	Sharp edge periodic constrictions	W_0	Channel width in the constriction
SPC	Smooth periodic constrictions		

References

(1) Crosby, T. Designing For the Future of Continuous Processing. *Pharm. Process.* **2006**, *22* (1).

(2) Mollan, M. J.; Lodaya, M. Continuous Processing in Pharmaceutical Manufacturing. *Pharmaceutical Manufacturing*. 2004, pp 1–10.

(3) Plumb, K. Continuous Processing in the Pharmaceutical Industry: Changing the Mind Set. *Chem. Eng. Res. Des.* **2005**, *83* (6), 730–738.

(4) Kossik, J. Think Small: Pharmaceutical Facilities Could Boost Capacity and Slash Costs by Trading in Certain Batch Operations for Continuous Versions. 2002.

(5) Swichtenberg, B. Moving Beyond the Batch. *Pharm. Manuf.* **2008**, *7* (1), 24–26.

(6) Manning, R.; Sciacca, R. *Continuous Manufacturing in Pharmaceutical Industry: Economic and Policy*

Issues; Bates White Economic Consulting, 2018.

(7) Dallinger, D.; Kappe, C. O. Why Flow Means Green – Evaluating the Merits of Continuous Processing in the Context of Sustainability. *Curr. Opin. Green Sustain. Chem.* **2017**, *7*, 6–12.

(8) Mullin, J. W. *Industrial Crystallization*; Springer US, 1976.

(9) Myerson, A. S. *Handbook of Industrial Crystallization*, 2nd ed.; Butterworth-Heinemann: Boston, 2002.

(10) Chen, J.; Sarma, B.; Evans, J. M. B.; Myerson, A. S. Pharmaceutical Crystallization. *Cryst. Growth Des.* **2011**, *11* (4), 887–895.

(11) Lee, S. L.; O'Connor, T. F.; Yang, X.; Cruz, C. N.; Chatterjee, S.; Madurawe, R. D.; Moore, C. M. V.; Yu, L. X.; Woodcock, J. Modernizing Pharmaceutical Manufacturing: From Batch to Continuous Production. *J. Pharm. Innov.* **2015**, *10* (3), 191–199.

(12) Lawton, S.; Steele, G.; Shering, P.; Zhao, L.; Laird, I.; Ni, X.-W. Continuous Crystallization of Pharmaceuticals Using a Continuous Oscillatory Baffled Crystallizer. *Org. Process Res. Dev.* **2009**, *13* (6), 1357–1363.

(13) Variankaval, N.; Cote, A. S.; Doherty, M. F. From Form to Function: Crystallization of Active Pharmaceutical Ingredients. *AIChE J.* **2008**, *54* (7), 1682–1688.

(14) Wang, T.; Lu, H.; Wang, J.; Xiao, Y.; Zhou, Y.; Bao, Y.; Hao, H. Recent Progress of Continuous Crystallization. *J. Ind. Eng. Chem.* **2017**, *54*, 14–29.

(15) Baxendale, I. R.; Braatz, R. D.; Hodnett, B. K.; Jensen, K. F.; Johnson, M. D.; Sharratt, P.; Sherlock, J. P.; Florence, A. J. Achieving Continuous Manufacturing: Technologies and Approaches for Synthesis, Workup, and Isolation of Drug Substance. *J. Pharm. Sci.* **2015**, *104* (3), 781–791.

(16) McGlone, T.; Briggs, N. E. B.; Clark, C. A.; Brown, C. J.; Sefcik, J.; Florence, A. J. Oscillatory Flow Reactors (OFRs) for Continuous Manufacturing and Crystallization. *Org. Process Res. Dev.* **2015**, *19* (9), 1186–1202.

(17) Mascia, S.; Heider, P. L.; Zhang, H.; Lakerveld, R.; Benyahia, B.; Barton, P. I.; Braatz, R. D.; Cooney, C. L.; Evans, J. M. B.; Jamison, T. F.; Jensen, K. F.; Myerson, A. S.; Trout, B. L. End-to-End Continuous Manufacturing of Pharmaceuticals: Integrated Synthesis, Purification, and Final Dosage Formation. *Angew. Chemie - Int. Ed.* **2013**, *52* (47), 12359–12363.

(18) Caldeira, R.; Ni, X. Evaluation and Establishment of a Cleaning Protocol for the Production of Vanisal Sodium and Aspirin Using a Continuous Oscillatory Baffled Reactor. *Org. Process Res. Dev.* **2009**, *13* (6), 1080–1087.

(19) Briggs, N. E. B. B.; Schacht, U.; Raval, V.; McGlone, T.; Sefcik, J.; Florence, A. J. Seeded

Crystallization of β-L-Glutamic Acid in a Continuous Oscillatory Baffled Crystallizer. *Org. Process Res. Dev.* **2015**, *19* (12), 1903–1911.

(20) Siddique, H.; Brown, C. J.; Houson, I.; Florence, A. J. Establishment of a Continuous Sonocrystallization Process for Lactose in an Oscillatory Baffled Crystallizer. *Org. Process Res. Dev.* **2015**, *19* (12), 1871–1881.

(21) Tahir, F.; Krzemieniewska-Nandwani, K.; Mack, J.; Lovett, D.; Siddique, H.; Mabbott, F.; Raval, V.; Houson, I.; Florence, A. Advanced Control of a Continuous Oscillatory Flow Crystalliser. *Control Eng. Pract.* **2017**, *67*, 64–75.

(22) Agnew, L. R.; McGlone, T.; Wheatcroft, H. P.; Robertson, A.; Parsons, A. R.; Wilson, C. C. Continuous Crystallization of Paracetamol (Acetaminophen) Form II: Selective Access to a Metastable Solid Form. *Cryst. Growth Des.* **2017**, *17* (5), 2418–2427.

(23) Jiang, M.; Ni, X.-W. Reactive Crystallization of Paracetamol in a Continuous Oscillatory Baffled Reactor. *Org. Process Res. Dev.* **2019**, *23* (5), 882–890.

(24) Brown, C. J.; Adelakun, J. A.; Ni, X.-W. Characterization and Modelling of Antisolvent Crystallization of Salicylic Acid in a Continuous Oscillatory Baffled Crystallizer. *Chem. Eng. Process. Process Intensif.* **2015**, *97*, 180–186.

(25) Peña, R.; Oliva, J. A.; Burcham, C. L.; Jarmer, D. J.; Nagy, Z. K. Process Intensification through Continuous Spherical Crystallization Using an Oscillatory Flow Baffled Crystallizer. *Cryst. Growth Des.* **2017**, *17* (9), 4776–4784.

(26) Zhao, L.; Raval, V.; Briggs, N. E. B.; Bhardwaj, R. M.; McGlone, T.; Oswald, I. D. H.; Florence, A. J. From Discovery to Scale-up: α-Lipoic Acid : Nicotinamide Co-Crystals in a Continuous Oscillatory Baffled Crystalliser. *CrystEngComm* **2014**, *16* (26), 5769–5780.

(27) Ejim, L. N.; Yerdelen, S.; McGlone, T.; Onyemelukwe, I.; Johnston, B.; Florence, A. J.; Reis, N. M. A Factorial Approach to Understanding the Effect of Inner Geometry of Baffled Meso-Scale Tubes on Solids Suspension and Axial Dispersion in Continuous, Oscillatory Liquid–Solid Plug Flows. *Chem. Eng. J.* **2017**, *308*, 669–682.

(28) Harvey, A. P.; Mackley, M. R.; Reis, N.; Teixeira, J. A.; Vicente, A. A. The Fluid Mechanics Relating to a Novel Oscillatory Flow Micro Reactor. *4th Eur. Congr. Chem. Eng.* **2003**, 0-6.4-004.

(29) Ferreira, A.; Rocha, F.; Teixeira, J. A.; Castro, F. Modular Oscillatory Flow Plate Reactor. WO 2017/175207 A1, 2017.

This page was intentionally left in blank

Chapter 2 - Crystallization Theory

Crystallization is an important separation and purification process, which is particularly critical for the pharmaceutical industry because more than 90% of all active pharmaceutical ingredients (APIs) are crystals of small organic molecules.[1] The crystallization process consists of a phase change in which a crystalline product is obtained from a solution, *i.e.* a mixture of two or more species that form a homogeneous single phase, which might be liquid, solid or gaseous.[2] Crystallization from liquid solutions, consisting of a solid solute dissolved in a liquid solvent, is the most common and will be covered in more detail in this work.

The concentration of saturation, or solubility, is the maximum amount of solute that can be dissolved in a given amount of solvent at a given temperature. Solutions are classified as unsaturated, saturated or supersaturated as the concentration of solute is less than, equal or greater than solubility, respectively.[2] The state of supersaturation is required for crystallization because the difference between the chemical potential of a given solute i in a supersaturated solution, μ_i^*, and in a saturated solution, μ_i^s, is the fundamental driving force for crystallization. The chemical potentials μ_i^* and μ_i^s are calculated as:

$$\mu_i^* = \mu_i^0 + RT \ln a_i^* = \mu_i^0 + RT \ln \gamma_i^* C_i^* \quad \textbf{(2.1)}$$

$$\mu_i^s = \mu_i^0 + RT \ln a_i^s = \mu_i^0 + RT \ln \gamma_i^s C_i^s \quad \textbf{(2.2)}$$

where R is the ideal gas constant, T is the temperature, μ^0 is the standard chemical potential, a is the activity, γ is the coefficient of activity, and C is the concentration in solution. The indices i, s and $*$ refer to solute i, in saturated solution and in supersaturated solution, respectively. Thus, the difference of chemical potentials, $\Delta\mu$, results from the subtraction of **Equations (2.1)** and **(2.2)**:

$$\frac{\Delta\mu}{RT} = \ln \frac{a_i^*}{a_i^s} = \ln \frac{\gamma_i^* C_i^*}{\gamma_i^s C_i^s} \quad \textbf{(2.3)}$$

However, the coefficient of activity of the solute is usually not known. Therefore, the supersaturation is usually expressed as concentration driving force, ΔC, supersaturation ratio, S, or relative supersaturation, σ.[2] These variables are defined as:

$$\Delta C = C - C^s \quad \textbf{(2.4)}$$

$$S = \frac{C}{C^s} \quad \textbf{(2.5)}$$

$$\sigma = \frac{C - C^s}{C^s} \quad \textbf{(2.6)}$$

2.1 Nucleation

Crystallization can be described as a two-step process. In the first step, a stable solid phase arises in the form of nuclei and in the second step these nuclei become larger crystals by subsequent deposition of solute. These two steps are known as nucleation and crystal growth, respectively.

The nucleation mechanism can be classified as either primary or secondary, as it occurs in the absence or in the presence of solute crystals, respectively. Primary nucleation can be further classified as heterogeneous or homogeneous as it occurs with or without the interference of foreign particles, respectively.[3] The Ostwald-Miers diagram shows the relationship between supersaturation and the probability of homogeneous (or spontaneous) nucleation – **Figure 2.1**. The solid line represents the solubility curve and the dashed line represents the supersaturation curve. The supersaturation curve is not as well defined as the solubility curve as its position in the diagram depends on, amongst other things, the rate at which supersaturation is generated and the intensity of agitation. The gap between the two curves defines the metastable zone.[4]

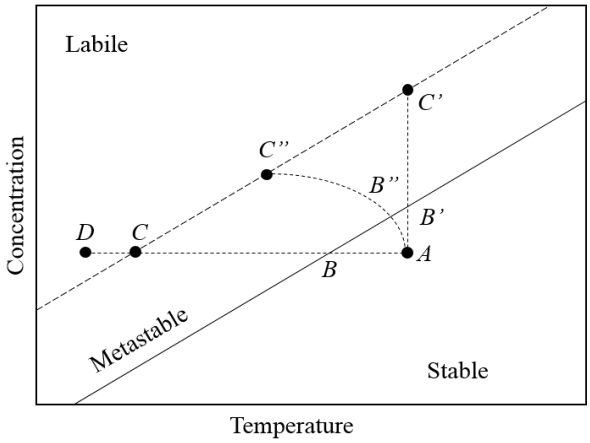


Figure 2.1 – Ostwald-Miers diagram. Adapted from reference 4.

The interpretation of this diagram implies the analysis of three zones: the stable (unsaturated) zone, where crystallization is impossible because the chemical potential of the solution is less than the chemical potential of the solid phase, and the crystal tends to dissolve; the metastable (supersaturated) zone, where spontaneous nucleation is improbable, but crystal growth may occur on the surface of a seed (solute crystal or impurity); and the unstable or labile (supersaturated) zone, where spontaneous nucleation is probable, but not inevitable.

2.1.1 Methods to Create Supersaturation

When a solution represented by point A in **Figure 2.1** is cooled down without loss of solvent, the nucleation process might be induced by seeding, agitation or mechanical shock somewhere between point B and C, or it might be spontaneously triggered by further cooling to some point D. This cooling trajectory is the most common method to generate supersaturation and induce nucleation.[4]

Alternatively, some of the solvent can be removed from the solution by evaporation to increase the concentration of the system and eventually achieve supersaturation. When this operation is carried out at constant temperature the system follows a trajectory similar to line AB'C' in **Figure 2.1**.[4] This method is often employed when the solvent is non-aqueous and has a relatively high vapor pressure.[2]

It is also very common to use a combination of cooling and evaporation to generate supersaturation by decreasing simultaneously the pressure and the temperature of the system.[5] Such operation is typically known as vacuum crystallization and follows a trajectory similar to line AB"C" in **Figure 2.1**.

The fourth option consists in adding a second solvent to the solution so as to create a mixed solvent system in which the solubility of the solute is greatly decreased. A material should be chosen that is miscible with the solute-solvent system and in which the solute is not soluble. This method is commonly known as drowning out or antisolvent and is particularly useful for the crystallization of organic compounds.[2]

Finally, it is also possible to generate supersaturation through chemical reaction of two soluble materials that form a product with low solubility. This method is commonly known as precipitation or reactive crystallization and is particularly useful for the crystallization of inorganic compounds.[2]

2.1.2 Primary Nucleation

Homogeneous Nucleation

At a given temperature, the average concentration of a supersaturated solution is constant, however, local fluctuations of concentration might lead to the formation of aggregates (or clusters). The classical nucleation theory states that these clusters are formed in solution through a mechanism of addition that succeeds until a critical size is reached.[6] Therefore, the nucleation rate, J, defined as the number of nuclei formed per unit of time per unit of volume, can be obtained from an Arrhenius-type equation as the product of the concentration of critical nuclei in solution – exponential term of **Equation (2.7)** – and the rate of addition of one further building block – pre-exponential term of **Equation (2.7)**:

$$J = A\exp\left(\frac{-\Delta G_{crit}}{kT}\right) \qquad \textbf{(2.7)}$$

where A is a factor related to the frequency of molecular collision, ΔG_{crit} is the excess free energy barrier that must be surpassed so that primary homogeneous nucleation occurs, k is the Boltzmann constant, and T is the temperature.[7]

The overall excess free energy between a particle of solute and the solute in solution, ΔG, results from the contribution of the surface excess free energy, ΔG_S, and the volume excess free energy, ΔG_V. Thus:

$$\Delta G = \Delta G_S + \Delta G_V = \beta L^2 \gamma + \alpha L^3 \Delta G_V \quad \textbf{(2.8)}$$

where γ is the surface tension, and β and α are the area and volume shape factors, based on the characteristic length L, respectively. Considering a spherical nuclei, whose characteristic length is the diameter, d, the area factor is $\beta = \pi$ and the volume factor is $\alpha = \pi/6$. Therefore, for a spherical nucleus:

$$\Delta G = 4\pi r^2 \gamma + \frac{4}{3}\pi r^3 \Delta G_V \quad \textbf{(2.9)}$$

where r is the nucleus radius.

The free energy diagram, where the excess free energies ΔG_S and ΔG_V as well as the overall excess free energy ΔG are plotted against the nucleus radius, is presented in **Figure 2.2**.

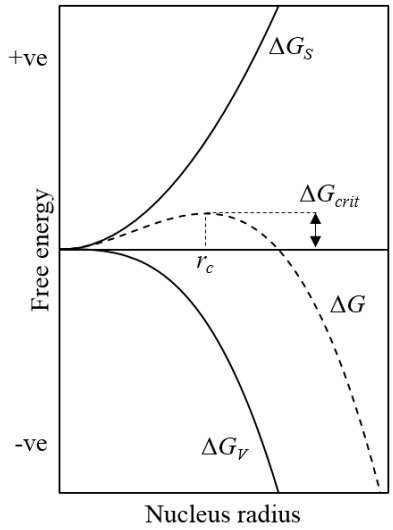


Figure 2.2 – Free energy diagram. Adapted from reference 8.

This figure shows that the overall excess free energy ΔG passes through a maximum because the excess free energies ΔG_S and ΔG_V are of opposite sign. The maximum value, ΔG_{crit}, corresponds to the critical nucleus, r_c,

which is thermodynamically stable. **Figure 2.2** shows that, since the system always evolves towards the minimum free energy, a newly created cluster will either grow or redissolve depending on its size. Clusters smaller than r_c will redissolve and clusters larger than r_c will continue to grow.[3] Therefore, ΔG_{crit} is the excess free energy barrier that must be surpassed so that primary nucleation occurs.

For a spherical nucleus, r_c is obtained by maximizing **Equation (2.9)** with $d\Delta G/dr = 0$*:*

$$\frac{d\Delta G}{dr} = 8\pi r_c \gamma + 4\pi r_c^2 \Delta G_V = 0 \qquad \textbf{(2.10)}$$

Therefore:

$$r_c = \frac{-2\gamma}{\Delta G_V} \qquad \textbf{(2.11)}$$

From **Equations (2.9)** and **(2.11)** we get:

$$\Delta G_{crit} = \frac{4\pi\gamma r_c^2}{3} \qquad \textbf{(2.12)}$$

On the other hand, the growth of clusters is governed by the Gibbs-Thompson equation:[9]

$$\ln S = \frac{2\gamma v}{kTr} \qquad \textbf{(2.13)}$$

where S is the supersaturation ratio, and v is the molecular volume. Joining **Equations (2.12)** and **(2.13)** together for $r = r_c$ we get:

$$\Delta G_{crit} = \frac{16\pi\gamma^3 v^2}{3(kT\ln S)^2} \qquad \textbf{(2.14)}$$

Hence, from **Equation (2.7)**:

$$J = A\exp\left(\frac{-16\pi\gamma^3 v^2}{3k^3T^3(\ln S)^2}\right) \qquad \textbf{(2.15)}$$

It is now clear that three main variables control the nucleation rate: the temperature, the supersaturation, and the surface tension. The supersaturation influences both terms of **Equation (2.15)**, but the dependence of the pre-exponential term is only linear, whereby it is often neglected. Moreover, the solvent is expected to influence the surface tension and also the pre-exponential term through the mobility of the molecules in the solution.[7]

However, it has been found that **Equation (2.15)** predicts nucleation rates only at extremely high supersaturation, whereby it is often approximated to a power law equation.[10] This equation is based on the concept of metastable limit and predicts the dependence of the nucleation rate, B_0, on the supersaturation, expressed as concentration driving force, ΔC, or relative supersaturation, σ, with two correlation parameters: the nucleation rate coefficient, k_b, and the nucleation rate order, b:

$$B_0 = k_b \Delta C^b \text{ or } B = k_b \sigma^b \tag{2.16}$$

Heterogeneous Nucleation

As previously mentioned, nucleation may also occur on the top of a foreign particle, which is known to reduce the overall excess free energy associated with the formation of a critical nucleus.[3] Therefore:

$$\Delta G_{crit}^{'} = \varphi \Delta G_{crit} \tag{2.17}$$

where $\Delta G_{crit}^{'}$ is the excess free energy associated with the formation of a critical nucleus under heterogeneous conditions, and φ is a factor less than unity. The factor φ depends on the angle of contact between the crystalline deposit and the surface of the foreign particle, θ, as:

$$\varphi = \frac{(2 + \cos\theta)(1 - \cos\theta)^2}{4} \tag{2.18}$$

The angle of contact depends on the surface tension between the three phases: the crystalline deposit, the foreign particle and the supersaturated solution. **Figure 2.3** shows a surface energy diagram for the three phases in contact. γ_{cl} is the surface tension between the crystalline deposit and the liquid, γ_{sl} is the surface tension between the foreign particle and the liquid, and γ_{cs} is the surface tension between the crystalline deposit and the foreign particle.

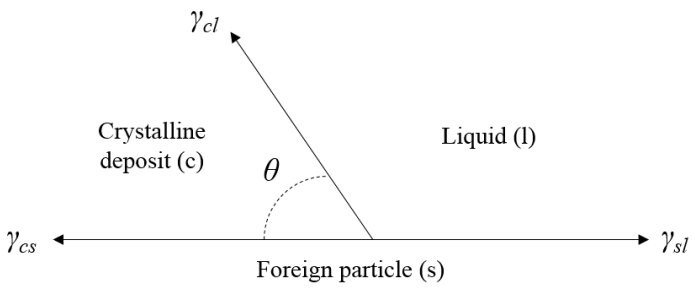


Figure 2.3 – Surface energy diagram. Adapted from reference 8.

In the horizontal direction:

$$\gamma_{sl} = \gamma_{cs} + \gamma_{cl}\cos\theta \Leftrightarrow \cos\theta = \frac{\gamma_{sl} - \gamma_{cs}}{\gamma_{cl}} \quad \textbf{(2.19)}$$

When the crystalline deposit has no affinity with the foreign particle: $\theta = 180°$, $\cos\theta = -1$ and $\varphi = 1$. Thus $\Delta G_{crit}^{'} = \Delta G_{crit}$, *i.e.* the overall excess free energy of nucleation is the same as that required for homogeneous nucleation. When the crystalline deposit has partial affinity with the foreign particle: $0° < \theta < 180°$ and $\varphi < 1$. Thus $\Delta G_{crit}^{'} < \Delta G_{crit}$, *i.e.* the overall excess free energy is less than that required for homogeneous nucleation. Finally, when the crystalline deposit has complete affinity with the foreign particle: $\theta = 0°$ and $\varphi = 0$. Thus $\Delta G_{crit}^{'} = 0$, *i.e.* the overall excess free energy required tends towards zero. This corresponds to seeding a supersaturated solution with crystals of solute – secondary nucleation. These three situations are presented in **Figure 2.4.**

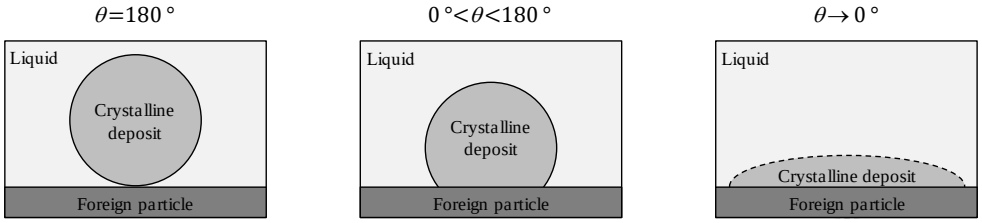


Figure 2.4 – Heterogeneous nucleation when θ=180 ° (on the left), 0 °<θ<180 ° (on the middle) and θ=0 ° (on the right).

2.1.3 Secondary Nucleation

Secondary nucleation occurs at or in the direct vicinity of a parent crystal surface, also known as a seed.[11] Several mechanisms are proposed in the literature to describe secondary nucleation. These mechanisms trace back the origin of secondary nuclei to the solution layer adjacent to the crystal surface or to the parent crystal itself.[12] The former category includes contact nucleation and fluid shear, while the latter includes initial breeding, needle breeding and attrition.[6]

Contact nucleation occurs when clusters of solute loosely ordered in the adsorption layer adjacent to the surface of a seed are torn away by mechanical forces.[6] The number of contact nuclei generated increases as supersaturation increases as a result of two main contributions: first, the critical nucleus size decreases with supersaturation, which increases the number of displaced clusters that subsist in the bulk; and second, the thickness of the adsorption layer adjacent to the surface of a seed increases with supersaturation, which increases the number of clusters available for contact nucleation.[13]

Fluid shear nucleation also relies on the principle of removing adsorbed molecules from the adsorption layer, but as a result of fluid shear instead of mechanical forces.[6,14] High levels of fluid shear are usually found in industrial crystallizers, however, for this mechanism to be dominant, it needs to be combined with high levels of supersaturation for a considerably extensive period of time.[13,15]

Initial breeding may occur when a seed is added to a supersaturated solution.[15] Small crystalline particles that occasionally grow on the surface of a seed are swept off when the seed comes into contact with the liquid. Some of these fragments may be larger than the critical nucleus size and act as stable nucleation sites.[6] However, the number of fines on the surface of a seed is limited and initial breeding cannot serve as a sustained source of nucleation.[13]

Needle breeding occurs when needle shaped crystalline structures growing from a parent crystal are broken off by mechanical or fluid shear forces. The formation of these surface irregularities requires a rather high supersaturation level or the presence of habit modifying additives,[14] whereby this mechanism is considered very unlikely in industrial crystallizers.[15]

Attrition refers to crystal breakage resulting from either mechanical forces, such as crystal-crystal, crystal-crystallizer and crystal-stirrer contact, or fluid shear.[6] Several factors, including the operation conditions, such as agitation rate,[12] suspension density[16] and retention time,[17] and the mechanical properties of the crystals, such as hardness, fracture resistance and Young modulus,[18,19] are known to have a great impact on attrition rate.[20]

Although both contact nucleation and attrition depend on the collision energy, different outcomes distinguish the two mechanisms. First, in contrast with contact nucleation, which is supersaturation dependent, attrition, being a mechanical process, is not.[13] And second, while damaged parent crystals and macro-fragments are immediately detected under attrition, no visual changes are found under contact nucleation, which requires a time delay for the appearance of secondary nuclei of a detectable size.[15] Moreover, the energy required for attrition is far higher and a transition from contact nucleation to attrition prevalence is likely to occur when the collision energy increases.[13]

Considering the great complexity of these phenomena, the various models presented in the literature to predict the secondary nucleation rate are necessarily based on oversimplified assumptions.[21] Nevertheless, several correlations based on the power law model have been used to explain most of the experimental data satisfactorily. The power law model that predicts the dependence of the secondary nucleation rate on the supersaturation is identical to **Equation (2.16)**. However, in the case of secondary nucleation, the nucleation rate coefficient depends on, amongst other things, the degree of agitation, the suspension density and the characteristic length of the parent crystals.[22]

2.2 Crystal Growth

As soon as stable nuclei are formed in a supersaturated solution, they start to grow into crystals of visible size. Several models have been proposed in the literature to describe crystal growth, including surface energy, adsorption layer, kinematic and diffusion layer theories and the birth and spread model.[23] The diffusion layer theory, in particular, provides a reasonable parallelism between the crystal growth theory and the practical world of industrial crystallization, and is commonly used to correlate most of the experimental data from industrial crystallization processes.[6]

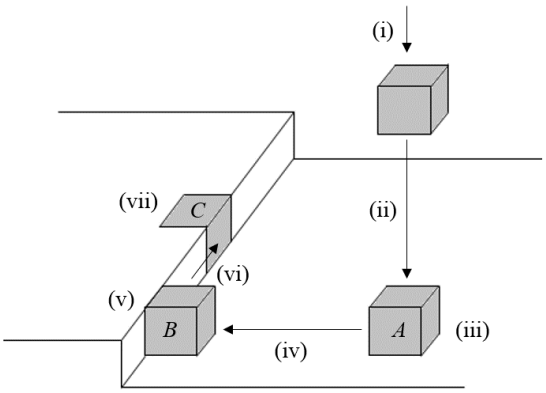


Figure 2.5 – Stages of crystal growth. Adapted from reference 8.

This theory envisages crystal growth as a two-step mechanism: first, the molecules of solute diffuse through the boundary layer to the crystal surface, and then are incorporated into the crystal surface. The molecules of solute can be incorporated into the crystal surface at three different sites, which can be distinguished by the number of bonds established between the molecule and the crystal. The three different sites are labeled as A, B and C on **Figure 2.5**. At site A, the molecule is attached only to the surface of a growing layer, at site B, the molecule is attached to both the surface and to a growing step, and at site C, the molecule is attached to more than two surfaces at what is known as a kink site. From an energetic point of view, C is more favorable than B, and B more favorable than A.[6] **Figure 2.5** also illustrates the different stages of crystal growth as explained by the diffusion layer theory: after the transport of solute to the neighborhood of the crystal surface (i) and subsequent diffusion through the boundary layer, adjacent to the surface (ii), the solute adsorbs on the crystal surface (iii), then diffuses over the surface (iv), attaches to a step (v), then diffuses along the step (vi) and finally integrates into the crystal at a kink site (vii).[24]

Therefore, for the single one-dimensional case shown in **Figure 2.6**, the rate of mass increase of the crystal must equal the diffusion rate through the boundary layer as:

$$\frac{dm}{dt} = k_d A(C - C_i) \tag{2.20}$$

where m is the mass of solid deposited in time t, k_d is the coefficient of mass transfer by diffusion, A is the surface area of the crystal, C is the concentration of solute in the bulk solution, and C_i is the concentration of solute at the crystal-solution interface.

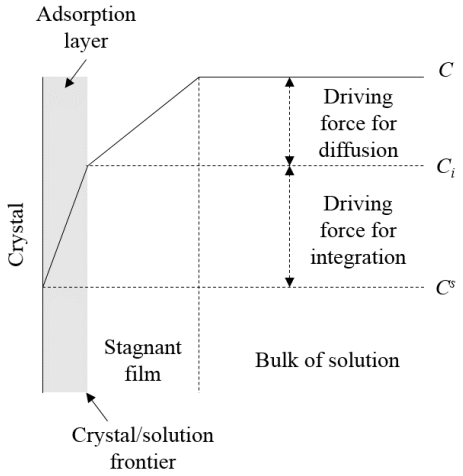


Figure 2.6 – Concentration driving forces. Adapted from reference 8.

On the other hand, the rate of solute integration into the crystal surface can be equated to an i-order reaction as:

$$\frac{dm}{dt} = k_i A(C_i - C^s)^i \tag{2.21}$$

where k_i is the coefficient of surface integration, and C^s is the solubility. If $i = 1$, then **Equations (2.20)** and **(2.21)** can be combined to obtain the overall crystal growth rate, R_G, as:

$$R_G = \frac{1}{A}\frac{dm}{dt} = k_g \Delta C \tag{2.22}$$

where:

$$\frac{1}{k_g} = \frac{1}{k_d} + \frac{1}{k_i} \tag{2.23}$$

where k_g is the overall coefficient of crystal growth.

In this case, when $k_d \ll k_i$, the crystal growth rate is diffusion controlled and $k_g = k_d$. When $k_i \ll k_d$, the crystal growth rate is integration controlled and $k_g = k_i$.

If $i = 2$, the combination of **Equations (2.20)** and **(2.21)** yields:

$$R_G = \frac{1}{2\,k_i/k_d^2}\left[1 + \frac{2k_i}{k_d}\Delta C - \left(\frac{4k_i}{k_d}\Delta C + 1\right)^{1/2}\right] \quad \textbf{(2.24)}$$

If $1 < i < 2$, an explicit expression cannot be obtained and the following approximation is typically used:

$$R_G = k_g \Delta C^g \quad \textbf{(2.25)}$$

where g is the growth rate order.

The overall coefficient of crystal growth, k_g, depends on the temperature and is usually fitted to an Arrhenius-type equation as:

$$k_g = A\exp\left(\frac{-E_G}{RT}\right) \quad \textbf{(2.26)}$$

where A is a constant and E_G is an activation energy. Therefore, a complete crystal growth rate expression that includes both the effect of temperature and supersaturation can be written as:

$$R_G = A\exp\left(\frac{-E_G}{RT}\right)\Delta C^g \quad \textbf{(2.27)}$$

The effectiveness factor for crystal growth, η, defined as the ratio of the measured growth rate to the expected growth rate with negligible diffusion resistance, provides a quantitative measure of the degree of diffusion or surface integration control.[25]

$$\eta = \frac{R_G}{k_i \Delta C^i} \quad \textbf{(2.28)}$$

As $\eta \to 1$, surface integration plays a larger and larger role in controlling growth rate.[6] When diffusion is the controlling step, the growth rate increases when the diffusion resistance in the boundary layer of the crystal surface decreases. This can be achieved by increasing the relative solid-liquid velocity, which is controlled by the mixing intensity. On the other hand, when surface integration is the controlling step, crystal growth rate increases rather weakly with mixing intensity.[26]

The crystal growth rate defined as a mass deposition rate, R_G (kg m^{-2} s^{-1}), can also be converted into an overall linear growth rate, G (m s^{-1}), or a mean face growth rate, $\bar{v}$ (m s^{-1}). The relationships between these quantities are:

$$R_G = k_g \Delta C^g = \frac{1}{A}\frac{dm}{dt} = \frac{3\alpha}{\beta}\rho_c G = \frac{3\alpha}{\beta}\rho_c \frac{dL}{dt} = \frac{6\alpha}{\beta}\rho_c \frac{dr}{dt} = \frac{6\alpha}{\beta}\rho_c \bar{v} \quad \textbf{(2.29)}$$

where ρ_c is the crystal density.

2.3 Agglomeration

Agglomeration occurs when smaller particles come together to form larger ones.[27] This term is understood to encompass three different phenomena: the formation of flocculates, whose cohesion forces are weak, the formation of agglomerates, whose cohesion forces are very strong, and the formation of aggregates, whose cohesion forces are intermediate to agglomerates and flocculates.[28] While flocculates and aggregates can be generated in saturated or undersaturated solutions, strong agglomerates, which are tightly bound by solid bridges, can only be generated in supersaturated solutions.[29] **Figure 2.7** shows that depending on the size of the particles, different force regimes are necessary. While intermolecular forces suffice to bind very small particles, liquid or solid bridges are necessary to bind larger ones.[28]

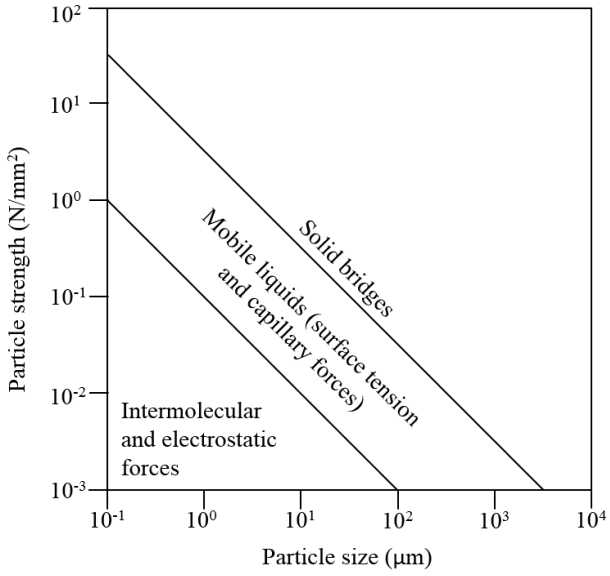


Figure 2.7 – Particle strength against particle size. Adapted from reference 29.

Agglomeration occurs in a two-step sequence of collision and adhesion. However, before colliding, the two particles have to be brought close together, which is only possible when the attractive forces prevail over the repulsive forces between them. Then, when the supersaturation is high and the two particles remain attached for

a sufficient period of time, a solid bridge is formed between the two particles which keeps them tightly bound together. This is illustrated in **Figure 2.8**.

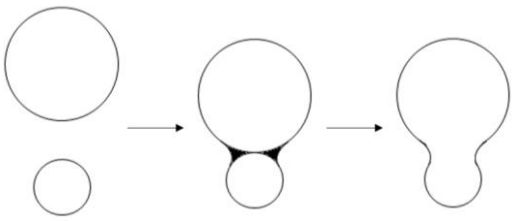


Figure 2.8 – Formation of a solid bridge after collision. Adapted from reference 29.

This mechanism is governed by a number of parameters, including the hydrodynamic conditions (such as mixing and local turbulence), the properties of the solvent (such as viscosity and density), the properties of the crystals (such as size and habit), the population density of the crystals, the supersaturation and respective growth rate, and the cohesion forces between the solvent, impurities, and the crystals.[29] As a rule, systems with high temperatures, low viscosities, small particle sizes, high particle concentrations and high diffusivities are prone to agglomeration. The role of the specific power input, which impacts the turbulence and the shear rate of the system, is more complex because it influences both the agglomeration rate and the disruption rate. However, it has often been observed that the increase of specific power input promotes first agglomeration and then disruption. Therefore, the size of the agglomerates is limited to a maximum value which corresponds to the maximum agglomeration rate.[29] This is illustrated in **Figure 2.9** where the number of particles per unit volume if qualitatively plotted against the specific power input for two different agglomerate sizes, L_{agg}, and two supersaturations, S.

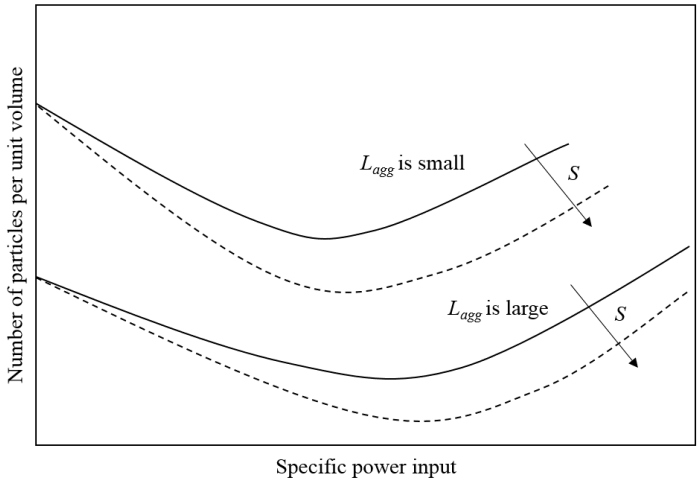


Figure 2.9 – Number of particles per unit volume against specific power input. Adapted from reference 29.

Notation

Acronyms	
API	Active pharmaceutical ingredient
Latin Symbols	
A	Pre-exponential constant
A	Crystal surface area
a_i^*	Activity of solute i in a supersaturated solution
a_i^s	Activity of solute i in a saturated solution
b	Nucleation rate order
B_0	Nucleation rate
C	Concentration of solute in the bulk
C	Concentration of solute at the crystal-solution interface
ΔC	Concentration driving force
C_i^*	Concentration of solute i in a supersaturated solution
C_i^s	Concentration of solute i in a saturated solution
d	Nucleus diameter
E_G	Activation energy
g	Growth rate order
G	Overall linear growth rate
ΔG	Overall excess free energy
ΔG_{crit}	Critical excess free energy for homogeneous nucleation
$\Delta G_{crit}^{'}$	Critical excess free energy for heterogeneous nucleation
ΔG_S	Surface excess free energy
ΔG_V	Volume excess free energy
i	Reaction order
J	Nucleation rate
k	Boltzmann constant
k_b	Nucleation rate coefficient
k_d	Diffusion mass transfer coefficient
k_g	Overall crystal growth coefficient
k_i	Surface integration coefficient
L	Characteristic length
L_{agg}	Agglomerate size
m	Mass of solid
r	Nucleus radius
R	Ideal gas constant
r_c	Nucleus critical radius
R_G	Overall crystal growth rate
S	Supersaturation ratio
t	Time
T	Temperature
v	Molecular volume
$\bar{v}$	Mean face growth rate
Greek Letters	
α	Volume shape factor
β	Area shape factor
γ	Surface tension
γ_{cl}	Surface tension between the crystalline deposit and the liquid
γ_{cs}	Surface tension between the crystalline deposit and the foreign particle
γ_i^*	Coefficient of activity of solute i in a supersaturated solution
γ_i^s	Coefficient of activity of solute i in a saturated solution
γ_{sl}	Surface tension between the foreign particle and the liquid
$\Delta\mu$	Difference of chemical potential
η	Crystal growth effectiveness factor
θ	Contact angle between the crystalline deposit and the foreign particle
μ_i^*	Chemical potential of a solute i in a supersaturated solution
μ_i^0	Standard chemical potential of solute i
μ_i^s	Chemical potential of a solute i in a saturated solution
ρ_c	Crystal density
σ	Relative supersaturation
φ	Factor less than unity

References

(1) Chen, J.; Sarma, B.; Evans, J. M. B.; Myerson, A. S. Pharmaceutical Crystallization. *Cryst. Growth Des.* **2011**, *11* (4), 887–895.

(2) Schwartz, A. M.; Myerson, A. S. Solutions and Solution Properties. In *Handbook of Industrial*

Crystallization; Myerson, A. S., Ed.; Elsevier: Boston, 2002; pp 1–31.

(3) Mullin, J. W. Nucleation. In *Crystallization*; Elsevier: Oxford, 2001; pp 181–215.

(4) Mullin, J. W. Solutions and Solubility. In *Crystallization*; Elsevier: Oxford, 2001; pp 86–134.

(5) Mersmann, A. Design of Crystallizers. In *Crystallization Technology Handbook*; Mersmann, A., Ed.; Marcel Dekker, Inc: New York, 2001; pp 323–392.

(6) Myerson, A. S.; Ginde, R. Crystals, Crystal Growth, and Nucleation. In *Handbook of Industrial Crystallization*; Myerson, A. S., Ed.; Butterworth-Heinemann: Boston, 2002; pp 33–65.

(7) Beckmann, W. Mechanisms of Crystallization. In *Crystallization: Basic Concepts and Industrial Applications*; Beckmann, W., Ed.; Wiley-VCH Verlag GmbH & Co. KGaA: Weinheim, Germany, 2013; pp 7–33.

(8) Mullin, J. W. *Crystallization*, 4th ed.; Butterworth-Heinemann: Oxford, 2001.

(9) Perez, M. Gibbs-Thomson Effects in Phase Transformations. *Scr. Mater.* **2005**, *52* (8), 709–712.

(10) Randolph, A. D.; Larson, M. A. Crystallization Kinetics. In *Theory of Particulate Processes*; Academic Press: New York and London, 1971; pp 101–110.

(11) van der Eerden, J. P.; Bruinsma, O. S. L. *Science and Technology of Crystal Growth*, 1st ed.; Springer Science & Business Media, B. V., 1995.

(12) Frawley, P. J.; Mitchell, N. A.; Ó'Ciardhá, C. T.; Hutton, K. W. The Effects of Supersaturation, Temperature, Agitation and Seed Surface Area on the Secondary Nucleation of Paracetamol in Ethanol Solutions. *Chem. Eng. Sci.* **2012**, *75*, 183–197.

(13) Agrawal, S. G.; Paterson, A. H. J. Secondary Nucleation: Mechanisms and Models. *Chem. Eng. Commun.* **2015**, *202* (5), 698–706.

(14) Melia, T. P.; Moffitt, W. P. Secondary Nucleation from Aqueous Solution. *Ind. Eng. Chem. Fundam.* **1964**, *3* (4), 313–317.

(15) Ottens, E. P. K. Nucleation in Continuous Agitated Crystallizers, PhD Thesis, Technical University of Delft, 1973.

(16) Ayazi Shamlou, P.; Jones, A. G.; Djamarani, K. Hydrodynamics of Secondary Nucleation in Suspension Crystallization. *Chem. Eng. Sci.* **1990**, *45* (5), 1405–1416.

(17) Nienow, A. W.; Conti, R. Particle Abrasion at High Solids Concentration in Stirred Vessels. *Chem. Eng. Sci.* **1978**, *33* (8), 1077–1086.

(18) Bravi, M.; Di Cave, S.; Mazzarotta, B.; Verdone, N. Relating the Attrition Behaviour of Crystals in a

Stirred Vessel to Their Mechanical Properties. *Chem. Eng. J.* **2003**, *94* (3), 223–229.

(19) Gahn, C.; Mersmann, A. Brittle Fracture in Crystallization Processes Part A. Attrition and Abrasion of Brittle Solids. *Chem. Eng. Sci.* **1999**, *54* (9), 1273–1282.

(20) Mersmann, A. Attrition and Attrition-Controlled Secondary Nucleation. In *Crystallization Technology Handbook*; Mersmann, A., Ed.; Marcel Dekker, Inc: New York, 2001; pp 187–234.

(21) Grootscholten, P. A. M.; De Leer, B. G. M.; De Jong, E. J.; Asselbergs, C. J. Factors Affecting Secondary Nucleation Rate of Sodium Chloride in an Evaporative Crystallizer. *AIChE J.* **1982**, *28* (5), 728–737.

(22) van der Heijden, A. E. D. M.; van der Eerden, J. P.; van Rosmalen, G. M. The Secondary Nucleation Rate: A Physical Model. *Chem. Eng. Sci.* **1994**, *49* (18), 3103–3113.

(23) Mullin, J. W. Crystal Growth. In *Crystallization*; Butterworth-Heinemann: Oxford, 2001; pp 216–288.

(24) Elwell, D.; Scheel, H. J. *Crystal Growth from High Temperature Solutions*; Academic Press, 1975.

(25) Garside, J. The Concept of Effectiveness Factors in Crystal Growth. *Chem. Eng. Sci.* **1971**, *26* (9), 1425–1431.

(26) Agrawal, S. G. Evaporative Crystallization of Alpha-Lactose Monohydrate, PhD Thesis, Massey University, 2012.

(27) Pietsch, W. *Agglomeration Processes: Phenomena, Technologies, Equipment*; Wiley-VCH Verlag GmbH: Weinheim, 2002.

(28) Beckmann, W. Agglomeration during Crystallization. In *Crystallization: Basic Concepts and Industrial Applications*; Beckmann, W., Ed.; Wiley-VCH Verlag GmbH & Co. KGaA: Weinheim, Germany, 2013; pp 75–84.

(29) Mersmann, A.; Braun, B. Agglomeration. In *Crystallization Technology Handbook*; Mersmann, A., Ed.; Marcel Dekker, Inc: New York, 2001; pp 235–284.

Chapter 3 - Literature Review

A conventional oscillatory flow crystallizer (OFC) is a tubular crystallizer with evenly spaced orifice baffles where a periodically oscillating motion is superimposed on the net flow. The OFC can be operated batchwise or continuously, in horizontal tubes or vertical columns. The oscillatory motion is created in the axial direction by moving baffles or moving fluid, by means of diaphragms, bellows or pistons, at one or both ends of the tube – **Figure 3.1**.[1]

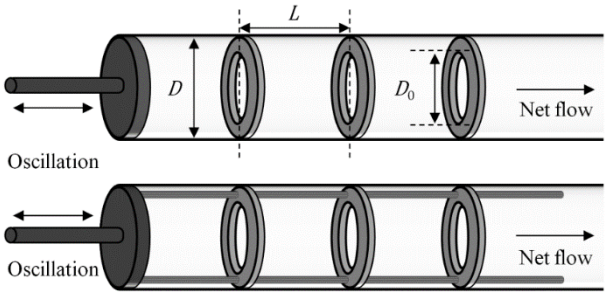


Figure 3.1 – OFC with moving fluid (on the top) and OFC with moving baffles (on the bottom). *D* is the tube diameter in the straight section; D_0 is the tube diameter in the constriction; *L* is the distance between constrictions.

While the mixed suspension mixed product removal (MSMPR) crystallizer and the plug flow crystallizer (PFC) rely on stirring mechanisms and turbulent flow conditions for mixing, the OFC relies on the interaction between the oscillating fluid and the baffles. The flow patterns in an OFC are generated by two half cycles. This mechanism is illustrated in **Figure 3.2**. First, the fluid accelerates as it passes through the baffles, forming vortex rings at downstream. Then, when the fluid reaches the maximum velocity, the flow is reversed and the vortices are swept into the bulk as the fluid decelerates.[2] The generation and cessation of vortices is controlled through a combination of geometric and operating parameters. This mechanism results in enhanced mixing in the region between two consecutive baffles, and the OFC itself can be regarded as a series of well mixed tanks with an overall plug flow behavior. Therefore, since mixing is independent of the throughput velocity, the OFC can be operated at low net flow rates, corresponding to the laminar regime in the absence of oscillations, while maintaining good mixing and plug flow behavior.[1] In this way, the OFC can accommodate longer residence times under effectively turbulent conditions with a reduced tube length compared to the corresponding PFC, which represents significant savings in terms of footprint and capital costs.[3]

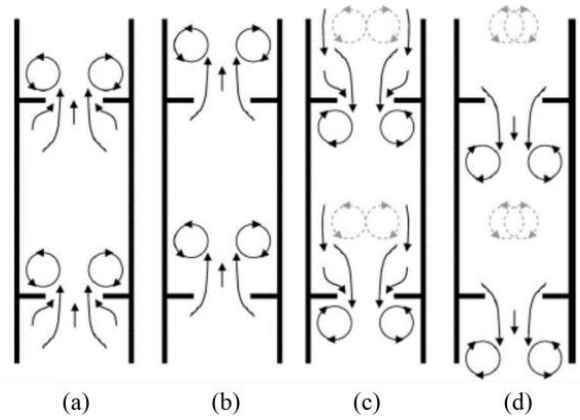


Figure 3.2 – Mechanism of oscillatory flow mixing. (a) start of up stroke; (b) maximum velocity in up stroke; (c) start of down stroke; (d) maximum velocity in down stroke. Reprinted from Chemical Engineering Journal, 112, Fitch, A. W., Jian, H., Ni, X., An investigation of the effect of viscosity on mixing in an oscillatory baffled column using digital particle image velocimetry and computational fluid dynamics simulation, 197–210, Copyright 2005, with permission from Elsevier B.V.

The overall fluid dynamic conditions in an OFC are governed by three dimensionless numbers: the net flow Reynolds number, Re, the oscillatory Reynolds number, $\mathrm{Re_o}$, and the Strouhal number, St. The net flow Reynolds number describes the ratio of inertial forces to viscous forces in a flowing fluid. Re is defined as:

$$\mathrm{Re} = \frac{uD\rho}{\mu} \tag{3.1}$$

where u is the superficial net flow velocity, D is the tube diameter in the straight section, ρ is the fluid density, and μ is the fluid viscosity. There is little advantage in using oscillatory flow if $\mathrm{Re} > 250$, as the effects of the net flow become more significant and the benefits of operating at laminar flow rates diminish.[4]

The oscillatory Reynolds number describes the mixing intensity applied to the tube. The definition of $\mathrm{Re_o}$ is similar to Re, but the superficial net flow velocity, u, is replaced by the maximum oscillation velocity, $2\pi f x_0$, as:

$$\mathrm{Re_o} = \frac{2\pi f x_0 D\rho}{\mu} \tag{3.2}$$

where f is the frequency of oscillation, and x_0 is the amplitude of oscillation (center-to-peak in the straight section). To ensure full flow reversal, the maximum oscillation velocity should be always higher than the net flow velocity through the tube. Therefore, the velocity ratio, Ψ, defined as $\Psi = \mathrm{Re_o}/\mathrm{Re}$, should be always greater than 1. Values in the range of 2-10 have been recommended for plug flow operation.[5]

Finally, the Strouhal number describes the ratio between the diameter of the tube and the amplitude of oscillation, measuring the actual propagation of the eddies.[6] St is defined as:

$$\mathrm{St} = \frac{D}{4\pi x_0} \tag{3.3}$$

Ni and Gough[6] also suggested a modified Strouhal number which uses the tube diameter in the constriction, D_0, as the characteristic length. The modified St number, St_0, is defined as:

$$\mathrm{St}_0 = \frac{D_0}{\pi x_0} \tag{3.4}$$

The constrictions are usually orifice baffles, however, several other baffle types, including integral, central axial, round-edged helical, sharp-edged helical, sharp-edged helical with a central insert and wire wool baffles, have also been tested – **Figure 3.3**.[7]

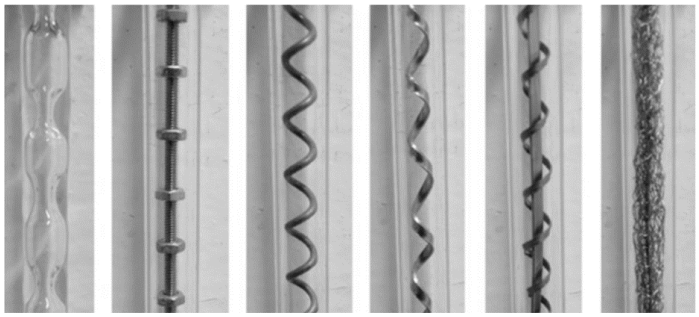


Figure 3.3 – Baffle geometries. (a) Integral baffles; (b) Central axial baffles; (c) Round-edged helical baffles; (d) Sharp-edged helical baffles; (e) Sharp-edged helical baffles with a central insert; (f) Wire wool baffle. Reprinted from Chemical Engineering Journal, 265, McDonough, J. R., Phan, A. N., Harvey, A. P., Rapid Process Development Using Oscillatory Baffled Mesoreactors – A State-of-the-Art Review, 110–121, Copyright 2014, with permission from Elsevier B.V.

3.1 Hydrodynamic Conditions in Tubular-OFCs

A great deal of research has been dedicated to the hydrodynamic characterization of baffled tubes. The suspension of solids and the mixing efficiency are generally evaluated in batch, while the axial dispersion is usually evaluated in continuous. **Table 3.1**, **Table 3.2** and **Table 3.3** summarize published studies on suspension of solids, mixing efficiency, and axial dispersion in baffled tubes, respectively.

Table 3.1 – Summary of published studies on suspension of solids in baffled tubes.

Reference	Baffle type	Oscillating mechanism	Diameter	Height	Frequency	Amplitude	Re_o	St	L/D	α	Particles type, mean diameter and concentration
Ejim *et al.*[9]	Integral	Moving fluid	10 mm	1 m	2-7 Hz	0-12 mm	NS	NS	1.5-3.0	0.12-0.25	Polyvinyl chloride, 141.30 µm, 10% (w/w)
Mackley *et al.*[10]	Orifice	Moving fluid	23 mm	1 m	4-20 Hz	1.5-4 mm	NS	NS	1.5	0.09	Ion exchange resin, 500 µm, up to 30% (w/w)
Reis *et al.*[11]	Integral	Moving fluid	4.4 mm	35 cm	0-25 Hz	0-20 mm	NS	NS	3	0.13	Ion exchange resin, 150-180 µm, up to 16% (w/w)
											Polyamine resin, 40-75 µm. up to 15% (w/w)
											Silica resin, 40-75 µm
Takriff *et al.*[12]	Orifice	Moving baffles	50 mm	1335 mm	0.5-5.0 rps	20 mm	400-900	NS	NS	0.08	Activated carbon, 1.7 mm
											Sand, 0.8 mm, up to 20% (w/w)
											Polyethylene terepthalate, 3.2 mm, up to 20% (w/w)

NS: not specified.

Table 3.2 – Summary of published studies on mixing efficiency in baffled tubes.

Reference	Baffle type	Oscillating mechanism	Diameter	Height	Frequency	Amplitude	Re_o	St	L/D	α	Method
Brunold *et al.*[13]	Orifice	Moving fluid	46 mm	NS	0.7 Hz	4-15 cm	NS	NS	1-2	0.45	(a)
Fitch and Ni[14]	Orifice	Moving fluid	50 mm	500 mm	NS	NS	0-6000	NS	1.5	0.22	(b)
Gough *et al.*[15]	Orifice and orifice+central	Moving baffles	50 mm	1 m	1-6 Hz	5-25 mm	NS	NS	0.7-2	0.26-0.47	(a)
Ni and Stevenson[16]	Orifice	Moving fluid	50 mm	950 mm	2-4 Hz	2.5-10 mm	1571-12564	NS	1.5	NS	(b)
Ni *et al.*[17]	Orifice	Moving baffles	90 mm	730 mm	1.7-4 Hz	10-30 mm	NS	NS	1-2.5	NS	(b)
		Moving fluid	50 mm	950 mm	1-5 Hz	2.5-10 mm	NS	NS	NS	0.11-0.51	(b)
Ni *et al.*[18]	Orifice	Moving fluid	50 mm	950 mm	2-4 Hz	3-6.5 mm	1884-12252	NS	1.5	0.21	(b)
Reis *et al.*[19]	Integral	Moving fluid	4.4 mm	350 mm	3-20 Hz	0.5-3.0 mm	NS	NS	3.0	0.13	(b)
Smith[20]	Orifice	Moving fluid	24 mm	1 m	0.1-0.3 Hz	1-2.25 mm	45-150	2-4	3	0.25	(a)
			54 mm	2m	NS	NS	10^2-10^5	0.5-4			(b)
			150 mm	4.5 m							

NS: not specified. Methods: (a) Flow visualization; (b) Tracer experiments

Table 3.3 – Summary of published studies on axial dispersion in baffled tubes.

Reference	Baffle type	Diameter	Length	Flow rate	Frequency	Amplitude	Re	Re_o	St	Model
Abbott *et al.*[21]	Orifice	25 mm	NS	86-304 mL min^{-1}	0.47-2.29 Hz	0.6-3.6 mm	73-259	127-905	3.32-0.55	(c)
Dickens *et al.*[22]	45º Orifice	23 mm	0.67 m	120 mL min^{-1}	3.5 Hz	0-4.7 mm	110	0-3000	∞-0.3	(a)
Ejim *et al.*[9]	Integral	10 mm	1 m	17.8 mL min^{-1}	5 Hz	NS	42	NS	NS	(a)
Howes and Mackley[23]	Orifice	51 mm	2.5 m	287 mL min^{-1}	NS	4 mm	40-106	~100-2500	2-0.7	(b)
Kacker *et al.*[24]	Integral	15 mm	NS	100-400 mL min^{-1}	0-4 Hz	0-10 mm	141-565	0-1508	NS	(a)
Mackley and Ni[25]	Orifice	25 mm	6.3 m	NS	NS	NS	0-3500	0-800	∞-0.33	(a)
Mackley and Ni[26]	Orifice	25 mm	1.08 m	NS	NS	NS	128	0-3600	∞-0.3	(a)
Mohd Rasdi *et al.*[27]	Integral and central	4-5 mm	NS	0.4-1.0 mL min^{-1}	NS	NS	1.56-4.67	80-200	0.20-0.80	(c)
Ni and Pereira[28]	Orifice	40 mm	25 m	NS	0-4 Hz	0-8 mm	0-2500	0-8032	∞-0.4	(a) and (b)
Oliva *et al.*[29]	Integral	6 mm	NS	10-30 mL min^{-1}	0.2-1 Hz	1-10 mm	34-96	9.6-482.2	22.5-NS	(a)
		15 mm	NS	15-154.7 mL min^{-1}	0.2-1 Hz	1-10 mm	22-241	1126.2	NS	(a)
Onyemelukwe et al.[30]	Integral	5 mm	5.4 m	2-5 mL min^{-1}	2-12 Hz	0.5-2 mm	8.2-21	31-740	0.8-0.2	(a)
Palma and Giudici[31]	Orifice	39.6 mm	~2.4 m	67-200 mL min^{-1}	0-4.5 Hz	5-25 mm	NS	NS	NS	(a)
Phan and Harvey[32]	Central, integral and helical	5 mm	NS	1-8 mL min^{-1}	0-6 Hz	0-4 mm	4.3-34	0-500	∞-0.1	(c)
Phan and Harvey[33]	Helical	5 mm	340 mm	0.3-2.0 mL min^{-1}	0-14 Hz	0-4 mm	1.25-10	0-800	∞-0.1	(c)
Phan *et al.*[34]	Central and integral	5 mm	0.34 m	0.3-0.6 mL min^{-1}	0-14 Hz	0-4 mm	1.25-2.55	0-700	∞-0.1	(c)
Slavnić *et al.*[35]	Orifice	26 and 44 mm	2.0 m	NS	0.5-2.0 Hz	1.40-13.30 mm	NS	NS	NS	(a)
Slavnić *et al.*[36]	Orifice	26 mm	2.0 m	11.4-44.1 L h^{-1}	0.5-2 Hz	3.02-13.03 mm	154-597	619-2707	0.68-0.16	(a)
Reis *et al.*[19]	Integral	4.4 mm	35 cm	1.94 mL min^{-1}	0-20 Hz	0-3 mm	~10	-	-	(b) and (d)
Reis *et al.*[37]	Integral	4.5 mm	35 cm	1.67-21.3 mL min^{-1}	0-20 Hz	0-3 mm	8-102	41-1629	NS	(a), (b) and (c)
Siddique *et al.*[38]	Orifice	69 mm	740-2500 mm	50-130 mL min^{-1}	2-8 Hz	1-2 mm	85.9-223.2	146.3-1170.3	1.0-0.5	(a)
Smith and Mackley[39]	Orifice	24; 54; 150 mm	1; 2; 4.5 m	NS	NS	NS	107	100-105	2-0.5	(a)
Stonestreet and van der Veeken[8]	Orifice	24 mm	2.9 m	NS	0-5 Hz	0-5 mm	95-252	0-2500	∞-0.4	(c)
Takriff and Masyithah[40]	Orifice	94 mm	282 mm	0-1.2 L min^{-1}	0.5-1.0 Hz	7.5-15 mm	NS	4429-8858	0.99-0.5	(b)
Zheng and Mackley[41]	Integral	5 mm	9 m	0-13.7 mL min^{-1}	0-15 Hz	0-4 mm	10-58	0-1000	∞-0.08	(a)

NS: not specified. Models: (a) Plug flow with axial dispersion model; (b) Stage-wise backmixing model; (c) Tanks-in-series model; (d) Differential backmixing model; (e) Diffusion model.

3.1.1 Suspension of Solids

Mackley *et al.*[10] demonstrated that particles can be kept in suspension in a baffled tube as long as the terminal velocity of the particles is surpassed by the velocity of the fluid in the opposite direction. The minimum oscillation intensity required to keep a given concentration of particles of a given size and density in suspension in a baffled tube is generally determined by visual inspection.[9,11,12] Takriff *et al.*[12] studied the effect of particle density and fluid viscosity on the suspension of solids in a baffled tube. They found that decreasing the particles density and increasing the fluid viscosity decreases the particles terminal velocity, which decreases the minimum oscillation intensity required to keep particles in suspension. Reis *et al.*[11] studied the effect of the frequency and amplitude of oscillation on the suspension of solids in a baffled tube. They found that it is easier to suspend particles at high frequencies and low amplitudes than at low frequencies and high amplitudes. In addition, they also found that it is easier to suspend particles when the baffled tube is held horizontally rather than vertically, presumably due to the difference of pressure drop between the two situations. Ejim *et al.*[9] studied the effect of operating and geometric parameters on the suspension of solids in baffled tubes. They found that the minimum amplitude of oscillation required to keep particles in suspension, which they designated as the critical amplitude, $x_{0,crit}$, generally decreases as the frequency of oscillation decreases. In addition, they also found that tubes with smooth periodic constrictions (SPC) require up to 50% lower $x_{0,crit}$ than tubes with sharp edge periodic constrictions (SEPC), presumably due to the presence of stagnant zones close to the SEPC. Finally, they also found that the effect of the geometric parameters on the suspension of solids does not follow a clear trend.

3.1.2 Mixing Efficiency

Flow visualization experiments have been conducted to characterize the mixing efficiency in baffled tubes.[13,15,20] In this type of experiments, a video camera records the movement of a suspension or a dye tracer in oscillation in the baffled tube. When a suspension is used, the fluid (usually water) and the particles in suspension in the fluid generally have similar densities so that the particles follow the same streamlines as the fluid. The main goal is to observe how the vortices are formed and disrupted, how they propagate within each inter-constriction cell, and how they interact with other vortices. Tracer experiments have also been conducted to characterize the mixing efficiency in baffled tubes. In some previous works, the mixing efficiency was quantified in the form of the mixing time, t_m, which is the time required to reach a specific degree of concentration uniformity after an injection of a tracer;[14,16–19] in other works, the mixing efficiency was quantified in the form of the axial dispersion coefficient, D_c, which characterizes the degree of backmixing in the axial direction.[14,16,18,20] Shorter mixing times and larger axial dispersion coefficients are indicative of better mixing efficiencies.

In relation to the effect of the operating conditions, the general conclusion is that increasing the frequency and the amplitude of oscillation increases the axial dispersion and, therefore, decreases the mixing time.[13–20] In relation to the effect of the geometric parameters, the conclusions are more complex. It has been reported that the cell aspect ratio, L/D, controls the shape and length of the vortices in a baffled tube. On the one hand, when L/D is too small, there is channeling of the flow through the center of the constriction, which suppresses the generation of vortices. On the other hand, when L/D is too large, the vortices are unable to spread through the full length of the inter-constriction cell and interact with other vortices, which results in the formation of stagnant zones.[13,17] It has also been reported that the ratio of the open constriction area, $\alpha = (D_0/D)^2$, controls the width of the vortices in a baffled tube. On the one hand, when α is too small, the vortices are unable to expand in the entire cross-section of the inter-constriction cell, which creates stagnant zones. On the other hand, when α is too large, there is channeling of the flow through the center of the constriction, which suppresses the generation of vortices.[15,17]

3.1.3 Axial Dispersion

Tracer experiments have been conducted to characterize the axial dispersion in baffled tubes. The parameters that characterize the axial dispersion are obtained from the residence time distribution (RTD) by fitting a phenomenological model to the experimental data. Several different models have been used to characterize the flow in baffled tubes. Most of the studies have implemented the plug flow with axial dispersion model which describes the system as a continuous path where a diffusion-like process is superimposed to the main flow.[9,22,37–39,41,24–26,28–31,36] The axial mixing is characterized by the axial dispersion coefficient, D_c, and the spread in the whole system is characterized by the vessel dispersion number, $D_c/(ul)$, where u is the average superficial flow velocity and l is the length of the tube. When $D_c/(ul) \to 0$ the dispersion is negligible, hence plug flow. When $D_c/(ul) \to \infty$ there is large dispersion, hence mixed flow. Alternatively, a compartment type model can be used to describe the system as a stage-wise process. An example is the stage-wise backmixing model which divides the system into a fixed number of ideal stages and quantifies the deviation from perfect plug flow with an inter-stage backmixing parameter, g.[19,23,28,37,40] Another example is the tanks-in-series model which describes the system as a variable number of ideal stirred tanks in series, N.[4,21,27,32–34,37]

The effect of operating and geometric parameters on the axial dispersion in baffled tubes has been widely investigated through both experimental work and numerical simulation. Despite their importance for the understanding of the fluid mechanics in baffled tubes, numerical simulation results will not be covered in detail in this work.[42–49]

Dickens *et al.*[22] investigated the effect of the amplitude of oscillation on the RTD in baffled tubes and discovered that, at low amplitudes, the RTD approaches a similar shape to that of laminar flow, then becomes sharp and

symmetric, and finally broadens about both sides of the peak at higher amplitudes. These results suggest that the increase of amplitude should drive the system towards an optimum condition with near plug flow behavior, from where the dispersion increases substantially due to the increase of the mixing length. Similar results were also reported by Mackley and Ni,[25] Reis *et al.*,[19,37] Zheng *et al.*,[41] Abbott *et al.*,[21] and Onyemelukwe *et al.*.[30]

Howes *et al.*[23] studied the effect of the frequency of oscillation on the RTD in baffled tubes and obtained a similar effect to that reported by Dickens *et al.*[22] for the amplitude. The authors suggested that the axial dispersion should decrease when the frequency increases due the increase of radial mixing and subsequent short-circuiting of fluid. However, when the frequency increases pass an optimum value, the axial dispersion should increase due to the increase of backmixing. Similar results were also reported by Palma *et al.*,[31] Reis *et al.*,[19,37] Abbott *et al.*,[21] Smith and Mackley,[39] and Oliva *et al.*.[29]

Stonestreet and van der Veeken[4] investigated the interaction between the oscillatory and the net flow components. The authors found that the axial dispersion decreases when the flow rate increases due to the formation of larger and more intense vortices at higher flow rates. Similar results were also reported by Ni *et al.*,[28] Abbott *et al.*,[21] Onyemelukwe *et al.*,[30] and Takriff and Masyithah.[40] The authors also claimed that a specific interaction between the oscillatory and the net flows exists and that $\Psi = \mathrm{Re_o}/\mathrm{Re} \cong 2$ is optimal to minimize the axial dispersion. However, Kacker *et al.*[24] found that Ψ is not sufficient to choose optimal operating conditions because different combinations of frequency and amplitude with the same Ψ provide distinct axial dispersion performances. A similar conclusion was also reported by Oliva *et al.*.[29]

Phan *et al.*[32] investigated the effect of net flow, oscillatory flow and their interdependence on the axial dispersion in three meso-scale baffled tubes with different baffles geometries: central, integral and helical. (The internal diameter of a meso-scale baffled tube ranges from 1 to 10 mm.) All the three baffle geometries provided a well-defined and symmetrical RTD, however, the broadness of the RTD curves highly depended on the net flow and oscillation conditions. The authors concluded that all the three baffle geometries could be used to produce plug flow at flow rates varying 1.0-8.0 mL min^{-1}. In a later study, the same research group characterized the axial dispersion in baffle tubes with central and integral geometries at very low flow rates (0.3-0.6 mL min^{-1}).[34] Two main conclusions were drawn from that study: first, at very low flow rates, baffled tubes with central baffles provide higher degrees of plug flow than baffled tubes with integral baffles, and second, the oscillation conditions have little influence on the axial dispersion in baffled tubes with integral baffles. Mohd Rasdi *et al.*[27] also characterized the axial dispersion in baffled tubes with central and integral geometries at low flow rates (0.4-1.0 mL min^{-1}). They also found that the central baffles provide higher degrees of plug flow than the integral baffles, however, in their study, the impact of the oscillation conditions on the axial dispersion in baffled tubes with integral baffles was found significant.

Ejim *et al.*[9] studied the effect of four geometrical parameters on the axial dispersion of solid-liquid systems in meso-scale baffled tubes with integral baffles. The parameters under study were the tube diameter in the constriction, the ratio of the open constriction area, the distance between constrictions, and the baffle geometry

(SEPC and SPC). The authors found that the SPC geometry provides a more uniform mixing and a lesser extent of backmixing than the SEPC geometry, and that the ratio of the open constriction area is the dominant parameter controlling the solids backmixing. Comparing their results with those of Reis *et al.*[37] for the liquid phase, the authors confirmed that the axial dispersion of the solid phase is comparable to the axial dispersion of the liquid phase. In addition, they also found that, on average, the solid phase spends more time in the tube than the liquid phase. Similar results were also reported by Onyemelukwe *et al.*[30] and Kacker *et al.*.[24]

In relation to scale-up, Smith and Mackley[39] found that the axial dispersion is similar in tubes with different diameters as long as the values of Re, Re_o and St are kept constant, and Ni *et al.*[50] found that the axial dispersion coefficient varies linearly upon scale-up; Smith and Mackley[39] demonstrated that a multi-orifice baffle could reproduce at a larger scale the fluid mechanics and the axial dispersion of laboratory scale baffled tubes, and Mackley and Ni[25] proposed that a multipass configuration could be used for scale-up in terms of mean residence time, and a multitube configuration could be used for scale-up in terms of flow rate.

Finally, several correlations have been proposed to describe the axial dispersion as a function of the experimental conditions. Some examples are the works of Smith and Mackley,[39] Ni *et al.*,[50] Takriff and Masyithah,[40] Abbott *et al.*[21] and Slavnić *et al.*.[35]

Great care must be taken when comparing the results of different studies regarding the effect of each parameter on the axial dispersion. First of all, different studies use different baffle tubes, either in diameter, baffle geometry or length, which influences the mixing conditions of each device. In addition, different studies make use of different models/parameters to characterize the flow, which can difficult the comparison of the results. For instance, when a plug flow with axial dispersion model is used to describe the flow, the effect of the flow rate on the axial dispersion can be characterized either by D_c or $D_c/(ul)$ (or $(ul)/D_c$). However, in the second case, the effect of the flow rate on the axial dispersion results from a compromise between D_c and u. Therefore, opposite results can be obtained depending on the parameter that is chosen to describe the axial dispersion. Furthermore, it is clear that the combination of net flow, oscillatory flow and baffle geometry changes the influence of each variable individually.

3.2 Batch Crystallization in Tubular-OFCs

Tubular-OFCs have been used for the batch crystallization of a variety of compounds, including paracetamol,[51–59] L-glutamic acid,[60–62] sodium chlorate,[63,64] adipic acid,[65] lactose,[38] butyl paraben,[66] α-lipoic acid:nicotinamide,[67] lysozyme[68] and an unspecified API.[3] Cooling crystallizations have been more common,[3,38,62–67,54–61] but some antisolvent,[52,53] salting-out[68] and reactive[51] crystallizations have also been performed. Additional auxiliary techniques, such as sonication[38] and seeding[3,59,62–64] have also been employed. **Table 3.4** summarizes published studies on batch crystallization in tubular-OFCs.

Table 3.4 – Summary of published studies on batch crystallization in tubular-OFCs.

Reference	Compound	Method	Diameter	Length	Volume	Batch time	Yield	Notes
Brown and Ni[52]	Paracetamol	Antisolvent	32 mm	NS	630 mL	NS	NS	- Effect of initial solvent composition and antisolvent addition rate on crystal growth rate
Brown and Ni[53]	Paracetamol	Antisolvent	32 mm	NS	630 mL	NS	NS	- Effect of supersaturation, antisolvent addition rate and mixing intensity on crystal growth rate
Brown and Ni[57]	Paracetamol	Cooling	32 mm	NS	200 mL	NS	NS	- Determination of MSZW and crystal size distribution by image analysis - Effect of mixing intensity on MSZW - Effect of mixing intensity on crystal size
Brown *et al.*[65]	Adipic acid	Cooling	40 mm	NS	1000 mL	NS	NS	- Detection of nucleation onset by turbidity and image analysis - Determination of nucleation and crystal growth kinetic parameters
Callahan and Ni[63]	Sodium chlorate	Cooling	50 mm	500 mm	500 mL	Overnight	NS	- Determination of nucleation mechanism - Effect of operating conditions on enantiomorphism
Callahan and Ni[64]	Sodium chlorate	Cooling	50 mm	500 mm	500 mL	Overnight	NS	- Effect of mixing intensity on enantiomorphism
Castro *et al.*[68]	Lysozyme	Salting-out	3 mm	35 cm	4 mL	24 h	8.2-76.0%	- Determination of a two-dimensional phase diagram for lysozyme - Determination of the induction time
Chew *et al.*[54]	Paracetamol	Cooling	32 mm	NS	500 mL	30 min	NS	- Comparison of crystal quality in an OFC and in a STC - Effect of mixing intensity and initial supersaturation on crystal size
Chew and Ristic[55]	Paracetamol	Cooling	32 mm	NS	500 mL	30 min	NS	- Comparison of crystal quality in an OFC and in a STC with identical power densities - Effect of initial supersaturation on crystal size
Cruz *et al.*[58]	Paracetamol	Cooling	4 mm	193 cm	22.5 mL	5-30 min	NS	- Effect of oscillation conditions on nucleation kinetic parameters - Effect of batch time, oscillation conditions and initial supersaturation on crystal size
Cruz *et al.*[59]	Paracetamol	Cooling	16 mm	45 cm	75 mL	6 min	NS	- Determination of the critical mixing intensity for secondary nucleation
Jiang and Ni[51]	Paracetamol	Reactive	76 mm	NS	1 L	NS	NS	- Effect of solvent on MSZW and nucleation kinetic parameters - Effect of solvent on crystal growth kinetic parameters - Effect of solvent and impurity on crystal shape
Lawton *et al.*[3]	API	Cooling	50 mm	NS	500 mL	NS	NS	- Effect of oscillation conditions, initial supersaturation and seeding on crystal size - Effect of cooling rate on crystal shape
McLachlan and Ni[69]	Urea	Cooling	76 mm	NS	1 L	NS	NS	- Comparison of crystal purity in an OFC and in a STC with identical power densities

NS: not specified.

Table 3.4 – Continued.

Reference	Compound	Method	Diameter	Length	Volume	Batch time	Yield	Notes
McLachlan and Ni[70]	Urea	Cooling	76 mm	NS	1 L	NS	NS	- Comparison of crystal purity in the presence of an impurity in an OFC and in a STC with identical power densities
Ni *et al*.[60]	L-Glutamic acid	Cooling	75 mm	340 mm	1.5 L	NS	NS	- Effect of cooling rate on MSZW - Comparison of MSZW in an OFC and in a STC - Effect of mixing intensity, cooling rate, final temperature and seeding on polymorphism.
Ni and Liao[61]	L-Glutamic acid	Cooling	50 mm	500 mm	1000 mL	NS	NS	- Effect of cooling rate and initial supersaturation on MSZW and nucleation kinetic parameters - Comparison of MSZW in an OFC and in a STC - Effect of cooling rate and initial supersaturation on crystal size - Effect of cooling rate and initial supersaturation on polymorphism
Ni and Liao[62]	L-Glutamic acid	Cooling	50 mm	500 mm	1000 mL	NS	NS	- Effect of mixing intensity and material of baffles on MSZW - Effect of mixing intensity on crystal size - Effect of mixing intensity, seeding, material of baffles and final temperature on polymorphism
Ristic[56]	Paracetamol	Cooling	32 mm	NS	500 mL	NS	NS	- Effect of hydrodynamics on interfacial morphological instabilities - Comparison of crystal quality in an OFC and in a STC with identical power densities - Effect of initial supersaturation on crystal size
Siddique *et al*.[38]	Lactose	Cooling	69 mm	500 mm	NS	2.5-4 h	17.4-28.3%	- Effect of batch time and sonication power on nucleation and crystal growth kinetic parameters - Effect of batch time and sonication power on yield and mean particle size
Yang *et al*.[66]	Butyl paraben	Cooling	16.3 mm	700 mm	120 mL	NS	NS	- Effect of oscillation conditions on nucleation kinetic parameters
Zhao *et al*.[67]	α-Lipoic acid: nicotinamide	Cooling	50 mm	NS	500 mL	1 h	65-71%	- Novel cocrystal - Preliminary experiments in batch and linear scale-up from batch to continuous

NS: not specified.

3.2.1 Crystallization Kinetics

Nucleation kinetics

Two main types of experimental methods have been employed to study the effect of the operating conditions on the nucleation kinetics in OFCs: polythermal methods, which are based on the determination of the metastable zone width (MSZW) as a function of the cooling rate, and isothermal methods, which are based on the determination of the induction time as a function of supersaturation.[71] Castro *et al*.[68] studied the salting-out crystallization of lysozyme in an OFC and reported, first, a significant reduction in the MSZW in the OFC in comparison with quiescent conditions and, second, a significant reduction in the induction time in the OFC in comparison with a stirred tank crystallizer (STC). Ni *et al*.[60] studied the cooling crystallization of L-glutamic acid from aqueous solutions in an OFC and investigated the effect of the cooling rate on the MSZW. The MSZW increased slightly as the cooling rate increased from 0.2 to 0.67 °C min^{-1}. In addition, a smaller MSZW was obtained in the OFC in comparison with a STC. Later, Ni and Liao[61] investigated the effects of the cooling rate and solution concentration on the MSZW and nucleation kinetic parameters for the same system. The MSZW increased as the cooling rate increased from 0.5 to 3.0 °C min^{-1}, but it remained practically unchanged as the supersaturation increased from 15 to 45 g L^{-1}. Then, the MSZW data was used to estimate the kinetic parameters by Nývlt's approach.[72,73] Surprisingly, the nucleation rate decreased as the supersaturation increased, which the authors attributed to the rather insignificant effect of supersaturation on the MSZW. However, this irregular result may also be due to the oversimplistic assumptions of Nývlt's approach, which can lead to order-of-magnitude errors, as previously demonstrated by Nagy *et al*..[74] Later, Ni and Liao[62] also investigated the effect of mixing intensity and baffle material on the MSZW for the same system. As expected, the MSZW decreased as the mixing intensity increased, with a stronger effect for higher cooling rates. In addition, the MSZW decreased as the baffle material changed from polyvinylidene difluoride to stainless steel, presumably as a result of a smaller contact angle between the solute and the surface of stainless steel in comparison to polyvinylidene difluoride.

Brown and Ni[57] studied the cooling crystallization of paracetamol from aqueous solutions in an OFC and investigated the effect of mixing intensity on the MSZW. The results presented a similar trend to that previously reported by Ni and Liao.[62] Later, Brown *et al*.[65] studied the cooling crystallization of adipic acid from aqueous solutions in an OFC and employed three different approaches to estimate the nucleation kinetic parameters from MSZW data: Nývlt's approach,[72,73] Kubota's approach,[75,76] and the population balance approach.[77] The authors reported that, due to their linear assumptions, Nývlt and Kubota's approaches were only accurate for slower cooling rates, whereas, due to its nonlinear nature, the population balance approach was accurate in the whole range of cooling rates. Later, Siddique *et al*.[38] also employed a population balance approach to estimate the nucleation kinetic parameters for the cooling sonocrystallization of lactose from aqueous solutions in an OFC.

Cruz *et al*.[58] studied the cooling crystallization of paracetamol from aqueous solutions in an OFC and applied the classical nucleation theory to estimate the effect of mixing intensity and temperature on the induction time and, subsequently, on the kinetic and thermodynamic parameters for nucleation. As anticipated, the induction time decreased as the mixing intensity increased. In addition, both the kinetic and thermodynamic parameters increased as the mixing intensity increased. The effect on the kinetic parameter was expected as it depends on the frequency of molecular collisions, whereas the effect on the thermodynamic parameter was rather surprising as, from a theoretical point of view, it should be independent of the mixing conditions. Additionally, the induction time decreased as the temperature increased. The kinetic parameter was little affected by changes in temperature, whereas the thermodynamic parameter decreased as the temperature increased, presumably due to the decrease of interfacial tension. Yang *et al*.[66] studied the cooling crystallization of butyl paraben from solutions of ethanol in an OFC and investigated the effect of the oscillation conditions on the nucleation rate in accordance with the classical nucleation theory. The authors suggested that, initially, the increase of shear rate due to the increase of the frequency and/or amplitude of oscillation should promote the formation of critical size clusters, which leads the nucleation rate towards a maximum, whereas the increase of shear rate beyond the maximum should promote the disruption of critical size clusters, which hinders nucleation.

More recently, Jiang and Ni[51] investigated the effect of the solvent on the MSZW and nucleation kinetic parameters for the reactive crystallization of paracetamol in an OFC. Three solvents consisting of mixtures of water and acetic acid with different compositions were tested. The MSZW increased as the cooling rate increased for all the three solvents, and, at a fixed cooling rate, the MSZW increased as the ratio of acetic acid to water decreased. In addition, the nucleation order, obtained from recrystallization experiments, increased as the ratio of acetic acid to water increased, presumably due to the increase of solubility.

Crystal Growth Kinetics

Brown and Ni[52] studied the antisolvent crystallization of paracetamol from mixtures of acetone and water (antisolvent) in an OFC and investigated the effect of the initial solvent composition and antisolvent addition rate on the crystal growth rate. The crystal growth rate increased as the initial water fraction increased from 30 to 50%, where it reached a maximum, and then it decreased as the initial water fraction further increased from 50 to 70%, a trend that the authors related to the effect of water content on solubility. In addition, the crystal growth rate increased as the antisolvent addition rate increased from 13 to 133 mL min^{-1} presumably because faster antisolvent addition rates produce larger changes in solubility. Later, Brown and Ni[53] investigated the effect of supersaturation, antisolvent addition rate and mixing intensity on the crystal growth rate and kinetic parameters for the same system. As expected, the crystal growth rate increased as the supersaturation, the antisolvent addition rate and the mixing intensity increased. A crystal growth rate order of 1.57 was obtained, which agrees reasonably well with the range reported by Granberg *et al*.[78] for stirred tanks with 1.45 in pure

acetone and 1.2 in pure water. The overall crystal growth coefficient remained practically constant as the initial water fraction increased from 25 to 60%, but increased drastically as the initial water fraction further increased to 70%. Notably, all the overall crystal growth coefficients obtained in the OFC (1.7×10^{-3} to 6.4×10^{-3} kg m^{-2} s^{-1}) were orders of magnitude larger than those obtained by Granberg *et al*.[78] in a stirred tank crystallizer (2.9×10^{-5} to 3.1×10^{-4} kg m^{-2} s^{-1}), which the authors attributed to the efficiency of mass transfer in the OFC. More recently, Jiang and Ni[51] investigated the effect of the solvent on the crystal growth rate and kinetic parameters for the reactive crystallization of paracetamol from mixtures of water and acetic acid in an OFC and found that the crystal growth rate order did not have a direct dependence on the composition of the solvent.

Brown *et al*.[65] studied the cooling crystallization of adipic acid in an OFC and employed a population balance model to estimate the crystal growth kinetic parameters. A similar approach was also employed by Siddique *et al*.[38] for the cooling sonocrystallization of lactose from aqueous solutions in an OFC. On the one hand, both the crystal growth rate order and the overall crystal growth coefficient decreased as the sonication power increased from 0.10 to 0.15 W g^{-1}. On the other hand, while both parameters decreased as the batch time increased from 2.5 to 4 h at 0.10 W g^{-1}, they increased as the batch time increased at 0.15 W g^{-1}.

3.2.2 Control of Final Properties

Control of Purity

One of the most important advantages of crystallization compared with other separation processes is that it is capable of yielding very high purity products. This is particularly important in the pharmaceutical industry, as impurities might have a significant impact on the quality, efficacy and safety of drugs. McLachlan and Ni[69] investigated the cooling crystallization of urea in an OFC and in an STC and compared the crystal purity of the products obtained from the two crystallizers at identical power densities. Nucleation occurred at a lower temperature and, consequently, at a higher supersaturation in the STC than in the OFC, which led to a higher nucleation rate and resulted in the formation of smaller single crystals in the STC than in the OFC. However, the mean diameter of the final product of the STC was larger than the mean diameter of the final product of the OFC because the final product of the STC was more agglomerated than the final product of the OFC. This is probably the reason why the final product of the OFC was purer than the final product of the STC, as large agglomerates are more likely to enclose mother liquor or impurities or both than single crystals. Later, McLachlan and Ni[70] performed a similar study to investigate the effect of an impurity, in this case biuret, on the crystal purity for the same system. In the presence of impurity, the final products of both crystallizers were less pure than in the absence of impurity, but the final product of the OFC was still purer than the final product of the STC.

Control of Crystal Size

The crystal size distribution (CSD) is one of the most important properties of crystals. This is because the CSD has a direct impact on the efficiency of downstream operations, such as filtration, washing and drying, as well as on the end-use properties of the compound. Prominent articles on the control of crystal size in OFCs are discussed below.

Chew *et al*.[54] studied the cooling crystallization of paracetamol from aqueous solutions in an OFC and in a STC. The OFC produced considerably smaller crystals than the STC, presumably due to a higher shear rate in the OFC, which induced a higher dynamical nucleation. The crystal size decreased as the mixing intensity increased in both crystallizers. The mixing intensity was characterized in the form of Re_o for the OFC (5660-9430) and impeller speed for the STC (600-800 rpm). In addition, the crystal size also decreased as the initial supersaturation increased from σ=0.1 to σ=0.5 in the STC, but remained practically unchanged in the OFC. Furthermore, the OFC produced crystals with smoother surfaces and less interface instabilities than the STC, presumably also due to a higher shear rate in the OFC, which enhanced the mass transfer in the solution layer adjacent to the growing crystal interface. However, in this study, the OFC and the STC were operated with distinct power densities, which raised the question of whether the difference in power densities could explain the difference of results between the two crystallizers. In order to clarify this matter, in later studies, Chew and Ristic[55,56] operated the OFC and the STC at the same power density (1.5 kW m^{-3}). The results obtained in these studies showed that the conclusions of the previous study are still valid when the OFC and the STC are operated with identical power densities. Brown and Ni[57] investigated the effect of mixing intensity and initial supersaturation on the crystal size for the same system. The crystal size decreased slightly as the initial supersaturation increased, which the authors attributed to the intensification of primary nucleation at higher supersaturations. In addition, the crystal size also decreased as the mixing intensity increased, following the trend reported in the previous studies. Cruz *et al*.[58] investigated the effect of batch time, initial supersaturation, frequency and amplitude of oscillation on the crystal size for the same system. As expected, the crystal size increased as the batch time increased, but accompanied by breakage and aggregation of the crystals. In addition, the crystal size decreased as the initial supersaturation increased due to the enhancement of primary nucleation. For the same reason, the crystal size also decreased as both the frequency and the amplitude of oscillation increased. Later, Cruz *et al*.[59] investigated the effect of mixing intensity on the crystal size for the same system, but with seeding. Below a critical level of mixing intensity, the crystal size increased as the mixing intensity increased due to enhancement of mass transfer for crystal growth, but above the critical level of mixing intensity, the crystal size decreased due to the intensification of secondary nucleation.

Ni and Liao[61] studied the cooling crystallization of L-glutamic acid from aqueous solutions in an OFC and investigated the effect of cooling rate and initial supersaturation on the crystal size. The crystal size increased as the initial concentration increased from 15 to 40 g L^{-1}. The effect of the cooling rate was less significant, except at the lower concentration, when the crystal size decreased as the cooling rate increased from 0.5 to

3.0 °C min^{-1}. Later, Ni and Liao[62] investigated the effect of mixing intensity and initial supersaturation on the crystal size for the same system. The crystal size decreased as the mixing intensity increased, presumably due to the intensification of erosion and attrition at higher mixing intensities. On the other hand, the crystal size remained practically unchanged as the initial concentration increased from 30 to 35 g L^{-1}, which seems to be inconsistent with the results reported in the previous study.[61] However, the differences between the two studies could be due to differences in mixing intensity, as Re_o varied between approximately 5000 and 30000 in this study, and remained fixed at 3142 in the previous study.

Lawton *et al.*[3] studied the cooling crystallization of an unspecified API in an OFC and investigated the effect of the oscillation conditions, initial supersaturation, and seeding on the crystal size. The crystal size decreased as the frequency and amplitude of oscillation increased, while the CSD remained narrow for all combinations of frequency and amplitude. In addition, the crystal size also decreased as the initial supersaturation increased. Finally, as expected, the crystal size increased in the presence of seeds.

Siddique *et al.*[38] studied the cooling sonocrystallization of lactose from aqueous solutions in an OFC and investigated the effect of batch time and sonication power on the crystal size. On the one hand, the mean crystal size increased as the batch time increased from 2.5 to 4 h, but with an increase in the percentage of fines, possibility due to the intensification of secondary nucleation or attrition. On the other hand, the mean crystal size decreased as the sonication power increased from 0.10 to 0.15 W g^{-1} due to the intensification of nucleation.

In conclusion, the effect of the operating conditions on crystal size depends on their relative effects on nucleation and crystal growth. Therefore, as a rule, the crystal size decreases when the experimental conditions stimulate nucleation, but increases when the experimental conditions promote crystal growth.

Control of Crystal Shape

Differences in crystal shape result from differences in crystal growth rate between different crystal faces. Therefore, producing the desired crystal shape is more complex than producing the desired crystal size. Ni and Liao[61] studied the cooling crystallization of $_L$-glutamic acid from aqueous solutions in an OFC and reported a change in crystal shape as a function of the cooling rate. While long and narrow needle-shaped crystals were formed at 0.5 °C min^{-1}, wider and thicker plate-shaped crystals were formed at 0.7-2.0 °C min^{-1}, and flower-shaped crystals were formed at 2.5-3.0 °C min^{-1}. Later, Lawton *et al.*[3] studied the cooling crystallization of an unspecified API in an OFC and observed the formation of several types of crystals depending on the cooling rate and the presence or absence of seeds. Rod-shaped crystals were formed at 1 °C min^{-1} without seeding, flake-shaped crystals were formed at 3 °C min^{-1} without seeding and plate-shaped crystals were formed at 5 °C min^{-1} with seeding. In a different work, Castro *et al.*[68] studied the salting-out crystallization of lysozyme in the presence of sodium chloride in an OFC and determined the phase diagram for lysozyme as a function of the

concentration of protein and precipitating agent. Several types of crystals, from tetragonal, orthorhombic and needle-shaped crystals to microcrystals and precipitate, were formed depending on the concentration of protein and precipitating agent. McLachlan and Ni[70] studied the cooling crystallization of urea in an OFC and reported a change in crystal habit from long needle-like crystals in the absence of impurity to cubic crystals in the presence of biuret, which the authors attributed to the incorporation of impurity into the crystal product. More recently, Jiang and Ni[51] studied the reactive crystallization of paracetamol from mixtures of water and acetic acid in an OFC and detected a change in crystal shape as a function of the composition of the solvent and the concentration of an impurity. Rectangle column-shaped crystals were formed regardless of the composition of the solvent, but the columns became longer and thinner as the ratio of acetic acid to water increased. In addition, the agglomeration degree also decreased as the ratio of acetic acid to water increased presumably due to the increase of solvent polarity. Furthermore, the crystals changed from plate-shaped to elongated depending on the concentration of the impurity.

Control of Polymorphism

Many compounds exhibit polymorphism, which can be problematic because sometimes different polymorphs have distinct physicochemical properties, such as density, hardness, chemical stability, solubility, dissolution rate in different solvents, melting point, and hygroscopicity. L-glutamic acid has been widely used as a model system to study the effect of the operating conditions on polymorphism. L-glutamic acid has two polymorphs: the metastable form α, with a prismatic morphology, and the stable form β, with a needle-shaped morphology. Ni *et al.*[60] studied the cooling crystallization of L-glutamic acid from aqueous solutions in an OFC and investigated the effect of the mixing intensity, cooling rate, final temperature and seeding on polymorphism. All the experiments were performed at a fixed solution concentration of 45 g L^{-1}. On the one hand, form β was obtained exclusively without seeding in the whole range of mixing intensities, cooling rates and final temperatures. On the other hand, form α was obtained exclusively upon seeding with crystals of form α, as it prevented the solution-mediated polymorphic transformation from the metastable to the stable polymorph. Later, Ni and Liao[61] investigated the effect of the cooling rate and solution concentration on polymorphism for the same system. On the one hand, at the highest solution concentration of 45 g L^{-1}, form β was produced exclusively in the whole range of cooling rates, which follows the same trend reported in the previous work. On the other hand, at the lower solution concentrations of 15 and 30 g L^{-1}, form α was produced exclusively in the whole range of cooling rates. Finally, Ni and Liao[62] also investigated the effect of mixing intensity, seeding, baffle material, and final temperature on polymorphism for the same system. Lower mixing intensities, lower concentrations, lower temperatures and faster cooling rates limited the solution-mediated polymorphic transformation from the metastable to the stable polymorph, which favored the production of form α. In

addition, seeding with crystals of form α and baffles with smoother surfaces also favored the production of form α. Such results are in good agreement with those reported in the two previous studies.

Control of Enantiomorphism

Callahan and Ni[63] studied the seeded cooling crystallization of sodium chlorate in an OFC and in an STC. Although sodium chlorate is a nonchiral substance, its crystals might possess either a left- or a right-handed enantiomorphism. The STC produced crystals with 100% similarity to the seed handedness, whereas the OFC produced crystals with mixed handedness. This result suggests that while secondary nucleation must be the only nucleation mechanism in the STC, some sort of primary nucleation must occur in the OFC, although secondary nucleation is still dominant. The authors hypothesized that the scraping action between the baffle edge and the wall of the crystallizer might be the origin of primary nucleation in the OFC. Later, Callahan and Ni[64] found that the introduction of scraping reduced the percentage of similarity to the seed handedness in both the STC and the OFC. However, while increasing the mixing intensity in the STC and the frequency of oscillation in the OFC did not have a significant effect on the percentage of similarity to the seed handedness, increasing the amplitude of oscillation in the OFC did, with lower amplitudes providing higher percentages of similarity to the seed handedness, presumably as consequence of lower fluid shearing.

3.3 Continuous Crystallization in Tubular-OFCs

Tubular-OFCs have been used for the continuous crystallization of a variety of compounds, including aspirin,[79] L-glutamic acid,[80] lactose,[38,81] paracetamol,[82,83] salicylic acid,[84] benzoic acid,[85] α-lipoic acid:nicotinamide[67] and an unspecified API[3]. Cooling crystallizations have been more common,[3,38,67,79–82] but some antisolvent[84,85] and reactive[83] crystallizations have also been performed. Additional auxiliary techniques, such as sonication[38] and seeding[3,67,80,83] have also been employed. **Table 3.5** summarizes published studies on continuous crystallization in tubular-OFCs.

Table 3.5 – Summary of published studies on continuous crystallization in tubular-OFCs.

Reference	Compound	Diameter	Length	Volume	Net flow rate	Residence time	Operating time	Yield	Notes
Agnew *et al.*[82]	Paracetamol	15 mm	970 cm	NS	50 mL min^{-1}	NS	NS	NS	- Comparison to MSMPR - Polymorph control
Briggs *et al.*[80]	L-Glutamic acid	15 mm	25 m	5.1 L	30 g min^{-1}	80 min	10 h	NS	- Seeding to reduce fouling
Brown *et al.*[84]	Salicylic acid	15 mm	700 mm	NS	80-120 mL min^{-1}	1-1.5 min	1.25- 6.25 h	NS	- Antisolvent crystallization
Caldeira *et al.*[79]	Vanisal sodium Aspirin	15 mm	12 m	2 L	NS	NS	7 days	NS	- Establishment of a cleaning protocol
Cruz *et al.*[58]	Paracetamol	4 mm	193 cm	22.5 mL	NS	0.47-2.15 min	NS	NS	- Production of particles of inhalable size
Jiang and Ni[83]	Paracetamol	15 mm	9.5 m	1.68 L	40 g min^{-1}	40 min	4 h	NS	- Reactive seeded cooling crystallization
Kacker *et al.*[86]	Melamine	15 mm	NS	1 L	100 mL min^{-1}	10 min	NS	NS	- Application of inline imaging for monitoring crystallization
Lawton *et al.*[3]	API	NS	12 m	12 L	NS	12 min	NS	NS	- Cooling crystallization
Liu *et al.*[87]	Paracetamol Benzoic acid	40 mm	246 mm	245 mL	5.45 mL min^{-1} 5.44 mL min^{-1}	45 min 45 min	NS	47.6% 47%	- OFC with moving baffles - Integration with continuous filtration carousel
Peña *et al.*[85]	Benzoic acid	NS	NS	1250 mL	NS	8.33, 10, 12.5 min	NS	NS	- Spherical crystallization
Raval *et al.*[88]	α-Lactose monohydrate Paracetamol	25 mm	NS	4×120 mL	4.4 g min^{-1} 18 g min^{-1}	90 min 20 min	15 h 1 h and 40 min	70% 85%	- Four-stage cascade of OFCs with moving baffles - Seeded cooling crystallization
Siddique *et al.*[38]	Lactose	69 mm	4×740 mm	NS	50 mL min^{-1}	4 h	12 h	38%	- Sonication
Tahir *et al.*[81]	Lactose	69 mm 15 mm	4×740 mm 14 m	2760 mL 2500 mL	NS	NS	NS	NS	- Application of an advanced control scheme
Yang *et al.*[66]	Butyl paraben	16.3 mm	2×700 mm	280 mL	0-100 mL min^{-1}	NS	NS	NS	- Effect of oscillation conditions on nucleation kinetic parameters
Zhao *et al.*[67]	α-Lipioic acid:nicotinamide	16 mm	24 m	4.2 L	70 mL min^{-1}	1 h	2-3 h	NS	- Novel cocrystal

NS: not specified.

3.3.1 Crystallization Kinetics

Nucleation Kinetics

The determination of nucleation kinetics, as well as crystal growth kinetics, for continuous crystallization in OFCs has been seldom reported. Must authors have chosen to investigate the nucleation and crystal growth kinetics in batch and then use this data to transfer the processes from batch to continuous. The few studies that addressed the determination of nucleation kinetics in continuous are discussed below.

Brown *et al.*[84] employed a population balance model to estimate the nucleation and crystal growth kinetic parameters for the antisolvent crystallization of salicylic acid from mixtures of 2-propanol and water (antisolvent) in an OFC. Cruz *et al.*[58] employed a different approach, based on the classical nucleation theory, to investigate the effect of temperature on the induction time and, subsequently, on the nucleation kinetic and thermodynamic parameters for the cooling crystallization of paracetamol from aqueous solutions in an OFC. Under the same levels of oscillation intensity and supersaturation, the induction time decreased as the temperature increased, which the authors attributed to the increase of probability of nucleation as a consequence of the increase of frequency of molecular collisions. Furthermore, while the kinetic parameter was not affected by the increase of temperature, the thermodynamic parameter was affected by the increase of temperature in accordance with its effect on the interfacial tension. Yang *et al.*[66] also employed the classical nucleation theory to investigate the effect of the operating conditions, namely the oscillation intensity and the flow rate, on the induction time and, subsequently, on the nucleation kinetics for the cooling crystallization of butyl paraben from solutions of ethanol in an OFC. The authors observed a transition from homogeneous to heterogeneous nucleation as the supersaturation decreased. In both cases, under comparable levels of supersaturation, the induction time decreased as the oscillation intensity and the flow rate increased presumably due to the increase of shear rate. Moreover, at higher shear rates, the transition from homogenous to heterogeneous nucleation occurred at a slightly lower level of supersaturation, which suggests that homogeneous nucleation is a little more favorable under higher shear rates. Furthermore, while the interfacial energy, obtained from the thermodynamic parameter, was little affected by the oscillation conditions and the net flow rate, the pre-exponential kinetic parameter increased as the average shear rate increased, with a stronger effect in the heterogeneous nucleation regime than in the homogeneous nucleation regime.

Crystal Growth Kinetics

The determination of crystal growth kinetics for continuous crystallization in OFCs has been limited to the estimation of a linear overall crystal growth rate based on the change of the crystal size over time. For example, Cruz *et al.*[58] estimated a linear growth rate of 1.43×10^{-6} m s^{-1} (86 μm min^{-1}) for the cooling crystallization of paracetamol from aqueous solutions, Jiang and Ni[83] estimated a linear growth rate of 3.14×10^{-7} m s^{-1} for the

reactive crystallization of paracetamol, and Raval *et al.*[88] estimated a linear growth rate of 8.90×10^{-8} m s^{-1} for the cooling crystallization of paracetamol from mixtures of water and isopropanol.

3.3.2 Control of Final Properties

Control of Crystal Size

Several works have demonstrated that the narrow RTD of OFCs allows the continuous crystallization of products with narrow CSDs. Briggs *et al.*[80] described the seeded cooling crystallization of L-glutamic acid from aqueous solutions in an OFC. The OFC was operated for 10 h and delivered the product with a narrow CSD with no visible signs of encrustation. Siddique *et al.*[38] investigated the cooling sonocrystallization of lactose in an OFC. The OFC was operated for 12-16 h and delivered the product with a narrower CSD than the traditional batch process with no fouling and agglomeration issues. Peña *et al.*[85,89] described the antisolvent crystallization of spherical agglomerates of benzoic acid in a MSMPR and in an OFC. The OFC delivered the product with a narrower and more uniform agglomerate size distribution than the MSMPR. Finally, Raval *et al.*[88] studied the seeded cooling crystallizations of α-lactose monohydrate and paracetamol in a four-stage cascade of OFCs with moving baffles. The crystallizer delivered both products with narrow CSDs and without significant agglomeration.

Several works have also demonstrated that the operating conditions can be manipulated to control the crystal size during continuous crystallization in OFCs. Lawton *et al.*[3] investigated the cooling crystallization of an unspecified API in an OFC and manipulated the cooling rate, the oscillation intensity, the concentration of API, and the presence or absence of seeds to produce different crystal sizes. Brown *et al.*[84] investigated the antisolvent crystallization of salicylic acid from mixtures of 2-propanol and water (antisolvent) in an OFC and manipulated the oscillation intensity to keep the crystals in suspension and prevent the blockage of the crystallizer, which also resulted in an impact on the crystal size. In this case, increasing the oscillation intensity led to an increase of crystal size, which was rather unexpected. This is because, in previous studies in batch, increasing the oscillation intensity led to a decrease in crystal size due to the intensification of primary nucleation. The opposite results of this work are probably due to the difference in the ability of different oscillation intensities to keep crystals of different sizes in suspension. This is because lower oscillation intensities were insufficient to keep the larger crystals in suspension, which implies that only the smaller crystals could be sampled, whereas higher oscillation intensities enabled the suspension of the larger crystals, which implies that both the smaller and the larger crystals could be sampled. As a consequence, the increase of oscillation intensity resulted in a perceived increase in the mean crystal size. Briggs *et al.*[80] investigated the seeded cooling crystallization of L-glutamic acid from aqueous solutions in an OFC and evaluated the impact of the feed solution concentration and seed loading on the crystal size. As anticipated from the mass balance, lower feed solution concentrations and higher seed loadings yielded smaller crystals than higher feed solution concentrations and lower seed loadings. Cruz

et al.[58] investigated the cooling crystallization of paracetamol from aqueous solutions in an OFC and found that shorter residence times, lower temperatures and higher supersaturations allowed the production of smaller crystals. Tahir *et al.*[81] investigated the cooling crystallization of lactose in two commercially available OFCs and used an advanced control scheme to drive the cooling profile, the concentration of lactose and the crystal size towards the desired setpoints in order to control the product quality in the face of raw material fluctuations. Peña *et al.*[85] investigated the continuous antisolvent crystallization of spherical agglomerates of benzoic acid in an OFC and found that increasing the oscillation intensity resulted in smaller agglomerates and narrower agglomerate size distributions. Finally, Jiang and Ni[83] studied the reactive seeded cooling crystallization of paracetamol in an OFC and found that increasing the oscillation intensity reduced the crystal size of the final product.

Control of Crystal Shape

Only three papers have discussed the control of crystal shape during continuous crystallization in OFCs. Lawton *et al.*[3] investigated the cooling crystallization of an unspecified API in an OFC and proposed that the operating conditions, such as the cooling rate, the oscillation intensity, the concentration of API, and the presence or absence of seeds, could be manipulated to produce crystals with different shapes, including small crystals, large rods, large agglomerates and mid sized crystals. Peña *et al.*[85] produced large spherical agglomerates composed of small individual crystals of benzoic acid via spherical crystallization in an OFC in order to improve the efficiency of downstream processing, while maintaining the biopharmaceutical benefits provided by small individual crystals. Finally, Agnew *et al.*[82] used metacetamol as a templating agent to force the selective crystallization of the metastable form II of paracetamol in detriment of the stable form I via cooling crystallization in an OFC, and observed that, in the presence of metacetamol, the two polymorphs exchanged their usual morphologies. Typically, form I crystallizes with a block-like morphology and form II crystallizes with a needle-like morphology, but in the presence of metacetamol, the opposite morphologies were observed.

Control of Polymorphism

Only two papers have discussed the control of polymorphism during continuous crystallization in OFCs. Briggs *et al.*[80] investigated the seeded cooling crystallization of $_{L}$-glutamic acid in an OFC and evaluated the effects of the feed solution concentration and seed loading on the polymorphic form. Seeds of form β were used in the experiments. While the metastable form α was exclusively crystallized in most unseeded experiments, the stable form β was crystallized in all the seeded experiments (with the exception of one experiment that was operated at high feed solution concentration and low seed loading). In addition, while steady state was never achieved in the unseeded experiments, steady state was achieved with respect to CSD and polymorphic form after 2

residences times in the seeded experiments. In a different approach, Agnew *et al.*[82] used metacetamol as a templating agent to produce form II of paracetamol by cooling crystallization in a two-stage MSMPR and in an OFC. The addition of 25% (w/w) of metacetamol forced the selective crystallization of the metastable form II in detriment of the stable form I. The authors hypothesized that this could be due to the inhibition of the solution-mediated polymorphic transformation that usually occurs in the absence of a templating agent. After optimizing the operating conditions, both continuous crystallizers delivered pure form II, while the corresponding batch crystallizer could not deliver form II without any trace of impurity (in this case, metacetamol hydrate).

Notation

Acronyms	
API	Active pharmaceutical ingredient
CSD	Crystal size distribution
MSMPR	Mixed suspension mixed product removal
MSZW	Metastable zone width
OFC	Oscillatory flow crystallizer
PFC	Plug flow crystallizer
RTD	Residence time distribution
SEPC	Sharp edge periodic constrictions
SPC	Smooth periodic constrictions
STC	Stirred tank crystallizer

Latin symbols	
D	Tube diameter in the straight section
D_0	Tube diameter in the constriction
D_c	Axial dispersion coefficient
f	Frequency of oscillation
g	Inter-stage backmixing parameter
l	Tube length
L	Distance between constrictions
N	Number of ideal stirred tanks in series
t_m	Mixing time
u	Superficial net flow velocity
x_0	Center-to-peak amplitude of oscillation
$x_{0,crit}$	Critical amplitude of oscillation

Greek Letters	
μ	Fluid viscosity
ρ	Fluid density
σ	Relative supersaturation

Dimensionless Numbers	
$\alpha = (D_0/D)^2$	Ratio of the open constriction area for tubular-OFCs
$D_c/(ul)$	Vessel dispersion number
L/D	Cell aspect ratio for tubular-OFCs
Re	Reynolds number
$\mathrm{Re_o}$	Oscillatory Reynolds number
St	Strouhal number
$\mathrm{St_0}$	Modified Strouhal number
Ψ	Velocity ratio

References

(1) McGlone, T.; Briggs, N. E. B.; Clark, C. A.; Brown, C. J.; Sefcik, J.; Florence, A. J. Oscillatory Flow Reactors (OFRs) for Continuous Manufacturing and Crystallization. *Org. Process Res. Dev.* **2015**, *19* (9), 1186–1202.

(2) Fitch, A. W.; Jian, H.; Ni, X. An Investigation of the Effect of Viscosity on Mixing in an Oscillatory Baffled Column Using Digital Particle Image Velocimetry and Computational Fluid Dynamics Simulation. *Chem. Eng. J.* **2005**, *112* (1–3), 197–210.

(3) Lawton, S.; Steele, G.; Shering, P.; Zhao, L.; Laird, I.; Ni, X.-W. Continuous Crystallization of Pharmaceuticals Using a Continuous Oscillatory Baffled Crystallizer. *Org. Process Res. Dev.* **2009**, *13* (6), 1357–1363.

(4) Stonestreet, P.; van Der Veeken, P. M. J. The Effects of Oscillatory Flow and Bulk Flow Components on Residence Time Distribution in Baffled Tube Reactors. *Chem. Eng. Res. Des.* **1999**, *77* (8), 671–684.

(5) Stonestreet, P.; Harvey, A. P. A Mixing-Based Design Methodology for Continuous Oscillatory Flow Reactors. *Chem. Eng. Res. Des.* **2002**, *80* (1), 31–44.

(6) Ni, X.; Gough, P. On the Discussion of the Dimensionless Groups Governing Oscillatory Flow in a Baffled Tube. *Chem. Eng. Sci.* **1997**, *52* (18), 3209–3212.

(7) Harvey, A. P.; Mackley, M. R.; Stonestreet, P. Operation and Optimization of an Oscillatory Flow Continuous Reactor. *Ind. Eng. Chem. Res.* **2001**, *40* (23), 5371–5377.

(8) McDonough, J. R.; Phan, A. N.; Harvey, A. P. Rapid Process Development Using Oscillatory Baffled Mesoreactors – A State-of-the-Art Review. *Chem. Eng. J.* **2015**, *265*, 110–121.

(9) Ejim, L. N.; Yerdelen, S.; McGlone, T.; Onyemelukwe, I.; Johnston, B.; Florence, A. J.; Reis, N. M. A Factorial Approach to Understanding the Effect of Inner Geometry of Baffled Meso-Scale Tubes on Solids Suspension and Axial Dispersion in Continuous, Oscillatory Liquid–Solid Plug Flows. *Chem. Eng. J.* **2017**, *308*, 669–682.

(10) Mackley, M. R.; Smith, K. B.; Wise, N. P. The Mixing and Separation of Particle Suspensions Using Oscillatory Flow in Baffled Tubes. *Trans. Inst. Chem. Eng.* **1993**, *71* (A), 649–656.

(11) Reis, N.; Harvey, A. P.; Mackley, M. R.; Vicente, A. A.; Teixeira, J. A. Fluid Mechanics and Design Aspects of a Novel Oscillatory Flow Screening Mesoreactor. *Chem. Eng. Res. Des.* **2005**, *83* (4), 357–371.

(12) Takriff, M. S.; Ramli, W.; Daud, W.; Fisal, Z.; Alam, Z. Mutiphase Oscillatory Flow in a Baffled Tube. *J. Ind. Technol.* **2000**, *9* (2), 75–84.

(13) Brunold, C. R.; Hunns, J. C. B.; Mackley, M. R.; Thompson, J. W. Experimental Observations on Flow Patterns and Energy Losses for Oscillatory Flow in Ducts Containing Sharp Edges. *Chem. Eng. Sci.* **1989**, *44* (5), 1227–1244.

(14) Fitch, A. On the Determination of Axial Dispersion Coefficient in a Batch Oscillatory Baffled Column Using Laser Induced Fluorescence. *Chem. Eng. J.* **2003**, *92* (1–3), 243–253.

(15) Gough, P.; Ni, X.; Symes, K. C. Experimental Flow Visualisation in a Modified Pulsed Baffled Reactor. *J. Chem. Technol. Biotechnol.* **1997**, *69* (3), 321–328.

(16) Ni, X.; Stevenson, C. C. On the Effect of Gap Size between Baffle Outer Diameter and Tube Inner Diameter on the Mixing Characteristics in an Oscillatory-Baffled Column. *J. Chem. Technol. Biotechnol.* **1999**, *74* (6), 587–593.

(17) Ni, X.; Brogan, G.; Struthers, A.; Bennett, D. C.; Wilson, S. F. A Systematic Study of the Effect of Geometrical Parameters on Mixing Time in Oscillatory Baffled Columns. *Chem. Eng. Res. Des.* **1998**, *76* (5), 635–642.

(18) Ni, X.; De Gélicourt, Y. S.; Neil, J.; Howes, T. On the Effect of Tracer Density on Axial Dispersion in a Batch Oscillatory Baffled Column. *Chem. Eng. J.* **2002**, *85* (1), 17–25.

(19) Reis, N.; Vicente, A. A.; Teixeira, J. A.; Mackley, M. R. Residence Times and Mixing of a Novel Continuous Oscillatory Flow Screening Reactor. *Chem. Eng. Sci.* **2004**, *59* (22–23), 4967–4974.

(20) Smith, K. B. The Scale-Up of Oscillatory Flow Mixing, PhD Thesis, University of Cambridge, 1999.

(21) Abbott, M. S. R.; Harvey, A. P.; Morrison, M. I. Rapid Determination of the Residence Time Distribution (RTD) Function in an Oscillatory Baffled Reactor (OBR) Using a Design of Experiments (DoE) Approach. *Int. J. Chem. React. Eng.* **2014**, *12* (1), 575–586.

(22) Dickens, A. W.; Mackley, M. R.; Williams, H. R. Experimental Residence Time Distribution Measurements for Unsteady Flow in Baffled Tubes. *Chem. Eng. Sci.* **1989**, *44* (7), 1471–1479.

(23) Howes, T.; Mackley, M. R. Experimental Axial Dispersion for Oscillatory Flow through a Baffled Tube. *Chem. Eng. Sci.* **1990**, *45* (5), 1349–1358.

(24) Kacker, R.; Regensburg, S. I.; Kramer, H. J. M. Residence Time Distribution of Dispersed Liquid and Solid Phase in a Continuous Oscillatory Flow Baffled Crystallizer. *Chem. Eng. J.* **2017**, *317*, 413–423.

(25) Mackley, M. R.; Ni, X. Experimental Fluid Dispersion Measurements in Periodic Baffled Tube Arrays. *Chem. Eng. Sci.* **1993**, *48* (18), 3293–3305.

(26) Mackley, M. R.; Ni, X. Mixing and Dispersion in a Baffled Tube for Steady Laminar and Pulsatile Flow. *Chem. Eng. Sci.* **1991**, *46* (12), 3139–3151.

(27) Mohd Rasdi, F. R.; Phan, A. N.; Harvey, A. P. Rapid Determination of the Reaction Kinetics of an N-Butylbenzaldimine Synthesis Using a Novel Mesoscale Oscillatory Baffled Reactor. *Procedia Eng.* **2012**, *42*, 1527–1539.

(28) Ni, X.; Pereira, N. E. Parameters Affecting Fluid Dispersion in a Continuous Oscillatory Baffled Tube. *AIChE J.* **2000**, *46* (1), 37–45.

(29) Oliva, J. A.; Pal, K.; Barton, A.; Firth, P.; Nagy, Z. K. Experimental Investigation of the Effect of Scale-up on Mixing Efficiency in Oscillatory Flow Baffled Reactors (OFBR) Using Principal Component

Based Image Analysis as a Novel Noninvasive Residence Time Distribution Measurement Approach. *Chem. Eng. J.* **2018**, *351*, 498–505.

(30) Onyemelukwe, I. I.; Nagy, Z. K.; Rielly, C. D. Solid-Liquid Axial Dispersion Performance of a Mesoscale Continuous Oscillatory Flow Crystalliser with Smooth Periodic Constrictions Using a Non-Invasive Dual Backlit Imaging Technique. *Chem. Eng. J.* **2020**, *382* (122862).

(31) Palma, M.; Giudici, R. Analysis of Axial Dispersion in an Oscillatory-Flow Continuous Reactor. *Chem. Eng. J.* **2003**, *94* (3), 189–198.

(32) Phan, A. N.; Harvey, A. Development and Evaluation of Novel Designs of Continuous Mesoscale Oscillatory Baffled Reactors. *Chem. Eng. J.* **2010**, *159* (1–3), 212–219.

(33) Phan, A. N.; Harvey, A. P. Characterisation of Mesoscale Oscillatory Helical Baffled Reactor—Experimental Approach. *Chem. Eng. J.* **2012**, *180*, 229–236.

(34) Phan, A. N.; Harvey, A.; Lavender, J. Characterisation of Fluid Mixing in Novel Designs of Mesoscale Oscillatory Baffled Reactors Operating at Low Flow Rates (0.3–0.6ml/Min). *Chem. Eng. Process. Process Intensif.* **2011**, *50* (3), 254–263.

(35) Slavnić, D. S.; Živković, L. V.; Bjelić, A. V.; Bugarski, B. M.; Nikačević, N. M. Residence Time Distribution and Peclet Number Correlation for Continuous Oscillatory Flow Reactors. *J. Chem. Technol. Biotechnol.* **2017**, *92* (8), 2178–2188.

(36) Slavnić, D.; Bugarski, B.; Nikačević, N. Solids Flow Pattern in Continuous Oscillatory Baffled Reactor. *Chem. Eng. Process. - Process Intensif.* **2019**, *135*, 108–119.

(37) Reis, N.; Vicente, A. A.; Teixeira, J. A. Liquid Backmixing in Oscillatory Flow through a Periodically Constricted Meso-Tube. *Chem. Eng. Process. Process Intensif.* **2010**, *49* (7), 793–803.

(38) Siddique, H.; Brown, C. J.; Houson, I.; Florence, A. J. Establishment of a Continuous Sonocrystallization Process for Lactose in an Oscillatory Baffled Crystallizer. *Org. Process Res. Dev.* **2015**, *19* (12), 1871–1881.

(39) Smith, K. B.; Mackley, M. R. An Experimental Investigation into the Scale-up of Oscillatory Flow Mixing in Baffled Tubes. *Chem. Eng. Res. Des.* **2006**, *84* (11), 1001–1011.

(40) Takriff, M. S.; Masyithah, Z. Interstage Backmixing in Oscillatory Flow in a Baffled Column. *Chem. Eng. Commun.* **2002**, *189* (12), 1640–1652.

(41) Zheng, M.; Mackley, M. The Axial Dispersion Performance of an Oscillatory Flow Meso-Reactor with Relevance to Continuous Flow Operation. *Chem. Eng. Sci.* **2008**, *63* (7), 1788–1799.

(42) Ni, X.; Jian, H.; Fitch, A. W. Computational Fluid Dynamic Modelling of Flow Patterns in an Oscillatory

Baffled Column. *Chem. Eng. Sci.* **2002**, *57* (14), 2849–2862.

(43) Jian, H.; Ni, X. A Numerical Study on the Scale-Up Behaviour in Oscillatory Baffled Columns. *Chem. Eng. Res. Des.* **2005**, *83* (10), 1163–1170.

(44) Sern, W. K.; Takriff, M. S.; Kamarudin, S. K.; Talib, M. Z. M.; Hasan, N. Numerical Simulation of Fluid Flow Behaviour on Scale up of Oscillatory Baffled Column. *J. Eng. Sci. Technol.* **2012**, *7* (1), 119–130.

(45) Manninen, M.; Gorshkova, E.; Immonen, K.; Ni, X.-W. Evaluation of Axial Dispersion and Mixing Performance in Oscillatory Baffled Reactors Using CFD. *J. Chem. Technol. Biotechnol.* **2013**, *88* (4), 553–562.

(46) Kimuli, E. N.; Onyemelukwe, I. I.; Benyahia, B.; Rielly, C. D. Characterisation of Axial Dispersion in a Meso-Scale Oscillatory Baffled Crystalliser Using a Numerical Approach. *Comput. Aided Chem. Eng.* **2017**, *40*, 223–228.

(47) González-Juárez, D.; Solano, J. P.; Herrero-Martín, R.; Harvey, A. P. Residence Time Distribution in Multiorifice Baffled Tubes: A Numerical Study. *Chem. Eng. Res. Des.* **2017**, *118*, 259–269.

(48) Sarkar, S.; Singh, K. K.; Shenoy, K. T. CFD Modelling of Oscillatory Flow in Columns Having Different Types of Internals. *Chem. Eng. Process. - Process Intensif.* **2020**, *155* (108052).

(49) Avila, M.; Fletcher, D. F.; Poux, M.; Xuereb, C.; Aubin, J. Mixing Performance in Continuous Oscillatory Baffled Reactors. *Chem. Eng. Sci.* **2020**, *219*, 115600.

(50) Ni, X.; De Gélicourt, Y. S.; Baird, M. H. I.; Rao, N. V. R. Scale-up of Single Phase Axial Dispersion Coefficients in Batch and Continuous Oscillatory Baffled Tubes. *Can. J. Chem. Eng.* **2001**, *79* (3), 444–448.

(51) Jiang, M.; Ni, X.-W. Effects of Solvents and Impurity on Crystallization Kinetics and Crystal Properties in a Reactive Crystallization of Paracetamol. *J. Cryst. Growth* **2019**, *523*, 125150.

(52) Brown, C. J.; Ni, X. Online Evaluation of Paracetamol Antisolvent Crystallization Growth Rate with Video Imaging in an Oscillatory Baffled Crystallizer. *Cryst. Growth Des.* **2011**, *11* (3), 719–725.

(53) Brown, C. J.; Ni, X.-W. Evaluation of Growth Kinetics of Antisolvent Crystallization of Paracetamol in an Oscillatory Baffled Crystallizer Utilizing Video Imaging. *Cryst. Growth Des.* **2011**, *11* (9), 3994–4000.

(54) Chew, C. M.; Ristic, R. I.; Dennehy, R. D.; De Yoreo, J. J. Crystallization of Paracetamol under Oscillatory Flow Mixing Conditions. *Cryst. Growth Des.* **2004**, *4* (5), 1045–1052.

(55) Chew, C. M.; Ristic, R. I. Crystallization by Oscillatory and Conventional Mixing at Constant Power Density. *AIChE J.* **2005**, *51* (5), 1576–1579.

(56) Ristic, R. I. Oscillatory Mixing for Crystallization of High Crystal Perfection Pharmaceuticals. *Chem. Eng. Res. Des.* **2007**, *85* (7), 937–944.

(57) Brown, C. J.; Ni, X.-W. Determination of Metastable Zone Width, Mean Particle Size and Detectable Number Density Using Video Imaging in an Oscillatory Baffled Crystallizer. *CrystEngComm* **2012**, *14* (8), 2944.

(58) Cruz, P.; Rocha, F.; Ferreira, A. Effect of Operating Conditions on Batch and Continuous Paracetamol Crystallization in an Oscillatory Flow Mesoreactor. *CrystEngComm* **2016**, *18* (47), 9113–9121.

(59) Cruz, P.; Rocha, F.; Ferreira, A. Determination of the Critical Mixing Intensity for Secondary Nucleation of Paracetamol in an Oscillatory Flow Crystallizer. *CrystEngComm* **2018**, *20* (6), 829–836.

(60) Ni, X.-W.; Valentine, A.; Liao, A.; Sermage, S. B. C.; Thomson, G. B.; Roberts, K. J. On the Crystal Polymorphic Forms of L-Glutamic Acid Following Temperature Programmed Crystallization in a Batch Oscillatory Baffled Crystallizer. *Cryst. Growth Des.* **2004**, *4* (6), 1129–1135.

(61) Ni, X.; Liao, A. Effects of Cooling Rate and Solution Concentration on Solution Crystallization of L-Glutamic Acid in an Oscillatory Baffled Crystallizer. *Cryst. Growth Des.* **2008**, *8* (8), 2875–2881.

(62) Ni, X.; Liao, A. Effects of Mixing, Seeding, Material of Baffles and Final Temperature on Solution Crystallization of l-Glutamic Acid in an Oscillatory Baffled Crystallizer. *Chem. Eng. J.* **2010**, *156* (1), 226–233.

(63) Callahan, C. J.; Ni, X.-W. Probing into Nucleation Mechanisms of Cooling Crystallization of Sodium Chlorate in a Stirred Tank Crystallizer and an Oscillatory Baffled Crystallizer. *Cryst. Growth Des.* **2012**, *12* (5), 2525–2532.

(64) Callahan, C. J.; Ni, X.-W. An Investigation into the Effect of Mixing on the Secondary Nucleation of Sodium Chlorate in a Stirred Tank and an Oscillatory Baffled Crystallizer. *CrystEngComm* **2014**, *16* (4), 690–697.

(65) Brown, C. J.; Lee, Y. C.; Nagy, Z. K.; Ni, X. Evaluation of Crystallization Kinetics of Adipic Acid in an Oscillatory Baffled Crystallizer. *CrystEngComm* **2014**, *16* (34), 8008.

(66) Yang, H.; Yu, X.; Raval, V.; Makkawi, Y.; Florence, A. Effect of Oscillatory Flow on Nucleation Kinetics of Butyl Paraben. *Cryst. Growth Des.* **2016**, *16* (2), 875–886.

(67) Zhao, L.; Raval, V.; Briggs, N. E. B.; Bhardwaj, R. M.; McGlone, T.; Oswald, I. D. H.; Florence, A. J. From Discovery to Scale-up: α-Lipoic Acid : Nicotinamide Co-Crystals in a Continuous Oscillatory Baffled Crystalliser. *CrystEngComm* **2014**, *16* (26), 5769–5780.

(68) Castro, F.; Ferreira, A.; Teixeira, J. A.; Rocha, F. Protein Crystallization As a Process Step in a Novel Meso Oscillatory Flow Reactor: Study of Lysozyme Phase Behavior. *Cryst. Growth Des.* **2016**, *16* (7),

3748–3755.

(69) McLachlan, H.; Ni, X.-W. An Investigation into Parameters Affecting Crystal Purity of Urea in a Stirred Tank and an Oscillatory Baffled Crystallizer. *Chem. Eng. Commun.* **2016**, *203* (9), 1189–1197.

(70) McLachlan, H.; Ni, X.-W. On the Effect of Added Impurity on Crystal Purity of Urea in an Oscillatory Baffled Crystallizer and a Stirred Tank Crystallizer. *J. Cryst. Growth* **2016**, *442*, 81–88.

(71) Xiao, Y.; Wang, J.; Huang, X.; Shi, H.; Zhou, Y.; Zong, S.; Hao, H.; Bao, Y.; Yin, Q. Determination Methods for Crystal Nucleation Kinetics in Solutions. *Cryst. Growth Des.* **2018**, *18* (1), 540–551.

(72) Nývlt, J. Kinetics of Nucleation in Solutions. *J. Cryst. Growth* **1968**, *3–4*, 377–383.

(73) Nývlt, J.; Rychlý, R.; Gottfried, J.; Wurzelová, J. Metastable Zone-Width of Some Aqueous Solutions. *J. Cryst. Growth* **1970**, *6* (2), 151–162.

(74) Nagy, Z. K.; Fujiwara, M.; Woo, X. Y.; Braatz, R. D. Determination of the Kinetic Parameters for the Crystallization of Paracetamol from Water Using Metastable Zone Width Experiments. *Ind. Eng. Chem. Res.* **2008**, *47* (4), 1245–1252.

(75) Kubota, N. A New Interpretation of Metastable Zone Widths Measured for Unseeded Solutions. *J. Cryst. Growth* **2008**, *310* (3), 629–634.

(76) Kobari, M.; Kubota, N.; Hirasawa, I. Computer Simulation of Metastable Zone Width for Unseeded Potassium Sulfate Aqueous Solution. *J. Cryst. Growth* **2011**, *317* (1), 64–69.

(77) Randolph, A. D.; Larson, M. A. *Theory of Particulate Processes*; Academic Press: New York and London, 1971.

(78) Granberg, R. A.; Bloch, D. G.; Rasmuson, Å. C. Crystallization of Paracetamol in Acetone–Water Mixtures. *J. Cryst. Growth* **1999**, *198–199*, 1287–1293.

(79) Caldeira, R.; Ni, X. Evaluation and Establishment of a Cleaning Protocol for the Production of Vanisal Sodium and Aspirin Using a Continuous Oscillatory Baffled Reactor. *Org. Process Res. Dev.* **2009**, *13* (6), 1080–1087.

(80) Briggs, N. E. B. B.; Schacht, U.; Raval, V.; McGlone, T.; Sefcik, J.; Florence, A. J. Seeded Crystallization of β-L-Glutamic Acid in a Continuous Oscillatory Baffled Crystallizer. *Org. Process Res. Dev.* **2015**, *19* (12), 1903–1911.

(81) Tahir, F.; Krzemieniewska-Nandwani, K.; Mack, J.; Lovett, D.; Siddique, H.; Mabbott, F.; Raval, V.; Houson, I.; Florence, A. Advanced Control of a Continuous Oscillatory Flow Crystalliser. *Control Eng. Pract.* **2017**, *67*, 64–75.

(82) Agnew, L. R.; McGlone, T.; Wheatcroft, H. P.; Robertson, A.; Parsons, A. R.; Wilson, C. C. Continuous

Crystallization of Paracetamol (Acetaminophen) Form II: Selective Access to a Metastable Solid Form. *Cryst. Growth Des.* **2017**, *17* (5), 2418–2427.

(83) Jiang, M.; Ni, X.-W. Reactive Crystallization of Paracetamol in a Continuous Oscillatory Baffled Reactor. *Org. Process Res. Dev.* **2019**, *23* (5), 882–890.

(84) Brown, C. J.; Adelakun, J. A.; Ni, X.-W. Characterization and Modelling of Antisolvent Crystallization of Salicylic Acid in a Continuous Oscillatory Baffled Crystallizer. *Chem. Eng. Process. Process Intensif.* **2015**, *97*, 180–186.

(85) Peña, R.; Oliva, J. A.; Burcham, C. L.; Jarmer, D. J.; Nagy, Z. K. Process Intensification through Continuous Spherical Crystallization Using an Oscillatory Flow Baffled Crystallizer. *Cryst. Growth Des.* **2017**, *17* (9), 4776–4784.

(86) Kacker, R.; Maaß, S.; Emmerich, J.; Kramer, H. Application of Inline Imaging for Monitoring Crystallization Process in a Continuous Oscillatory Baffled Crystallizer. *AIChE J.* **2018**, *64* (7), 2450–2461.

(87) Liu, Y. C.; Domokos, A.; Coleman, S.; Firth, P.; Nagy, Z. K. Development of Continuous Filtration in a Novel Continuous Filtration Carousel Integrated with Continuous Crystallization. *Org. Process Res. Dev.* **2019**, *23* (12), 2655–2665.

(88) Raval, V.; Siddique, H.; Brown, C. J.; Florence, A. J. Development and Characterisation of a Cascade of Moving Baffle Oscillatory Crystallisers (CMBOC). *CrystEngComm* **2020**, *22* (13), 2288–2296.

(89) Peña, R.; Nagy, Z. K. Process Intensification through Continuous Spherical Crystallization Using a Two-Stage Mixed Suspension Mixed Product Removal (MSMPR) System. *Cryst. Growth Des.* **2015**, *15* (9), 4225–4236.

Chapter 4 - Suspension of Solids in Planar Oscillatory Flow Crystallizers

This chapter is reproduced in part with permission from Cruz, P. C.; Silva, C. R.; Rocha, F. A.; Ferreira, A. M. Mixing Performance of Planar Oscillatory Flow Reactors with Liquid Solutions and Solid Suspensions. Ind. Eng. Chem. Res. 2021, 60 (6), 2663–2676. Copyright 2021 American Chemical Society.

https://pubs.acs.org/doi/full/10.1021/acs.iecr.0c04991

4.1 Introduction

The state of mixing in an oscillatory flow crystallizer (OFC) defines the environment in which the crystals nucleate and grow. In particular, the state of mixing controls the state of suspension inside the crystallizer.[1] To keep crystals in suspension in an OFC, the crystals terminal velocity must be lower than the fluid velocity in the opposite direction; when the OFC is operated vertically, that is the axial velocity; when the OFC is operated horizontally, that is the radial velocity.[2] Therefore, below a minimum oscillation intensity, the crystals will be totally or partially deposited on the base of the OFC, and above that level, the crystals will be completely suspended in the bulk of the fluid.

The minimum oscillation intensity required to keep crystals in suspension in an OFC depends on two main factors: the crystals terminal velocity, which is affected by the properties of the crystals (including size and density), the properties of the fluid (including density and viscosity), and the properties of the suspension (including the concentration of crystals in suspension); and the mixing efficiency, which is affected by the orientation of the OFC (vertical or horizontal), the oscillation conditions (including the frequency and amplitude of oscillation), and the geometry of the OFC (including the baffle type, the cell aspect ratio, and the ratio of the open constriction area).[3–5]

In this work, the minimum mixing intensity required to fully suspend different concentrations of polyvinyl chloride (PVC) particles in water was determined in three planar-OFCs with different geometries. The main goal was to investigate the impact of the oscillation conditions and geometric parameters on the suspension of solids in planar-OFCs. The experimental conditions were chosen to simulate typical conditions during pharmaceutical crystallization: diameter of the particles between 100 and 200 µm, density of the fluid close to 1 g cm^{-3} and concentration of solids between 10 and 30% (w/w).

4.2 Materials and Methods

4.2.1 Crystallizers

The experiments were performed in three Perspex® planar-OFCs – **Figure 4.1**. The crystallizers were operated horizontally. The dimensions of each planar-OFC including the channel width in the straight section, W, the channel width in the constriction, W_0, the distance between constrictions, L, the constriction length, L_1, the straight section length, L_2, the channel height, H, the volume of each inter-constriction cell, V_{cell}, the cell aspect ratio, L/W, the ratio of the open constriction area, $\alpha = W_0/W$, the total volume, V, and the total length, l, are presented in **Table 4.1**.



Figure 4.1 – Plate-like planar-OFC.

The dimensions of the three planar-OFCs were chosen based on the work of Pereira,[6] who used numerical optimization to minimize the mixing time as a function of the geometric parameters of planar-OFCs. Crystallizer 2 (L/W=4.25 and α=0.19) was designed with the dimensions that provided the lowest mixing time, according to Pereira;[6] Crystallizer 3 (L/W=4.25 and α=0.41) is a variant of Crystallizer 2 with a wider constriction, corresponding to α=0.41, which roughly matches the upper limit recommended by Gough *et al.*[7] for efficient mixing in a conventional tubular-OFC; and, finally, Crystallizer 1 (L/W=3.00 and α=0.41) is a variant of Crystallizer 3 with a shorter distance between constrictions, corresponding to L/W=3.00, the same value used by Reis *et al.*[8] in a tubular-OFC with smooth periodic constrictions (SPC), where unmatched performances were achieved.

Table 4.1 – Dimensions of each planar-OFC.

Parameter	Crystallizer 1	Crystallizer 2	Crystallizer 3
W (mm)	8	8	8
W_0(mm)	3.3	1.5	3.3
$L = L_1 + L_2$ (mm)	24	34	34
L_1 (mm)	11	8	8
L_2 (mm)	13	26	26
H (mm)	5	5	5
V_{cell} (mm^3)	831	1230	1266
L/W	3.00	4.25	4.25
$\alpha = W_0/W$	0.41	0.19	0.41
V (mL)	111	117	123
l (m)	3.35	3.27	3.27

4.2.2 Experimental Procedure

A stream of distilled water was injected into the crystallizer by a peristaltic pump (BT300-2J, Longer Pump). When the crystallizer was completely full with distilled water, a suspension of PVC particles (160 μm of mean diameter) was continuously injected and kept in oscillation, which forced the water out of the crystallizer. The oscillation was provided by a linear motor (H01-23x166/80, LinMot) actuating a piston with a 12.8 mm diameter. When the crystallizer was completely and homogeneously filled with the suspension, the flow and the oscillation were stopped and the particles were allowed to settle. Then the oscillation was reactivated to determine the minimum amplitude, x_0, required to fully suspend the particles at fixed frequency, f. This value is herein identified as the critical amplitude for total suspension of solids, $x_{0,crit}$. To determine $x_{0,crit}$, the amplitude of oscillation was progressively increased by 0.5 mm increments at the piston, corresponding to 1.6 mm in the straight section. Therefore, the determination of $x_{0,crit}$ had an associated error of 1.6 mm.

An image analysis technique was employed to determine $x_{0,crit}$. The technique consisted in focusing a video camera (Leica DMS300) at the base of a mixing cell, and placing a light source (Leica LED30000 BLI) at the top, to record the oscillating particles – **Figure 4.2**.

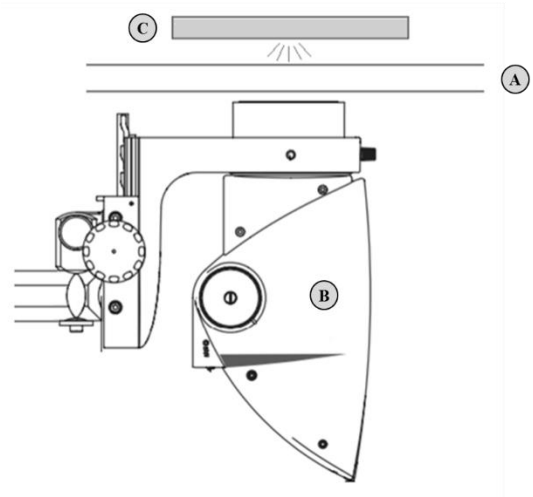


Figure 4.2 – Experimental set-up for the determination of the critical amplitude for total suspension of solids. A – planar-OFC; B – video camera; C – light source.

A series of frames were captured for each combination of x_0 and f. Then, the images were analyzed by an image analysis algorithm developed in Matlab®. This algorithm reduces the color depth of the image from 256 to 2 levels of gray, eliminates the objects that contact the boarder of the image, identifies the particles in the image, and determines the number and total area of the particles. This sequence of image processing steps is shown in **Figure 4.3**. The algorithm only identifies the particles that are not suspended because they produce a darker print in the image than the moving particles, which blend with the background. The number and total area of the non-suspended particles were determined in 5 frames for each combination of x_0 and f. Then, the mean and the standard deviation of the number and total area of the non-suspended particles of the 5 frames were calculated. The critical amplitude for total suspension of solids was reached when the mean number and the mean total area of the non-suspended particles reached simultaneously 10% and 15% of the initial values (without oscillation), respectively. Simultaneous application of these two criteria reduced the error associated with the image analysis technique and matched with a visual inspection of good particle suspension.

Suspensions with three different concentrations of PVC particles in water were tested: 10, 20 and 30% (w/w) as mass of particles per mass of water, corresponding to 9, 17 and 23% (w/w) as mass of particles per total mass. Suspensions with higher concentrations were also tested but it was not possible to determine whether the solids were suspended or not due to the high density of particles. This experimental procedure was repeated in the three planar-OFCs.

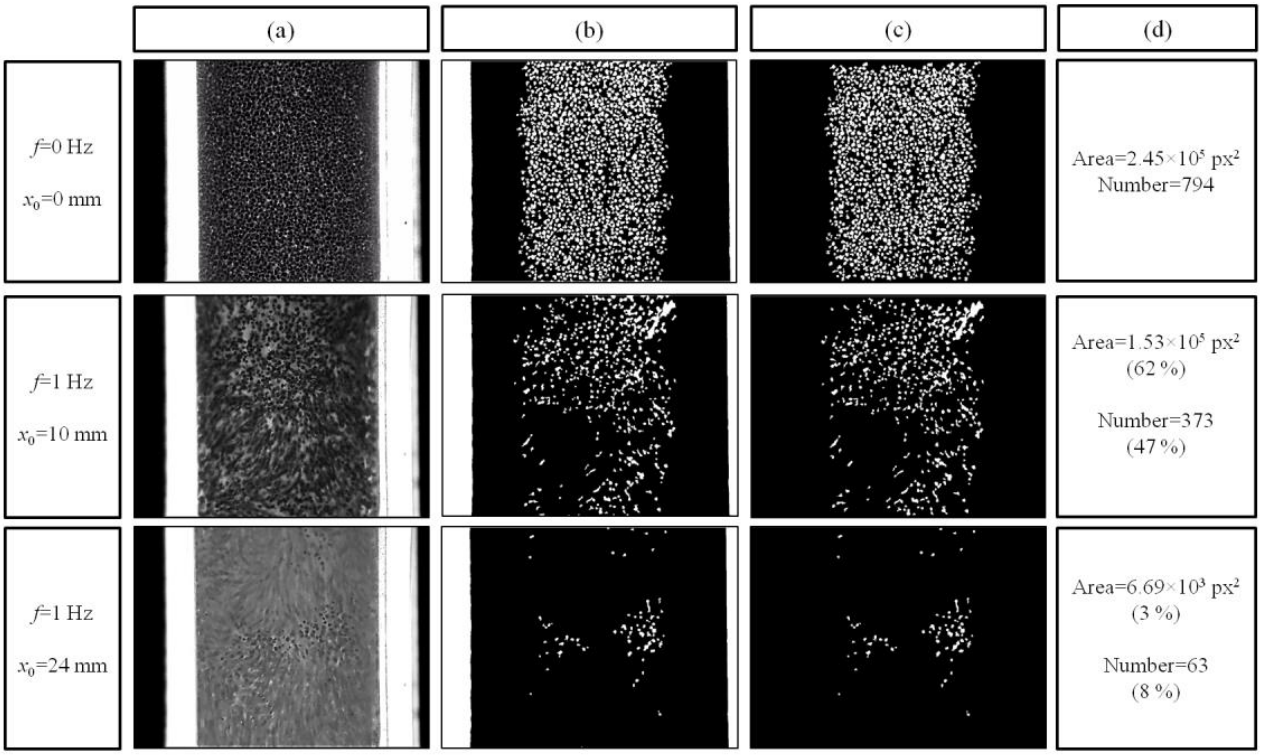


Figure 4.3 – Image processing steps. Crystallizer 1 with a 10% (w/w) suspension. (a) Original image. (b) Reduction of color depth from 256 to 2 levels of gray. (c) Elimination of objects that contact the boarder of the image and the identification of the particles. (d) Determination of the number and total area of the particles.

4.3 Results and Discussion

In this work, $x_{0,crit}$ was determined in a range of frequencies (1-8 Hz) and concentration of solids (10-30% (w/w)) in three horizontal planar-OFCs with different geometries. The determination of $x_{0,crit}$ is illustrated in **Figure 4.4**. This figure shows that when Crystallizer 1 operates at f=1 Hz with a 10% (w/w) suspension, the percentage of particles decreases below 10% and, simultaneously, the percentage of total area decreases below 15% when x_0=24 mm. So, x_0=24 mm is the critical amplitude of oscillation under these operating conditions. This method was applied to all the operating conditions under study.

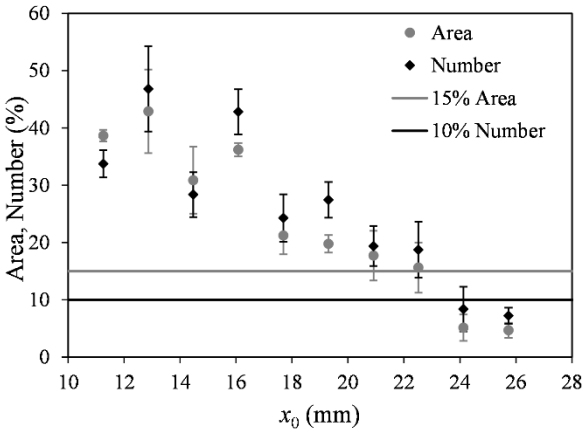


Figure 4.4 – Percentage of particles and total area as a function of the amplitude in Crystallizer 1 operating at f=1 Hz with a 10% (w/w) suspension. The error bars represent the standard deviation of 5 frames.

The velocity ratio, defined as the ratio between the peak oscillatory axial velocity, $v_{osc} = 2\pi f x_0$, and the terminal velocity of a single particle, v_t, was calculated for $x_{0,crit}$. This dimensionless group was proposed by Mackley *et al.*[2] and has been used to compare the efficiency of OFCs to suspend solids with different operating conditions[4] and geometries,[5] and also to classify the solids flow regime.[9] The ratio between the input axial velocity and the generated radial velocity depends on the operating conditions and geometry of the OFC. Therefore, a lower velocity ratio is an indicator that a particular operating condition or geometry is more effective in generating the radial velocity required to fully suspend the solids.

In the laminar flow regime, the terminal (or settling) velocity of an individual particle can be calculated from Stokes' law[10] as:

$$v_t = \frac{g d_p^2 (\rho_p - \rho)}{18\mu} \qquad \textbf{(4.1)}$$

where g is the gravitational acceleration, d_p is the particle diameter, ρ_p is the particle density, ρ is the fluid density, and μ is the fluid viscosity. Stokes' law assumes that the motion of an individual particle is unaffected by the motion of other particles. However, when a large number of particles are present, the surrounding particles interfere with the motion of the individual particles. This is because the particles displace the fluid as they settle, and the upward displacement of the fluid reduces significantly the terminal velocity of the individual particles. Therefore, the actual terminal velocity in this hindered flow is less than would be calculated from Stokes' law.

The effective slurry viscosity, μ_m, can be calculated as:

$$\mu_m = \frac{\mu}{\psi_p} \tag{4.2}$$

where ψ_p is an empirical correction, which can be calculated as:[10]

$$\psi_p = \frac{1}{10^{1.82(1-\varepsilon)}} \tag{4.3}$$

where ε is the volume fraction of the slurry occupied by the fluid. Therefore, the slurry density, ρ_m, can be calculated as:

$$\rho_m = \varepsilon\rho + (1-\varepsilon)\rho_p \tag{4.4}$$

Substituting ρ by ρ_m and μ by μ_m in **Equation (4.1)** and considering that the actual terminal velocity is ε times the velocity calculated by Stokes' law, **Equation (4.1)** becomes:

$$v_t = \frac{g d_p^2(\rho_p - \rho)}{18\mu}(\varepsilon^2\psi_p) \tag{4.5}$$

Finally, the suspension of solids also depends on the energy input, expressed as the power input per unit volume, P/V, calculated as:

$$\frac{P}{V} = \frac{2N_c\rho(2\pi f x_0)^3}{3\pi C_0^2}\left(\frac{1}{\alpha^2} - 1\right) \tag{4.6}$$

where N_c is the number of identical constrictions per unit length and C_0 is the standard orifice discharge coefficient usually taken as 0.7.[9,11]

Figure 4.5, **Figure 4.6** and **Figure 4.7** display the experimental results for $x_{0,crit}$, v_{osc}/v_t and P/V. It should be noted that when Crystallizer 3 was operated at f=1 Hz and f=8 Hz the solids were not fully suspended even with the maximum amplitude provided by the linear motor (20 mm in the piston, corresponding to 32 mm in the channel straight section). For this reason, $x_{0,crit}$, v_{osc}/v_t and P/V are not provided for these conditions in **Figure 4.5**, in **Figure 4.6** and in **Figure 4.7**, respectively.

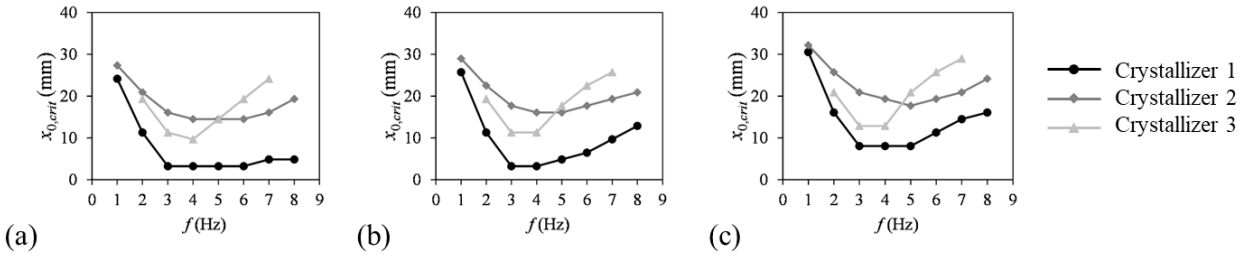


Figure 4.5 – Critical amplitude of oscillation for total suspension of solids as a function of the frequency of oscillation in three planar-OFCs operating with (a) 10% (w/w), (b) 20% (w/w), and (c) 30% (w/w) suspensions.

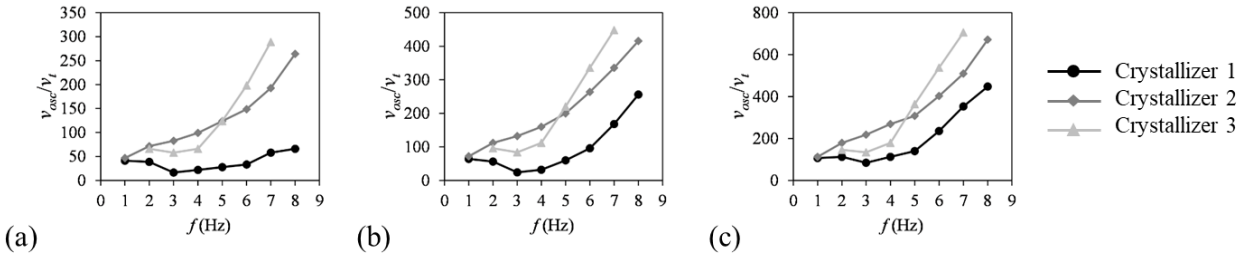


Figure 4.6 – Velocity ratio at the critical amplitude of oscillation for total suspension of solids as a function of the frequency of oscillation in three planar-OFCs operating with (a) 10% (w/w), (b) 20% (w/w), and (c) 30% (w/w) suspensions.

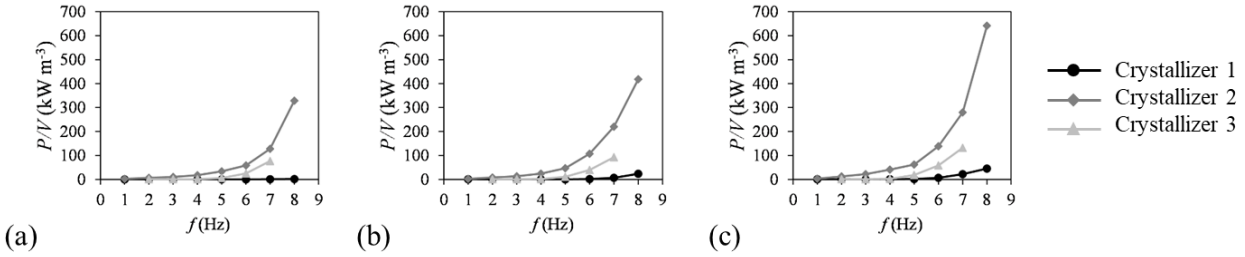


Figure 4.7 – Power input per unit volume at the critical amplitude of oscillation for total suspension of solids as a function of the frequency of oscillation in three planar-OFCs operating with (a) 10% (w/w), (b) 20% (w/w), and (c) 30% (w/w) suspensions.

Figure 4.5 shows that $x_{0,crit}$ increases when the concentration of solids increases from 10 to 30% (w/w) in the three crystallizers. Previous studies in tubular-OFCs have reported a maximum limit of 20% (w/w) to suspend solids,[3–5] but this limit was exceeded in this work with planar-OFCs operating with 30% (w/w) suspensions.

Figure 4.5 also shows that the dependency of $x_{0,crit}$ on f can be generally described as a "U" shape response, with $x_{0,crit}$ decreasing as f increases from 1 to 4 Hz, and $x_{0,crit}$ increasing as f increases from 4 to 8 Hz, in the three crystallizers. The first part of this trend follows the results previously obtained in tubular-OFCs,[3–5] but the second part follows an opposite trajectory. It was observed that when high levels of f are combined with low levels of x_0 two mixing zones are formed: one with high mixing intensity near the constrictions, and another with very low mixing intensity in the center of the straight section. This phenomenon is illustrated in **Figure 4.8**. Visual inspection of this phenomenon shows that when f>4 Hz the vortices do not have time to distort and expand through the full volume of the cell before the direction of the flow is reversed, which creates stagnant zones in the middle of the cell. Therefore, when f>4 Hz, x_0 must increase significantly to enable the full suspension of solids.

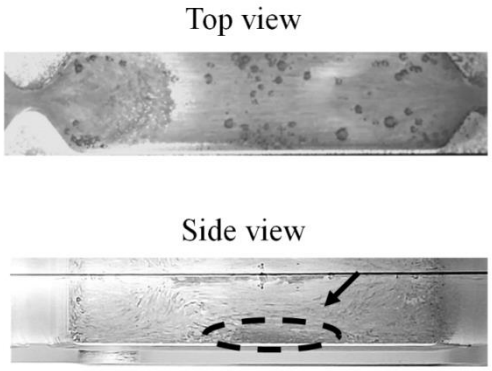


Figure 4.8 – Typical top and side views of a particle suspension in a planar-OFC operating below $x_{0,crit}$ with f>5Hz. The deposit of particles is identified with an arrow.

In a tubular-OFC, the cell aspect ratio is defined as L/D, where L is the distance between constrictions, and D is the tube diameter in the straight section; and the ratio of the open constriction area is defined as $\alpha = (D_0/D)^2$, where D_0 the tube diameter in the constriction. Ejim *et al.*[5] determined $x_{0,crit}$ in 10 tubular-OFCs, 5 with smooth periodic constrictions (SPC) (Tubes A, B, C, D and E) and 5 with sharp edge periodic constrictions (SEPC) (Tubes F, G, H, I and J), with L/D ranging between 1.5 and 3.0 and α ranging between 0.12 and 0.25. $x_{0,crit}$ was determined at f=2, 5 and 7 Hz with a concentration of solids of 10% (w/w). $x_{0,crit}$ decreased as f increased in all the tubes, except Tube E. In the case of Tube E, when f increased from 5 to 7 Hz there was a slight increase of $x_{0,crit}$. The geometry of tube E was the closest to the geometry of Crystallizer 1 (Tube E: α=0.25

and L/D=3.0; Crystallizer 1: α=0.41 and L/W=3.0), which suggests that the loss of mixing efficiency at higher frequencies may also occur in tubular-OFCs, depending on their geometry.

With respect to the velocity ratio, **Figure 4.6** shows that, at low frequencies, between 1 and 3 Hz, v_{osc}/v_t generally decreases as f decreases, which means that it is easier to suspend particles at high frequencies and low amplitudes than at low frequencies and high amplitudes. This agrees with the findings of Reis *et al.*[4] and Ejim *et al.*.[5] On the other hand, at high frequencies, between 3 and 8 Hz, v_{osc}/v_t generally increases as f decreases, which must be a result of the mixing problems previously mentioned for higher frequencies. So, f=3 Hz is clearly the optimum frequency of oscillation to suspend solids. f=3 Hz also enables the suspension of solids with the lowest values of P/V. Channel 2 is the exception to this rule as v_{osc}/v_t and P/V increase monotonically with f. It is also noteworthy that v_{osc}/v_t is higher than 7 in the whole range of frequencies in the three crystallizers, and P/V is higher than 227 W m^{-3} in most cases, which corresponds to the "Solids washout" regime, as defined by Slavnić *et al.*.[9]

Figure 4.5, **Figure 4.6** and **Figure 4.7** also present the effects of L/W and α on the suspension of solids. These figures show that ranging L/W between 3.00 and 4.25 (compare Crystallizer 1 and Crystallizer 3) has a stronger effect on the suspension of solids than ranging α between 0.19 and 0.41 (compare Crystallizer 2 and Crystallizer 3). **Figure 4.5** also shows that $x_{0,crit}$ increases as L/W increases from 3.00 to 4.25, in the whole range of frequencies, which suggests that increasing L/W reduces the efficiency of vortex propagation and interaction between vortices. A similar conclusion can be drawn from **Figure 4.6** for the velocity ratio. These results follow the work of Gough *et al.*[7] in a conventional tubular-OFC, where the authors reported that x_0 should be increased when L/D increases in order to obtain identical mixing efficiencies in OFCs with different L/D. Similar results were also reported by Ejim *et al.*[5] in tubular-OFCs with SEPC, however, with SPC the results were less regular. With SPC, the effect of L/D on $x_{0,crit}$ depended on α: on the one hand, $x_{0,crit}$ increased as L/D increased at α=0.25, on the other hand $x_{0,crit}$ decreased as L/D increased at α=0.12. Considering that α=0.25 is the closest to α=0.41, the basis of comparison in the present work, the results reported here seem to be aligned with those reported by Ejim *et al.*.

Figure 4.5 also shows that $x_{0,crit}$ increases as α decreases from 0.41 to 0.19 when f<4 Hz, but it decreases when f>4 Hz. Once again, a similar conclusion can be drawn from **Figure 4.6** for the velocity ratio. Let us first consider the first part of this trend. When f<4 Hz, while a lower value of α restrains the propagation of the vortices, which are unable to expand in the entire cross-section of the inter-constrictions cell, a higher value of α allows the expansion of the vortices in the full volume of the inter-constrictions cell and promotes the interaction between vortices. Therefore, when f<4 Hz, $x_{0,crit}$ decreases as α increases. Let us now consider the second part of the trend. As previously mentioned, when f>4 Hz, there is a strong contrast between the mixing intensity in the constriction and the straight section. However, the contrast diminishes as α decreases due to the contraction of the fluid, which increases the velocity in the constriction and, consequently, also in the straight

section, and improves the suspension of solids. Therefore, when f>4 Hz, $x_{0,crit}$ decreases as α decreases. With respect to the work of Ejim *et al.*,[5] in the case of tubular-OFCs with SEPC, the effect of α on $x_{0,crit}$ was quite regular, with $x_{0,crit}$ increasing as α increased; on the other hand, in the case of tubular-OFCs with SPC, the effect of α on $x_{0,crit}$ was less regular, with $x_{0,crit}$ decreasing as α increased at L/D=1.5, and $x_{0,crit}$ increasing as α increased at L/D=3.0. Taking into consideration all these results, it seems that the effects of L/W and α on the suspension of solids depend not only on the combination of frequency and amplitude of oscillation, but also on each other. Therefore, all the interactions between geometric and operating parameters should be considered in order to optimize the geometry of an OFC (planar or not) for a given application.

4.4 Conclusion

This study shows that both operating and geometric parameters have a great influence on the suspension of solids in planar-OFCs. It was found that moderate levels of frequency, around 3 Hz, enable the suspension of solids at lower levels of amplitude. In addition, it was also found that the geometry of the channel, particularly the cell aspect ratio, has a significant impact on the suspension of solids.

In summary, this study shows that the effects of the operating and geometric parameters on the suspension of solids in planar-OFCs follow similar trends to those reported in tubular-OFCs, which suggests that the potential benefits of a planar-OFC, such as allowing the flow of solids in a less constricted path, can be added to the well-known benefits of a tubular-OFC.

Notation

Acronyms	
OFC	Oscillatory flow crystallizer
PVC	Polyvinyl chloride
SEPC	Sharp edge periodic constrictions
SPC	Smooth periodic constrictions
Latin symbols	
C_0	Standard orifice discharge coefficient
D	Tube diameter in the straight section
D_0	Tube diameter in the constriction
d_p	Particle diameter
f	Frequency of oscillation
g	Gravitational acceleration
H	Channel height
l	Total length
L	Distance between constrictions
L_1	Constriction length
L_2	Straight section length
N_c	Number of identical constrictions per unit length
P/V	Power input per unit volume
V	Total volume
V_{cell}	Volume of each inter-constriction cell
v_{osc}	Peak oscillatory axial velocity
v_t	Terminal velocity
W	Channel width in the straight section
W_0	Channel width in the constriction
x_0	Center-to-peak amplitude of oscillation
$x_{0,crit}$	Critical amplitude of oscillation

Greek Letters		Dimensionless Numbers	
ε	Volume fraction of the slurry occupied by the fluid	$\alpha = (D_0/D)^2$	Ratio of the open constriction area for tubular-OFCs
μ	Fluid viscosity	$\alpha = W_0/W$	Ratio of the open constriction area for planar-OFCs
μ_m	Effective slurry viscosity	L/D	Cell aspect ratio for tubular-OFCs
ρ	Fluid density	L/W	Cell aspect ratio for planar-OFCs
ρ_m	Slurry density	v_{osc}/v_t	Velocity ratio
ρ_p	Particle density		
ψ_p	Empirical correction		

References

(1) Nienhaus, B. Mixing in Crystallization Processes. In *Crystallization: Basic Concepts and Industrial Applications*; Beckmann, W., Ed.; Wiley-VCH Verlag GmbH & Co. KGaA: Weinheim, Germany, 2013; pp 247–274.

(2) Mackley, M. R.; Smith, K. B.; Wise, N. P. The Mixing and Separation of Particle Suspensions Using Oscillatory Flow in Baffled Tubes. *Trans. Inst. Chem. Eng.* **1993**, *71* (A), 649–656.

(3) Takriff, M. S.; Ramli, W.; Daud, W.; Fisal, Z.; Alam, Z. Mutiphase Oscillatory Flow in a Baffled Tube. *J. Ind. Technol.* **2000**, *9* (2), 75–84.

(4) Reis, N.; Harvey, A. P.; Mackley, M. R.; Vicente, A. A.; Teixeira, J. A. Fluid Mechanics and Design Aspects of a Novel Oscillatory Flow Screening Mesoreactor. *Chem. Eng. Res. Des.* **2005**, *83* (4), 357–371.

(5) Ejim, L. N.; Yerdelen, S.; McGlone, T.; Onyemelukwe, I.; Johnston, B.; Florence, A. J.; Reis, N. M. A Factorial Approach to Understanding the Effect of Inner Geometry of Baffled Meso-Scale Tubes on Solids Suspension and Axial Dispersion in Continuous, Oscillatory Liquid–Solid Plug Flows. *Chem. Eng. J.* **2017**, *308*, 669–682.

(6) Pereira, F. J. D. Numerical Optimization of an Oscillatory Flow Meso Reactor, Master's Thesis, University of Porto, 2017.

(7) Gough, P.; Ni, X.; Symes, K. C. Experimental Flow Visualisation in a Modified Pulsed Baffled Reactor. *J. Chem. Technol. Biotechnol.* **1997**, *69* (3), 321–328.

(8) Reis, N. Novel Oscillatory Flow Reactors for Biotechnological Applications, PhD Thesis, University of Minho, 2006.

(9) Slavnić, D.; Bugarski, B.; Nikačević, N. Solids Flow Pattern in Continuous Oscillatory Baffled Reactor.

Chem. Eng. Process. - Process Intensif. **2019**, *135*, 108–119.

(10) Geankoplis, C. J. Mechanical-Physical Separation Processes. In *Transport Processes and Unit Operations*; Prentice-Hall International, Inc: New Jersey, 2003; pp 800–849.

(11) Stonestreet, P.; Harvey, A. P. A Mixing-Based Design Methodology for Continuous Oscillatory Flow Reactors. *Chem. Eng. Res. Des.* **2002**, *80* (1), 31–44.

This page was intentionally left in blank

Chapter 5 - Mixing Times in Planar Oscillatory Flow Crystallizers

This chapter is reproduced in part with permission from Cruz, P. C.; Silva, C. R.; Rocha, F. A.; Ferreira, A. M. Mixing Performance of Planar Oscillatory Flow Reactors with Liquid Solutions and Solid Suspensions. Ind. Eng. Chem. Res. 2021, 60 (6), 2663–2676. Copyright 2021 American Chemical Society.

https://pubs.acs.org/doi/full/10.1021/acs.iecr.0c04991

5.1 Introduction

The state of mixing in an oscillatory flow crystallizer (OFC) not only determines the state of suspension, but also the concentration gradients in the liquid and solid phases, which define the distribution of supersaturation inside the crystallizer.

Tracer experiments have been conducted to investigate the impact of operating conditions and geometric parameters on the state of mixing in OFCs. In some works, the state of mixing was quantified in the form of the mixing time, which is the time required to reach a specific degree of concentration uniformity after an injection of a tracer;[5–9] in other works, the state of mixing was quantified in the form of the axial dispersion coefficient, which characterizes the degree of backmixing in the axial direction.[4,6,7,9] Shorter mixing times and larger axial dispersion coefficients are indicative of better mixing efficiencies.

In relation to the effect of the operating conditions, the general conclusion is that increasing the frequency and the amplitude of oscillation increases the axial dispersion and, therefore, decreases the mixing time.[2–9] In relation to the effect of the geometric parameters, the conclusions are more complex. It has been reported that the cell aspect ratio, L/D, controls the shape and length of the vortices: when L/D is too small, there is channeling of the flow through the center of the constriction, which suppresses the generation of vortices; when L/D is too large, the vortices are unable to spread through the full length of the inter-constriction cell and interact with other vortices, which results in the formation of stagnant zones.[2,5] It has also been reported that the ratio of the open constriction area, $\alpha = (D_0/D)^2$, controls the width of the vortices: when α is too small, the vortices are unable to expand in the entire cross-section of the inter-constriction cell, which creates stagnant zones; when α is too large, there is channeling of the flow through the center of the constriction, which suppresses the generation of vortices.[3,5] **Table 5.1** summarizes optimal values/ranges for L/D and α reported in different works.

Table 5.1 – Optimal values/ranges for L/D and α reported in different works.

Reference	Baffle geometry	Oscillating mechanism	Range tested	Optimal value/range	Criteria
Brunold *et al.*[2]	Orifice	Moving fluid	$1<L/D<2$ $\alpha=0.45$	$L/D=1.5$	Effective mixing in the widest range of amplitudes
Gough *et al.*[3]	Orifice	Moving baffles	$0.7<L/D<2$	$L/D=2$	Efficient mixing with the smallest area of the internal surfaces
			$0.26<\alpha<0.47$	$0.32<\alpha<0.40$	Efficient mixing
Ni and Gao[10]	Orifice	Moving fluid	$1<L/D<2$ $\alpha=0.34$	$L/D=1.8$	Highest mass transfer coefficient
Ni *et al.*[5]	Orifice	Moving baffles	$1<L/D<2.5$	$L/D=2$	Lowest mixing time
		Moving fluid	$0.11<\alpha<0.51$	$0.20<\alpha<0.22$	

In this work, the mixing time was determined in three planar oscillatory flow crystallizers (planar-OFCs) with different geometries. The mixing time was determined for a homogeneous system using indigo carmine as a liquid tracer, and also for a heterogeneous system using particles of polyvinyl chloride (PVC) as a solid tracer. The main goal was to investigate the impact of the oscillation conditions and geometric parameters on the mixing time of the liquid and solid phases in planar-OFCs.

5.2 Materials and Methods

5.2.1 Crystallizers

The mixing time was determined in three planar-OFCs with different geometries. The crystallizers were operated horizontally. The dimensions of each planar-OFC including the channel width in the straight section, W, the channel width in the constriction, W_0, the distance between constrictions, L, the constriction length, L_1, the straight section length, L_2, the channel height, H, the volume of each inter-constriction cell, V_{cell}, the cell aspect ratio, L/W, the ratio of the open constriction area, $\alpha = W_0/W$, the total volume, V, and the total length, l, are presented in **Chapter 4**, **Table 4.1**.

5.2.2 Experimental Procedure

The experimental set-up used for the determination of the mixing time is presented in **Figure 5.1**. The mixing time was determined in the first 135 cm section of each crystallizer. This section was chosen to avoid the long experiments required to determine t_m over the total length of more than 3 m of each crystallizer. First, a stream of distilled water was injected into the crystallizer by a peristaltic pump (BT300-2J, Longer Pump) and the

oscillation was activated. The oscillation was provided by a linear motor (H01-23x166/80, LinMot) actuating a piston with a 12.8 mm diameter. Then, 2 mL of tracer was quickly injected at the crystallizer inlet. A 0.4 g L^{-1} aqueous solution of indigo carmine (dye tracer) was used as a liquid tracer and a 40% (w/w) suspension of PVC particles in water was used as a solid tracer. The concentration of tracer was measured in a flow through cell at 135 cm downstream of the crystallizer inlet by a spectrometer (SPEC RES+ UV/VIS-Sarspec). This experimental procedure was repeated in the three planar-OFCs.

The mixing time was determined at different frequencies, f, and amplitudes of oscillation, x_0. The effect of the amplitude was standardized as the ratio between the volume displaced in a complete peak-to-peak oscillation and the volume of each inter-constriction cell, V_d/V_{cell}, to facilitate the comparison between crystallizers. f ranged between 2 and 4 Hz, and V_d/V_{cell} ranged between 1.1 and 1.3. The range of f was chosen around f=3 Hz, which is optimal to suspend solids (**Chapter 4**), and the range of V_d/V_{cell} with V_d/V_{cell}>1 was chosen to ensure the interaction between two consecutive cells (with V_d/V_{cell} <1 the tracer was confined to the initial cells and did not spread through the crystallizer).

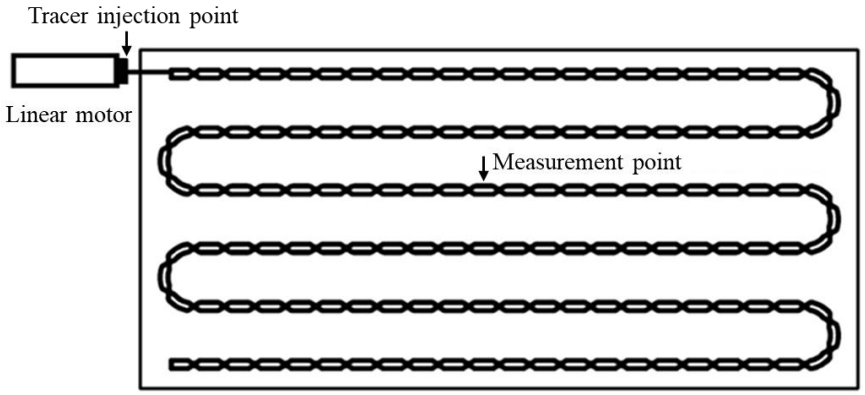


Figure 5.1 – Experimental set-up for the determination of the mixing time.

5.2.3 Calibration Curves

The concentration of tracer was measured at the wavelengths, λ, of 581 nm and 655 nm for the liquid and the solid tracers, respectively. The wavelengths were chosen based on the linearity of the measurements. The coefficient of determination, R^2, was calculated for each wavelength in the range of 162-909 nm – **Figure 5.2 (a)** and **Figure 5.3 (a)** – and the wavelength that gives the best linearity was chosen to perform the experiments.[11] The calibration curves that were used in this work to measure the concentration of liquid and solid tracers are shown in **Figure 5.2 (b)** and **Figure 5.3 (b)**, respectively.

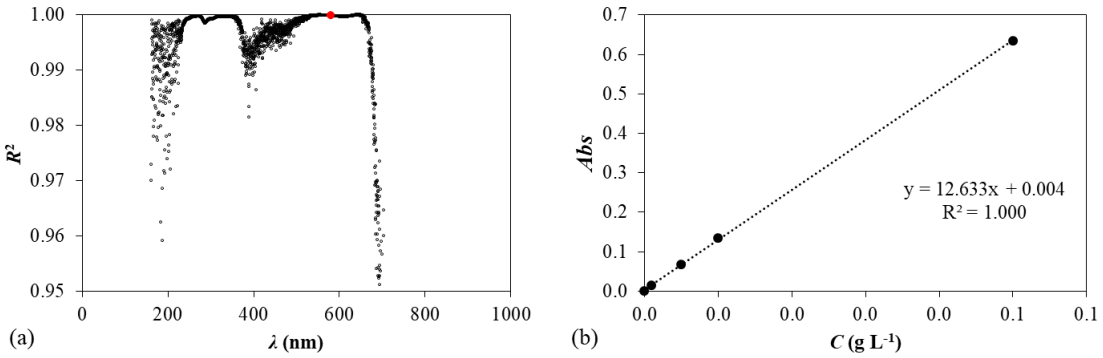


Figure 5.2 – (a) Coefficient of determination as a function of the wavelength for the calibration curve of indigo carmine. (b) Calibration curve for the concentration of indigo carmine at λ=581 nm. *Abs* is the absorbance.

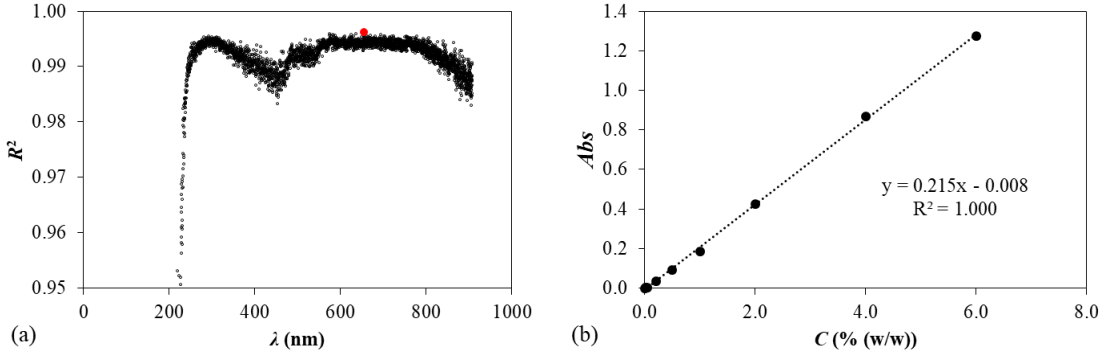


Figure 5.3 – (a) Coefficient of determination as a function of the wavelength for the calibration curve of PVC particles. (b) Calibration curve for the concentration of PVC particles at λ=655 nm. *Abs* is the absorbance.

5.2.4 Design of Experiments

A full factorial experiment was created in Minitab® to study the effects of f and V_d/V_{cell} on the mixing time of the liquid and solid tracers. Each factor was studied at two levels. In coded units, the low level and the high level are defined as −1 and +1, respectively. All the four possible combinations of the two factors were tested in triplicate. This design was augmented with three center points to test for the curvature of the response. The center points are set halfway between the low and high levels of each factor with three replicates to estimate the error. In coded units, the center points are defined as 0. All the four possible combinations of the two factors plus the center point, each with three replicates, resulted in a total of (4+1)×3=15 runs. The factor space of this experimental design is presented in **Figure 5.4**.

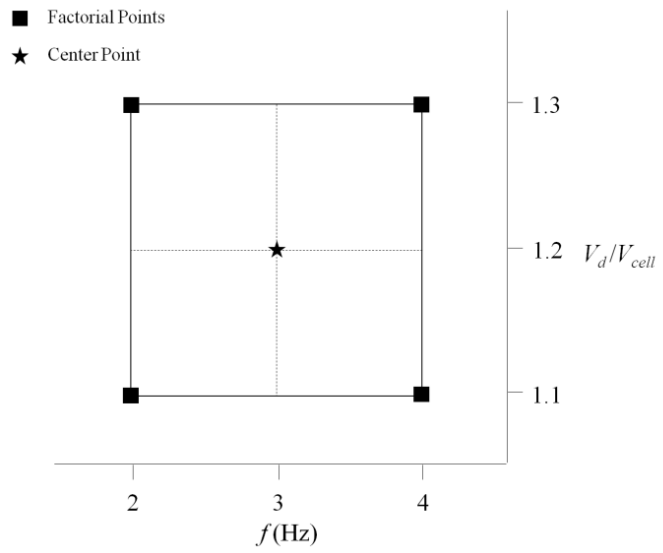


Figure 5.4 – Factor space for the determination of the mixing time.

The experimental conditions of each run are presented in **Table 5.2**. The oscillatory Reynolds number, Re_o, and the Strouhal number, St, that characterize each experimental condition are also presented in **Table 5.2**. Re_o and St were calculated based on the hydraulic diameter, D_h, defined as:

$$D_h = 4\frac{A_{cs}}{P_{cs}} \tag{5.1}$$

where A_{cs} is the cross-sectional area of the channel and P_{cs} is the wetted perimeter of the cross-section.

Table 5.2 – Experimental conditions and respective dimensionless numbers in each run.

			Crystallizer 1			Crystallizer 2			Crystallizer 3		
Run	f **(Hz)**	V_d/V_{cell}	x_0 **(mm)**	Re_o	St	x_0 **(mm)**	Re_o	St	x_0 **(mm)**	Re_o	St
1	2	1.1	11.4	883	0.043	16.9	1308	0.029	17.4	1346	0.028
2	4	1.1	11.4	1767	0.043	16.9	2616	0.029	17.4	2692	0.028
3	2	1.3	13.5	1044	0.036	20.0	1546	0.025	20.6	1591	0.024
4	4	1.3	13.5	2088	0.036	20.0	3091	0.025	20.6	3182	0.024
5	3	1.2	12.5	1445	0.039	18.5	2140	0.027	19.0	2203	0.026

5.3 Results and Discussion

5.3.1 Determination of the Mixing Time

The mixing time was obtained from the concentration curve for each experimental condition under study. The concentration curve that was obtained with the liquid tracer at f=3 Hz and V_d/V_{cell}=1.1 in Crystallizer 3 is presented in **Figure 5.5** (a). This example will be used to illustrate how t_m was determined for each experimental condition. Three zones can be distinguished in **Figure 5.5** (a): Zone I, at the beginning, where the concentration is practically constant, followed by Zone II, where the concentration increases rapidly, and Zone III, where the concentration stabilizes and the mass transfer rate decreases.

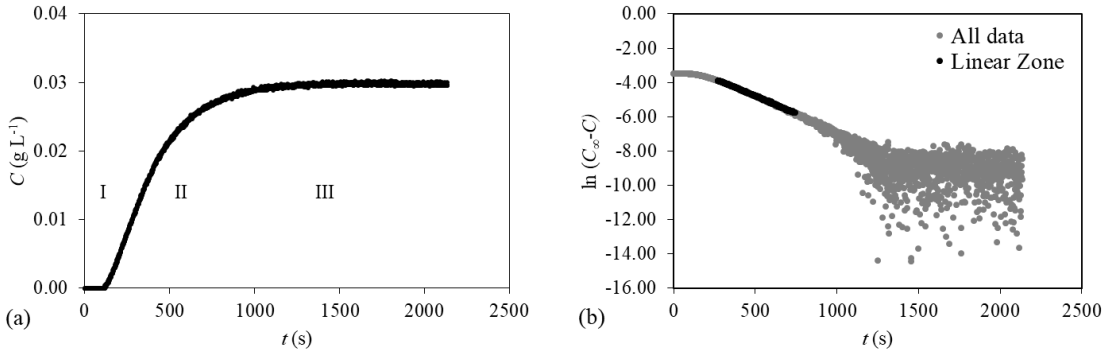


Figure 5.5 – (a) Concentration curve of indigo carmine. (b) Application of *F* test. (f=3 Hz and V_d/V_{cell}=1.1 in Crystallizer 3).

When the concentration curve is represented as a semi logarithmic plot of $\ln(C_\infty - C)$ versus t, where C_∞ is the concentration of tracer at infinite time, C is the concentration of tracer at the measurement point, and t is time, a linear zone, corrresponding to Zone II of the concentration curve, is found – **Figure 5.5 (b)**. Therefore, the stabilization zone, corresponding to Zone III of the concentration curve, starts at the end of the linear zone of $\ln(C_\infty - C)$ versus t. This criterion was used to measure the time needed to achieve a specific degree of concentration homogeneity after the injection of tracer, t_m.

The linear zone was delimited using the statistical method *F* test.[12] This method computes the optimum number of points, n_p, for a linear regression of experimental data. First, the two linear regression parameters, the slope, b, and the intersection, c, together with parameter F^* are calculated for a short data interval. Parameter F^* is defined as:

$$F^* = \frac{1}{n_p - 1}\sqrt{\frac{\sum(y_{est} - y)^2}{\sum y^2}} \qquad \textbf{(5.2)}$$

where y and y_{est} are the experimental and the estimated value, respectively. y_{est} is calculated as $y_{est} = bx + c$. Then, an increment in n_p is added to the data interval at each iteration and the two linear regression parameters, b and c, are recalculated to minimize parameter F^*.

Initially, a fixed initial point is defined at the middle of Zone II, where de linear zone is located. Then, *F* test is executed to the left and the right hand sides of the initial point. Finally, t_m is calculated as the time interval between the beginning of the experiment and the last point of the linear zone, taken from the optimum number of points for the right hand side. In **Figure 5.5 (b)**, the linear zone that was used to determine t_m is identified. This procedure was employed to determine t_m for the liquid tracer, t_m^L, and for the solid tracer, t_m^S, for Runs 1-5. The results are presented in **Table 5.3, Table 5.4**, and **Table 5.5** for Crystallizers 1, 2 and 3, respectively.

Table 5.3 – $t_m{}^L$ and $t_m{}^S$ obtained in Crystallizer 1 in each run.

			t_m^L(s)			t_m^S(s)		
Run	f **(Hz)**	V_d/V_{cell}	**1**	**2**	**3**	**1**	**2**	**3**
1	2	1.1	2670	2287	2897	4763	4286	4074
2	4	1.1	1086	1033	1192	1541	1610	1679
3	2	1.3	1725	2280	2061	2583	2900	3025
4	4	1.3	941	1019	770	981	1286	1197
5	3	1.2	1424	1773	1660	2205	1923	1930

Table 5.4 – $t_m{}^L$ and $t_m{}^S$ obtained in Crystallizer 2 in each run.

			t_m^L(s)			t_m^S(s)		
Run	f **(Hz)**	V_d/V_{cell}	**1**	**2**	**3**	**1**	**2**	**3**
1	2	1.1	731	671	648	953	924	901
2	4	1.1	427	418	513	431	510	442
3	2	1.3	527	595	458	704	726	716
4	4	1.3	356	311	389	429	441	457
5	3	1.2	430	494	421	534	527	622

Table 5.5 – $t_m{}^L$ and $t_m{}^S$ obtained in Crystallizer 3 in each run.

			t_m^L(s)			t_m^S(s)		
Run	f **(Hz)**	V_d/V_{cell}	**1**	**2**	**3**	**1**	**2**	**3**
1	2	1.1	1742	2060	1926	2165	2600	2733
2	4	1.1	762	637	814	1696	1837	1352
3	2	1.3	1372	1390	2176	2311	2269	1843
4	4	1.3	554	603	545	779	1254	1204
5	3	1.2	946	952	1008	1805	1577	1227

Figure 5.6 displays t_m^L and **Figure 5.7** displays t_m^S as a function of f and V_d/V_{cell} in each crystallizer, respectively. **Figure 5.8** displays t_m as a function of $\mathrm{Re_o}$ for both the liquid and solid tracers and **Figure 5.9** displays of t_m as a function of $1/\mathrm{St}$ for both the liquid and solid tracers. In these figures, the error bars represent the interval between the minimum and maximum values of the three replicates.

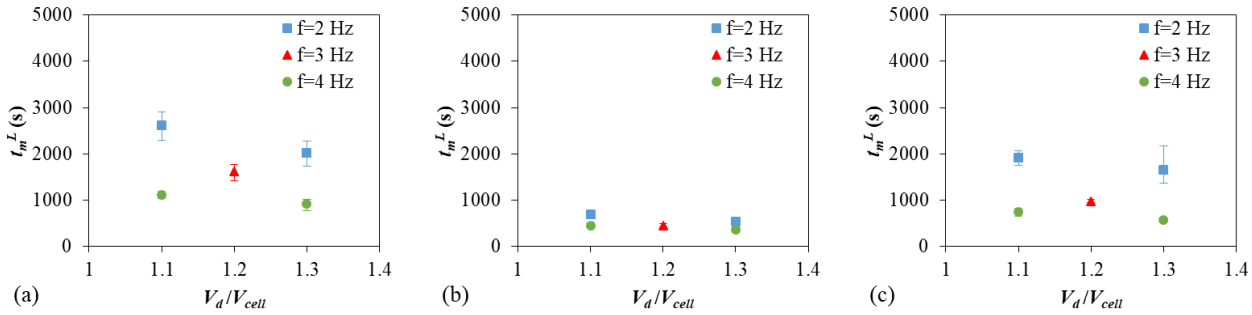


Figure 5.6 – t_m^L as a function of the oscillation conditions in (a) Crystallizer 1, (b) Crystallizer 2, and (c) Crystallizer 3.

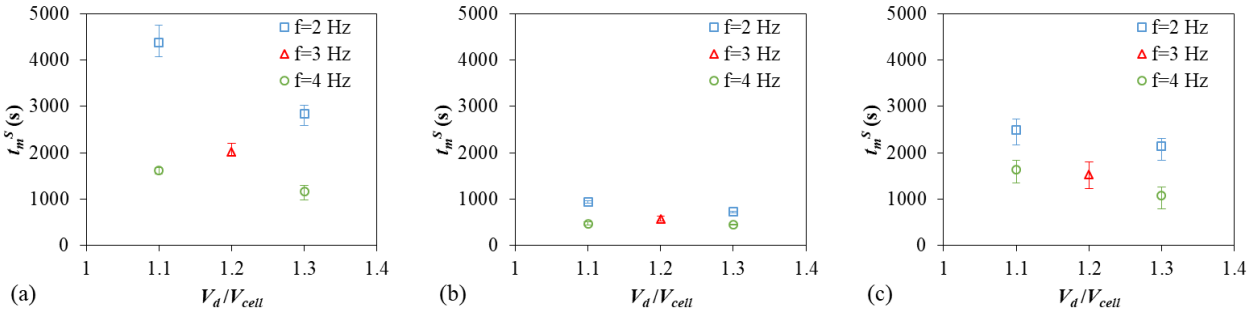


Figure 5.7 – t_m^S as a function of the oscillation conditions in (a) Crystallizer 1, (b) Crystallizer 2, and (c) Crystallizer 3.

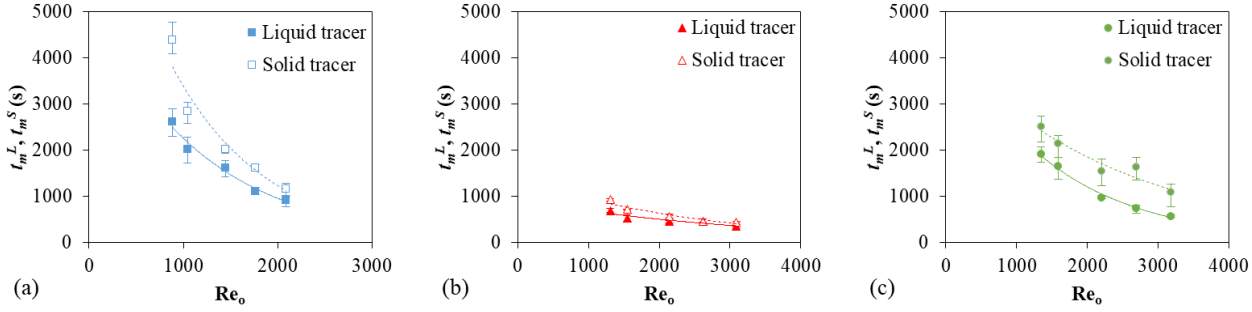


Figure 5.8 – t_m^L and t_m^S as a function of $\mathrm{Re_o}$ in (a) Crystallizer 1, (b) Crystallizer 2, and (c) Crystallizer 3.

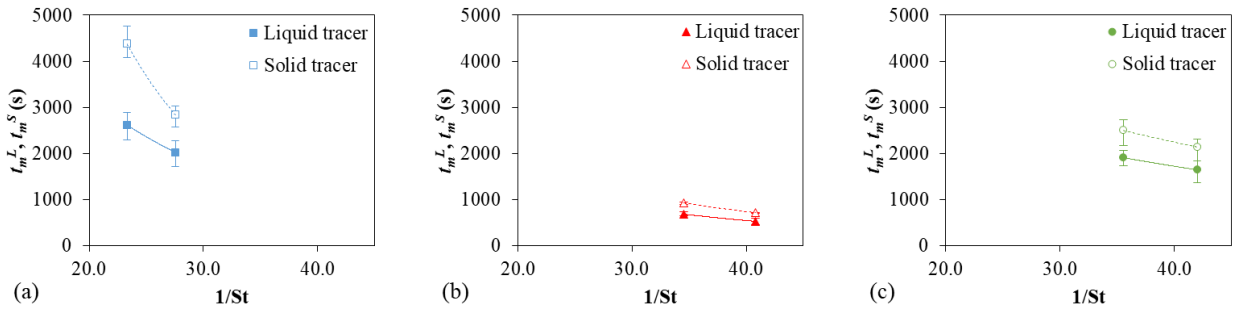


Figure 5.9 – t_m^L and t_m^S as a function of St (f=2 Hz) in (a) Crystallizer 1, (b) Crystallizer 2, and (c) Crystallizer 3.

5.3.2 Comparison of Mixing Times for the Liquid and Solid Tracers

t_m^L varied between 311 and 2897 s, and t_m^S varied between 429 and 4763 s. To the best of our knowledge, this is the first time that values of t_m are reported for a solid tracer, however, several other studies have reported values of t_m for liquid tracers in tubular-OFCs. For example, Ni *et al.*[5] reported values of t_m between 100 and 1500 s in a tubular-OFC with 50 mm of diameter and 865 mm of operational height, Ni and Stevenson[6] reported values of t_m between 100 and 2000 s in a tubular-OFC with 50 mm of diameter and 730 mm of operational height and Ni *et al.*[7] reported values of t_m between 84 and 919 s in a tubular-OFC with 50 mm of diameter and 865 mm of operational height. So, the results obtained in this work, although in the same order of magnitude, are still higher than those previously reported in tubular-OFCs. Nevertheless, such difference is probably due to the baffle geometry and the much smaller cross-sectional areas of the crystallizers of this work (40 mm^2 in the straight section) in comparison with other works (1963 mm^2 in the straight section).

It was found that, under identical conditions, t_m^S is considerably higher than t_m^L. This was rather expected because, while the liquid tracer seems to behave as a microfluid, completely mixed into the fluid at a molecular level, the solid tracer seems to behave as a macrofluid. This is because the molecules of the liquid tracer lose their identity into the fluid, whereas the particles of the solid tracer retain their identity as distinct aggregates of molecules.[13] What is more, the solid tracer seems to offer a greater resistance to flow than the liquid tracer due to the difference of densities between the solid (~1.4 g cm^{-3}) and the liquid phases (~1.0 g cm^{-3}).

5.3.3 Effect of the Oscillation Conditions on the Mixing Time

It was found that t_m decreases as both f and V_d/V_{cell} increase. This agrees with previous works in tubular-OFCs, which have linked the increase of f and x_0 to the increase of radial and axial mixing, respectively, with both phenomena contributing to decrease t_m.[5,8,9,14] It was also found that, in the range of operating conditions

under study in this work, t_m is more sensitive to f than to V_d/V_{cell}. This finding could be thought to be opposite to that reported by Reis *et al.*[8] in a tubular-OFC, because, in their work, the mixing time was found more sensitive to x_0 than to f. However, the experimental results of these two studies are actually in good agreement. In their work, Reis *et al.* covered a range of frequencies between 3 and 20 Hz, and a range of amplitudes between 0.5 and 3 mm, and found that x_0 and f affect the mixing time in a non-linear way: initially, there is a strong decrease in the mixing time as both f and x_0 increase, but then, as f and x_0 are further increased, the decrease in the mixing time becomes rather weak. Therefore, while the range of frequencies under study in the present work (2-4 Hz) represents the first part of that trend, when the frequency is expected to have a strong impact on the mixing time, the range of amplitudes (11.4-13.5 mm in Crystallizer 1, 16.9-20.0 mm in Crystallizer 2, and 17.4-20.6 mm in Crystallizer 3) represents the last part of that trend, when the amplitude is expected to have a rather weak impact on the mixing time.

It was also found that t_m decreases as $\mathrm{Re_o}$ increases, with a greater degree of decrease at lower values of $\mathrm{Re_o}$ and a lesser degree of decrease at higher values of $\mathrm{Re_o}$. Similar results were previously reported by Ni *et al.*[5] and Fitch and Ni[9] in conventional tubular-OFCs. This result suggests the existence of a threshold in the uniformity of mixing, so that, once the OFC reaches such a level of uniformity, a further increase of $\mathrm{Re_o}$, in the form of either the frequency or amplitude of oscillation, would lead to a much smaller decrease of t_m. Finally, it was also found that t_m decreases as $1/\mathrm{St}$ increases. $1/\mathrm{St}$ represents the effect of x_0 weighted by the hydraulic diameter of the channel, which is comparable with V_d/V_{cell}. Therefore, the effect of $1/\mathrm{St}$ is identical to the effect of V_d/V_{cell}.

5.3.4 Effect of the Geometric Parameters on the Mixing Time

The lowest values of t_m were achieved in Crystallizer 2, followed by Crystallizer 3, and finally by Crystallizer 1. In addition, the smallest difference between t_m^S and t_m^L was achieved in Crystallizer 2, followed by Crystallizer 3, and finally by Crystallizer 1. This means that the difference between t_m^S and t_m^L increases as t_m increases, which suggests that the loss of mixing efficiency for liquids translates into an even greater loss of mixing efficiency for solids, which might be critical for applications that involve the direct contact between a liquid and a solid phase, such as crystallization.

The effect of L/W on t_m can be assessed by comparison of Crystallizers 1 and 3, which have the same α and different L/W, and the effect of α on t_m can be assessed by comparison of Crystallizers 2 and 3, which have the same L/W and different α. It was found that lower values of t_m are achieved with smaller values of α and larger values of L/W, with the first parameter showing a more significant effect. It was also found that the degree of decrease in t_m as a function of $\mathrm{Re_o}$ was considerably smaller for Crystallizer 2, with a lower value of α, than for Crystallizer 1 and 3, with a larger value of α. This shows, once again, that α has a much stronger

impact on t_m than L/W. These results are completely aligned with the simulation results of Pereira[15], who predicted that the dimensions of Crystallizer 2 should provide the shortest mixing times.

In a tubular-OFC, the cell aspect ratio is defined as L/D, where L is the distance between constrictions, and D is the tube diameter in the straight section; and the ratio of the open constriction area is defined as $\alpha = (D_0/D)^2$, where D_0 the tube diameter in the constriction. Ni *et al.*[5] determined t_m in a conventional tubular-OFC and found that t_m generally increases as α increases from 0.11 to 0.51, with an optimal range between 0.20 and 0.22 for the shortest mixing times, which is fairly close to 0.19, the value of α in Crystallizer 2, where the shortest mixing times were produced in the present work. On the other hand, the authors also found that increasing L/D from 1 to 2.5 produced a less well-defined effect on t_m, but L/D=2 generally produced the shortest mixing times. Unfortunately, comparisons between that work and the present work are somewhat limited, considering that significantly higher values of L/W (3.00-4.25) were used in the present work.

5.3.5 Model Development

The experiments were performed according to a DoE approach. First, a full factorial design was used to predict the effects of f and V_d/V_{cell} on t_m^L and t_m^S. Each combination of factors was tested in triplicate. A first order model was formulated to describe the relationship between the response, t_m^L or t_m^S, and the two factors, f and V_d/V_{cell}, in each crystallizer as follows:

$$t_m^L \text{ (or } t_m^S) = \beta_0 + \beta_1 f + \beta_2 V_d/V_{cell} + \beta_{12} f V_d/V_{cell} \quad \textbf{(5.3)}$$

where β_0 is a constant, β_1 and β_2 are linear coefficients, and β_{12} is an interaction coefficient.

In order to stabilize the variance of the response, a Box-Cox transformation with λ=0 was used. When λ=0, the transformed response is $t_m^{'} = \ln(t_m)$. Therefore **Equation (5.3)** becomes:

$$t_m^{L\prime}(\text{or } t_m^{S\prime}) = \beta_0' + \beta_1' f + \beta_2' V_d/V_{cell} + \beta_{12}' f V_d/V_{cell} \quad \textbf{(5.4)}$$

The p-value of each term of the model was compared with the significance level of 5% in order to assess its significance. The p-value measures the evidence against the null hypothesis, which states that the coefficient associated to the term is equal to zero, or in other words, that the term has no significant effect.[16] Then, the significant terms were selected and the insignificant terms were eliminated from the model by a backward stepwise technique. **Table 5.6** presents the coded coefficients for the transformed response of each model and the respective coefficient of determination and **Figure 5.10** shows the quality of the fit of each model to the experimental data. In most cases, the interaction coefficient $\beta_{12}^{'}$ is not listed in **Table 5.6** because it was found not significant.

The center points were used to test for curvature. This test compares the mean response at the center points to the expected response considering a linear relationship between the factors and the response. The curvature is considered significant when the p-value for curvature is less than or equal to a suitable significance level. The p-value for curvature measures the evidence against the null hypothesis, which assumes that all the relationships between the factors and the response are linear.[16] In this study, the curvature of t_m was found not significant with a significance level of 5% in all cases. These models may now be used to predict t_m^L and t_m^S as a function of the oscillation conditions in each crystallizer.

Table 5.6 – Coded coefficients for the transformed response and coefficient of determination of each model.

	Crystallizer 1		Crystallizer 2		Crystallizer 3	
Coefficient	$t_m^{L\prime}$	$t_m^{S\prime}$	$t_m^{L\prime}$	$t_m^{S\prime}$	$t_m^{L\prime}$	$t_m^{S\prime}$
β_0'	7.3335	7.6732	6.1720	6.3906	6.9495	7.4312
β_1' (s)	-0.4149	-0.4752	-0.2041	-0.2952	-0.4991	-0.2834
β_2'	-0.1145	-0.1929	-0.1289	-0.0744	-0.1070	-0.1451
β_{12}' (s)	-	-	-	0.0547	-	-
R^2 (%)	93.31	96.81	84.85	95.59	93.45	74.08

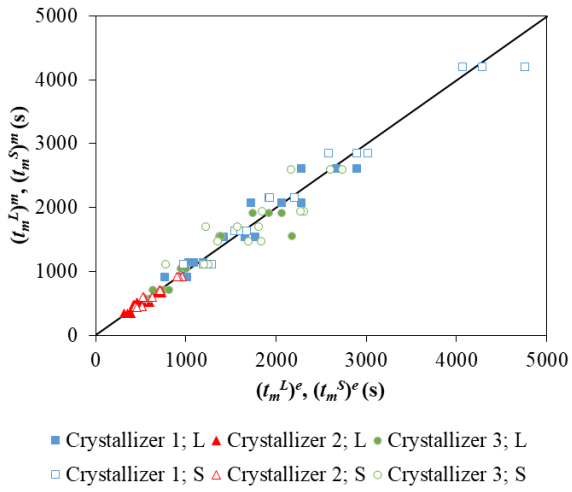


Figure 5.10 – Comparison of $t_m{}^L$ and $t_m{}^S$ obtained from the model, $(t_m{}^L)^m$ and $(t_m{}^S)^m$, and obtained experimentally, $(t_m{}^L)^e$ and $(t_m{}^S)^e$ in each crystallizer. L stands for liquid tracer and S stands for solid tracer.

The main effects plot is presented in **Figure 5.11**. The main effects plot displays the average response, $\overline{t_m^L}$ and $\overline{t_m^S}$, for each level of f and V_d/V_{cell}. **Figure 5.11** shows that f, and V_d/V_{cell} have similar negative effects on t_m^L and t_m^S in the three crystallizers. It also shows that, in the range of operating conditions under study, t_m^L and t_m^S are more sensitive to f than to V_d/V_{cell}, because the linear coefficient associated with of f (β_1') is

significantly larger than the linear coefficient associated with V_d/V_{cell} (β_2'). This is coherent with the previous findings.

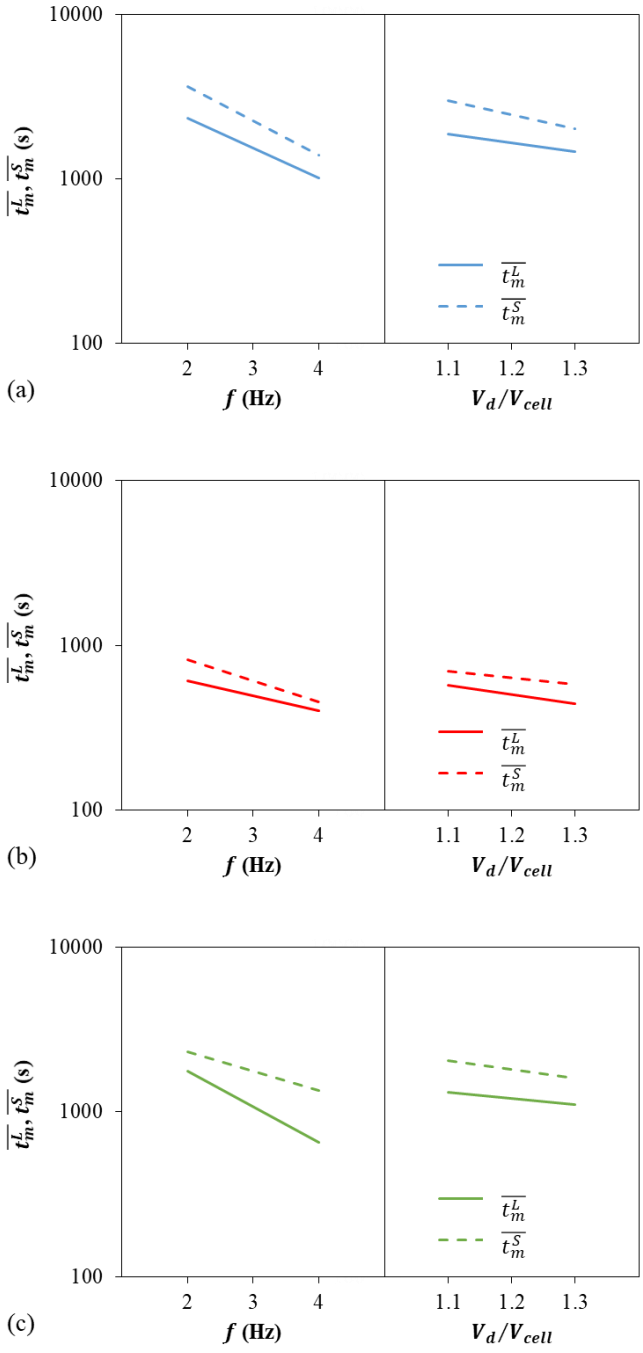


Figure 5.11 – Main effects plot for $t_m{}^L$ and $t_m{}^S$ in (a) Crystallizer 1, (b) Crystallizer 2, and (c) Crystallizer 3.

5.4 Conclusion

This study shows that both operating and geometric parameters have a great influence on the mixing time in planar-OFCs. It was found that the combination of high levels of frequency and amplitude reduces the mixing time of both liquids and solids, but, under the same operating conditions, the mixing time is considerably higher for solids than for liquids and the difference between the two phases is affected by the geometry of the channel, particularly the ratio of the open constriction area. Therefore, the geometry of the channel should be carefully chosen to ensure the mixing similarity between the liquid and solid phases, which might be particularly critical for applications that involve the direct contact between the two phases, such as crystallization.

Notation

Acronyms	
OFC	Oscillatory flow crystallizer
PVC	Polyvinyl chloride
Latin symbols	
Abs	Absorbance
A_{cs}	Channel cross-sectional area
b	Slope
c	Intersection
C	Concentration of tracer
C_∞	Concentration of tracer at infinite time
D	Tube diameter in the straight section
D_0	Tube diameter in the constriction
D_h	Hydraulic diameter
f	Frequency of oscillation
F^*	F test parameter
H	Channel height
l	Total length
L	Distance between constrictions
L_1	Constriction length
L_2	Straight section length
n_p	Optimal number of points for a linear regression
P_{cs}	Channel cross-sectional wetted perimeter
R^2	Coefficient of determination
t	Time
t_m	Mixing time
t_m^L	Mixing time for the liquid tracer
$\overline{t_m^L}$	Average mixing time for the liquid tracer
$(t_m^L)^e$	Mixing time for the liquid tracer obtained Experimentally
$(t_m^L)^m$	Mixing time for the liquid tracer obtained from the model
t_m^S	Mixing time for the solid tracer
$\overline{t_m^S}$	Average mixing time for the solid tracer
$(t_m^S)^e$	Mixing time for the solid tracer obtained experimentally
$(t_m^S)^m$	Mixing time for the solid tracer obtained from the model
V	Total volume
V_{cell}	Volume of each inter-constriction cell
V_d/V_{cell}	Ratio of the volume displaced peak-to-peak in a complete oscillation to the volume of each inter-constriction cell
W	Channel width in the straight section
W_0	Channel width in the constriction
x_0	Center-to-peak amplitude of oscillation
y	Experimental value
y_{est}	Estimated value
Greek Letters	
β_0	Average response for all observations
β_0'	Average transformed response for all observations
β_1 and β_2	Linear coefficients
β_1' and β_2'	Linear coefficients for the transformed response
β_{12}	Two-way interaction coefficient
β_{12}'	Two-way interaction coefficient for the transformed response
λ	Wavelength

Dimensionless Numbers

$\alpha = (D_0/D)^2$	Ratio of the open constriction area for tubular-OFCs
$\alpha = W_0/W$	Ratio of the open constriction area for planar-OFCs
L/D	Cell aspect ratio for tubular-OFCs
L/W	Cell aspect ratio for planar-OFCs
$\mathrm{Re_o}$	Oscillatory Reynolds number
St	Strouhal number

References

(1) Nienhaus, B. Mixing in Crystallization Processes. In *Crystallization: Basic Concepts and Industrial Applications*; Beckmann, W., Ed.; Wiley-VCH Verlag GmbH & Co. KGaA: Weinheim, Germany, 2013; pp 247–274.

(2) Brunold, C. R.; Hunns, J. C. B.; Mackley, M. R.; Thompson, J. W. Experimental Observations on Flow Patterns and Energy Losses for Oscillatory Flow in Ducts Containing Sharp Edges. *Chem. Eng. Sci.* **1989**, *44* (5), 1227–1244.

(3) Gough, P.; Ni, X.; Symes, K. C. Experimental Flow Visualisation in a Modified Pulsed Baffled Reactor. *J. Chem. Technol. Biotechnol.* **1997**, *69* (3), 321–328.

(4) Smith, K. B. The Scale-Up of Oscillatory Flow Mixing, PhD Thesis, University of Cambridge, 1999.

(5) Ni, X.; Brogan, G.; Struthers, A.; Bennett, D. C.; Wilson, S. F. A Systematic Study of the Effect of Geometrical Parameters on Mixing Time in Oscillatory Baffled Columns. *Chem. Eng. Res. Des.* **1998**, *76* (5), 635–642.

(6) Ni, X.; Stevenson, C. C. On the Effect of Gap Size between Baffle Outer Diameter and Tube Inner Diameter on the Mixing Characteristics in an Oscillatory-Baffled Column. *J. Chem. Technol. Biotechnol.* **1999**, *74* (6), 587–593.

(7) Ni, X.; De Gélicourt, Y. S.; Neil, J.; Howes, T. On the Effect of Tracer Density on Axial Dispersion in a Batch Oscillatory Baffled Column. *Chem. Eng. J.* **2002**, *85* (1), 17–25.

(8) Reis, N.; Vicente, A. A.; Teixeira, J. A.; Mackley, M. R. Residence Times and Mixing of a Novel Continuous Oscillatory Flow Screening Reactor. *Chem. Eng. Sci.* **2004**, *59* (22–23), 4967–4974.

(9) Fitch, A. On the Determination of Axial Dispersion Coefficient in a Batch Oscillatory Baffled Column Using Laser Induced Fluorescence. *Chem. Eng. J.* **2003**, *92* (1–3), 243–253.

(10) Ni, X.; Gao, S. Mass Transfer Characteristics of a Pilot Pulsed Baffled Reactor. *J. Chem. Technol.*

Biotechnol. **1996**, *65* (1), 65–71.

(11) Owen, T. *Fundamentals of UV-Visible Spectroscopy: A Primer*; Hewlett-Packard: Germany, 1996.

(12) Mena, P.; Ferreira, A.; Teixeira, J. A.; Rocha, F. Effect of Some Solid Properties on Gas–Liquid Mass Transfer in a Bubble Column. *Chem. Eng. Process. Process Intensif.* **2011**, *50* (2), 181–188.

(13) Levenspiel, O. Basics of Non-Ideal Flow. In *Chemical Reaction Engineering*; John Wiley & Sons, Inc.: New York, 1999; pp 257–282.

(14) Zheng, M.; Mackley, M. The Axial Dispersion Performance of an Oscillatory Flow Meso-Reactor with Relevance to Continuous Flow Operation. *Chem. Eng. Sci.* **2008**, *63* (7), 1788–1799.

(15) Pereira, F. J. D. Numerical Optimization of an Oscillatory Flow Meso Reactor, Master's Thesis, University of Porto, 2017.

(16) Montgomery, D. C. *Design and Analysis of Experiments*, 5th ed.; John Wiley & Sons, Inc.: New York, 2007.

Chapter 6 - Axial Dispersion in Planar Oscillatory Flow Crystallizers

This chapter is reproduced in part with permission from Cruz, P. C.; Silva, C. R.; Rocha, F. A.; Ferreira, A. M. The Axial Dispersion of Liquid Solutions and Solid Suspensions in Planar Oscillatory Flow Crystallizers. AIChE J. 2019, 65 (9), e16683. Copyright 2019 American Institute of Chemical Engineers.

https://aiche.onlinelibrary.wiley.com/doi/full/10.1002/aic.16683

6.1 Introduction

One of the major benefits of an oscillatory flow crystallizer (OFC) in comparison with other crystallizers is its ability to operate with reduced axial dispersion and, consequently, narrow residence time distribution (RTDs), which allows to produce crystals with narrow crystal size distributions (CSDs).[1]

Tracer experiments have been conducted to investigate the impact of operating conditions and geometric parameters on the axial dispersion in OFCs. Two different methods have been employed: the perfect and the imperfect pulse methods. The perfect pulse method consists in injecting a tracer into the crystallizer and then measuring its concentration profile at one point downstream from the injection point; whereas the imperfect pulse method consists in injecting a tracer into the crystallizer and then measuring its concentration profile at two points downstream from the injection point.[2] The parameters that characterize the axial dispersion are obtained by fitting a suitable axial dispersion model to the experimental data. Several different models have been used. Most works have used the plug flow with axial dispersion model, which describes the system as a continuous path where a diffusion-like process is superimposed to the main flow.[3–16] The axial mixing is characterized by the axial dispersion coefficient, D_c, and the spread in the whole system is characterized by the vessel dispersion number, $D_c/(ul)$, where u is the average superficial flow velocity and l is the length of the tube. When $D_c/(ul) \to 0$ the dispersion is negligible, hence plug flow. When $D_c/(ul) \to \infty$ there is large dispersion, hence mixed flow. Other works have used a compartment type model, which describes the system as a stage-wise process. An example is the stage-wise backmixing model which divides the system into a fixed number of ideal stages and quantifies the deviation from perfect plug flow with an inter-stage backmixing parameter, g.[5,12,17–19] Another example is the tanks-in-series model which describes the system as a variable number of ideal stirred tanks in series, N.[5,20–25]

The effects of the oscillatory and net flow components on the axial dispersion have been investigated in a wide variety of OFCs with different diameters, lengths, baffle types and geometries. The general conclusion is that although the individual effects of the oscillatory and net flow components are reasonably similar across different OFCs, the optimal operating conditions, which maximize the radial mixing and minimize the axial dispersion, can be significantly different in different OFCs.

In this work, the axial dispersion was determined in three planar-OFCs with different geometries. The main goal was to investigate the impact of the operating conditions and geometric parameters on the axial dispersion of the liquid and solid phases in planar-OFCs. The axial dispersion was determined for a homogeneous system using indigo carmine as a liquid tracer, and also for a heterogeneous system using particles of polyvinyl chloride (PVC) as a solid tracer. In addition, the seeded continuous cooling crystallization of paracetamol from aqueous solutions was used as a model system to assess the impact of the axial dispersion on the final crystal size distribution (CSD).

6.2 Materials and Methods

6.2.1 Crystallizers

The axial dispersion was determined in three planar-OFCs with different geometries. The crystallizers were operated horizontally. The dimensions of each planar-OFC including the channel width in the straight section, W, the channel width in the constriction, W_0, the distance between constrictions, L, the constriction length, L_1, the straight section length, L_2, the channel height, H, the volume of each inter-constriction cell, V_{cell}, the cell aspect ratio, L/W, the ratio of the open constriction area, $\alpha = W_0/W$, the total volume, V, and the total length, l, are presented in **Chapter 4**, **Table 4.1**.

6.2.2 Experimental Procedure

A stream of distilled water was continuously injected into the crystallizer by a peristaltic pump (BT300-2J, Longer Pump) and the oscillation was activated. The oscillation was provided by a linear motor (H01-23x166/80, LinMot) actuating a piston with a 12.8 mm diameter. At time zero, a pulse tracer of 2 mL was quickly injected at 30 cm downstream of the inlet in Crystallizer 1, and at 24.5 cm downstream of the inlet in Crystallizers 2 and 3. A 0.4 g L^{-1} aqueous solution of indigo carmine was used as liquid tracer, and a 40% (w/w) suspension of PVC particles with a mean diameter of 160 μm was used as solid tracer, in separate experiments. The concentration of tracer was measured in a flow through cell in the crystallizer outlet, at 3.11 m from the injection point, by a spectrometer (SPEC RES+ UV/VIS-Sarspec). The calibration curves for the liquid and

solid tracers are presented in **Chapter 5**, **Section 5.2.3**. This experimental procedure was repeated in the three planar-OFCs. The experimental set-up is presented in **Figure 6.1**.

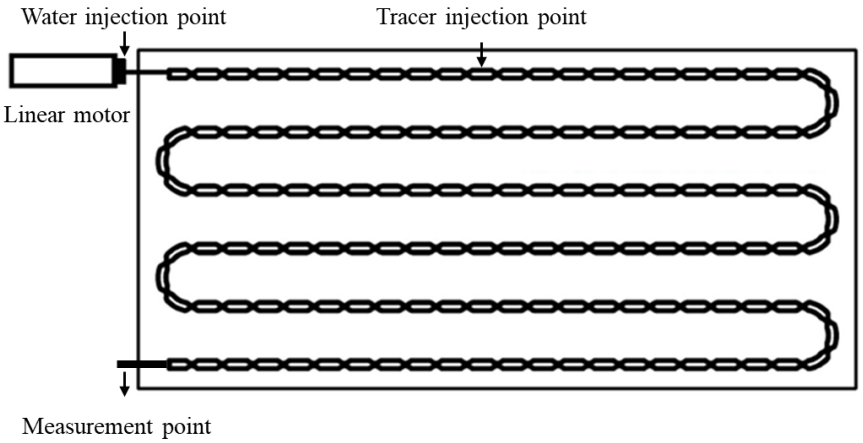


Figure 6.1 – Experimental set-up for the determination of the axial dispersion.

The axial dispersion was characterized at different flow rates, Q, frequencies of oscillation, f, and amplitudes of oscillation, x_0. The effect of x_0 was standardized as the ratio of the volume displaced in a complete peak-to-peak oscillation to the volume of each inter-constriction cell, V_d/V_{cell}, to facilitate the comparison between crystallizers. Each factor was studied at two levels: 16 and 109 mL min^{-1} for Q, 3 and 6 Hz for f, and 0.6 and 1 for V_d/V_{cell}. The range of operating conditions was chosen to guarantee the full suspension of the solids (**Chapter 4**).

6.2.3 Design of Experiments

A full factorial experiment was designed in Minitab® to assess the effects of Q, f, and V_d/V_{cell} on the axial dispersion of the liquid and solid tracers. Each factor was studied at two levels. In coded units, the low level is defined as –1 and the high level is defined as +1. Each combination of factors was tested in triplicate. This design was augmented with five center points to test for the curvature of the response. The center points are set halfway between the low and high levels of each factor with five replicates to estimate the error. When the curvature was found not significant, a first order model was built for each response variable. When the curvature was found significant, the design was augmented with axial points and turned into a face-centered composite design, and a second order model was built for each response variable. The axial points are at the center of each face of the factorial space. The factor space of this experimental design is presented in **Figure 6.2**.

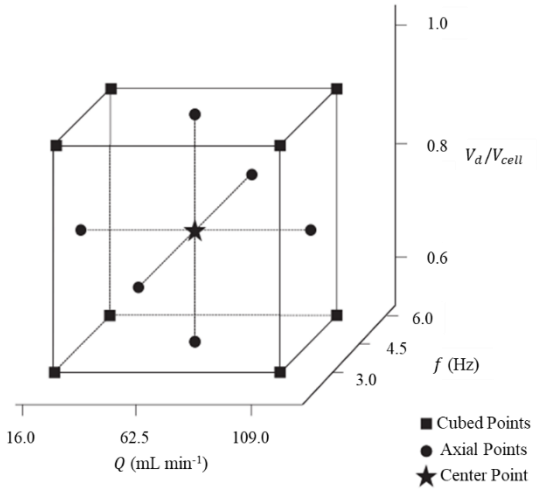


Figure 6.2 – Factor space for the determination of the axial dispersion.

The experimental conditions of each run are presented in **Table 6.1**. The net flow Reynolds number, Re, the oscillatory Reynolds number, Re_o, and the Strouhal number, St, that characterize each experimental condition are also presented in **Table 6.1**. Re, Re_o and St were calculated based on the hydraulic diameter, D_h, defined as:

$$D_h = 4\frac{A_{cs}}{P_{cs}} \tag{6.1}$$

where A_{cs} is the cross-sectional area of the channel and P_{cs} is the wetted perimeter of the cross-section.

Table 6.1 – Experimental conditions and respective dimensionless numbers in each run.

					Crystallizer 1			Crystallizer 2			Crystallizer 3		
Run	**Q (mL min^{-1})**	**Re**	**f (Hz)**	**V_d/V_{cell}**	**x_0 (mm)**	**Re_o**	**St**	**x_0 (mm)**	**Re_o**	**St**	**x_0 (mm)**	**Re_o**	**St**
1	16	40	3.0	0.6	6.2	723	0.08	9.2	1069	0.05	9.5	1101	0.05
2	109	281	3.0	0.6	6.2	723	0.08	9.2	1069	0.05	9.5	1101	0.05
3	16	40	6.0	0.6	6.2	1445	0.08	9.2	2139	0.05	9.5	2201	0.05
4	109	281	6.0	0.6	6.2	1445	0.08	9.2	2139	0.05	9.5	2201	0.05
5	16	40	3.0	1.0	10.4	1204	0.05	15.4	1782	0.03	15.8	1835	0.03
6	109	281	3.0	1.0	10.4	1204	0.05	15.4	1782	0.03	15.8	1835	0.03
7	16	40	6.0	1.0	10.4	2408	0.05	15.4	3565	0.03	15.8	3669	0.03
8	109	281	6.0	1.0	10.4	2408	0.05	15.4	3565	0.03	15.8	3669	0.03
9	62.5	160	4.5	0.8	8.3	1445	0.06	12.3	2139	0.04	12.7	2201	0.04
10	16	40	4.5	0.8	8.3	1445	0.06	-	-	-	-	-	-
11	109	281	4.5	0.8	8.3	1445	0.06	-	-	-	-	-	-
12	62.5	160	3.0	0.8	8.3	963	0.06	-	-	-	-	-	-
13	625	160	6.0	0.8	8.3	1927	0.06	-	-	-	-	-	-
14	62.5	160	4.5	0.6	6.2	1084	0.08	-	-	-	-	-	-
15	62.5	160	4.5	1.0	10.4	1806	0.05	-	-	-	-	-	-

6.2.4 Continuous Crystallization Experiments

The seeded continuous cooling crystallization of paracetamol from aqueous solutions was used as model system to study the impact of the axial dispersion on the final CSD. Paracetamol (CAS number 103-90-02, min. 99 % purity) was supplied by Sigma-Aldrich, and ultrapure water was obtained from a Millipore ultrapure water system.

A 17.40 g kg^{-1} (g of paracetamol per kg of water) aqueous solution of paracetamol at 40 °C was continuously injected at 60 mL min^{-1} at the crystallizer inlet. Simultaneously, a 15.50 g kg^{-1} (g of seeds per kg of solution) suspension of paracetamol seeds in an aqueous solution of paracetamol saturated at 15 °C was continuously injected at 40 mL min^{-1} at 30 cm downstream of the inlet in Crystallizer 1, and at 24.5 cm downstream of the inlet in Crystallizers 2 and 3. The oscillation conditions were set at f=6 Hz and V_d/V_{cell}=1. The crystallizer was kept at 15 °C by a refrigerated bath (Ministat 125, Huber). The final product was collected at the crystallizer outlet in a large volume of an aqueous solution of paracetamol saturated at room temperature. This avoided crystal growth during size analysis. The particles were analyzed by a stereoscopic zoom microscope (SMZ1500, Nikon) coupled to a video camera (DS-Ri1, Nikon) and several images were taken before being processed by an image analysis software.[26–29] The software classifies the particles as single crystals or agglomerates and measures the equivalent diameter of each one. To ensure the sample statistical significance, the equivalent mean diameter of at least 500 single crystals was obtained for each run.

6.3 Results and Discussion

6.3.1 Determination of the Axial Dispersion

The experimental RTD profiles obtained at the crystallizer outlet were converted into normalized RTD profiles, $E(\theta)$, where dimensionless time and length are considered. The dimensionless time, θ, is calculated as:

$$\theta = \frac{t}{\bar{t}} \tag{6.2}$$

where t is the time from the injection of tracer, and $\bar{t}$ is the mean residence time, calculated as:

$$\bar{t} = \frac{\int_0^\infty tCdt}{\int_0^\infty Cdt} \tag{6.3}$$

where C is the concentration of tracer.

The dimensionless length, z, is calculated as:

$$z = \frac{x}{l} \tag{6.4}$$

where x is the axial position, and l is the length of the test section.

Then, the normalized RTD profiles were fitted to three different models: the plug flow with axial dispersion model for small deviation from plug flow (Model 1 – **Equation (6.5)**), the plug flow with axial dispersion model for large deviation from plug flow (Model 2 – **Equation (6.6)**), and the tanks-in-series-model (Model 3 – **Equation (6.7)**):

$$E(\theta) = \frac{1}{\sqrt{4\pi \frac{D_C}{ul}}} exp\left[\frac{-(1-\theta)^2}{4\frac{D_C}{ul}}\right] \tag{6.5}$$

$$E(\theta) = \frac{1}{\sqrt{4\pi\theta \frac{D_C}{ul}}} exp\left[\frac{-(1-\theta)^2}{4\theta\frac{D_C}{ul}}\right] \tag{6.6}$$

$$E(\theta) = \frac{N(N\theta)^{N-1}\exp(-N\theta)}{(N-1)!} \tag{6.7}$$

Figure 6.3 and **Figure 6.4** show the quality of the fit of each model to the experimental data of two runs performed in Crystallizer 1 with the liquid and the solid tracer, respectively. **Figure 6.3** and **Figure 6.4** helped us to choose the best model to characterize the axial dispersion in each crystallizer. It was found that Model 3 gives the best fit to the experimental data of Run 1 and the worst fit to the experimental data of Run 2. On the other hand, Models 1 and 2 give quite good fits to the experimental data of both runs. Runs 1 and 2 differ from each other in terms of flow rate. Model 3 was excluded because it failed to describe the flow at high flow rates. The choice between Models 1 and 2 was based on the coefficient of determination, R^2, of each model to both runs. Model 1 provided slightly higher R^2 and was therefore chosen to describe the flow of the remaining runs.

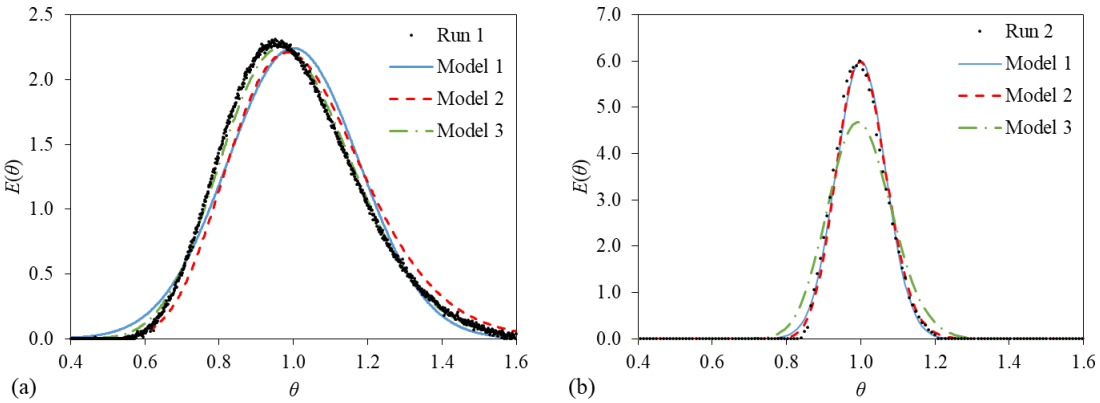


Figure 6.3 – Normalized RTD profile with liquid tracer in Crystallizer 1 for (a) Run 1 and (b) Run 2.

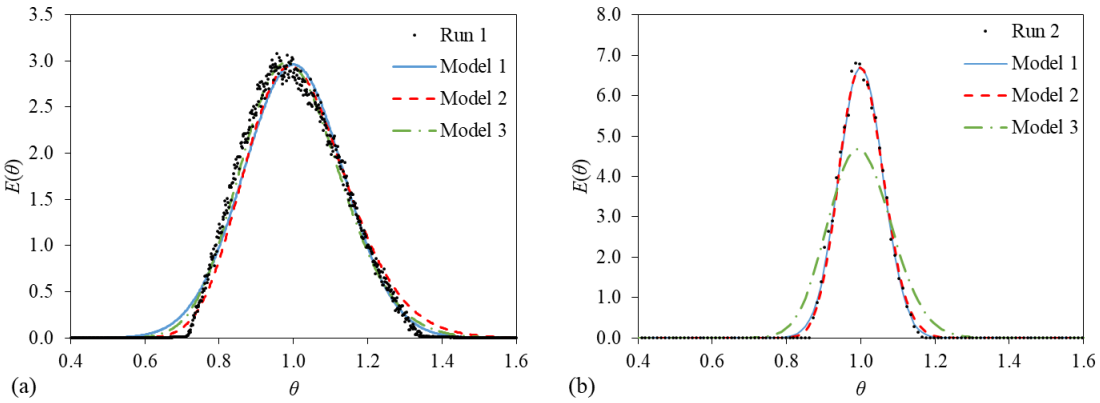


Figure 6.4 – Normalized RTD profile with solid tracer in Crystallizer 1 for (a) Run 1 and (b) Run 2.

The coefficient of determination of Model 1 was calculated for each run. The minimum and the maximum coefficients of determination, R^2_{min} and R^2_{max}, respectively, are presented in **Table 6.2**. The relatively high values of R^2, between 92.2% and 99.8%, speak for the quality of the fit of this model.

Table 6.2 – Minimum and maximum coefficients of determination of Model 1, and maximum deviation of mean residence time to hydraulic time for each crystallizer.

	Crystallizer 1		Crystallizer 2		Crystallizer 3	
	Liquid Tracer	**Solid Tracer**	**Liquid Tracer**	**Solid Tracer**	**Liquid Tracer**	**Solid Tracer**
R^2_{min} (%)	96.0	96.4	96.8	96.5	95.8	92.2
R^2_{max} (%)	99.5	99.8	99.6	99.5	99.8	99.7
δ_{max} (%)	3	10	4	11	6	12

The deviation, δ, between the mean residence time, $\bar{t}$, and the hydraulic time, $\tau = l/u$, was calculated for each run as:

$$\delta(\%) = 100\% \left| \frac{\tau - \bar{t}}{\tau} \right| \qquad \textbf{(6.8)}$$

The maximum deviation, δ_{max}, is also presented in **Table 6.2.** δ_{max} is relatively small in the three crystallizers (3%<δ_{max}<12%), which suggests that all the three crystallizers have small percentages of bypassing or stagnant zones and close to plug flow behavior. These deviations are considerably smaller than those previously reported in tubular-OFCs with both smooth periodic constrictions (SPC) and sharp edge periodic constrictions (SEPC). For example, Reis *et al.*[18] reported deviations in the order of 32.5% for a liquid tracer in a tubular-OFC with SPC; Ejim *et al.*[4] reported deviations between 17% and 52% for a solid tracer in tubular-OFCs with SEPC and SPC; Kacker *et al.*[9] reported deviations between 0% and 29% for a liquid tracer and between 14% and 28% for

a solid tracer in a tubular-OFC with SEPC; in addition, Phan *et al*.[22] reported deviations between 8.5% and 22% for a liquid tracer in tubular-OFCs with integral, helical and central baffles.

The axial dispersion was characterized by the reciprocal of the vessel dispersion number, $D_{ax} = ul/Dc$, for the liquid tracer, D_{ax}^{L}, and for the solid tracer, D_{ax}^{S}, in each crystallizer. The results are presented in **Table 6.3, Table 6.4** and **Table 6.5** for Crystallizers 1, 2 and 3, respectively.

Table 6.3 – Experimental conditions and results obtained in Crystallizer 1 with the liquid and the solid tracers.

				D_{ax}^{L}					D_{ax}^{S}				
Run	**Q (mL min^{-1})**	**f (Hz)**	**V_d/V_{cell}**	**1**	**2**	**3**	**4**	**5**	**1**	**2**	**3**	**4**	**5**
1	16	3.0	0.6	63	77	71			110	125	129		
2	109	3.0	0.6	455	405	470			566	575	603		
3	16	6.0	0.6	211	168	186			167	198	197		
4	109	6.0	0.6	559	542	446			684	783	738		
5	16	3.0	1.0	36	34	36			50	50	48		
6	109	3.0	1.0	274	255	272			292	407	383		
7	16	6.0	1.0	196	157	189			208	217	281		
8	109	6.0	1.0	393	498	535			458	555	505		
9	62.5	4.5	0.8	183	176	179	187	197	217	246	258	235	230
10	16	4.5	0.8	56					114				
11	109	4.5	0.8	331					409				
12	62.5	3.0	0.8	253					275				
13	625	6.0	0.8	358					442				
14	62.5	4.5	0.6	201					293				
15	62.5	4.5	1.0	127					212				

Table 6.4 – Experimental conditions and results obtained in Crystallizer 2 with the liquid and the solid tracers.

				D_{ax}^{L}					D_{ax}^{S}				
Run	**Q (mL min^{-1})**	**f (Hz)**	**V_d/V_{cell}**	**1**	**2**	**3**	**4**	**5**	**1**	**2**	**3**	**4**	**5**
1	16	3.0	0.6	66	89	66			84	95	107		
2	109	3.0	0.6	283	322	316			250	278	360		
3	16	6.0	0.6	104	170	111			113	138	117		
4	109	6.0	0.6	409	369	371			432	425	408		
5	16	3.0	1.0	45	58	36			59	46	45		
6	109	3.0	1.0	232	269	227			223	210	213		
7	16	6.0	1.0	95	108	107			72	66	57		
8	109	6.0	1.0	260	305	244			256	289	226		
9	62.5	4.5	0.8	208	222	207	196	167	227	203	228	226	162

Table 6.5 – Experimental conditions and results obtained in Crystallizer 3 with the liquid and the solid tracers.

				D_{ax}^{L}					D_{ax}^{S}				
Run	**Q (mL min^{-1})**	**f (Hz)**	**V_d/V_{cell}**	**1**	**2**	**3**	**4**	**5**	**1**	**2**	**3**	**4**	**5**
1	16	3.0	0.6	48	45	48			61	51	56		
2	109	3.0	0.6	395	356	323			353	407	331		
3	16	6.0	0.6	156	237	253			216	216	208		
4	109	6.0	0.6	463	504	433			629	647	539		
5	16	3.0	1.0	27	26	28			33	35	44		
6	109	3.0	1.0	196	183	173			204	227	217		
7	16	6.0	1.0	158	128	264			128	185	171		
8	109	6.0	1.0	422	378	392			388	450	424		
9	62.5	4.5	0.8	265	237	221	181	353	228	262	325	207	228

Figure 6.5 displays D_{ax}^{L} and **Figure 6.6** displays D_{ax}^{S} as a function of f, V_d/V_{cell} and Q for the factorial and center points in each crystallizer, respectively. In **Figure 6.5 (a)**, the error bars represent the interval between the minimum and maximum values of the three/five replicates. In the remaining plots the error bars are not presented for the sake of clarity.

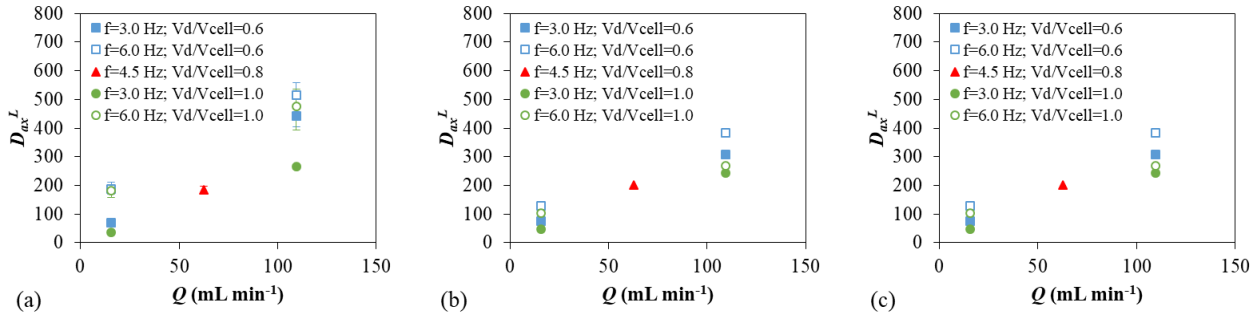


Figure 6.5 – D_{ax}^{L} as a function of the operating conditions for the factorial and center points in (a) Crystallizer 1, (b) Crystallizer 2 and (c) Crystallizer 3.

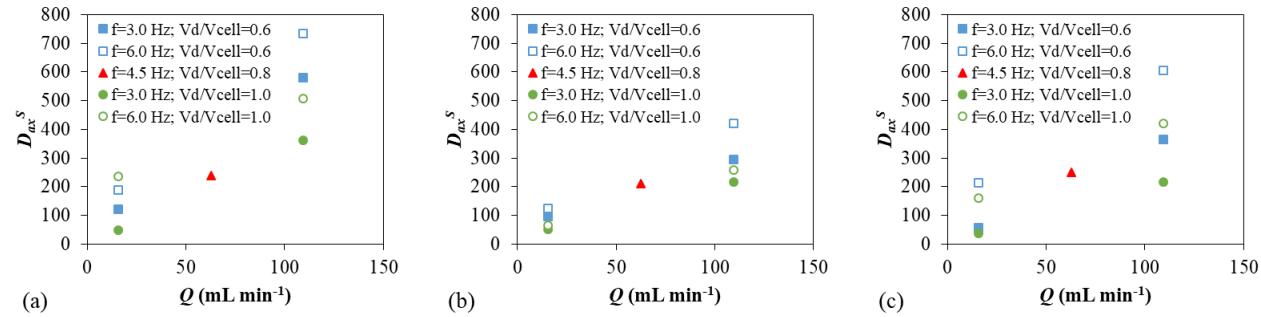


Figure 6.6 – D_{ax}^{S} as a function of the operating conditions for the factorial and center points in (a) Crystallizer 1, (b) Crystallizer 2 and (c) Crystallizer 3.

6.3.2 Comparison of Axial Dispersion for the Liquid and Solid Tracers

Under identical conditions, the deviation between the mean residence time and the hydraulic time is slightly larger for the solid tracer than for the liquid tracer, whereas the axial dispersion is slightly larger for the liquid tracer than for the solid tracer. This was rather expected because the liquid tracer behaves as a microfluid, whereas the solid tracer behaves as a macrofluid. This is because the molecules of the liquid tracer lose their identity into the fluid, whereas the particles of the solid tracer retain their identity as distinct aggregates of molecules.[30] In addition, the solid tracer seems to offer a greater resistance to flow than the liquid tracer due to the difference of densities between the solid (~1.4 g cm^{-3}) and the liquid phases (~1.0 g cm^{-3}). Similar results were also reported by Ejim *et al.*[4] and Kacker *et al.*[9] in tubular-OFCs.

6.3.3 Effect of the Operating Conditions on the Axial Dispersion

Figure 6.5 and **Figure 6.6** present the effects of Q, f and V_d/V_{cell} on D_{ax}^L and D_{ax}^S in each crystallizer. In general, D_{ax}^L and D_{ax}^S increased as Q and f increased, and decreased as V_d/V_{cell} increased in the three crystallizers. This suggests that, in the range of operating conditions under study, increasing Q reduces the physical backmixing[8,17] and increasing f increases the radial mixing,[17,18] which reduces the axial dispersion and, consequently, increases D_{ax}; whereas increasing V_d/V_{cell} increases the axial mixing,[22] which increases the axial dispersion and, consequently, decreases D_{ax}.[18] These results are in good agreement with previous works in tubular-OFCs. For example, Zheng and Mackley[8] found that while the axial dispersion coefficient, D_c, increases as Q increases, the dimensionless dispersion number, $D_c/(ul)$, (which is the reciprocal of D_{ax}) decreases as Q increases; this suggests that increasing Q increases more u than increases D_c. Similarly, Howes and Mackley,[17] Stonestreet and van Der Veeken,[25] Abbott *et al.*,[20] and Kacker *et al.*[9] found that increasing Q reduces the axial dispersion and amplifies the plug flow behavior. In addition, Reis *et al.*[18] and Zheng and Mackley[8] found that, below f ≈10 Hz, the axial dispersion decreases as f increases due to the increase of radial mixing, while, above f ≈10 Hz, the axial dispersion increases as f increases due to the intensification of backmixing. Furthermore, Dickens *et al.*,[3] Mackley and Ni,[10] Reis *et tal.*[18] and Zheng and Mackley[8] found that, below x_0 ≈1 mm, the axial dispersion decreases as x_0 increases, while, above x_0 ≈1 mm, the axial dispersion increases as x_0 increases due to the increase of the mixing length. Therefore, considering that, in this work, f was well below 10 Hz, and x_0 was well above 1 mm, our results seem to be in good agreement with those described in previous works. However, it should be noted that some other works reported distinct results from those previously mentioned. For example, in the case of Abbott *et al.*,[20] the axial dispersion reached its minimum at x_0 =1.5-3 mm and f=1.00-1.75 Hz; in the case of Howes and Mackley,[17] the axial dispersion reached its minimum at different values of Re_o, depending on both St and Re; in the case of Mackley and Ni,[10] at fixed St, the axial dispersion was found relatively independent of Re_o and Re; and in the case of Palma and Giudici,[15] at x_0=10-25 mm, the axial dispersion increased as f increased from 0 to 5 Hz, whereas, at x_0=5 mm, the axial dispersion was

practically not affected by f. Such a variety of results suggest that the optimal operating conditions probably depend on the geometry of the OFC, and thus should be assessed case by case.

6.3.4 Effect of the Geometric Parameters on the Axial Dispersion

Figure 6.5 and **Figure 6.6** present the effects of L/W and α on D_{ax}^{L} and D_{ax}^{S}. The effect of L/W can be assessed by comparison of D_{ax}^{L} and D_{ax}^{S} in Channels 1 and 3, which have the same α and different L/W, and the effect of α can be assessed by comparison of D_{ax}^{L} and D_{ax}^{S} in Channels 2 and 3, which have the same L/W and different α. In general, D_{ax}^{L} and D_{ax}^{S} increase as L/W decreases and α increases; interestingly, the difference between D_{ax}^{L} and D_{ax}^{S} also increases as L/W decreases and α increases.

In a tubular-OFC, the cell aspect ratio is defined as L/D, where L is the distance between constrictions, and D is the tube diameter in the straight section; and the ratio of the open constriction area is defined as $\alpha = (D_0/D)^2$, where D_0 the tube diameter in the constriction. Palma and Giudici[15] determined the axial dispersion in a tubular-OFC with D=39.6 mm and L varying between 25, 50 and 100 mm, corresponding to L/D=0.63, 1.26 and 2.53, respectively, and found that, in general, the axial dispersion decreased as L/D increased. Although this result seems to be opposite to that reported in the present work, the difference in the range of L/D (or L/W) under study in the two works should not be disregarded. More recently, Ejim *et al.*[4] determined the axial dispersion in 10 tubular-OFCs, 5 with SPC and 5 with SEPC. In the case of the tubes with SPC, whose geometry is the closest to our crystallizers, the effect of L/D on the axial dispersion depended on α: at α=0.12, the axial dispersion decreased as L/D increased, whereas, at α=0.25, the axial dispersion increased as L/D increased; similarly, the effect of α on the axial dispersion depended on L/D: at L/D=1.5, the axial dispersion decreased as α increased, whereas, at L/D=3.0, the axial dispersion increased as α increased. This great variety of results shows, once again, the interdependence of the two geometrical parameters and highlights the importance of determining the optimal operating conditions case by case.

6.3.5 Model Development

The experiments were performed according to a DoE approach. First, a full factorial design with five center points was used to predict the effects of Q, f, and V_d/V_{cell} on D_{ax}^{L} and D_{ax}^{S}. Each combination of factors was tested in triplicate. A first order model was formulated to describe the relationship between the response, D_{ax}^{L} or D_{ax}^{S}, and the three factors, Q, f and V_d/V_{cell}, in each crystallizer as follows:

$$D_{ax}^{L}(\text{or } D_{ax}^{S}) = \beta_0 + \beta_1 Q + \beta_2 f + \beta_3 V_d/V_{cell} + \beta_{12} Qf + \beta_{13} QV_d/V_{cell} + \beta_{23} fV_d/V_{cell} + \beta_{123} QfV_d/V_{cell} \quad \textbf{(6.9)}$$

where β_0 is a constant, β_1, β_2 and β_3 are linear coefficients, β_{12}, β_{13} and β_{23} are two-way interaction coefficients, and β_{123} is a three-way interaction coefficient.

The significance of each term of the model was determined by comparison of the p-value of each term to the significance level of 5%. The p-value measures the evidence against the null hypothesis, which states that there is no association between the term and the response. A backward stepwise elimination technique was applied to select the significant terms, and to eliminate the insignificant terms from the model.

The center points were used to test for the curvature of the response. This test compares the mean response at the center points to the expected response considering a linear relationship between the terms of the model and the response. The p-value for curvature was then compared to the significance level of 5% to assess the null hypothesis. The p-value measures the evidence against the null hypothesis, which states that all the relationships between the factors and the response are linear. The response is said to have curvature when p-value≤0.05.[31] In this study, the curvature of both responses D_{ax}^{L} and D_{ax}^{S} was only found significant in Crystallizer 1. In these two cases, axial points were added to the design. Face-centered axial points were chosen to guarantee that the PVC particles were fully suspended in the whole range of operating conditions under study. Thus, a second order model was formulated to describe the relationship between the response, D_{ax}^{L} or D_{ax}^{S}, and the three factors, Q, f and V_d/V_{cell}, in Crystallizer 1 as follows:

$$D_{ax}^{L}(\text{or } D_{ax}^{S}) = \beta_0 + \beta_1 Q + \beta_2 f + \beta_3 V_d/V_{cell} + \beta_{11} Q^2 + \beta_{22} f^2 + \beta_{33}(V_d/V_{Cell})^2 + \beta_{12} Qf + \beta_{13} Q V_d/V_{cell} + \beta_{23} f V_d/V_{cell} \quad \textbf{(6.10)}$$

where β_{11}, β_{22} and β_{33} are square coefficients. Then, a backward stepwise elimination technique was applied to select the significant terms, and to eliminate the insignificant terms from the model. The coded coefficients and the coefficient of determination of each model are presented in **Table 6.6**. The quality of the fit of each model to the experimental data is shown in **Figure 6.7**.

Table 6.6 – Coded coefficients and coefficient of determination of each model.

	Crystallizer 1		**Crystallizer 2**		**Crystallizer 3**	
Coefficient	$\boldsymbol{D_{ax}^{L}}$	$\boldsymbol{D_{ax}^{S}}$	$\boldsymbol{D_{ax}^{L}}$	$\boldsymbol{D_{ax}^{S}}$	$\boldsymbol{D_{ax}^{L}}$	$\boldsymbol{D_{ax}^{S}}$
$\boldsymbol{\beta_0}$	182.0	246.0	195.31	193.58	237.69	257.61
$\boldsymbol{\beta_1}$	151.98	194.85	106.32	107.11	116.63	142.22
$\boldsymbol{\beta_2}$	66.84	70.08	26.79	26.19	80.80	90.94
$\boldsymbol{\beta_3}$	-32.78	-57.78	-28.80	-43.59	-36.94	-50.34
$\boldsymbol{\beta_{22}}$	92.5	101.9				
$\boldsymbol{\beta_{12}}$				15.57		20.62
$\boldsymbol{\beta_{13}}$	-21.79	-53.16	-15.76	-17.75	-23.91	-32.63
$\boldsymbol{\beta_{23}}$	20.41			-12.09		
$\boldsymbol{\beta_{123}}$						
$\boldsymbol{R^2}$ (%)	96.33	97.00	96.36	95.57	91.66	96.94

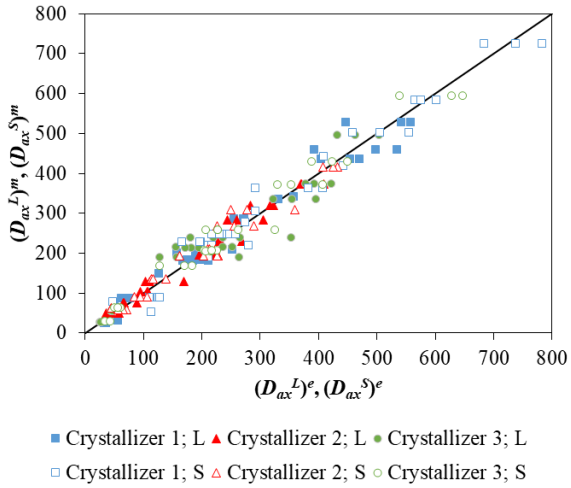


Figure 6.7 – Comparison of $D_{ax}{}^{L}$ and $D_{ax}{}^{S}$ obtained from the model, $(D_{ax}{}^{L})^{m}$ and $(D_{ax}{}^{S})^{m}$, and obtained experimentally, $(D_{ax}{}^{L})^{e}$ and $(D_{ax}{}^{S})^{e}$ in each crystallizer. L stands for liquid tracer and S stands for solid tracer.

The main effects plot is presented in **Figure 6.8**. The main effects plot displays the average response, $\overline{D_{ax}^{L}}$ and $\overline{D_{ax}^{S}}$, for each level of Q, f, and V_d/V_{cell}. **Figure 6.8** shows that Q, f, and V_d/V_{cell} have similar effects on D_{ax}^{L} and D_{ax}^{S} in each crystallizer. In Crystallizer 1, Q has a linear positive effect, f has a quadratic effect with an "U" shape, and V_d/V_{cell} has a linear negative effect; in Crystallizers 2 and 3, Q and f have linear positive effects, and V_d/V_{cell} has linear negative effects. This figure also shows that the main effect of Q is stronger than the main effects of f and V_d/V_{cell}, because the linear coefficient associated with of Q (β_1) is significantly larger than the linear coefficients associated with f (β_2) and V_d/V_{cell} (β_3). This is coherent with the previous findings.

In this study, different interactions were found significant for different models. Nevertheless, the interaction between Q and V_d/V_{cell} was always significant, and the most significant of all interactions because the p-value for QV_d/V_{cell} was the lowest for all models. The interaction plot between Q and V_d/V_{cell} for D_{ax}^{L} in Crystallizer 1 is presented in **Figure 6.9**. Similar trends were obtained in the other crystallizers with both the liquid and the solid tracers. The interaction plot displays one line for the mean response for each level of Q at V_d/V_{cell}=0.6, another line at V_d/V_{cell}=0.8, and another at V_d/V_{cell}=1.0. **Figure 6.9** shows that the change in the mean response from the low to the high level of Q depends on the level of V_d/V_{cell}, this effect being more pronounced at V_d/V_{cell}=0.6, than at V_d/V_{cell}=0.8 or V_d/V_{cell}=1. Stonestreet and van Der Veeken[25] had already suggested that a specific interaction between the oscillatory and the net flow components exists, but their one-factor-at-a-time approach could not quantify this effect. This was possible in this study thanks to the DoE approach.

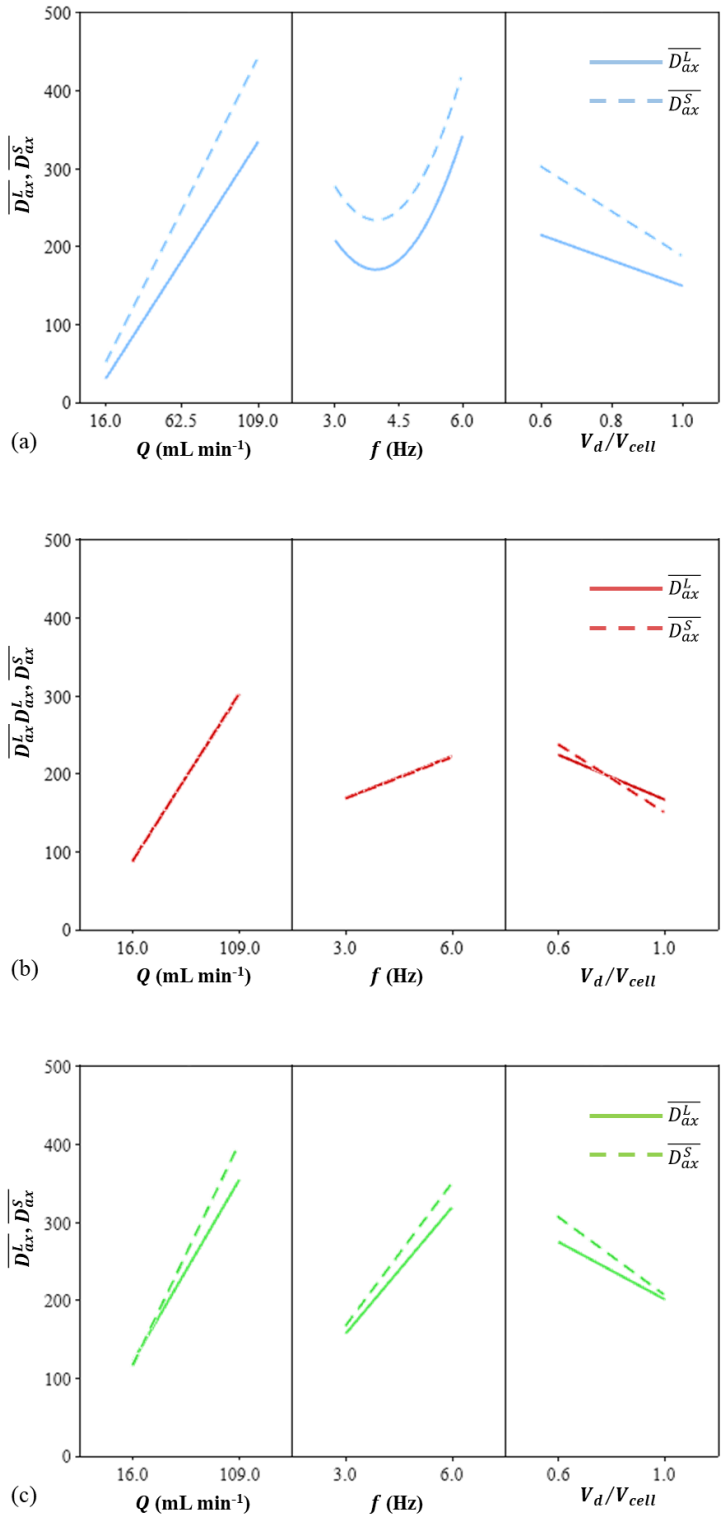


Figure 6.8 – Main effects plot for $D_{ax}{}^{L}$ and $D_{ax}{}^{S}$ in (a) Crystallizer 1, (b) Crystallizer 2, and (c) Crystallizer 3.

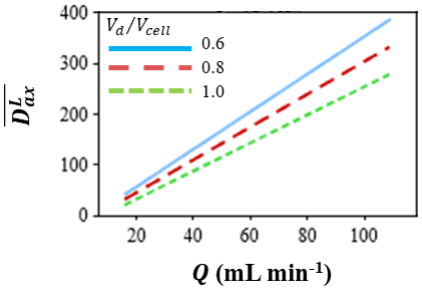


Figure 6.9 – Interaction plot between Q and V_d/V_{cell} for $D_{ax}{}^{L}$ in Crystallizer 1.

6.3.6 Continuous Crystallization Experiments

As a consequence of their impact on the axial dispersion in planar-OFCs, the geometric parameters α and L/W should also have an impact on the final CSD obtained from a continuous crystallization experiment. In this work, the seeded continuous cooling crystallization of paracetamol from aqueous solutions was used as model system to study this effect. The solutions were seeded to avoid spontaneous nucleation, which allowed to isolate the effect of axial dispersion on crystal growth.

Table 6.7 presents the volume-based CSD parameters of the seeds and final products obtained in each crystallizer, where d_m is the volume-based mean crystal size, and d_{10}, d_{50} and d_{90} are the volume-based crystal sizes corresponding to the 10th, 50th and 90th percentile of the cumulative CSD, respectively. The volume-based CSDs, $f_V(d)$, are presented in **Figure 6.10**. It is interesting to note that the mode of the final CSD is similar in crystallizers with the same α (Crystallizers 1 and 3), whereas the peak of frequency is similar in crystallizers with the same L/W (Crystallizers 2 and 3). It is also interesting to note that the narrowest CSD was obtained in Crystallizer 2, which has the smallest difference between D_{ax}^{L} and D_{ax}^{S}, and not in Crystallizer 1, which has the closest behavior to plug flow, with the highest values of D_{ax}^{L} and D_{ax}^{S} and the smallest δ. This result suggests that having similar axial dispersions in the liquid and the solid phases is crucial to obtain narrow CSDs.

Table 6.7 –Volume-based CSD parameters of the seeds and final products obtained in each crystallizer.

Parameter	Seeds	Crystallizer 1	Crystallizer 2	Crystallizer 3
d_m (µm)	398	558	491	509
d_{10} (µm)	209	349	312	325
d_{50} (µm)	475	671	570	620
d_{90} (µm)	851	1138	900	933
$d_{90} - d_{10}$ (µm)	641	788	587	608

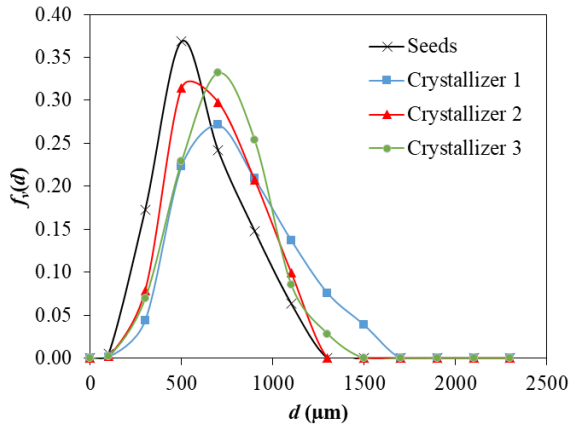


Figure 6.10 – Volume-based CSD of the seeds and final products obtained in each crystallizer (Q=100 mL min^{-1}, f=6 Hz, and V_d/V_{cell}=1).

6.4 Conclusion

RTD experiments with a liquid and a solid tracer were performed to evaluate the axial dispersion in three planar-OFCs with different geometries. A DoE approach was developed so as to assess the effects of Q, f, and V_d/V_{cell} on D_{ax}^L and D_{ax}^Sin each crystallizer.

It was found that Q, f, and V_d/V_{cell} have similar main effects on D_{ax}^L and D_{ax}^S in the three crystallizers. In Crystallizer 1, Q has a linear positive effect, f has a quadratic effect with an "U" shape, and V_d/V_{cell} has a linear negative effect; in Crystallizers 2 and 3, Q and f have linear positive effects, and V_d/V_{cell} has linear negative effects. It was also found that the interaction between Q and V_d/V_{cell} is the most significant interaction for both D_{ax}^L and D_{ax}^S in all the three crystallizers. The interaction plot shows that the effect of Q is more pronounced at low levels of V_d/V_{cell}. Therefore, in the range of operating conditions under study here, the optimal operating conditions, which minimize the axial dispersion and maximize D_{ax}, are high levels of Q and f, and low levels of V_d/V_{cell}.

Furthermore, the highest values of D_{ax}^L and D_{ax}^S, and the smallest value of δ were obtained in Crystallizer 1, whereas the most similar values of D_{ax}^L and D_{ax}^S were obtained in Crystallizer 2. Continuous crystallization experiments showed that Crystallizer 2 provides the narrowest CSDs, which suggests that similar axial dispersions in the liquid and solid phases is a key factor controlling the final CSD due to the migration of molecules between the supersaturated solution and the growing crystals.

Notation

Acronyms

CSD	Crystal size distribution
OFC	Oscillatory flow crystallizer
PVC	Polyvinyl chloride
RTD	Residence time distribution
SEPC	Sharp edge periodic constrictions
SPC	Smooth periodic constrictions

Latin symbols

A_{cs}	Channel cross-sectional area
C	Concentration of tracer
d	Crystal size
D	Tube diameter in the straight section
D_0	Tube diameter in the constriction
D_c	Axial dispersion coefficient
D_h	Hydraulic diameter
d_m	Volume-based mean crystal size
d_{10}, d_{50} and d_{90}	Volume-based crystal size corresponding to the 10th, 50th and 90th percentile of the cumulative CSD, respectively
$E(\theta)$	Normalized residence time distribution profile
f	Frequency of oscillation
$f_V(d)$	Volume-based CSD
g	Inter-stage backmixing parameter
H	Channel height
l	Total length
L	Distance between constrictions
L_1	Constriction length
L_2	Straight section length
N	Number of ideal stirred tanks in series
P_{cs}	Channel cross-sectional wetted perimeter
Q	Flow rate
R^2	Coefficient of determination
R^2_{min}	Minimum coefficient of determination
R^2_{max}	Maximum coefficient of determination
t	Time
$\bar{t}$	Mean residence time
V	Total volume
V_{cell}	Volume of each inter-constriction cell
V_d/V_{cell}	Ratio of the volume displaced in a complete peak-to-peak oscillation to the volume of each inter-constriction cell
W	Channel width in the straight section
W_0	Channel width in the constriction
x	Axial position
x_0	Center-to-peak amplitude of oscillation
z	Dimensionless length

Greek Letters

β_0	Average response for all observations
β_1, β_2 and β_3	Linear coefficients
β_{11}, β_{22} and β_{33}	Square coefficients
β_{12}, β_{13} and β_{23}	Two-way interaction coefficients
β_{123}	Three-way interaction coefficient
δ	Deviation between the mean residence time and the hydraulic time
δ_{max}	Maximum deviation between the mean residence time and the hydraulic time
θ	Dimensionless time
τ	Hydraulic time

Dimensionless Numbers

$\alpha = (D_0/D)^2$	Ratio of the open constriction area for tubular-OFCs
$\alpha = W_0/W$	Ratio of the open constriction area for planar-OFCs
D_{ax}	Reciprocal of the vessel dispersion number
D_{ax}^L	Reciprocal of the vessel dispersion number for the liquid tracer
$\overline{D_{ax}^L}$	Average reciprocal of the vessel dispersion number for the liquid tracer
$(D_{ax}^L)^e$	Reciprocal of the vessel dispersion number for the liquid tracer obtained experimentally
$(D_{ax}^L)^m$	Reciprocal of the vessel dispersion number for the liquid tracer obtained from the model
D_{ax}^S	Reciprocal of the vessel dispersion number for the solid tracer
$\overline{D_{ax}^S}$	Average reciprocal of the vessel dispersion number for the solid tracer
$(D_{ax}^S)^e$	Reciprocal of the vessel dispersion number for the solid tracer obtained experimentally
$(D_{ax}^S)^m$	Reciprocal of the vessel dispersion number for the solid tracer obtained from the model
$D_c/(ul)$	Vessel dispersion number
L/D	Cell aspect ratio for tubular-OFCs
L/W	Cell aspect ratio for planar-OFCs
Re	Reynolds number
$\mathrm{Re_o}$	Oscillatory Reynolds number
St	Strouhal number

References

(1) McGlone, T.; Briggs, N. E. B.; Clark, C. A.; Brown, C. J.; Sefcik, J.; Florence, A. J. Oscillatory Flow Reactors (OFRs) for Continuous Manufacturing and Crystallization. *Org. Process Res. Dev.* **2015**, *19* (9), 1186–1202.

(2) Levenspiel, O. *Chemical Reaction Engineering*, 3rd ed.; John Wiley & Sons, Inc.: New York, 1999.

(3) Dickens, A. W.; Mackley, M. R.; Williams, H. R. Experimental Residence Time Distribution Measurements for Unsteady Flow in Baffled Tubes. *Chem. Eng. Sci.* **1989**, *44* (7), 1471–1479.

(4) Ejim, L. N.; Yerdelen, S.; McGlone, T.; Onyemelukwe, I.; Johnston, B.; Florence, A. J.; Reis, N. M. A Factorial Approach to Understanding the Effect of Inner Geometry of Baffled Meso-Scale Tubes on Solids Suspension and Axial Dispersion in Continuous, Oscillatory Liquid–Solid Plug Flows. *Chem. Eng. J.* **2017**, *308*, 669–682.

(5) Reis, N.; Vicente, A. A.; Teixeira, J. A. Liquid Backmixing in Oscillatory Flow through a Periodically Constricted Meso-Tube. *Chem. Eng. Process. Process Intensif.* **2010**, *49* (7), 793–803.

(6) Siddique, H.; Brown, C. J.; Houson, I.; Florence, A. J. Establishment of a Continuous Sonocrystallization Process for Lactose in an Oscillatory Baffled Crystallizer. *Org. Process Res. Dev.* **2015**, *19* (12), 1871–1881.

(7) Smith, K. B.; Mackley, M. R. An Experimental Investigation into the Scale-up of Oscillatory Flow Mixing in Baffled Tubes. *Chem. Eng. Res. Des.* **2006**, *84* (11), 1001–1011.

(8) Zheng, M.; Mackley, M. The Axial Dispersion Performance of an Oscillatory Flow Meso-Reactor with Relevance to Continuous Flow Operation. *Chem. Eng. Sci.* **2008**, *63* (7), 1788–1799.

(9) Kacker, R.; Regensburg, S. I.; Kramer, H. J. M. Residence Time Distribution of Dispersed Liquid and Solid Phase in a Continuous Oscillatory Flow Baffled Crystallizer. *Chem. Eng. J.* **2017**, *317*, 413–423.

(10) Mackley, M. R.; Ni, X. Experimental Fluid Dispersion Measurements in Periodic Baffled Tube Arrays. *Chem. Eng. Sci.* **1993**, *48* (18), 3293–3305.

(11) Mackley, M. R.; Ni, X. Mixing and Dispersion in a Baffled Tube for Steady Laminar and Pulsatile Flow. *Chem. Eng. Sci.* **1991**, *46* (12), 3139–3151.

(12) Ni, X.; Pereira, N. E. Parameters Affecting Fluid Dispersion in a Continuous Oscillatory Baffled Tube. *AIChE J.* **2000**, *46* (1), 37–45.

(13) Oliva, J. A.; Pal, K.; Barton, A.; Firth, P.; Nagy, Z. K. Experimental Investigation of the Effect of Scale-up on Mixing Efficiency in Oscillatory Flow Baffled Reactors (OFBR) Using Principal Component Based Image Analysis as a Novel Noninvasive Residence Time Distribution Measurement Approach. *Chem. Eng. J.* **2018**, *351*, 498–505.

(14) Onyemelukwe, I. I.; Nagy, Z. K.; Rielly, C. D. Solid-Liquid Axial Dispersion Performance of a Mesoscale Continuous Oscillatory Flow Crystalliser with Smooth Periodic Constrictions Using a Non-Invasive Dual Backlit Imaging Technique. *Chem. Eng. J.* **2020**, *382* (122862).

(15) Palma, M.; Giudici, R. Analysis of Axial Dispersion in an Oscillatory-Flow Continuous Reactor. *Chem. Eng. J.* **2003**, *94* (3), 189–198.

(16) Slavnić, D.; Bugarski, B.; Nikačević, N. Solids Flow Pattern in Continuous Oscillatory Baffled Reactor. *Chem. Eng. Process. - Process Intensif.* **2019**, *135*, 108–119.

(17) Howes, T.; Mackley, M. R. Experimental Axial Dispersion for Oscillatory Flow through a Baffled Tube. *Chem. Eng. Sci.* **1990**, *45* (5), 1349–1358.

(18) Reis, N.; Vicente, A. A.; Teixeira, J. A.; Mackley, M. R. Residence Times and Mixing of a Novel Continuous Oscillatory Flow Screening Reactor. *Chem. Eng. Sci.* **2004**, *59* (22–23), 4967–4974.

(19) Takriff, M. S.; Masyithah, Z. Interstage Backmixing in Oscillatory Flow in a Baffled Column. *Chem. Eng. Commun.* **2002**, *189* (12), 1640–1652.

(20) Abbott, M. S. R.; Harvey, A. P.; Morrison, M. I. Rapid Determination of the Residence Time Distribution (RTD) Function in an Oscillatory Baffled Reactor (OBR) Using a Design of Experiments (DoE) Approach. *Int. J. Chem. React. Eng.* **2014**, *12* (1), 575–586.

(21) Mohd Rasdi, F. R.; Phan, A. N.; Harvey, A. P. Rapid Determination of the Reaction Kinetics of an N-Butylbenzaldimine Synthesis Using a Novel Mesoscale Oscillatory Baffled Reactor. *Procedia Eng.* **2012**, *42*, 1527–1539.

(22) Phan, A. N.; Harvey, A. Development and Evaluation of Novel Designs of Continuous Mesoscale Oscillatory Baffled Reactors. *Chem. Eng. J.* **2010**, *159* (1–3), 212–219.

(23) Phan, A. N.; Harvey, A. P. Characterisation of Mesoscale Oscillatory Helical Baffled Reactor—Experimental Approach. *Chem. Eng. J.* **2012**, *180*, 229–236.

(24) Phan, A. N.; Harvey, A.; Lavender, J. Characterisation of Fluid Mixing in Novel Designs of Mesoscale Oscillatory Baffled Reactors Operating at Low Flow Rates (0.3–0.6ml/Min). *Chem. Eng. Process. Process Intensif.* **2011**, *50* (3), 254–263.

(25) Stonestreet, P.; van Der Veeken, P. M. J. The Effects of Oscillatory Flow and Bulk Flow Components on Residence Time Distribution in Baffled Tube Reactors. *Chem. Eng. Res. Des.* **1999**, *77* (8), 671–684.

(26) Faria, N.; Pons, M. N.; Feyo de Azevedo, S.; Rocha, F. A.; Vivier, H. Quantification of the Morphology of Sucrose Crystals by Image Analysis. *Powder Technol.* **2003**, *133* (1–3), 54–67.

(27) Ferreira, A.; Faria, N.; Rocha, F.; Feyo De Azevedo, S.; Lopes, A. Using Image Analysis to Look into the Effect of Impurity Concentration in NaCl Crystallization. *Chem. Eng. Res. Des.* **2005**, *83* (4), 331–338.

(28) Ferreira, A.; Faria, N.; Rocha, F.; Teixeira, J. A. Using an Online Image Analysis Technique to Characterize Sucrose Clystal Morphology Durring a Crystallization Run. *Ind. Eng. Chem. Res.* **2011**, *50*, 6990–7002.

(29) Ferreira, A.; Pereira, G.; Teixeira, J. A.; Rocha, F. Statistical Tool Combined with Image Analysis to Characterize Hydrodynamics and Mass Transfer in a Bubble Column. *Chem. Eng. J.* **2012**, *180*, 216–228.

(30) Levenspiel, O. Basics of Non-Ideal Flow. In *Chemical Reaction Engineering*; John Wiley & Sons, Inc.: New York, 1999; pp 257–282.

(31) Montgomery, D. C. *Design and Analysis of Experiments*, 5th ed.; John Wiley & Sons, Inc.: New York, 2007.

Chapter 7 - Nucleation Kinetics in a Planar Oscillatory Flow Crystallizer

Reproduced from Cruz, P. C.; Rocha, F. A.; Ferreira, A. M. Crystallization of Paracetamol from Aqueous Solutions in a Planar Oscillatory Flow Crystallizer: Effect of the Oscillation Conditions on the Nucleation Kinetics.CrystEngComm 2021, 23 (39), 6930-6941 with permission from the Royal Society of Chemistry.

https://pubs.rsc.org/en/content/articlelanding/2021/ce/d1ce00922b

7.1 Introduction

Crystallization is a complex phase transition process, which involves the separation of a solute from a supersatured solution. This process is traditionally described as a sequence of two major steps. In the first step, known as nucleation, a crystalline phase emerges in the form of nuclei, and in the second step, known as crystal growth, the nuclei become larger crystals by subsequent deposition of solute.[1] Both nucleation and crystal growth compete for the consumption of supersaturation, so the relative magnitudes of the two steps will have a major impact on the properties of the final product, in particular the crystal size distribution (CSD).[2] Nucleation sets the initial CSD at the beginning of unseeded batch crystallization processes or during the start-up of continuous crystallization processes, which highlights the importance of being able to estimate the nucleation kinetics under industrially relevant conditions.

The nucleation kinetics can be estimated by several methods.[3] Deterministic methods, based on the multi-nuclei model, are usually employed to estimate the nucleation kinetics for large crystallizer volumes, when the dispersion of the experimental results can be neglected. On the other hand, probability methods, based on the single nucleus model, are usually employed to estimate the nucleation kinetics for small crystallizer volumes, in order to capture the stochastic nature of nucleation. This latter category includes a variety of methods, some performed under stagnant conditions, and others performed under agitated conditions. Methods based on stagnant conditions, such as the droplet based, double-pulse and microfluidic methods, have been widely used to verify the classical nucleation theory or develop new nucleation theories; but, methods based on agitated conditions, such as the stirred small volume solution methods, reflect the industrial crystallization processes more accurately due to the presence of stirring.[4–12] However, even in this case, transferring the kinetic parameters obtained at the laboratorial scale to the industrial scale is not necessarily straightforward because both the induction time and the metastable zone width (MSZW) are volume-dependent.[13,14] What is more, the geometry of the industrial crystallizer might also differ significantly from the traditional small stirred tank

crystallizer from the laboratory in terms of aspect ratio, stirring mechanism, or even the presence/absence of stirring.

The stirred tank crystallizer (STC) remains as the standard equipment for batch crystallization of active pharmaceutical ingredients (APIs) and pharmaceutical intermediates from the first development stages to manufacturing. However, in the last decades, the advent of continuous manufacturing in the pharmaceutical industry has stimulated the development of new crystallizers specifically designed for continuous crystallization.[15] The oscillatory flow crystallizer (OFC) is one of the examples.[16] OFCs have been widely used for both batch and continuous crystallization,[16] but only a few publications have explored the effect of the operating conditions on the nucleation kinetics in OFCs. Two main types of experimental methods have been employed:[3] polythermal methods, which are based on the determination of the MSZW as a function of the cooling rate,[17–21] and isothermal methods, which are based on the determination of the induction time as a function of supersaturation.[22,23] Additionally, population balance approaches have also been employed.[20,24,25]

In this work, the isothermal batch crystallization of paracetamol from aqueous solutions in a planar-OFC was used as a model system to explore the effect of the oscillation conditions on the nucleation kinetics. The planar-OFC is a relatively new variant of OFCs where the traditional circular cross-section of conventional tubular-OFCs is replaced by a rectangular cross-section.[26] This design was developed to overcome the limitations of tubular-OFCs, where several problems related to the suspension and flowability of solids are commonly reported.[27–29] The detection time was measured for several combinations of frequency and amplitude of oscillation and several replicates were performed for each experimental condition. Then, the nucleation rate was obtained from the cumulative probability distribution of detection times. The nucleation rate was measured at different supersaturations levels, and the classical nucleation theory was applied to estimate the kinetic and thermodynamic parameters for nucleation.

7.1.1 Theoretical Background

Jiang and ter Horst[7] proposed a stochastic model for the determination of the nucleation rate from the variation in the detection time. This model is based on the single nucleus mechanism (which postulates the loss of metastability due to the nucleation of a single nucleus, followed by the growth of this single nucleus to a particular size, the formation of crystal fragments due to secondary nucleation of the same single crystal, and finally the growth of the crystal fragments), and on the assumption that the appearance of a nucleus in a supersaturated solution is a random process independent of the appearance of other nuclei in the same volume. This model was previously employed to determine the nucleation rates of *m*-aminobenzoic acid,[7] L-histidine,[7] isonicotinamide,[6] *p*-aminobenzoic acid,[9] benzoic acid,[9] risperidone,[10] racemic diprophylline,[4] salicylic acid,[11] and salicylamide.[12] In addition, a similar model, based on the variation in the MSZW, was previously employed

to measure the nucleation rates of paracetamol,[5] isonicotinamide,[5,6] and salicylic acid.[11] The mathematical description of Jiang and ter Horst's model is presented below.

The appearance of a nucleus is generally perceived as a random event. When the appearance of a nucleus is independent of the appearance of other nuclei in the same volume, the probability of finding m nuclei within a time interval, P_m, at constant supersaturation, S, and temperature, T, can be described by the Poisson distribution[30] as:

$$P_m(t) = \frac{N^m}{m!}\exp[-N(t)] \tag{7.1}$$

where $N(t)$ is the average number of nuclei formed in the time interval t. Therefore, the probability of finding no nuclei within the time interval, P_0, and the probability of finding at least 1 nucleus within the time interval, $P_{\geq 1}$, can be calculated as:

$$P_0(t) = \exp[-N(t)] \tag{7.2}$$

$$P_{\geq 1}(t) = 1 - P_0(t) = 1 - \exp[-N(t)] \tag{7.3}$$

The average number of nuclei formed in the time interval, $N(t)$, depends on the volume, V, and the nucleation rate, J, as:

$$N(t) = JVt \tag{7.4}$$

Hence, **Equation (7.3)** becomes:

$$P(t) = 1 - \exp(-JVt) \tag{7.5}$$

However, there is a time delay between the onset of nucleation and its detection. If this time delay, also known as growth time, is equal for all detections, then **Equation (7.5)** becomes:

$$P(t_d) = 1 - \exp\left[-JV(t_d - t_g)\right] \tag{7.6}$$

where t_d is the detection time and t_g is the growth time. **Equation (7.6)** describes the variation in the detection time measured under constant supersaturation, temperature and volume. The probability distribution of detection times is experimentally accessible from a large number of detection time measurements performed at constant supersaturation, temperature and volume. The experimental probability can be calculated as:

$$P(t_d) = \frac{M^+(t_d)}{M} \tag{7.7}$$

where $M^+(t)$ is the number of experiments in which nucleation occurred at time t_d and M is the total number of experiments. Then, Equation (7.6) can be linearized and fitted to the experimental data in order to obtain J and t_g from the slope and the intercept, respectively.

After measuring the nucleation rate at different supersaturations, the classical nucleation theory[31] can be applied to express the nucleation rate as a function of supersaturation ratio, S, as:

$$J = AS\exp\left(\frac{-B}{\ln^2 S}\right) \quad \textbf{(7.8)}$$

where the pre-exponential factor A represents the kinetic parameter, and the exponential factor B represents the thermodynamic parameter. Then, equation (7.8) can be linearized and fitted to the experimental data in order to obtain A and B from the intercept and the slope, respectively.

7.2 Materials and Methods

7.2.1 Material

Paracetamol (CAS number 103-90-02, min. 99% purity) was supplied by Sigma-Aldrich and ultrapure water was obtained from a Millipore ultrapure water system.

7.2.2 Crystallizer

A schematic representation of the planar-OFC is presented in **Figure 7.1**. The planar-OFC consists of a plate-like crystallizer with three stacked plates screwed together: two polycarbonate plates, one at the base and one at the top, and one aluminum plate coated with Halar® (ethylene-chlorotrifluoroethylene copolymer, ECTFE) in the middle – **Figure 7.1 (a)**. The crystallization process takes place in a channel designed with smooth periodic constrictions located between the middle and top plates, and the water of a cooling/heating jacket circulates in a straight channel located between the base and middle plates. The two channels were carved in the middle plate; the top plate seals the crystallization channel and the base plate seals the jacket channel. The crystallization channel has 6 access points (one main inlet, one main outlet and four intermediate inlets/outlets) and comprises a volume of approximately 71 mL (operational volume). The dimensions of each inter-constriction cell are presented in **Figure 7.1 (b)**.

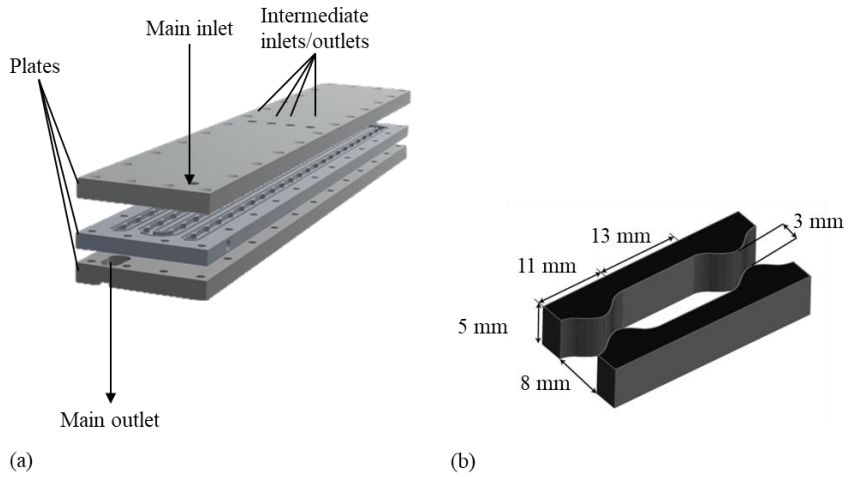


Figure 7.1 – Plate-like planar-OFC. (a) Three stacked plates. (b) Dimensions of each inter-constriction cell.

Two separate circuits of cooling/heating water were connected to the planar-OFC: cold water thermostated at 5 °C by a cooling bath (Ministat 125, Huber), and hot water thermostated at 55 °C by a heating bath (Ministat 125, Huber). Each circuit was controlled by two 3-way valves.

7.2.3 Experimental Procedure

The experimental set-up is presented in **Figure 7.2**. Five aqueous solutions of paracetamol with different concentrations (19.17, 20.45, 22.37, 24.28 and 25.56 g of paracetamol/kg of water), corresponding to five supersaturation levels (1.50, 1.60, 1.75, 1.90 and 2.00, corresponding to the saturation temperatures of 34, 36, 39, 42 and 43 °C, respectively) were prepared by dissolving an appropriate amount of paracetamol (3.83, 4.09, 4.47, 4.86 and 5.11 g, respectively) in 200 g of ultrapure water in a 250 mL flask. The solutions were stirred at 200 rpm and kept at 55 °C on a hotplate stirrer for 1 hour. Initially, the circuit of hot water was opened and the circuit of cold water was closed. The hot water was circulated in the jacket channel to keep the crystallization channel at 45.0±0.5 °C. The aqueous solution of paracetamol was pumped from the flask into the crystallization channel by a peristaltic pump (BT300-2J, Longer Pump) and recirculated back to the flask to eliminate the air bubbles. When the crystallization channel was completely free from air bubbles, the recirculation was stopped. Then, the circuit of hot water was closed and the circuit of cold water was opened. The cold water was circulated in the jacket channel to reduce the temperature in the crystallization channel. The concentration of paracetamol in the mother liquor was measured at 247 nm by an attenuated total reflectance (ATR) immersion probe (Katana 6, Hellma) connected to an UV/Vis spectrometer (SPEC RES+ UV/VIS-Sarspec), which was placed at the first intermediate inlet of the crystallizer, and the temperature of the mother liquor was recorded by a Pt100 thermometer (HD 9214, Delta OHM), which was placed at the third intermediate inlet of the crystallizer. When

the temperature in the crystallization channel reached 25 °C, the circuit of cold water was closed, and then, the temperature in the crystallization channel was allowed to further decrease to 20.0±0.5 °C. When the temperature in the crystallization channel finally reached 20.0±0.5 °C, the oscillation was activated at a predefined frequency, f, and amplitude of oscillation, x_0. The oscillation was provided by a linear motor (H01-23x166/80, LinMot) actuating a piston with a diameter of 10.3 mm. The onset of nucleation was detected due to the sudden drop in the concentration of paracetamol in the mother liquor measured by the ATR-UV/Vis probe. The results obtained from the ATR-UV/Vis probe matched quite well the detection of the first crystals by naked eye observation. Shortly after the onset of nucleation, the circuit of hot water was opened and the suspension was recirculated in the crystallization channel. When all the crystals were dissolved, the solution was kept in recirculation for more 30 min at 45.0±0.5 °C. After that, a new experiment was started. Each experimental condition was replicated 14 more times, totalizing 15 runs for each experimental condition. Finally, the nucleation rate was calculated as described in the previous section. This set of experiments was then repeated for the other four supersaturation levels, and both the kinetic and thermodynamic parameters were estimated as described in the previous section. Finally, the kinetic and the thermodynamic parameters were obtained for different combinations of frequency and amplitude of oscillation.

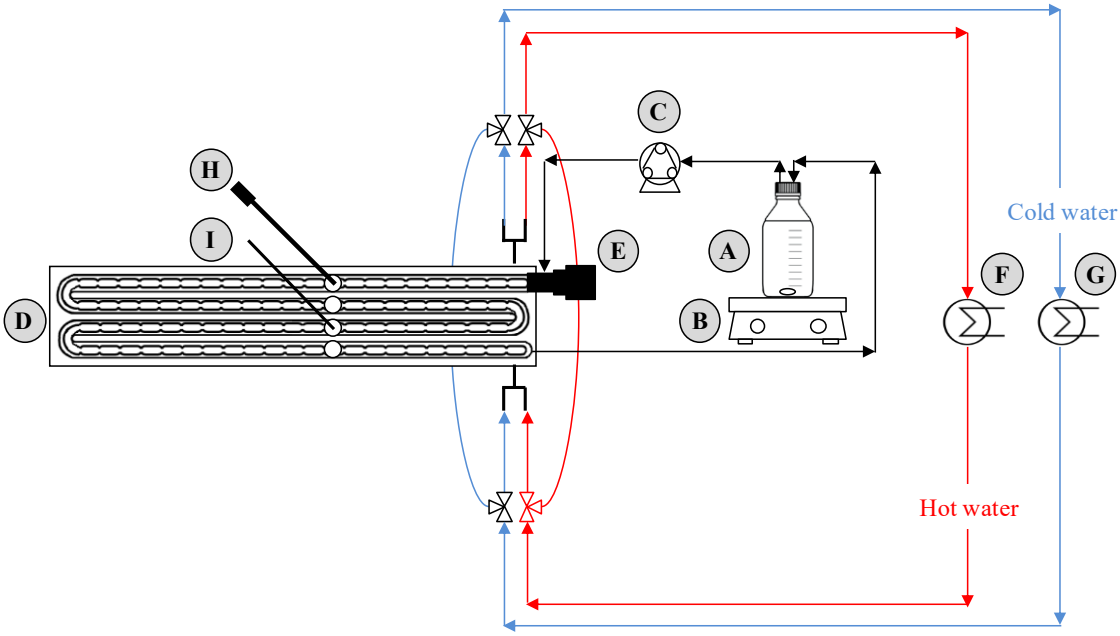


Figure 7.2 – Experimental set-up for the determination of the nucleation kinetics. A – aqueous solution of paracetamol; B – hotplate stirrer; C – peristaltic pump; D – planar-OFC; E – linear motor; F – heating bath; G – cooling bath; H – ATR-UV/Vis immersion probe; I – Pt100 thermometer.

7.2.4 Design of Experiments

A full factorial design with two center points was created in Minitab® to investigate the effects of the frequency and amplitude of oscillation on the kinetic and thermodynamic parameters of nucleation. Each factor was tested at two levels: 3 and 6 Hz for the frequency, and 6 and 12 mm (center-to-peak in the straight section) for the amplitude. The center points were set halfway between the low and high levels of each factor, in this case f =4.5 Hz and x_0=9 mm. Then, an extra experimental condition, in this case f =4 Hz and x_0=10 mm, was tested. In total, 525 single detection time experiments were performed (4 factorial points, plus 2 center points and 1 test point equals 7 experimental conditions; each experimental condition was tested at 5 supersaturation levels; each supersaturation level was replicated 15 times; totalizes 7×5×15=525 experiments).

7.3 Results and Discussion

7.3.1 Determination of the Detection Time

In this work, the onset of nucleation was detected by ATR-UV/Vis spectroscopy. ATR probes had already been used to detect the onset of nucleation in many previous works.[32–39] In most works, the detection time measured by the ATR probe was similar to the detection time measured by naked eye observation[33,34] or alternative technologies, such as focused beam reflectance measurement (FBRM),[33–35] *in situ* video imaging (invasive),[36] bulk video imaging (noninvasive),[37] and turbidity measurements.[38,39] **Figure 7.3** illustrates how the detection time was obtained from the experimental data. The detection time is the time interval between the achievement of constant supersaturation and the detection of the onset of nucleation. In this work, the supersaturation became constant when the temperature of the mother liquor reached 20.0±0.5 °C, represented as t_0 in **Figure 7.3**, and the onset of nucleation was detected as a sudden drop in the concentration of paracetamol, represented as t_d in **Figure 7.3**. Therefore, the detection time is the time interval between t_0 and t_d. This procedure was replicated 15 times for each supersaturation level, for all the four possible combinations of frequency and amplitude of oscillation of a two-level full factorial design with two factors (2^2).

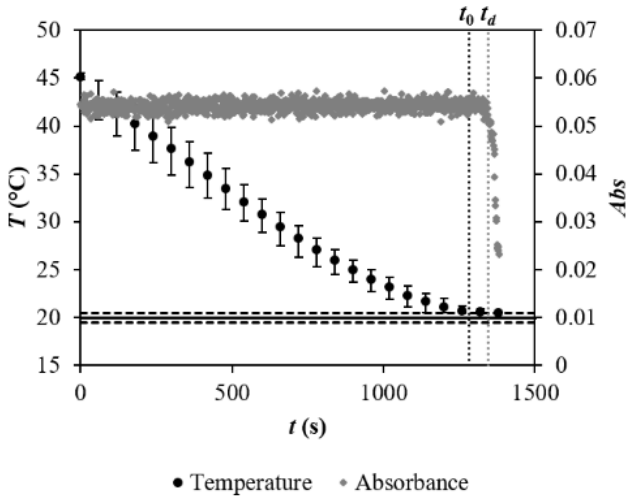


Figure 7.3 – Evolution of the temperature and absorbance over time. t_0 is the moment when the temperature reaches 20.0±0.5 °C, and t_d is the moment when the ATR-UV/Vis probe detects a sudden drop in the concentration of paracetamol, corresponding to the onset of nucleation.

7.3.2 Effect of the Oscillation Conditions on the Detection Time

Figure 7.4 presents de mean detection time, $\bar{t}_d$, as a function of supersaturation for each experimental condition. The error bars display the dispersion of detection times between the minimum and maximum detection times of 15 replicates.

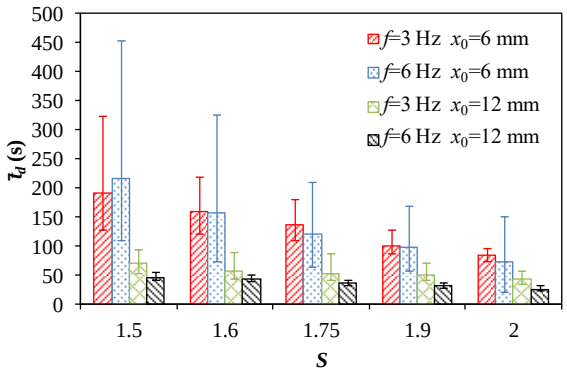


Figure 7.4 – Mean detection time as a function of supersaturation for each experimental condition.

Figure 7.4 shows that the dispersion of detection times between replicates is significant. This result suggests that a deterministic approach based on a single measurement of the detection time could potentially lead to ambiguous conclusions. The dispersion of detection times is due to the stochastic nature of nucleation, which is

coherent with the assumption of a single nucleus mechanism. Actually, Kadam *et al*.[8] had already reported that paracetamol crystallizes from water through a single nucleus mechanism.

The mean detection time and the dispersion of detection times are related to the nucleation rate. This is because the probability that nucleation occurs within a certain time interval increases as the nucleation rate increases.[4] **Figure 7.4** shows that both the mean detection time and the dispersion of detection times decrease as the amplitude increases from x_0=6 mm to x_0=12 mm at both f=6 Hz and f=12 Hz. Similarly, both the mean detection time and the dispersion of detection times decrease as the frequency increases from f=6 Hz to f=12 Hz at x_0=12 mm. On the other hand, while the mean detection time is very similar for f=3 Hz and f=6 Hz at x_0=6 mm, the dispersion of detection times is considerably larger for f=6 Hz. In addition, **Figure 7.4** also shows that the amplitude seems to have a stronger effect on the detection time than the frequency, particularly at lower supersaturations. Therefore, the nucleation rate should be the highest with f=6 Hz and x_0=12 mm, followed by f=3 Hz and x_0=12 mm, f=3 Hz and x_0=6 mm, and, finally, f=6 Hz and x_0=6 mm.

Figure 7.5 presents the probability distributions of detection times for each experimental condition. The results presented in this figure corroborate the previous observations regarding the effect of the frequency and amplitude on the detection time and dispersion of detection times.

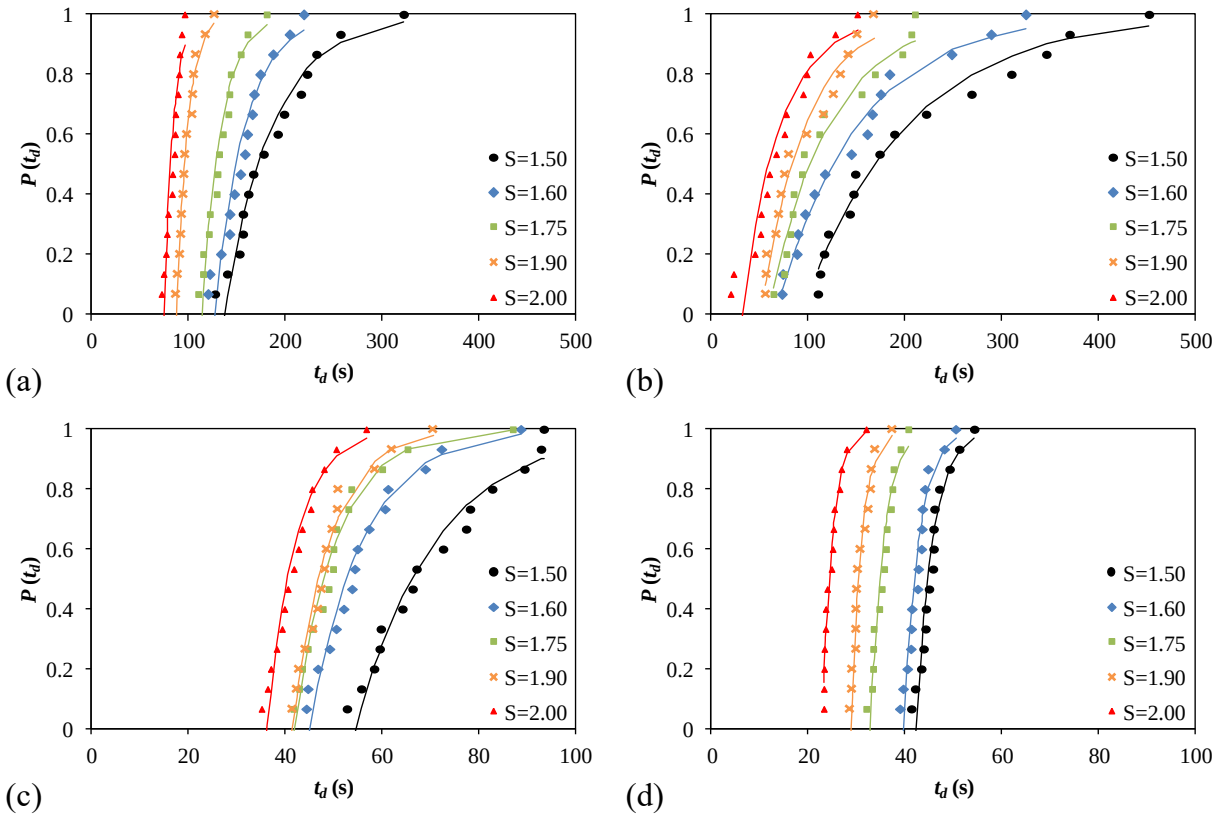


Figure 7.5 – Probability distribution of detection times at (a) f=3 Hz and x_0=6 mm; (b) f=6 Hz and x_0=6 mm; (c) f=3 Hz and x_0=12 mm; (d) f=6 Hz and x_0=12 mm.

7.3.3 Effect of the Oscillation Conditions on the Growth Time

Equation (7.6) was linearized and fitted to the experimental data presented in **Figure 7.5** to get an estimate of t_g and J. **Figure 7.6 (a)** presents the growth time, t_g, as a function of supersaturation for each experimental condition. This figure shows that the growth time decreases as both the frequency and the amplitude increase. In addition, it also shows that the growth time decreases as the supersaturation increases. The growth time accounts for the time needed for the first single nucleus to grow to a particular size, the time needed for the first single crystal undergo secondary nucleation, and the time needed for the secondary nuclei to grow until a significant decrease in the concentration of paracetamol is detected.[7] In a previous work, we have found that attrition is one of the main sources of secondary nuclei in an OFC.[40] Therefore, on the one hand, since the growth rate increases as the supersaturation increases, increasing the supersaturation decreases the time needed for the single nucleus to grow to its attrition size and the time needed for the attrition fragments to grow until a significant decrease in the concentration of paracetamol is detected; on the other hand, since the attrition rate increases as the oscillation intensity increases, increasing the frequency or the amplitude of oscillation decreases the time needed for the first single crystal undergo attrition.

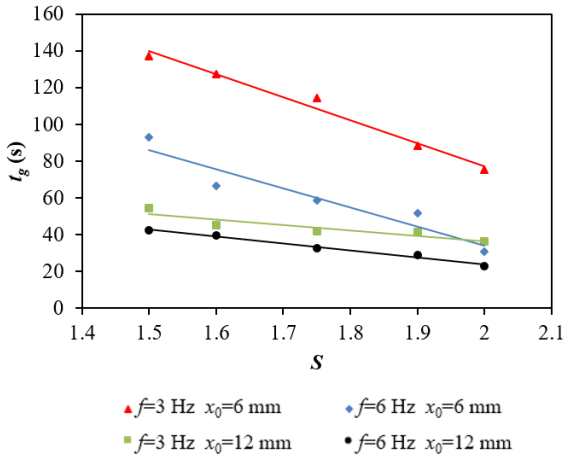


Figure 7.6 – Growth time as a function of supersaturation for each experimental condition.

7.3.4 Effect of the Oscillation Conditions on the Nucleation Rate

In **Figure 7.7**, J is plotted as function of S, and $\ln(J/S)$ is plotted as a function of $1/\ln^2 S$ for each experimental condition. The kinetic parameter A and the thermodynamic parameter B were estimated from the intercept and the slope of $\ln(J/S)$ vs $1/\ln^2 S$, respectively. The results are presented in **Table 7.1**.

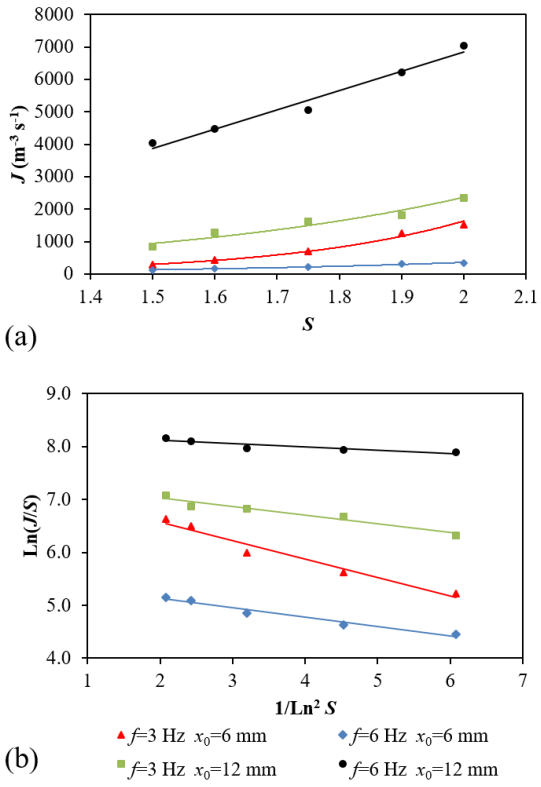


Figure 7.7 – (a) J as a function of S and (b) ln(J/S) as a function of 1/Ln^2 S for each experimental condition.

The oscillatory Reynolds number, $\mathrm{Re_o}$, and the Strouhal number, St, that characterize each experimental condition are also presented in **Table 7.1**. $\mathrm{Re_o}$ and St were calculated based on the hydraulic diameter, D_h, defined as:

$$D_h = 4\frac{A_{cs}}{P_{cs}} \tag{7.9}$$

where A_{cs} is the cross-sectional area of the channel and P_{cs} is the wetted perimeter of the cross-section.

Table 7.1 – Results obtained from the experimental data for each experimental condition.

	f (Hz)	x_0 (mm)	Re_o	St	A (m^{-3} s^{-1})	B	γ_{ef} (mJ m^{-2})	φ
Factorial points	3	6	696	0.08	1448	0.35	3.32	0.12
	6	6	1392	0.08	241	0.18	2.66	0.09
	3	12	1392	0.04	1566	0.16	2.56	0.09
	6	12	2784	0.04	3776	0.06	1.85	0.06
Center points	4.5	9	1566	0.05	1843	0.18	2.66	0.09
	4.5	9	1566	0.05	1985	0.19	2.71	0.09
Test point	4	10	1547	0.05	1662	0.20	2.76	0.10

7.3.5 Effect of the Oscillation Conditions on the Kinetic Parameter

Theoretical estimations of the kinetic parameter, A, are in the order of 10^{30} m^{-3} s^{-1}, plus or minus a few orders of magnitude, for homogeneous nucleation, and 10^{10}-10^{20} m^{-3} s^{-1} for heterogeneous nucleation.[41] Although the values of A that were obtained in this work (241-3776 m^{-3} s^{-1}) are very low in comparison to theoretical estimations, Kadam *et al*.[5] have reported similar values (1000-2900 m^{-3} s^{-1}) for the cooling crystallization of paracetamol from aqueous solutions. These low values of A suggest that heterogeneous nucleation should be the dominant nucleation mechanism in this work. The pre-exponential term from equation (7.8), AS, depends on the Zeldovich factor, z, which accounts for the probability of clusters that are larger than the critical nucleus size to dissolve rather than grow, the attachment frequency, f^*, and the concentration of active nucleation sites, C_0, as defined by:

$$AS = zf^*C_0 \qquad \textbf{(7.10)}$$

Therefore, since z is expected to remain constant, either a low attachment frequency or a low concentration of active nucleation sites (heterogeneous particles) could explain the low values of A that were obtained in this work.

The combination of high levels of frequency and amplitude (f=6 Hz and x_0=12 mm) generated the highest A (3776 m^{-3} s^{-1}). This was rather anticipated as higher mixing intensities are expected to provide higher attachment frequencies and also lower energy barriers for diffusion or desolvation.[23] However, the combination of low levels of frequency and amplitude (f=3 Hz and x_0=6 mm) did not generate the lowest A. The lowest A (241 m^{-3} s^{-1}) was generated by the combination of a high level of frequency and a low level of amplitude (f=6 Hz and x_0=6 mm). This result follows the results previously reported for the effect of the oscillation conditions on the suspension of solids (**Chapter 4**). When high levels of frequency are combined with low levels of amplitude two distinct zones are created in the crystallizer: one zone with high mixing intensity close to the constrictions, and another zone with very low mixing intensity in the center of the straight section. Visual inspection of this phenomenon showed that with such combinations of frequency and amplitude the vortices do not have time to distort and expand before the direction of the flow is reversed, which creates stagnant zones. This seems to explain the results obtained in this work: the formation of stagnant zones decreased the overall mixing intensity in the crystallizer, which resulted in lower values of A. Interestingly, the combination of a high level of frequency and a low level of amplitude (f=6 Hz and x_0=6 mm) and the combination of a low level of frequency and a high level of amplitude (f=3 Hz and x_0=12 mm), which are characterized by the same Re_o, generated distinct values of A (241 and 1566 m^{-3} s^{-1}, respectively), which suggests that the effects of the frequency and amplitude should be assessed individually, and not condensed as Re_o.

7.3.6 Effect of the Oscillation Conditions on the Thermodynamic Parameter

The thermodynamic parameter, B, accounts for the free energy barrier for the formation of the new phase and is expressed as:

$$B = \frac{4}{27}\frac{c^3 v^2 \gamma_{ef}^3}{k^3 T^3} \quad \textbf{(7.11)}$$

where c is the shape factor ($c = (36\pi)^{1/3}$ for spheres), v is the molecular volume of the crystalline phase (1.94×10^{-28} m^3 for paracetamol[42]), γ_{ef} is the effective interfacial energy for heterogeneous nucleation, k is the Boltzmann constant (1.38×10^{-23} J K^{-1}) and T is the temperature in K (in this case 293.15 K). The effective interfacial energy for heterogeneous nucleation was estimated from **Equation (7.11)** using the obtained values of B. The results are presented in **Table 7.1**. The effective interfacial energies obtained in this work (1.85-3.32 mJ m^{-2}) agree reasonably well with the value previously reported by Omar *et al.*[43] for the solid-liquid interfacial energy of paracetamol in water (2.91±1.17 mJ m^{-2}).

The effective interfacial energy for heterogeneous nucleation, γ_{ef}, is related to the theoretical interfacial energy for homogeneous nucleation, γ, by the activity factor, φ, as defined by:

$$\varphi = \frac{\gamma_{ef}}{\gamma} \quad \textbf{(7.12)}$$

where $0 < \varphi < 1$. The activity factor accounts for the reducing effect of heterogeneous particles on the interfacial energy between the solid and the liquid, as compared to homogeneous nucleation. The theoretical interfacial energy for homogeneous nucleation was calculated using Mersmann's equation,[44] which establishes a relation between solubility and the interfacial energy, with a corrected shape factor of 0.514 for spherical nuclei,[31] as defined by:

$$\gamma = 0.514kT\frac{1}{v^{2/3}}\ln\frac{1}{N_a v C^*} \quad \textbf{(7.13)}$$

where N_a is the Avogadro constant (6.023×10^{23} mol^{-1}) and C^* is the molar solubility (85 mol m^{-3} in the case of an aqueous solution of paracetamol at 20 °C). A theoretical interfacial energy for homogenous nucleation of γ=29 mJ m^{-2} was obtained. Then, the activity factor was calculated from **Equation (7.12)**. The results are presented in **Table 7.1**. The low values of γ_{ef} (1.85-3.32 mJ m^{-2}) as compared to γ (29 mJ m^{-2}), which resulted in low values of φ (0.06-0.12), confirm that heterogeneous nucleation should be the dominant mechanism in this work.

The combination of high levels of frequency and amplitude (f=6 Hz and x_0=12 mm) generated the lowest B (0.06), whereas the combination of low levels of frequency and amplitude (f=3 Hz and x_0=6 mm) generated the highest B (0.35). The other two combinations generated intermediate values of B (0.16 and 0.18). From a theoretical point of view, B should be independent of the oscillation conditions, so, the variation between

different combinations of frequency and amplitude should be due to errors associated to the determination of the nucleation rate. A possible source of errors is the assumption that t_g is equal in all replicates. This is because besides crystal growth, which is essentially deterministic, t_g also covers secondary nucleation, which is not deterministic. Therefore, assuming that t_g is equal in all replicates might have introduced errors into the estimation of the nucleation rate, the extent of which depends on the impact of each combination of frequency and amplitude on the probability of secondary nucleation for each supersaturation level.

7.3.7 Model development

A model was developed to predict the value of the kinetic parameter as a function of the frequency and amplitude of oscillation. A similar model was not developed for the thermodynamic parameter as it should be independent of the oscillation conditions. A first order model was formulated to describe the relationship between the response, A, and the two factors, f and x_0. The terms of a first order model are either linear or an interaction between factors and have an associated coefficient that delivers the best fit between the model and the experimental data, as described by:

$$A = \beta_0 + \beta_1 f + \beta_2 x_0 + \beta_{12} f x_0 \quad \textbf{(7.14)}$$

where β_0 is a constant, β_1 and β_2 are linear coefficients, and β_{12} is an interaction coefficient. **Table 7.2** presents the coefficients and the coefficient of determination, R^2, and **Figure 7.8** shows the quality of the fit of the model to the experimental data.

Table 7.2 – Coefficients and coefficient of determination.

β_0 (m^{-3} s^{-1})	β_1 (m^{-3})	β_2 (m^{-3} s^{-1} mm^{-1})	β_{12} (m^{-3} s^{-1} mm^{-1})	R^2
6006	-1541	-549.8	189.8	99.35

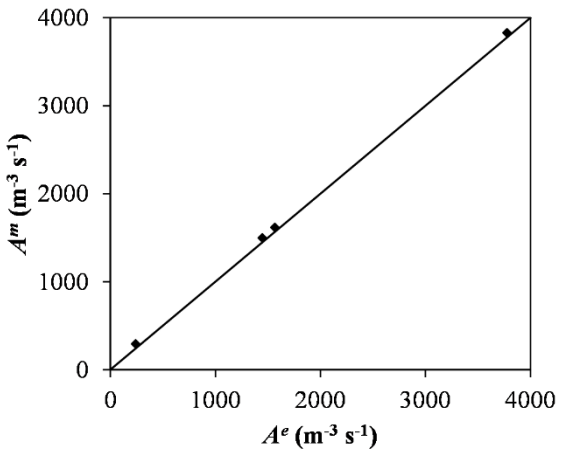


Figure 7.8 – Comparison of A obtained from the model, A^m, and obtained experimentally, A^e.

The two-level full factorial design was augmented with two center points to test for the curvature of the response. The results obtained for the center points are presented in **Table 7.1**. The curvature is considered significant when the p-value for curvature is less than or equal to a suitable significance level, typically 5 %. The p-value for curvature measures the evidence against the null hypothesis, which states that all the relationships between the factors and the response are linear.[45] In this work, a p-value for curvature of p-value=0.323 was obtained. This value is extremely high, and well above the typical significance level of 5%, which suggests that there is no evidence of curvature.

The main effects plot is presented in **Figure 7.9**. The main effects plot displays the average response, $\bar{A}$, for each level of frequency and amplitude. **Figure 7.9** shows that A increases as both the frequency and the amplitude increase. It also shows that the main effect of the amplitude is clearly stronger than the main effect of the frequency.

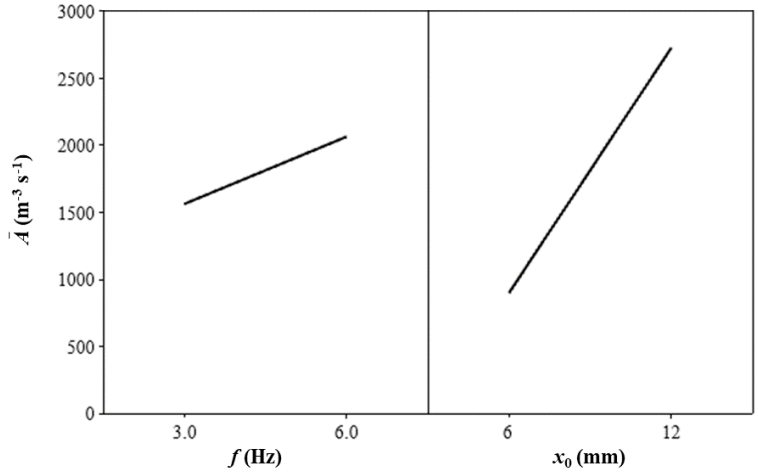


Figure 7.9 – Main effects plot for A.

The interaction plot is presented in **Figure 7.10**. The interaction plot displays one line for the mean response for each level of frequency at x_0=6 mm, and another line at x_0=12 mm. **Figure 7.10** shows that the interaction between the frequency and the amplitude is represented by non-parallel lines, which suggests a strong interaction between the two factors.

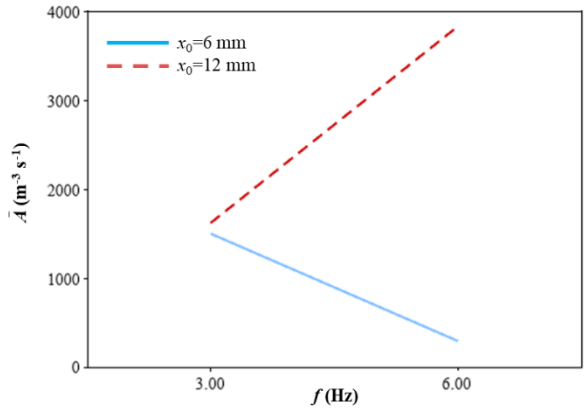


Figure 7.10 – Interaction plot between f and x_0 for A.

The contour plot is presented in **Figure 7.11**. The contour plot displays a two-dimensional map in which points with the same response are connected by contour lines. **Figure 7.11** shows that, when high frequencies are combined with high amplitudes, high values of A are generated, which results in high nucleation rates. Therefore, these oscillation conditions should be preferred to produce a large number of small crystals. **Figure 7.11** also shows that, when high frequencies are combined with low amplitudes, low values of A are generated, which results in low nucleation rates. Therefore, these oscillation conditions should be preferred to produce a small number of large crystals. Nevertheless, such combinations of frequency and amplitude can result in the formation of poor mixing zones and lead to fouling, or even clogging, in the crystallizer, which should be avoided. Therefore, to avoid these problems and still generate low nucleation rates, low amplitudes should be combined with slightly lower frequencies (f<5 Hz).

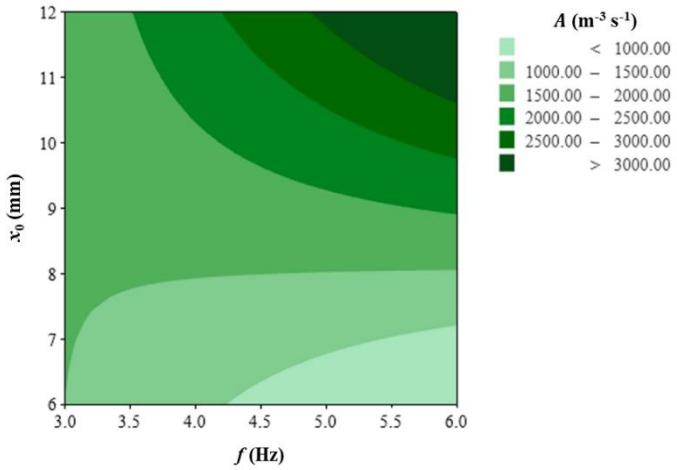


Figure 7.11 – Contour plot.

One additional experimental condition, in this case f=4 Hz and x_0=10 mm, was tested in order to access the capability of the model to predict A for a given combination of frequency and amplitude. The results obtained for the test point are presented in **Table 7.1**. **Table 7.3** presents the prediction, the prediction interval, and the experimental result for the test point. The prediction interval represents a range of likely values for a single new observation. The experimental result is contained within the prediction interval of the model, which confirms its validity.

Table 7.3 – Prediction, prediction interval and experimental result for the test point.

f (Hz)	x_0 (mm)	Prediction (m^{-3} s^{-1})	95% Prediction interval (m^{-3} s^{-1})	Experimental result (m^{-3} s^{-1})
4	10	1935.75	(1240.37; 2631.13)	1662

7.4 Conclusion

The isothermal method was employed to study the effect of the oscillation conditions on the nucleation kinetics for the isothermal batch crystallization of paracetamol from aqueous solutions in a planar-OFC. As anticipated, it was found that the oscillation conditions have a significant impact on the nucleation rate. This impact is essentiality due to the effect of the oscillation conditions on the kinetic parameter, A, which is related to the attachment frequency, and not so much due to their effect on the thermodynamic parameter, B, which, by definition, should be independent of the oscillation conditions. It was also found that A increases as the amplitude increases at both low and high frequencies. A also increases as the frequency increases at high amplitudes, but it decreases at low amplitudes. These results enabled the identification of optimal oscillation

conditions according to the desired final product properties. On the one hand, when a large number of small crystals are desired, high frequencies should be combined with high amplitudes to generate high nucleation rates. On the other hand, when a small number of large crystals are desired, intermediate to high frequencies should be combined with low amplitudes to generate low nucleation rates.

Notation

Acronyms

API	Active pharmaceutical ingredient
ATR	Attenuated total reflectance
CSD	Crystal size distribution
ECTFE	Ethylene-chlorotrifluoroethylene copolymer
FBRM	Focused beam reflectance measurement
MSZW	Metastable zone width
OFC	Oscillatory flow crystallizer
STC	Stirred tank crystallizer

Latin symbols

A	Nucleation kinetic parameter
$\bar{A}$	Average nucleation kinetic parameter
A^e	Nucleation kinetic parameter obtained experimentally
A^m	Nucleation kinetic parameter obtained from the model
A_{cs}	Channel cross-sectional area
B	Nucleation thermodynamic parameter
c	Shape factor
C^*	Molar solubility
C_0	Concentration of active nucleation sites
D_h	Hydraulic diameter
f	Frequency of oscillation
f^*	Attachment frequency
J	Nucleation rate
k	Boltzmann constant
m	Number of nuclei
M	Total number of experiments
$M^+(t)$	Number of experiments in which nucleation occurred at time t_d
N_a	Avogadro constant
$N(t)$	Average number of nuclei formed in the time interval t
P_{cs}	Channel cross-sectional wetted perimeter
P_0	Probability of finding no nuclei within a time interval
$P_{\geq 1}$	Probability of finding at least 1 nucleus within a time interval
P_m	Probability of finding m nuclei within a time interval
$P(t)$	Probability distribution of detection times
R^2	Coefficient of determination
S	Supersaturation ratio
t	Time
t_0	Time when the temperature of the mother liquor reached 20.0±0.5 °C
t_d	Detection time
t_g	Growth time
$\bar{t_d}$	Mean detection time
T	Temperature
v	Molecular volume of the crystalline phase
V	Volume
x_0	Center-to-peak amplitude of oscillation
z	Zeldovich factor

Greek Letters

β_0	Average response for all observations
β_1 and β_2	Linear coefficients
β_{12}	Two-way interaction coefficient
γ	Theoretical interfacial energy for homogeneous nucleation
γ_{ef}	Effective interfacial energy for heterogeneous nucleation
φ	Activity factor

Dimensionless Numbers

$\mathrm{Re_o}$	Oscillatory Reynolds number
St	Strouhal number

References

(1) Mullin, J. W. *Crystallization*, 4th ed.; Butterworth-Heinemann: Oxford, 2001.

(2) Myerson, A. S. *Handbook of Industrial Crystallization*, 2nd ed.; Butterworth-Heinemann: Boston, 2002.

(3) Xiao, Y.; Wang, J.; Huang, X.; Shi, H.; Zhou, Y.; Zong, S.; Hao, H.; Bao, Y.; Yin, Q. Determination Methods for Crystal Nucleation Kinetics in Solutions. *Cryst. Growth Des.* **2018**, *18* (1), 540–551.

(4) Brandel, C.; ter Horst, J. H. Measuring Induction Times and Crystal Nucleation Rates. *Faraday Discuss.* **2015**, *179*, 199–214.

(5) Kadam, S. S.; Kulkarni, S. A.; Coloma Ribera, R.; Stankiewicz, A. I.; ter Horst, J. H.; Kramer, H. J. M. A New View on the Metastable Zone Width during Cooling Crystallization. *Chem. Eng. Sci.* **2012**, *72*, 10–19.

(6) Kulkarni, S. A.; Kadam, S. S.; Meekes, H.; Stankiewicz, A. I.; ter Horst, J. H. Crystal Nucleation Kinetics from Induction Times and Metastable Zone Widths. *Cryst. Growth Des.* **2013**, *13* (6), 2435–2440.

(7) Jiang, S.; ter Horst, J. H. Crystal Nucleation Rates from Probability Distributions of Induction Times. *Cryst. Growth Des.* **2011**, *11* (1), 256–261.

(8) Kadam, S. S.; Kramer, H. J. M.; ter Horst, J. H. Combination of a Single Primary Nucleation Event and Secondary Nucleation in Crystallization Processes. *Cryst. Growth Des.* **2011**, *11* (4), 1271–1277.

(9) Sullivan, R. A.; Davey, R. J.; Sadiq, G.; Dent, G.; Back, K. R.; ter Horst, J. H.; Toroz, D.; Hammond, R. B. Revealing the Roles of Desolvation and Molecular Self-Assembly in Crystal Nucleation from Solution: Benzoic and p -Aminobenzoic Acids. *Cryst. Growth Des.* **2014**, *14* (5), 2689–2696.

(10) Mealey, D.; Zeglinski, J.; Khamar, D.; Rasmuson, Å. C. Influence of Solvent on Crystal Nucleation of Risperidone. *Faraday Discuss.* **2015**, *179*, 309–328.

(11) Mealey, D.; Croker, D. M.; Rasmuson, Å. C. Crystal Nucleation of Salicylic Acid in Organic Solvents. *CrystEngComm* **2015**, *17* (21), 3961–3973.

(12) Kakkar, S.; Devi, K. R.; Svärd, M.; Rasmuson, Å. Crystal Nucleation of Salicylamide and a Comparison with Salicylic Acid. *CrystEngComm* **2020**, *22* (19), 3329–3339.

(13) Kubota, N. Analysis of the Effect of Volume on Induction Time and Metastable Zone Width Using a Stochastic Model. *J. Cryst. Growth* **2015**, *418*, 15–24.

(14) Steendam, R. R. E.; Keshavarz, L.; Blijlevens, M. A. R.; de Souza, B.; Croker, D. M.; Frawley, P. J. Effects of Scale-Up on the Mechanism and Kinetics of Crystal Nucleation. *Cryst. Growth Des.* **2018**, *18* (9), 5547–5555.

(15) Jiang, M.; Braatz, R. D. Designs of Continuous-Flow Pharmaceutical Crystallizers: Developments and Practice. *CrystEngComm* **2019**, *21* (23), 3534–3551.

(16) McGlone, T.; Briggs, N. E. B.; Clark, C. A.; Brown, C. J.; Sefcik, J.; Florence, A. J. Oscillatory Flow Reactors (OFRs) for Continuous Manufacturing and Crystallization. *Org. Process Res. Dev.* **2015**, *19* (9), 1186–1202.

(17) Ni, X.; Liao, A. Effects of Cooling Rate and Solution Concentration on Solution Crystallization of L-Glutamic Acid in an Oscillatory Baffled Crystallizer. *Cryst. Growth Des.* **2008**, *8* (8), 2875–2881.

(18) Ni, X.; Liao, A. Effects of Mixing, Seeding, Material of Baffles and Final Temperature on Solution Crystallization of l-Glutamic Acid in an Oscillatory Baffled Crystallizer. *Chem. Eng. J.* **2010**, *156* (1), 226–233.

(19) Brown, C. J.; Ni, X.-W. Determination of Metastable Zone Width, Mean Particle Size and Detectable Number Density Using Video Imaging in an Oscillatory Baffled Crystallizer. *CrystEngComm* **2012**, *14* (8), 2944.

(20) Brown, C. J.; Lee, Y. C.; Nagy, Z. K.; Ni, X. Evaluation of Crystallization Kinetics of Adipic Acid in an Oscillatory Baffled Crystallizer. *CrystEngComm* **2014**, *16* (34), 8008.

(21) Jiang, M.; Ni, X.-W. Effects of Solvents and Impurity on Crystallization Kinetics and Crystal Properties in a Reactive Crystallization of Paracetamol. *J. Cryst. Growth* **2019**, *523*, 125150.

(22) Cruz, P.; Rocha, F.; Ferreira, A. Effect of Operating Conditions on Batch and Continuous Paracetamol Crystallization in an Oscillatory Flow Mesoreactor. *CrystEngComm* **2016**, *18* (47), 9113–9121.

(23) Yang, H.; Yu, X.; Raval, V.; Makkawi, Y.; Florence, A. Effect of Oscillatory Flow on Nucleation Kinetics of Butyl Paraben. *Cryst. Growth Des.* **2016**, *16* (2), 875–886.

(24) Siddique, H.; Brown, C. J.; Houson, I.; Florence, A. J. Establishment of a Continuous Sonocrystallization Process for Lactose in an Oscillatory Baffled Crystallizer. *Org. Process Res. Dev.* **2015**, *19* (12), 1871–1881.

(25) Brown, C. J.; Adelakun, J. A.; Ni, X.-W. Characterization and Modelling of Antisolvent Crystallization of Salicylic Acid in a Continuous Oscillatory Baffled Crystallizer. *Chem. Eng. Process. Process Intensif.* **2015**, *97*, 180–186.

(26) Ferreira, A.; Rocha, F.; Teixeira, J. A.; Castro, F. Modular Oscillatory Flow Plate Reactor. WO 2017/175207 A1, 2017.

(27) Agnew, L. R.; McGlone, T.; Wheatcroft, H. P.; Robertson, A.; Parsons, A. R.; Wilson, C. C. Continuous Crystallization of Paracetamol (Acetaminophen) Form II: Selective Access to a Metastable Solid Form. *Cryst. Growth Des.* **2017**, *17* (5), 2418–2427.

(28) Briggs, N. E. B. B.; Schacht, U.; Raval, V.; McGlone, T.; Sefcik, J.; Florence, A. J. Seeded Crystallization of β-L-Glutamic Acid in a Continuous Oscillatory Baffled Crystallizer. *Org. Process Res. Dev.* **2015**, *19* (12), 1903–1911.

(29) Peña, R.; Oliva, J. A.; Burcham, C. L.; Jarmer, D. J.; Nagy, Z. K. Process Intensification through Continuous Spherical Crystallization Using an Oscillatory Flow Baffled Crystallizer. *Cryst. Growth Des.* **2017**, *17* (9), 4776–4784.

(30) Krishnan, V. *Probability and Random Processes*; John Wiley & Sons, Inc: New Jersey, 2006.

(31) Kashchiev, D.; van Rosmalen, G. M. Review: Nucleation in Solutions Revisited. *Cryst. Res. Technol.* **2003**, *38* (7–8), 555–574.

(32) Lewiner, F.; Klein, J. .; Puel, F.; Févotte, G. On-Line ATR FTIR Measurement of Supersaturation during Solution Crystallization Processes. Calibration and Applications on Three Solute/Solvent Systems. *Chem. Eng. Sci.* **2001**, *56* (6), 2069–2084.

(33) Nagy, Z. K.; Fujiwara, M.; Woo, X. Y.; Braatz, R. D. Determination of the Kinetic Parameters for the Crystallization of Paracetamol from Water Using Metastable Zone Width Experiments. *Ind. Eng. Chem. Res.* **2008**, *47* (4), 1245–1252.

(34) Fujiwara, M.; Chow, P. S.; Ma, D. L.; Braatz, R. D. Paracetamol Crystallization Using Laser Backscattering and ATR-FTIR Spectroscopy: Metastability, Agglomeration, and Control. *Cryst. Growth Des.* **2002**.

(35) O'Grady, D.; Barrett, M.; Casey, E.; Glennon, B. The Effect of Mixing on the Metastable Zone Width and Nucleation Kinetics in the Anti-Solvent Crystallization of Benzoic Acid. *Chem. Eng. Res. Des.* **2007**, *85* (7), 945–952.

(36) Gherras, N.; Fevotte, G. Comparison between Approaches for the Experimental Determination of Metastable Zone Width: A Case Study of the Batch Cooling Crystallization of Ammonium Oxalate in Water. *J. Cryst. Growth* **2012**, *342* (1), 88–98.

(37) Simon, L. L.; Nagy, Z. K.; Hungerbuhler, K. Comparison of External Bulk Video Imaging with Focused

Beam Reflectance Measurement and Ultra-Violet Visible Spectroscopy for Metastable Zone Identification in Food and Pharmaceutical Crystallization Processes. *Chem. Eng. Sci.* **2009**, *64* (14), 3344–3351.

(38) Groen, H.; Roberts, K. J. Nucleation, Growth, and Pseudo-Polymorphic Behavior of Citric Acid As Monitored in Situ by Attenuated Total Reflection Fourier Transform Infrared Spectroscopy. *J. Phys. Chem. B* **2001**, *105* (43), 10723–10730.

(39) Groen, H.; Roberts, K. J. An Examination of the Crystallization of Urea from Supersaturated Aqueous and Aqueous−Methanol Solutions as Monitored In-Process Using ATR FTIR Spectroscopy. *Cryst. Growth Des.* **2004**, *4* (5), 930–936.

(40) Cruz, P.; Rocha, F.; Ferreira, A. Determination of the Critical Mixing Intensity for Secondary Nucleation of Paracetamol in an Oscillatory Flow Crystallizer. *CrystEngComm* **2018**, *20* (6), 829–836.

(41) Lewis, A.; Seckler, M. M.; Kramer, H.; van Rosmalen, G. *Industrial Crystallization: Fundamentals and Applications*, 1st ed.; Cambridge University Press: Cambridge, 2015.

(42) Shekunov, B. Y.; Grant, D. J. W.; Latham, R. J.; Sherwood, J. N. In Situ Optical Interferometric Studies of the Growth and Dissolution Behavior of Paracetamol (Acetaminophen) Crystals. 3. Influence of Growth in the Presence of p-Acetoxyacetanilide. *J. Phys. Chem. B* **1997**, *101* (44), 9107–9112.

(43) Omar, W.; Mohnicke, M.; Ulrich, J. Determination of the Solid Liquid Interfacial Energy and Thereby the Critical Nucleus Size of Paracetamol in Different Solvents. *Cryst. Res. Technol.* **2006**, *41* (4), 337–343.

(44) Mersmann, A. Calculation of Interfacial Tensions. *J. Cryst. Growth* **1990**, *102* (4), 841–847.

(45) Montgomery, D. C. *Design and Analysis of Experiments*, 5th ed.; John Wiley & Sons, Inc.: New York, 2007.

Chapter 8 - Crystal Growth Kinetics in a Planar Oscillatory Flow Crystallizer

Reproduced from Cruz, P. C.; Rocha, F. A.; Ferreira, A. M. Crystallization of Paracetamol from Mixtures of Ethanol and Water in a Planar Oscillatory Flow Crystallizer: Effect of the Oscillation Conditions on the Crystal Growth Kinetics. CrystEngComm 2021, Advance Article, DOI: 10.1039/D1CE00858G with permission from the Royal Society of Chemistry.

https://pubs.rsc.org/en/Content/ArticleLanding/2021/CE/D1CE00858G

8.1 Introduction

Crystallization is an important separation and purification process in the manufacturing of pharmaceuticals and other fine and specialty chemicals because it defines the final product properties, including purity, polymorphism, morphology, size and crystal size distribution (CSD).[1] The crystallization process starts with the birth of a new crystalline phase. This first stage, known as nucleation, occurs when the solute molecules in a supersaturated solution aggregate into stable clusters or nuclei. Then, the crystallization process proceeds as the nuclei become larger crystals by subsequent deposition of solute. This second stage, known as crystal growth, occurs by diffusion of solute molecules from the bulk through the boundary layer to the crystal surface, followed by surface integration into the crystal surface. The relative magnitudes of nucleation and crystal growth determine the number and size of the crystals in the final product, which directly impacts the final products properties, particularly the CSD.[2] Therefore, the design and operation of industrial crystallization processes can benefit from knowing the nucleation and crystal growth kinetics.

Two types of experimental methods to measure crystal growth rates have been employed: direct methods, based on the direct measurement of the change in mass or size of a crystal, and indirect methods, based on the measurement of the concentration profile. The two most common methods are the single-crystal experiments, a direct method, and the seeded desupersaturation experiments, an indirect method.[2] Single-crystal experiments focus on individual face growth rates and are usually conducted in growth cells under the microscope. These experiments are beneficial to investigate crystal growth mechanisms. However, information extracted from such experiments might not be used in the direct design and operation of industrial crystallization processes. This is because, first, it is difficult to obtain statistically significant data from the limited number of crystals examined, and, second, because the hydrodynamic conditions in such experiments are distinct from those of industrial crystallization processes. Seeded desupersaturation experiments focus on the average crystal growth rate of a

suspension of crystals and are usually conducted in stirred tank crystallizers (STCs). These experiments allow for the determination of statistically representative average crystal growth rates for numerous crystals at industrially relevant hydrodynamic conditions. However, information related to the crystal growth mechanism is more difficult to extract.[3,4]

Paracetamol has been used as a model compound to investigate the crystal growth kinetics in several studies – **Table 8.1**. Single-crystal experiments have been performed to investigate the effects of several operating conditions, such as supersaturation,[5–8] temperature,[7,8] concentration of additives (including *p*-acetoxyacetanilide,[9] acetanilide and metacetamol[10]) and pH,[8] on the crystal growth kinetics of paracetamol. It has been often reported that changing the operating conditions alters the growth rate of different faces in the crystal to different degrees, which results in a significant impact on crystal habit. For example, Finnie *et al.*[5] observed columnar crystals with dominant {110} faces at lower supersaturations, and plate-like crystals with large {001} faces at higher supersaturations; Shekonov *et al.*[7] observed plate-like crystals with dominant {001} faces at lower temperatures, around 3 °C, and prismatic crystals with dominant {110} faces at higher temperatures, around 47 °C; Shekunov *et al.*[9] reported that the presence of *p*-acetoxyacetanilide has a more substantial influence on the {110} faces than on the others, and, as a result, needle-like crystals with dominant {110} faces are formed in the presence of this additive; finally, Thompson *et al.*[10] also reported that the presence of metacetamol has a more substantial impact on the crystal habit than acetanilide. It has also been reported that, sometimes, when exposed to constant conditions of supersaturation, temperature and hydrodynamics, different crystals of paracetamol grow at different rates. This phenomenon, known as growth rate dispersion, was reported by Finnie *et al.*[5] and Omar *et al.*.[8]

Seeded desupersaturation experiments have also been performed for paracetamol crystallization. A variety of pure solvents (water,[11] ethanol[12,13] and methanol[14]), binary mixtures (methanol-water,[15] acetone-water,[16,17] and acetone-toluene[17]), and even ternary mixtures (water-acetone-toluene[17]) were tested. Supersaturation was created by cooling in most works,[11–14,16,17] and by the addition of an antisolvent in only one work.[15] In most works, the crystal growth rate was expressed as a function of supersaturation in the form of an empirical power law equation as:[11–17]

$$G = k_g \Delta C^g \tag{8.1}$$

where G is the overall linear growth rate, k_g is the overall coefficient of crystal growth, g is the growth rate order, and ΔC is the concentration driving force, calculated as $\Delta C = C - C_s$, where C is the concentration of solute in the bulk solution, and C_s is the solubility. In some works, the relative supersaturation, $\sigma = C/C_s - 1$, replaced ΔC in the crystal growth rate equation.[11,14] In addition, in some works, the overall coefficient of crystal growth was expressed as a function of temperature by an Arrhenius-type equation as:[12–14]

$$k_g = k_{g,0} \exp\left(\frac{-E_a}{RT}\right) \tag{8.2}$$

where $k_{g,0}$ is a constant, E_a is the activation energy, R is the ideal gas constant and T is the temperature (in Kelvin). In some works, the crystal growth rate was expressed as a function of supersaturation by two mechanistic models, the Burton Cabrera Frank (BCF) model, which is usually more suitable for low to moderate supersaturations, and the Birth and Spread (B+S) model, which is generally ideal for higher supersaturations.[14,17] In some works, the crystal growth rate equations were integrated into mass balance equations,[14,16,17] or into population balance equations.[11–13,15]

Several studies were conducted to investigate the effect of initial supersaturation, temperature, seed loading and seed size on the crystal growth kinetics of paracetamol. As expected, the crystal growth rate was faster at higher supersaturations, temperatures, seed loadings and smaller seed sizes.[12,15] Other studies were conducted to explore the effect of solvent composition on the crystal growth kinetics of paracetamol. Granberg *et al.*[16] found that the crystal growth rate of paracetamol in mixtures of acetone and water correlates well with the solubility and that both exhibit a maximum at approximately 20% (w/w) of water. Granberg and Rasmuson[17] investigated the crystal growth kinetics of paracetamol in binary and ternary mixtures of water, acetone and toluene and found the lowest and highest crystal growth rates in the (0+50+50) and (70+30+0) mixtures, respectively. Ó'Ciardhá *et al.*[15] found that the crystal growth rate of paracetamol in mixtures of methanol and water decreases as the water mass fraction increases from 40% to 60%, and increases as the water mass fraction increases from 60% to 68%.

In all these studies, g ranged from approximately 1.2-1.3 in pure water[11,16] to 2.239 in a mixture of methanol and water.[15] The relatively high values of g suggest that surface integration was the rate-controlling step of crystal growth. Furthermore, E_a varied between 40.56-41.6 kJ mol^{-1} in pure ethanol[12,13] and 47.35 kJ mol^{-1} in pure methanol.[14] The relatively high values of E_a also suggest that surface integration was the rate-controlling step of crystal growth.[18] Finally, in some works, the mass transfer coefficient, k_d, was estimated to assess if the crystal growth kinetics were affected by diffusional limitations.[12–15] In all these works, the experimental growth rates were significantly lower than the predicted growth rates under diffusion control, which also suggests that surface integration was the rate-controlling step of crystal growth.

Two alternative methods have also been employed to investigate the crystal growth kinetics of paracetamol.[14,19] Nagy *et al.*[19] conducted metastable zone width experiments to estimate simultaneously the nucleation and crystal growth kinetic parameters for the cooling crystallization of paracetamol from water. These experiments were performed by spontaneous nucleation followed by crystal growth at different cooling rates and initial supersaturations. Soto *et al.*[14] conducted rotating disk experiments to measure the crystal growth rate for the cooling crystallization of paracetamol from methanol. In these experiments, several individual seed crystals were kept at constant supersaturation, and the crystal growth rate was determined for two directions simultaneously.

Crystal growth kinetic data extracted from small batch experiments are typically used to scale-up the crystallization processes from the laboratory to the industrial scale. However, the scale-up of STCs is not exactly

trivial.[20] On the other hand, other crystallizers are much simpler to scale-up. The oscillatory flow crystallizer (OFC) is one of the examples.[21] Several studies have demonstrated that OFCs can be scaled-up linearly as long as the geometric similarity is kept constant and the hydrodynamic similarity is maintained by the same dimensionless numbers.[21–25] Up to now, eight papers have reported data related to the growth kinetics of paracetamol[26–31] and other compounds in OFCs. [32,33]

In this work, the isothermal batch crystallization of paracetamol from a 40% (v/v) mixture of ethanol and water in a planar-OFC was used as model system to study the effect of the oscillation conditions on the crystal growth kinetics. The planar-OFC is a relatively new variant of OFCs where the traditional circular cross-section of conventional tubular-OFCs is replaced by a rectangular cross-section.[34] This design was developed to overcome the limitations of tubular-OFCs, where several problems related to the suspension and flowability of solids are commonly reported.[35–37] To the best of our knowledge, this is the first time that seeded desupersaturation experiments are performed in an OFC. In addition, it is also the first time that crystal growth kinetic data is reported for a planar-OFC.

Table 8.1 – Published studies on paracetamol crystal growth kinetics.

Reference	Experimental method	Supersaturation method	Crystallizer	Solvent	Temperature	K_g, k_g, $k_{g,0}$ and/or E_a	g
Brown and Ni[26]	Spontaneous nucleation followed by crystal growth	Antisolvent	OFC	Acetone-water	23 °C		
Brown and Ni[27]	Spontaneous nucleation followed by crystal growth	Antisolvent	OFC	Acetone-water	23 °C	K_g=1.7×10^{-3}-6.4×10^{-3} kg m^{-2} s^{-1}	1.570
Cornel and Mazzotti[11]	Seeded desupersaturation experiments	Cooling	STC	Water	20 °C	k_g=0.68±0.04×10^{-6} m s^{-1} (calibration-based) k_g=0.67±0.03×10^{-6} m s^{-1} (calibration-free)	1.29±0.03 1.26±0.02
Finnie *et al.*[5]	Single crystal experiments	Cooling	Growth cell	Water			
Granberg *et al.*[16]	Seeded desupersaturation experiments	Cooling	STC	Acetone-water	16 °C	k_g ≈25×10^{-5} m s^{-1} in pure water k_g ≈5-×10^{-5} m s^{-1} in pure acetone	1.2 in pure water 1.45 in pure acetone
Granberg and Rasmuson[17]	Seeded desupersaturation experiments	Cooling	STC	Water-acetone-toluene	16 °C		
Jiang and Ni [28]	Spontaneous nucleation followed by crystal growth	Reactive	OFC	Acetic Acid-Water	20 °C		1.72, 4.27 and 12.62
Mitchell *et al.*[12]	Seeded desupersaturation experiments	Cooling	STC	Ethanol	10, 20 and 30 °C	$k_{g,0}$=9.979 m s^{-1} (m^3 kmol^{-1})^g E_a=40.56 kJ mol^{-1}	1.602
Nagy *et al.*[19]	Metastable zone width experiments	Cooling	STC	Water		$-\ln k_g$=4.11±1.23	1.54±0.48
Ó'Ciardhá *et al.*[15]	Seeded desupersaturation experiments	Antisolvent	STC	Methanol-water	25 °C	k_g=3.46×10^{-5}-1.86×10^{-4} m s^{-1}	1.604-2.239

Table 8.1 – Continued.

Reference	Experimental method	Supersaturation method	Crystallizer	Solvent system	Temperature	K_g, k_g, $k_{g,0}$ and/or E_a	g
Omar *et al.*[8]	Single crystal experiments	Cooling	Growth cell	Water	25 and 40 °C		
Shekunov *et al.*[7]	Single crystal experiments	Cooling	Growth cell	Water	3-50 °C		
Shekunov and Grant[6]	Single crystal experiments	Cooling	Growth cell	Water	5-40 °C		
Shekunov *et al.*[9]	Single crystal experiments	Cooling	Growth cell	Water	35.5 °C		
Soto *et al.*[14]	Seeded desupersaturation experiments and rotating disk experiments	Cooling	STC	Methanol	288, 293, 298 and 303 K	$k_{g,0}$=454±317 m s^{-1} E_a=47.35±1.70 kJ mol^{-1}	1.51±0.03
Thompson *et al.*[10]	Single crystal experiments	Cooling	Growth cell	Water	25 °C		
Worlitschek and Mazzotti[13]	Seeded desupersaturation experiments	Cooling	STC	Ethanol	8-30 °C	$k_{g,0}$=21.0 m s^{-1} (m^3 kmol^{-1})^g E_a=4.16 × 10^7 J/kmol	1.9

8.2 Materials and Methods

8.2.1 Material

Paracetamol (CAS number 103-90-02, min. 99% purity) was supplied by Sigma-Aldrich, ethanol (CAS number 64-17-5, min. 99.5% purity) was supplied by VWR Chemicals, and ultrapure water was obtained from a Millipore ultrapure water system.

8.2.2 Calibration Curves

An analytic method was developed to measure the concentration of paracetamol in a 40% (v/v) mixture of ethanol and water, C, at 10 °C. Standard solutions of paracetamol were prepared in triplicates and kept at 10 °C in a cooling/heating bath (Ministat 125, Huber). The absorbance, Abs, of each standard solution was measured at 249 nm by an attenuated total reflectance (ATR) immersion probe (Katana 6, Hellma) connected to an UV/Vis spectrometer (SPEC RES+ UV/VIS-Sarspec). Then, the linear regression equation was fitted to the experimental data by the method of least squares. The same experimental procedure was then repeated at 15, 20, 25, 30 and 35 °C. The experimental data and the calibration curves are presented in **Figure 8.1**. Further details are provided in **Appendix A**.

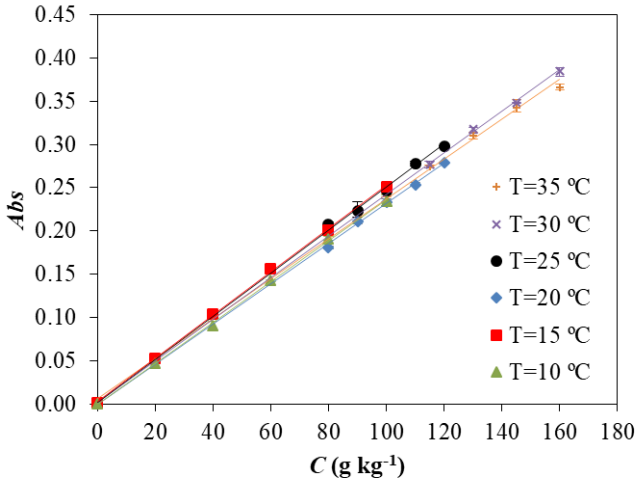


Figure 8.1 – Calibration curve for the absorbance as a function of the concentration of paracetamol in a 40% (v/v) mixture of ethanol and water at different temperatures. The error bars represent the interval between the minimum and maximum values of the three replicates.

8.2.3 Solubility

A solution of paracetamol in a 40% (v/v) mixture of ethanol and water with an excess of paracetamol was prepared in a jacketed glass vessel (Schott glass reactor) with 1 L of maximum capacity. The temperature in the jacket was kept constant at 10 °C by a cooling/heating bath, and stirring was provided by a magnetic stirrer (C-MAG HS 7 digital, IKA). The absorbance of the solution was monitored at 249 nm by the ATR immersion probe connected to the UV/Vis spectrometer, and the concentration of paracetamol was calculated from the calibration curve at 10 °C. When the solution reached equilibrium, the final concentration of paracetamol in solution was taken as the solubility of paracetamol in a 40% (v/v) mixture of ethanol and water at 10 °C, C_s. The same procedure was then repeated at 15, 20, 25, 30 and 35 °C. The results are presented in **Table 8.2**.

Table 8.2 – Solubility data.

T (°C)	10	15	20	25	30	35
C_s (g kg^{-1})	65.55	77.31	93.05	110.51	131.64	157.62

The following exponential equation was fitted to the experimental data:

$$C_s = 45.913 \exp(0.0352T) \quad \textbf{(8.3)}$$

where C_s is the solubility of paracetamol in a 40% (v/v) mixture of ethanol and water in g kg^{-1}, and T is the temperature in °C.

8.2.4 Preparation of the Seeds

The seeds were prepared by cooling crystallization in a STC. The STC consisted of a jacketed glass vessel with 1 L of maximum capacity. The temperature in the jacket was controlled by a cooling/heating bath, and stirring was provided by a magnetic stirrer. A solution was prepared by dissolving 75 g of paracetamol in 250 g of solvent in a 500 mL flask. The solvent consisted of a 70% (v/v) mixture of ethanol and water. The solution was stirred at 200 rpm and kept at 35 °C on a hotplate magnetic stirrer for 1 hour. Then, the solution was quickly transferred to the STC, which was previously thermostated at 2 °C. After that, the solution was kept under stirring at 300 rpm by a magnetic bar. The rapid cooling forced nucleation at a high level of supersaturation, which resulted in a large number of crystals. After 2 h, the stirring was stopped, the slurry was filtered, and the final product was left to dry in an oven at 80 °C overnight. Then, the final product was sieved in a vibratory sieve shaker (AS 200 Control, Retsch) using three stainless steel woven wire mesh sieves, with 90, 125, and 180 μm sieve mesh sizes, respectively. Crystals in the sieve fraction between 125-180 μm were used as seeds

in the following crystal growth experiments. The CSD of the seeds was measured by a laser diffraction particle size analyzer (LS230, Beckman Coulter), and images of the seeds were acquired using a stereoscopic zoom microscope (SMZ1500, Nikon) coupled to a video camera (DS-Ri1, Nikon).

8.2.5 Crystallizer

A schematic representation of the planar-OFC is presented in **Figure 7.1**. The planar-OFC consists of a plate-like crystallizer with three stacked plates screwed together: two polycarbonate plates, one at the base and one at the top, and one aluminum plate coated with Halar® (ethylene-chlorotrifluoroethylene copolymer, ECTFE) in the middle – **Figure 8.2 (a)**. The crystallization process takes place in a channel designed with smooth periodic constrictions located between the middle and top plates, and the water of a cooling/heating jacket circulates in a straight channel located between the base and middle plates. The two channels were carved in the middle plate; the top plate seals the crystallization channel and the base plate seals the jacket channel. The crystallization channel has 6 access points (one main inlet, one main outlet and four intermediate inlets/outlets) and comprises a volume of approximately 71 mL (operational volume). The dimensions of each inter-constriction cell are presented in **Figure 8.2 (b)**.

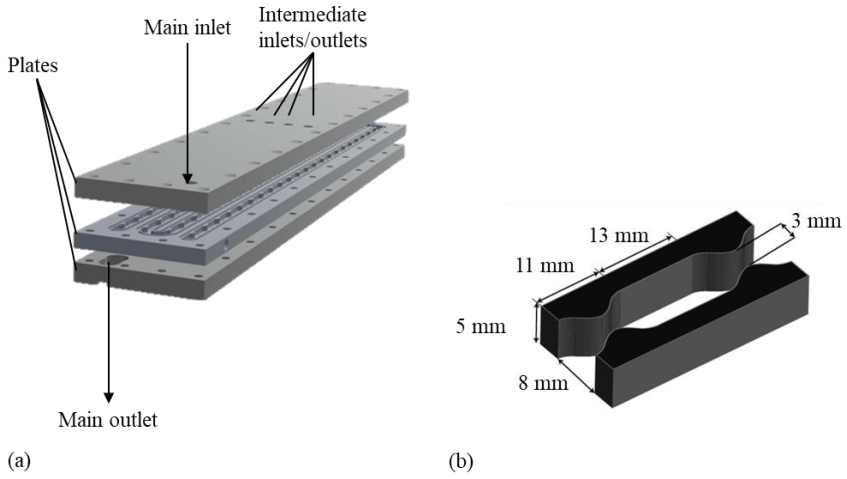


Figure 8.2 – Plate-like planar-OFC. (a) Three stacked plates. (b) Dimensions of each inter-constriction cell.

8.2.6 Crystal Growth Experiments

The experimental set-up is presented in **Figure 8.3.** A solution of paracetamol was prepared in a 40% (v/v) mixture of ethanol and water in a 250 mL flask. The solution was stirred at 200 rpm and kept at 10 °C above its saturation temperature on a hotplate stirrer for 1 h. Then, the solution was slowly cooled down to its saturation temperature and kept under stirring. Then, a known amount of seeds was added to the solution.

The suspension was pumped from the flask into the crystallizer (BT300-2J, Longer Pump), which was previously thermostated at the final temperature, and the oscillation was activated at a predefined frequency and amplitude of oscillation. The temperature in the crystallizer was controlled by a cooling/heating bath, and the frequency and amplitude of oscillation were controlled by a linear motor actuating a piston diameter of 10.3 mm (H01-23x166/80, LinMot). When the crystallizer was completely filled with the suspension, the pumping was stopped. The suspension was quickly cooled down to the final temperature in the crystallizer, and the seeds were allowed to grow at constant temperature. The absorbance of the mother liquor was measured at 249 nm by the ATR immersion probe connected to the UV/Vis spectrometer, which was placed in the first intermediate inlet of the crystallizer, and the concentration of paracetamol in solution was calculated from the respective calibration curve. The temperature of the mother liquor was recorded by a thermocouple connected to a data acquisition system (NI cDAQ-9171, National Instruments), which was placed in the third intermediate inlet of the crystallizer. After 2 h of crystal growth, the oscillation was stopped, and the slurry was collected at the crystallizer outlet. The final product was filtered and then left to dry in an oven at 80 °C overnight. Then, the CSD of the final product was measured using the laser diffraction particle size analyzer, and the images of the crystals were acquired using the stereoscopic zoom microscope coupled to the video camera. Finally, the crystal growth kinetic parameters were estimated from the desupersaturation curve. This procedure was repeated for different combinations of frequency and amplitude of oscillation.

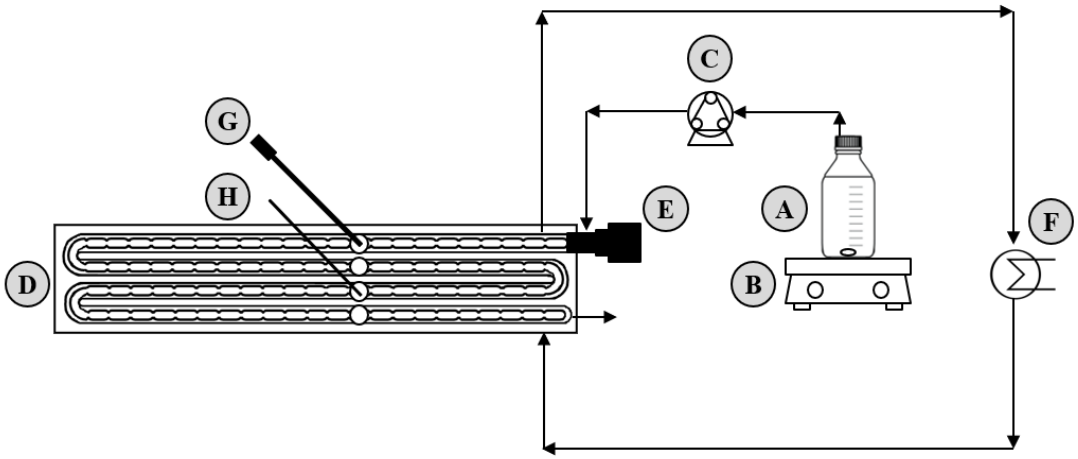


Figure 8.3 – Experimental set-up for the determination of the crystal growth kinetics. A – suspension with seeds; B – hotplate stirrer; C – peristaltic pump; D – planar-OFC; E – linear motor; F – cooling bath; G – ATR-UV/Vis immersion probe; H – thermocouple.

8.2.7 Design of experiments

A full factorial design with three center points was created in Minitab® to investigate the effects of the frequency, f, and amplitude of oscillation, x_0, on the crystal growth kinetic parameters, k_g and g. Each factor was tested at two levels: 2 and 4 Hz for the frequency, and 12 and 16 mm for the amplitude. The center points were set halfway between the low and high levels of each factor, in this case, f =3 Hz and x_0=14 mm. In addition, two more experiments were performed at f=2 Hz and x_0=12 mm at different temperatures. In total, 9 runs were performed. The experimental conditions of each run are presented in **Table 8.3**. In this table, T_i is the initial temperature, T_f is the final temperature, C_i is the initial concentration, C_f is the final concentration, $\Delta C_i = C_i - C_f$ is the initial concentration driving force, $S_i = C_i/C_f$ is the initial supersaturation ratio, m_{seeds} is the mass of seeds added, $\mathrm{Re_o}$ is the oscillatory Reynolds number, and St is the Strouhal number. $\mathrm{Re_o}$ and St were calculated based on the hydraulic diameter, D_h, defined as:

$$D_h = 4\frac{A_{cs}}{P_{cs}} \tag{8.4}$$

where A_{cs} is the cross-sectional area of the channel and P_{cs} is the wetted perimeter of the cross-section.

Table 8.3 – Experimental conditions of each run.

Run	T_i (°C)	T_f (°C)	C_i (g kg^{-1})	C_f (g kg^{-1})	ΔC_i (g kg^{-1})	S_i	m_{seeds} (g)	f (Hz)	x_0 (mm)	$\mathrm{Re_o}$	St
1	25	20	111.66	93.05	18.61	1.2	0.1807	2	12	886	0.041
2	25	20	111.66	93.05	18.61	1.2	0.1812	4	12	1771	0.041
3	25	20	111.66	93.05	18.61	1.2	0.1804	2	16	1181	0.031
4	25	20	111.66	93.05	18.61	1.2	0.1806	4	16	2362	0.031
5	25	20	111.66	93.05	18.61	1.2	0.1805	3	14	1550	0.035
6	25	20	111.66	93.05	18.61	1.2	0.1810	3	14	1550	0.035
7	25	20	111.66	93.05	18.61	1.2	0.1809	3	14	1550	0.035
8	15	10	78.66	65.55	13.11	1.2	0.1866	2	12	886	0.041
9	35	30	157.97	131.64	26.33	1.2	0.1740	2	12	886	0.041

8.3 Results and Discussion

In **Chapter 7**, the isothermal batch crystallization of paracetamol from water was used as a model system to investigate the effect of the oscillation conditions on the nucleation kinetics in a range of frequencies between 3 and 6 Hz and in a range of amplitudes between 6 and 12 mm. In the present chapter, the initial intention was to use the same model system to investigate the effect of the oscillation conditions on the crystal growth kinetics in the same range of oscillation conditions. However, the solubility of paracetamol in water is too low to be accurately measured by the ATR-UV/Vis probe (12.78 g kg^{-1} at 20 °C, according to Granberg and Rasmuson[38]).

Therefore, water was replaced by a 40% (v/v) mixture of ethanol and water because the solubility of paracetamol in this solvent is high enough to be accurately measured by the ATR-UV/Vis probe (93.05 g kg^{-1} at 20 °C, according to our results). In addition, the range of frequencies was decreased from 3-6 Hz to 2-4 Hz so as to reduce the probability of primary/secondary nucleation, attrition and breakage; and the range of amplitudes was increased from 6-12 mm to 12-16 mm to keep the crystals in suspension in the new solvent, which is less dense than water.

8.3.1 Estimation of crystal growth kinetic parameters

The overall crystal growth rate, R_G, can be expressed as:

$$R_G = \frac{1}{A}\frac{dm}{dt} \tag{8.5}$$

where A is the crystal surface area, and m is the mass of solute deposited in time t. A and m are calculated as:

$$A = \beta L^2 \tag{8.6}$$

$$m = \alpha \rho_c L^3 \tag{8.7}$$

where β is the surface area shape factor, α is the volume shape factor, ρ_c is the crystal density, and L is the mean crystal size. Then, **Equation (8.5)** becomes:

$$R_G = \frac{\alpha \rho_c}{\beta L^2}\frac{dL^3}{dt} \tag{8.8}$$

Assuming that α, β and R_G are constant over a small time interval, $\Delta t = t_{i+1} - t_i$, equation (8.8) can be integrated as:

$$R_{G,i+1} = 3\frac{\alpha \rho_c}{\beta \Delta t}(L_{i+1} - L_i) = 3\frac{\alpha \rho_c L_i}{\beta \Delta t}\left(\frac{L_{i+1}}{L_i} - 1\right) \tag{8.9}$$

where $R_{G,i+1}$ is the overall crystal growth rate at t_{i+1}, and L_i and L_{i+1} are the mean crystal size at t_i and t_{i+1}, respectively. L_i and L_{i+1} are related to the mass of the crystals as:

$$\frac{m_{i+1}}{m_i} = \left(\frac{L_{i+1}}{L_i}\right)^3 \tag{8.10}$$

where m_i and m_{i+1} are the mass of the crystals at t_i and t_{i+1}, respectively. Hence, **Equation (8.9)** becomes:

$$R_{G,i+1} = 3\frac{\alpha \rho_c L_i}{\beta \Delta t}\left[\left(\frac{m_{i+1}}{m_i}\right)^{\frac{1}{3}} - 1\right] \tag{8.11}$$

Then, **Equation (8.11)** can be rearranged as:

$$m_{i+1} = m_i \left(1 + \frac{\beta \Delta t R_{G,i+1}}{3\alpha\rho_c L_i}\right)^3 \quad \textbf{(8.12)}$$

and $R_{G,i+1}$ can be calculated for each small time interval as:

$$R_{G,i+1} = K_g \left(\frac{C_i + C_{i+1}}{2} - C_s\right)^g \quad \textbf{(8.13)}$$

where C_i and C_{i+1} are the concentration of solute at t_i and t_{i+1}, respectively, $(C_i + C_{i+1})/2$ is the mean concentration of solute in the time interval $\Delta t = t_{i+1} - t_i$, K_g is the overall coefficient of crystal growth, and g is the growth rate order.

To estimate K_g and g, a nonlinear least-squares optimization procedure was employed, which consisted in minimizing the objective function:

$$\min_{\theta} \Phi(\theta) = \sum_{i=0}^{n} \left(m_{i+1}^{exp} - m_{i+1}^{cal}\right)^2 \quad \textbf{(8.14)}$$

where θ is the vector of model parameters, $\theta = [K_g, g]$, m_{i+1}^{exp} and m_{i+1}^{cal} are the experimental and calculated values of m_{i+1}, respectively, $\Phi(\theta)$ is the total sum of the square error between m_{i+1}^{exp} and m_{i+1}^{cal}, and n is the total number of time intervals. Finally, R_G was converted into the overall linear growth rate, G, as:

$$G = \frac{\beta}{3\alpha\rho_c} R_G \quad \textbf{(8.15)}$$

And the overall coefficient of crystal growth expressed in kg m^{-2} s^{-1}, K_g, was converted into the overall coefficient of crystal growth defined in m s^{-1}, k_g, as:

$$k_g = \frac{\beta}{3\alpha\rho_c} K_g \quad \textbf{(8.16)}$$

8.3.2 Effect of the Oscillation Conditions on the Crystal Growth Kinetic Parameters

Seven isothermal seeded batch desupersaturation experiments were performed to study the effect of the frequency, f, and amplitude of oscillation, x_0, on the crystal growth kinetic parameters, k_g and g, for the isothermal crystallization of paracetamol from a 40% (v/v) mixture of ethanol and water at 20 °C. **Figure 8.4** presents the volume-based CSD, $f_V(d)$, of the seeds and final products. This figure shows that the percentage of small particles (<10 μm) decreased in all runs in comparison with the seeds. Furthermore, it also indicates that the percentage of large particles (> 500 μm) remained low in all runs. This suggests that the formation of

small particles due to primary/secondary nucleation, attrition and/or breakage, and the formation of large particles due to agglomeration was not significant in all runs. Therefore, the growth of the seeds should have dominated the consumption of supersaturation in these experiments. Furthermore, **Figure 8.4** also shows that the narrow CSD of the seeds was largely preserved in the final products, as confirmed by the nearly constant coefficients of variation of the CSD, CV, presented in **Figure 8.5**, which suggests negligible crystal growth rate dispersion.

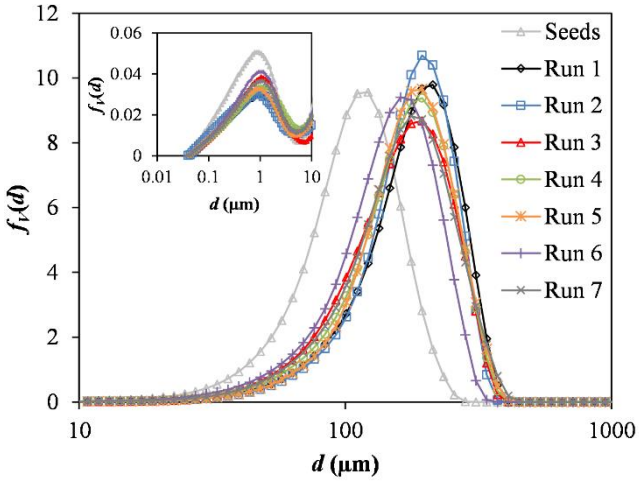


Figure 8.4 – Volume-based CSD of the seeds and final products. The inset shows the CSD for the smaller sizes.

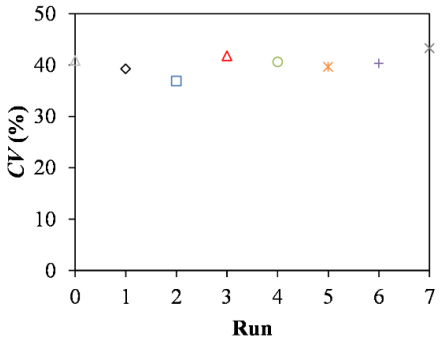


Figure 8.5 – Coefficient of variation of the CSD for the seeds and final products of each run.

Microscope images of the seeds and final products are presented in **Figure 8.6**. This figure clearly shows that the seeds had a significant increase in size in all runs. It also shows that some mild agglomeration could not be prevented. Nevertheless, Schöll *et al.*[39] have demonstrated that the desupersaturation profile is not significantly affected by agglomeration, even at high agglomeration rates.

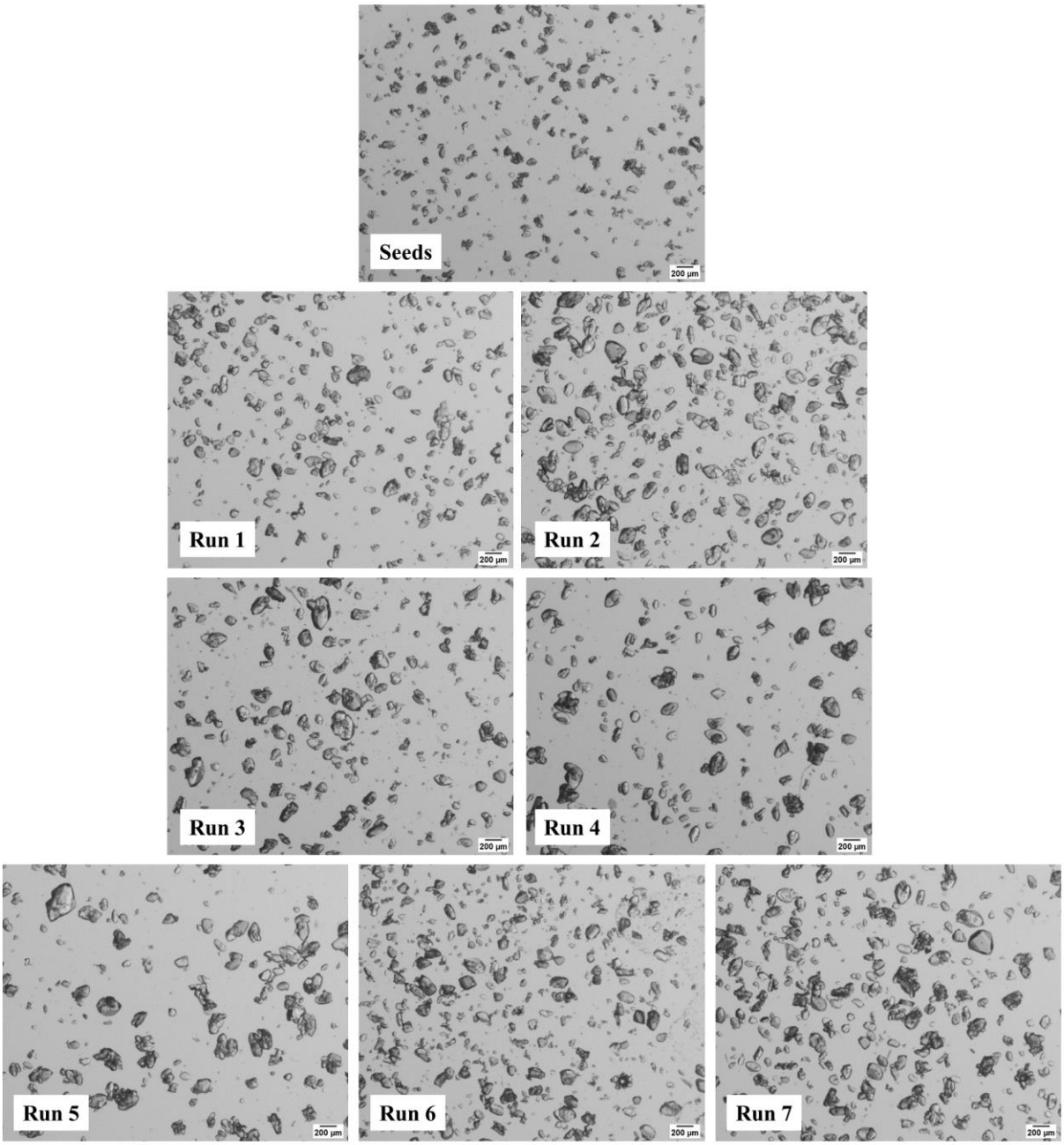


Figure 8.6 – Microscope images of the seeds and final products. The scale bar represents 200 µm.

Figure 8.7 presents the evolution of supersaturation ratio, S, and temperature, T, in each run. This figure shows that the suspension reached the final temperature (20 °C) very quickly, ensuring that crystal growth occurred at a constant temperature. In addition, **Figure 8.7** also shows that the desupersaturation curves for the three replicates (Runs 5, 6 and 7) almost overlap, which demonstrates the reproducibility of the experiments. Finally, **Figure 8.7** also shows that the desupersaturation curves are also very similar for the remaining runs, suggesting that the oscillation conditions should have a minor effect on crystal growth. To confirm this hypothesis, the

crystal growth kinetic parameters, k_g and g, were estimated for each run from the respective desupersaturation curve.

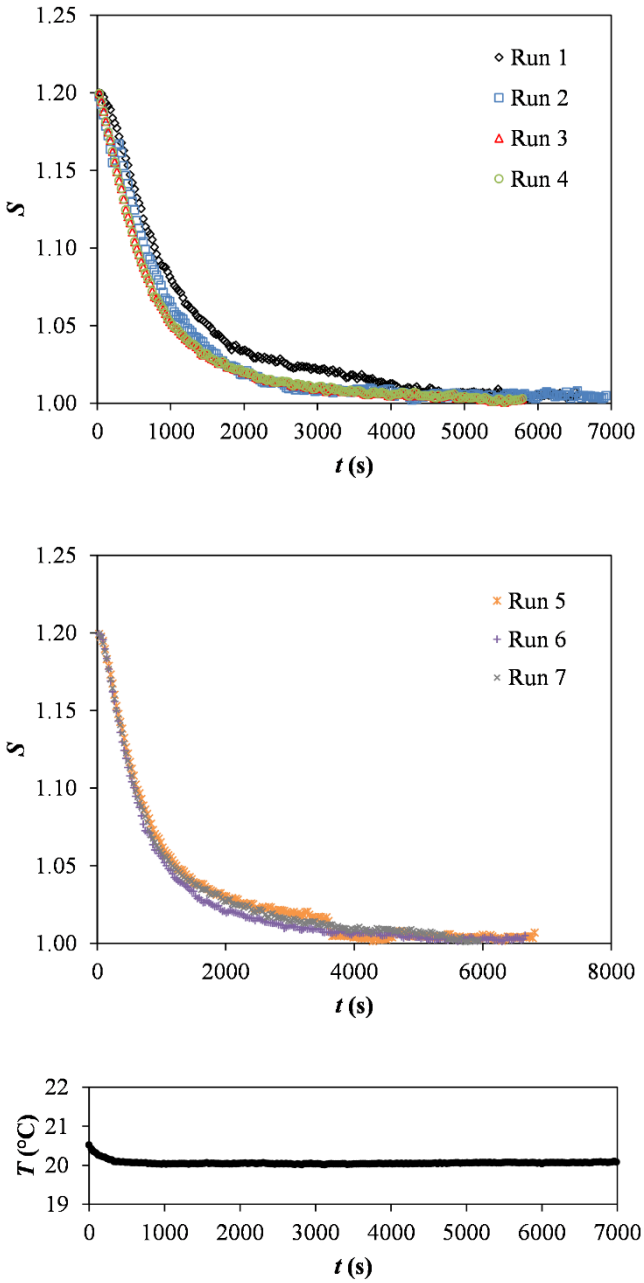


Figure 8.7 – Evolution of supersaturation ratio and temperature in Runs 1-7.

Figure 8.8 presents the overall linear growth rate, G, as a function of the concentration driving force, ΔC, for each run. This figure shows that almost all curves practically overlap, except for Runs 1 and 4. Run 1, with the lowest crystal growth rates, was performed with the lowest oscillation intensity (Re_o=886). In contrast, Run 4, with the highest crystal growth rates, was performed with the highest oscillation intensity (Re_o=2362). If the

difference of crystal growth rates between Runs 1 and 4 is statistically significant, then the increase of crystal growth rate caused by an increase of oscillation intensity suggests that diffusion is the rate-controlling step of crystal growth. On the other hand, if the difference is not statistically significant, then surface integration is probably the rate-controlling step of crystal growth. This is discussed in more detail below.

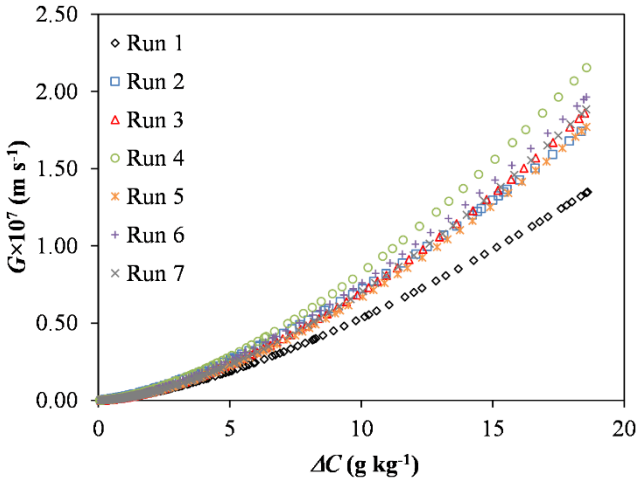


Figure 8.8 – Overall linear growth rate as a function of the concentration driving force for Runs 1-7.

Table 8.4 presents the crystal growth kinetic parameters, k_g and g, obtained in Runs 1-7. **Table 8.4** also presents the 95% confidence intervals for k_g and g, $CI(k_g)$ and $CI(g)$, respectively, determined by the bootstrap method with 200 simulations, as described by Hu *et al.*,[40] as well as the sum of squared residuals, SSR. The low sum of squared residuals and the narrow confidence intervals suggest that the model is suitable for describing the experimental data. This is further supported by the parity plots presented in **Figure 8.9**, where the calculated supersaturation ratio, S_{cal}, is plotted against the experimental supersaturation ratio, S_{exp}, for each run. Clearly, the model predictions are in good agreement with the experimental data.

Table 8.4 – Crystal growth kinetic parameters obtained in Runs 1-7.

Run	f (Hz)	x_0 (mm)	Re_o	St	k_g (m s^{-1})	$CI(k_g)$ (m s^{-1})	g	$CI(g)$	SSR (g^2)
1	2	12	886	0.041	5.32×10^{-5}	1.72×10^{-6}	1.500	0.006	1.05×10^{-4}
2	4	12	1771	0.041	5.84×10^{-5}	1.50×10^{-8}	1.455	0.003	1.09×10^{-4}
3	2	16	1181	0.031	1.06×10^{-4}	1.36×10^{-6}	1.591	0.003	5.96×10^{-5}
4	4	16	2362	0.031	1.04×10^{-4}	3.37×10^{-6}	1.550	0.005	1.76×10^{-5}
5	3	14	1550	0.035	9.78×10^{-5}	4.95×10^{-6}	1.584	0.009	1.42×10^{-4}
6	3	14	1550	0.035	9.13×10^{-5}	1.24×10^{-6}	1.541	0.003	4.04×10^{-5}
7	3	14	1550	0.035	1.11×10^{-4}	2.50×10^{-6}	1.601	0.004	8.38×10^{-5}

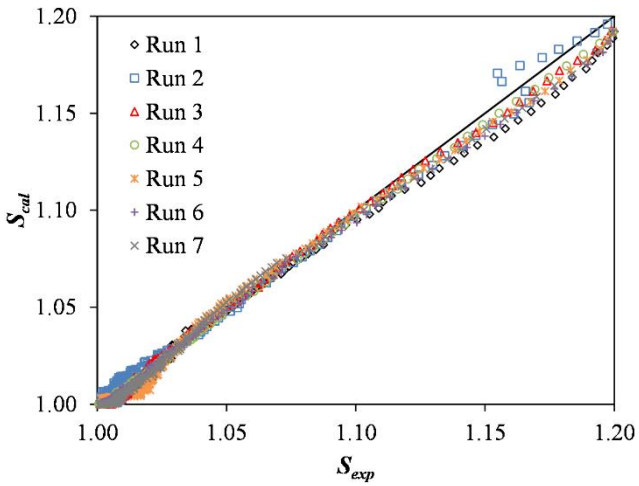


Figure 8.9 – Parity plots for Runs 1-7.

The crystal growth kinetic parameters obtained in each run are plotted as a function of f and x_0 in **Figure 8.10**. This figure shows that while increasing f barely affected k_g, increasing x_0 resulted in an increase in k_g. Furthermore, it also indicates that increasing either f or x_0 barely affected g.

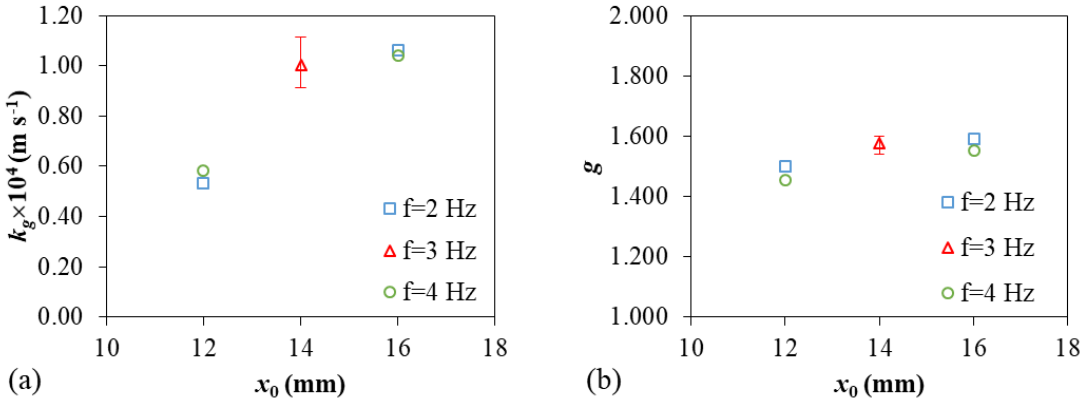


Figure 8.10 – (a) Overall coefficient of crystal growth and (b) growth rate order as a function of the frequency and amplitude of oscillation. The error bars represent the interval between the minimum and maximum values of the three replicates.

To assess the significance of the main effects of f and x_0 and their interaction, fx_0, on k_g and g, the factorial design was analyzed in Minitab®. Two multiple linear regression models were formulated to describe the relationship between the two factors, f and x_0, and the two response variables, k_g and g, as:

$$k_g \text{ (or } g) = \beta_0 + \beta_1 f + \beta_2 x_0 + \beta_{12} f x_0 \quad \textbf{(8.17)}$$

where β_0 is a constant, β_1 and β_2 are linear coefficients, and β_{12} is an interaction coefficient. The p-value of each term of the model was compared with the significance level of 5% to assess its significance. The p-value measures the evidence against the null hypothesis, which states that the coefficient associated to the term is equal to zero or, in other words, that the term has no significant effect.[41] The p-values for all terms of the two models are presented in **Table 8.5**. In this work, the p-value was higher than the significance level of 5% for all terms of the two models, which suggests that none of the terms is statistically significant. Furthermore, the additional three center points were used to test for the curvature of the response. The curvature is considered significant when the p-value for curvature is less than or equal to the significance level. The p-value for curvature measures the evidence against the null hypothesis, which states that all the relationships between the factors and the response are linear.[41] The p-values for curvature for the two models are also presented in **Table 8.5**. In this work, the p-value for curvature was higher than the significance level of 5% for the two models, which suggests that there is no evidence of curvature.

Table 8.5 – *p*-values for the two models.

	***p*-value**	
Term	k_g	g
f	0.932	0.424
x_0	0.064	0.138
fx_0	0.844	0.962
Curvature	0.127	0.163

8.3.3 Effect of Temperature on the Crystal Growth Kinetic Parameters

Three isothermal seeded batch desupersaturation experiments were performed to study the effect of temperature, T, on the crystal growth kinetic parameters, k_g and g, for the isothermal crystallization of paracetamol from a 40% (v/v) mixture of ethanol and water. The three experiments were performed at f=2 Hz and x_0=12 mm.

Figure 8.11 presents the evolution of supersaturation ratio, S, and temperature, T, in each run. This figure shows that the suspension reached the final temperatures very quickly, ensuring that crystal growth occurred at a constant temperature. **Figure 8.11** also shows that the supersaturation was consumed faster at higher temperatures, reflecting the well-known effect of temperature on the crystal growth rate.

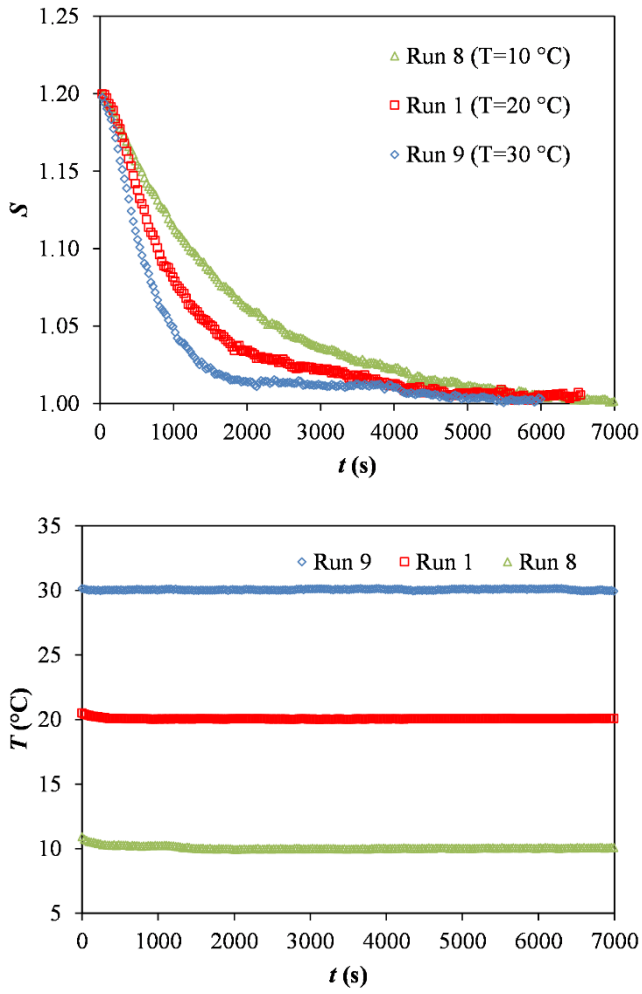


Figure 8.11 – Evolution of supersaturation ratio and temperature in Runs 1, 8 and 9.

The crystal growth kinetic parameters, k_g and g, obtained in each run are presented in **Table 8.6**. Once again, the low sum of squared residuals and the narrow confidence intervals suggest that the model is suitable for describing the experimental data. This is further supported by the parity plots presented in **Figure 8.12.**

Table 8.6 – Crystal growth kinetic parameters obtained in Runs 1, 8 and 9.

Run	T (°C)	k_g (m s^{-1})	$CI(k_g)$ (m s^{-1})	g	$CI(g)$	SSR (g^2)
8	10	2.64×10^{-5}	4.79×10^{-7}	1.371	0.003	4.36×10^{-5}
1	20	5.32×10^{-5}	1.72×10^{-6}	1.500	0.006	1.05×10^{-4}
9	30	8.75×10^{-5}	2.04×10^{-8}	1.589	0.002	3.07×10^{-4}

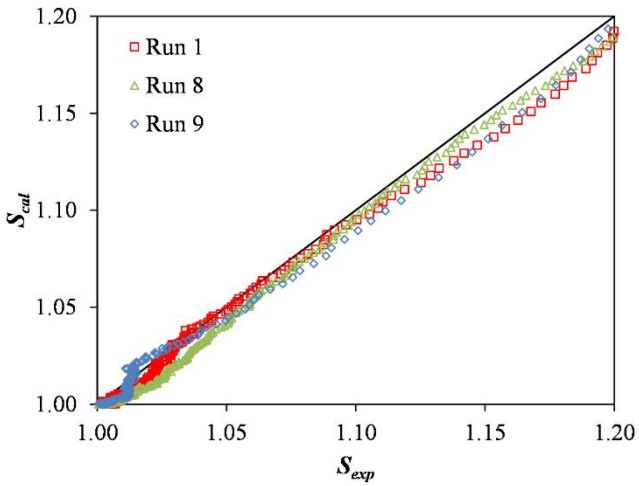


Figure 8.12 – Parity plots for Runs 1, 8 and 9.

Equation (8.2) was linearized and fitted to the experimental data to estimate the activation energy, E_a, and the constant, $k_{g,0}$, from the slope and the intercept of ln k_g vs $1/T$, respectively. The results are presented in **Table 8.7.**

Table 8.7 – Parameters obtained from fitting equation (8.2) to the experimental data.

Parameter	Value	*CI*
$k_{g,0}$ (m s^{-1})	2123	324
E_a (kJ mol^{-1})	42.8	0.3

8.3.4 Rate controlling step of crystal growth

It is generally assumed that crystal growth proceeds as a sequence of diffusion and surface integration. Typically, diffusion is the rate-controlling step at high supersaturations and temperatures, whereas surface integration is the rate-controlling step at moderate to low supersaturations and temperatures. This is because surface integration has a stronger dependence on supersaturation and temperature than diffusion.[18] In addition, generally, diffusion is the rate-controlling step at low mixing intensities, whereas surface integration is the rate-controlling step at high mixing intensities. This is because the relative velocity between the crystal and the mother liquor increases as the mixing intensity increases, which decreases the diffusion resistance in the boundary layer.[42] Therefore, the combination of high oscillation intensities (886<Re_o<2362), low supersaturations ($S_i = 1.2$) and low temperatures (10<T<30 °C) should have contributed to reduce the diffusion limitations in this work.

It is common to use the values of crystal growth kinetic parameters estimated from empirical power-law models to speculate about the rate-controlling step of crystal growth. On the one hand, $g \approx 1$ and $10 < E_a < 20$ kJ mol^{-1} are typically values for diffusion controlled crystal growth, on the other hand, $g \approx 2$ and $40 < E_a < 60$ kJ mol^{-1} are typically values for surface integration controlled crystal growth.[18] In this work, g ranged between 1.371 and 1.601, and E_a was estimated as 42.8 kJ mol^{-1}. Therefore, the relatively high values of g and E_a suggest that, in this work, surface integration is the rate-controlling step of crystal growth. Furthermore, the statistical independence of the crystal growth kinetics from the oscillation conditions also support this conclusion.

To investigate whether the crystal growth rate is affected by diffusional limitations, the concept of diffusion control index was used. The diffusion control index, $q_d = G/G_d$, was defined by Nielsen and Toft[43] as the ratio between the experimental growth rate, G, and the diffusion limited growth rate, G_d. On the one hand, when the growth rate is controlled by diffusion, the experimental growth rate is of the same order of magnitude as the diffusion limited growth rate, hence $1/q_d \approx 1$. On the other hand, when the growth rate is controlled by surface integration, the experimental growth rate is much lower than the diffusion limited growth rate, hence $1/q_d \gg 1$.

The diffusion limited crystal growth rate was calculated as:[44]

$$G_d = k_d \frac{\beta M}{3\alpha\rho_c}(C - C_s) \tag{8.18}$$

where k_d is the mass transfer coefficient, β is the surface shape factor, α is the volume shape factor (β/α=7.09 for crystals of paracetamol with the shape of a truncated octahedron),[27] M is the molar mass of paracetamol (0.15117 kg mol^{-1}), ρ_c is the crystal density (1296 kg m^{-3}), C is the concentration of paracetamol in solution and C_s is the solubility of paracetamol, both in molar units of mol m^{-3}. The mass transfer coefficient was estimated using the Sherwood correlation as:[45]

$$k_d = \frac{D}{L}\left(2 + 0.8\left(\frac{\varepsilon L^4}{\upsilon^3}\right)^{\frac{1}{5}} \mathrm{Sc}^{\frac{1}{3}}\right) \tag{8.19}$$

where D is the diffusivity or diffusion coefficient, L is the crystal size, ε is the average power input, υ is the kinematic viscosity (2.76×10^{-6} m^2 s^{-1} at 20 °C for a 40% (v/v) mixture of ethanol and water)[46] and Sc is the Schmidt number ($\mathrm{Sc} = \upsilon/D$). The diffusion coefficient, D, was calculated by the Stokes-Einstein equation as:[47]

$$D = \frac{kT}{3\pi\mu d_m} \tag{8.20}$$

where k is the Boltzmann constant (1.38065×10^{-23} J K^{-1}), T is the temperature in Kelvin, and μ is the dynamic viscosity of the fluid (2.6163×10^{-3} kg m^{-1} s^{-1} at 20 °C for a 40% (v/v) mixture of ethanol and water)[46] and d_m is the molecular diameter. The molecular diameter was calculated as:

$$d_m = \sqrt[3]{\frac{1}{c_c N_A}} \tag{8.21}$$

where c_c is the molar density of the paracetamol (8.8113 kmol m^{-3}), and N_A is Avogadro's constant (6.022×10^{26} $kmol^{-1}$). Therefore, d_m=5.73×10^{-10} m and D=2.86×10^{-10} m^2 s^{-1}. For planar-OFCs, the average power input, ε, can be estimated as:[48]

$$\varepsilon = \frac{2N_c(2\pi f x_0)^3}{3\pi C_0^2}\left[\left(\frac{W}{W_0}\right)^2 - 1\right] \tag{8.22}$$

where N_c is the number of identical constrictions per unit length (the planar-OFC comprises 88 identical constrictions in a 2.22 m long channel, hence N_c=88/2.22=39.6 m^{-1}), C_0 is the standard orifice discharge coefficient (usually taken as 0.7), W is the channel width in the straight section (8 mm), and W_0 is the channel width in the constriction (3.3 mm). The average power input was calculated for Runs 1-7 and, then, the mass transfer coefficient was estimated for each run assuming the initial average crystal size of L=1.15×10^{-4} m. The results are presented in **Table 8.8**.

Table 8.8 – Average power input and mass transfer coefficient for Runs 1-7.

Run	f (Hz)	x_0 (mm)	ε (W kg^{-1})	k_d (m s^{-1})
1	2	12	0.287	5.54×10^{-5}
2	4	12	2.297	8.14×10^{-5}
3	2	6	0.681	6.49×10^{-5}
4	4	16	5.444	9.58×10^{-5}
5, 6 and 7	3	14	1.539	7.55×10^{-5}

Then, G_d and G were calculated for Runs 1-7 for the initial supersaturation ratio of S=1.2 (ΔC=18.61 g kg^{-1}= 116.6 mol m^{-3}). The inverse of the diffusion control index is plotted for each run in **Figure 8.13**. This figure shows that $1/q_d$ is well above the unity for all runs, which confirms that surface integration is the rate-controlling step of crystal growth.

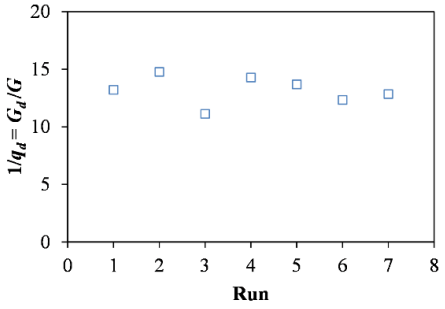


Figure 8.13 – Inverse of the diffusion control index for Runs 1-7 (S=1.2).

8.3.5 Comparison with other works

The crystal growth rates obtained in this work for the isothermal crystallization of paracetamol in a 40% (v/v) mixture of ethanol and water, in the range between 10^{-10} and 10^{-7} m s^{-1} for $1.0<S<1.2$, are in good agreement with those obtained in other solvents for similar levels of supersaturation, including water,[11,19] ethanol,[12] methanol[14], binary mixtures of methanol and water,[15] acetone and water,[16,17,27] acetone and toluene[17], and acetic acid and water,[28] and also ternary mixtures of water, acetone and toluene.[17] Furthermore, the overall coefficients of crystal growth obtained in this work, in the range between 2.64×10^{-5} and 1.11×10^{-4} m s^{-1}, are comparable with those reported for binary mixtures of acetone and water,[16] and methanol and water,[15] and the growth rate orders obtained in this work, in the range between 1.371 and 1.601, are as well comparable with those reported for other solvents, from 1.2 in pure water[16] to 12.62 in a binary mixture of acetic acid and water.[28] In addition, the activation energy estimated in this work as 42.8 kJ mol^{-1} is also very similar to the activations energies obtained in other solvents, such as 40.56 and 41.6 kJ mol^{-1}, both in ethanol,[12,13] and 47.35 kJ mol^{-1} in methanol.[14] Finally, surface integration has also been reported as the rate-controlling step for the crystal growth of paracetamol in several systems, including cooling crystallization from ethanol in a STC with a working volume of 500 mL operating with a stirrer speed of 200 rpm at 10-30 °C,[12] cooling crystallization from ethanol in a STC with a working volume of 1 L operating with a stirrer speed of 600 rpm at 8-30 °C,[13] antisolvent crystallization from mixtures of methanol and water in a STC with a working volume of 400 mL operating with a stirrer speed of 250 rpm at 25 °C,[15] and cooling crystallization from methanol in a STC with a working volume of 250 mL with a stirrer speed of 250 rpm at 288-303 K.[14]

8.4 Conclusion

In this work, crystal growth kinetic data for the isothermal batch crystallization of paracetamol from a 40% (v/v) mixture of ethanol and water in a planar-OFC was extracted from isothermal seeded desupersaturation experiments. A model comprising a mass balance equation expressing the mass of paracetamol crystallized as a function of time and an empirical power law equation describing the crystal growth rate as a function of supersaturation was fitted to the experimental desupersaturation data to estimate the crystal growth kinetic parameters for different combinations of frequency and amplitude of oscillation. This model was able to fit the experimental data with good accuracy, and the estimated crystal growth kinetic parameters are in good agreement with others previously obtained in different solvents.

The results obtained in this work suggest that surface integration is the rate-controlling step of crystal growth. The reasons for this are based on three findings: first, the crystal growth is practically independent of the oscillation conditions; second, the relatively high values of the growth rate order (1.371-1.601) and activation energy (42.8 kJ mol^{-1}) that were obtained in this work are indicative of surface integration control; and third, a

separate mass transfer analysis confirmed that diffusion limitations have little impact on the crystal growth rate. Ultimately, this means that the control of the CSD cannot rely on the effect of the oscillation conditions on the crystal growth step alone but rather on their relative impact on the nucleation and crystal growth steps.

It is also worth noting that while in previous works, when the experiments were conducted in OFCs, the crystal growth rates were extracted from solid phase data, in this work, the crystal growth rates were extracted from liquid phase data. This is relevant because liquid phase data is much less affected by secondary processes, such as agglomeration and breakage, than solid phase data. Therefore, the method employed in this work should estimate crystal growth rates with significantly less error than other methods previously used in OFCs.

Notation

Acronyms

ATR	Attenuated total reflectance
BCF	Burton Cabrera Frank
B+S	Birth and Spread
CSD	Crystal size distribution
ECTFE	Ethylene-chlorotrifluoroethylene copolymer
OFC	Oscillatory flow crystallizer
STC	Stirred tank crystallizer

Latin symbols

A	Crystal surface area
Abs	Absorbance
A_{cs}	Channel cross-sectional area
C	Concentration of solute in the bulk
C_0	Standard orifice discharge coefficient
c_c	Molar density
CI	95% confidence interval
C_i	Concentration of solute at t_i
C_{i+1}	Concentration of solute at t_{i+1}
C_i	Initial concentration
C_f	Final concentration
CV	Coefficient of variation
C_s	Solubility
ΔC	Concentration driving force
ΔC_i	Initial concentration driving force
d	Crystal size
D	Diffusivity
d_m	Molecular diameter
D_h	Hydraulic diameter
E_a	Activation energy
f	Frequency of oscillation
$f_V(d)$	Volume-based CSD
g	Growth rate order
G	Overall linear growth rate
G_d	Diffusion limited growth rate
k	Boltzmann constant
k_d	Mass transfer coefficient
k_g	Overall coefficient of crystal growth (m s^{-1})
K_g	Overall coefficient of crystal growth (kg m^{-2} s^{-1})
$k_{g,0}$	Pre-exponential constant
L	Mean crystal size
L_i	Mean crystal size at t_i
L_{i+1}	Mean crystal size at t_{i+1}
m	Mass of solute
M	Molar mass
m_i	Crystal mass at t_i
m_{i+1}	Crystal mass at t_{i+1}
m_{i+1}^{exp}	Experimental crystal mass at t_{i+1}
m_{i+1}^{cal}	Calculated crystal mass at t_{i+1}
m_{seeds}	Mass of seeds
n	Number of time intervals
N_a	Avogadro constant
N_c	Number of identical constrictions per unit length
P_{cs}	Channel cross-sectional wetted perimeter
q_d	Diffusion control index
R	Ideal gas constant
R_g	Overall crystal growth rate
$R_{G,i+1}$	Overall crystal growth rate at t_{i+1}
S	Supersaturation ratio
S_{cal}	Calculated supersaturation ratio
S_{exp}	Experimental supersaturation ratio
S_i	Initial supersaturation ratio
SSR	Sum of squared residuals

t	Time	β_{12}	Two-way interaction coefficient
Δt	Time interval between t_{i+1} and t_i	ε	Average power input
T	Temperature	θ	Vector of model parameters
T_i	Initial temperature	μ	Dynamic viscosity
T_f	Final temperature	υ	Kinematic viscosity
W	Channel width in the straight section	ρ_c	Crystal density
W_0	Channel width in the constriction	σ	Relative supersaturation
x_0	Center-to-peak amplitude of oscillation	$\Phi(\theta)$	Total sum of the square error

Greek Letters

α	Volume shape factor
β	Surface area shape factor
β_0	Average response for all observations
β_1 and β_2	Linear coefficients

Dimensionless Numbers

$\mathrm{Re_o}$	Oscillatory Reynolds number
Sc	Schmidt number
St	Strouhal number

References

(1) Kirwan, D. J.; Orella, C. J. Crystallization in the Pharmaceutical and Bioprocessing Industries. In *Handbook of Industrial Crystallization*; Myerson, A. S., Ed.; Butterworth-Heinemann: Boston, 2002; pp 249–266.

(2) Myerson, A. S.; Ginde, R. Crystals, Crystal Growth, and Nucleation. In *Handbook of Industrial Crystallization*; Myerson, A. S., Ed.; Butterworth-Heinemann: Boston, 2002; pp 33–65.

(3) Tavare, N. S. Characterization of Crystallization Kinetics from Batch Experiments. In *Industrial crystallization: process simulation analysis and design*; Springer Science+Business Media, LLC: New York, 1995; pp 141–198.

(4) Garside, J.; Mersmann, A.; Nývlt, J. *Measurement of Crystal Growth and Nucleation Rates*, 2nd ed.; Institution of Chemical Engineers, 2002.

(5) Finnie, S. D.; Ristic, R. I.; Sherwood, J. N.; Zikic, A. M. Morphological and Growth Rate Distributions of Small Self-Nucleated Paracetamol Crystals Grown from Pure Aqueous Solutions. *J. Cryst. Growth* **1999**, *207* (4), 308–318.

(6) Shekunov, B. Y.; Grant, D. J. W. In Situ Optical Interferometric Studies of the Growth and Dissolution Behavior of Paracetamol (Acetaminophen). 1. Growth Kinetics. *J. Phys. Chem. B* **1997**, *101* (20), 3973–3979.

(7) Shekunov, B. Y.; Aulton, M. E.; Adama-Acquah, R. W.; Grant, D. J. W. Effect of Temperature on

Crystal Growth and Crystal Properties of Paracetamol. *J. Chem. Soc. Faraday Trans.* **1996**, *92* (3), 439.

(8) Omar, W.; Al-Sayed, S.; Sultan, A.; Ulrich, J. Growth Rate of Single Acetaminophen Crystals in Supersaturated Aqueous Solution under Different Operating Conditions. *Cryst. Res. Technol.* **2008**, *43* (1), 22–27.

(9) Shekunov, B. Y.; Grant, D. J. W.; Latham, R. J.; Sherwood, J. N. In Situ Optical Interferometric Studies of the Growth and Dissolution Behavior of Paracetamol (Acetaminophen) Crystals. 3. Influence of Growth in the Presence of p-Acetoxyacetanilide. *J. Phys. Chem. B* **1997**, *101* (44), 9107–9112.

(10) Thompson, C.; Davies, M. C.; Roberts, C. J.; Tendler, S. J. .; Wilkinson, M. J. The Effects of Additives on the Growth and Morphology of Paracetamol (Acetaminophen) Crystals. *Int. J. Pharm.* **2004**, *280* (1–2), 137–150.

(11) Cornel, J.; Mazzotti, M. Estimating Crystal Growth Rates Using in Situ ATR-FTIR and Raman Spectroscopy in a Calibration-Free Manner. *Ind. Eng. Chem. Res.* **2009**, *48* (23), 10740–10745.

(12) Mitchell, N. A.; Ó'Ciardhá, C. T.; Frawley, P. J. Estimation of the Growth Kinetics for the Cooling Crystallisation of Paracetamol and Ethanol Solutions. *J. Cryst. Growth* **2011**, *328* (1), 39–49.

(13) Worlitschek, J.; Mazzotti, M. Model-Based Optimization of Particle Size Distribution in Batch-Cooling Crystallization of Paracetamol. *Cryst. Growth Des.* **2004**, *4* (5), 891–903.

(14) Soto, R.; Verma, V.; Lynch, A.; Hodnett, B. K.; Rasmuson, Å. C. Crystal Growth Kinetics of Pharmaceutical Compounds. *Cryst. Growth Des.* **2020**, *20* (12), 7626–7639.

(15) Ó'Ciardhá, C. T.; Mitchell, N. A.; Hutton, K. W.; Frawley, P. J. Determination of the Crystal Growth Rate of Paracetamol As a Function of Solvent Composition. *Ind. Eng. Chem. Res.* **2012**, *51* (12), 4731–4740.

(16) Granberg, R. A.; Bloch, D. G.; Rasmuson, Å. C. Crystallization of Paracetamol in Acetone–Water Mixtures. *J. Cryst. Growth* **1999**, *198–199*, 1287–1293.

(17) Granberg, R. A.; Rasmuson, Å. C. Crystal Growth Rates of Paracetamol in Mixtures of Water + Acetone + Toluene. *AIChE J.* **2005**, *51* (9), 2441–2456.

(18) Mullin, J. W. Crystal Growth. In *Crystallization*; Butterworth-Heinemann: Oxford, 2001; pp 216–288.

(19) Nagy, Z. K.; Fujiwara, M.; Woo, X. Y.; Braatz, R. D. Determination of the Kinetic Parameters for the Crystallization of Paracetamol from Water Using Metastable Zone Width Experiments. *Ind. Eng. Chem. Res.* **2008**, *47* (4), 1245–1252.

(20) McKeown, R. R.; Wertman, J. T.; Dell'Orco, P. C. Crystallization Design and Scale-Up. In *Chemical Engineering in the Pharmaceutical Industry*; John Wiley & Sons, Inc.: Hoboken, NJ, USA, 2010; pp 213–247.

(21) Smith, K. B.; Mackley, M. R. An Experimental Investigation into the Scale-up of Oscillatory Flow Mixing in Baffled Tubes. *Chem. Eng. Res. Des.* **2006**, *84* (11), 1001–1011.

(22) Lawton, S.; Steele, G.; Shering, P.; Zhao, L.; Laird, I.; Ni, X.-W. Continuous Crystallization of Pharmaceuticals Using a Continuous Oscillatory Baffled Crystallizer. *Org. Process Res. Dev.* **2009**, *13* (6), 1357–1363.

(23) Ni, X.; Mackley, M. R.; Harvey, A. P.; Stonestreet, P.; Baird, M. H. I.; Rama Rao, N. V. Mixing Through Oscillations and Pulsations—A Guide to Achieving Process Enhancements in the Chemical and Process Industries. *Chem. Eng. Res. Des.* **2003**, *81* (3), 373–383.

(24) Jian, H.; Ni, X. A Numerical Study on the Scale-Up Behaviour in Oscillatory Baffled Columns. *Chem. Eng. Res. Des.* **2005**, *83* (10), 1163–1170.

(25) Ni, X.; De Gélicourt, Y. S.; Baird, M. H. I.; Rao, N. V. R. Scale-up of Single Phase Axial Dispersion Coefficients in Batch and Continuous Oscillatory Baffled Tubes. *Can. J. Chem. Eng.* **2001**, *79* (3), 444–448.

(26) Brown, C. J.; Ni, X. Online Evaluation of Paracetamol Antisolvent Crystallization Growth Rate with Video Imaging in an Oscillatory Baffled Crystallizer. *Cryst. Growth Des.* **2011**, *11* (3), 719–725.

(27) Brown, C. J.; Ni, X.-W. Evaluation of Growth Kinetics of Antisolvent Crystallization of Paracetamol in an Oscillatory Baffled Crystallizer Utilizing Video Imaging. *Cryst. Growth Des.* **2011**, *11* (9), 3994–4000.

(28) Jiang, M.; Ni, X.-W. Effects of Solvents and Impurity on Crystallization Kinetics and Crystal Properties in a Reactive Crystallization of Paracetamol. *J. Cryst. Growth* **2019**, *523*, 125150.

(29) Cruz, P.; Rocha, F.; Ferreira, A. Effect of Operating Conditions on Batch and Continuous Paracetamol Crystallization in an Oscillatory Flow Mesoreactor. *CrystEngComm* **2016**, *18* (47), 9113–9121.

(30) Jiang, M.; Ni, X.-W. Reactive Crystallization of Paracetamol in a Continuous Oscillatory Baffled Reactor. *Org. Process Res. Dev.* **2019**, *23* (5), 882–890.

(31) Raval, V.; Siddique, H.; Brown, C. J.; Florence, A. J. Development and Characterisation of a Cascade of Moving Baffle Oscillatory Crystallisers (CMBOC). *CrystEngComm* **2020**, *22* (13), 2288–2296.

(32) Brown, C. J.; Lee, Y. C.; Nagy, Z. K.; Ni, X. Evaluation of Crystallization Kinetics of Adipic Acid in an Oscillatory Baffled Crystallizer. *CrystEngComm* **2014**, *16* (34), 8008.

(33) Siddique, H.; Brown, C. J.; Houson, I.; Florence, A. J. Establishment of a Continuous Sonocrystallization Process for Lactose in an Oscillatory Baffled Crystallizer. *Org. Process Res. Dev.* **2015**, *19* (12), 1871–1881.

(34) Ferreira, A.; Rocha, F.; Teixeira, J. A.; Castro, F. Modular Oscillatory Flow Plate Reactor. WO 2017/175207 A1, 2017.

(35) Agnew, L. R.; McGlone, T.; Wheatcroft, H. P.; Robertson, A.; Parsons, A. R.; Wilson, C. C. Continuous Crystallization of Paracetamol (Acetaminophen) Form II: Selective Access to a Metastable Solid Form. *Cryst. Growth Des.* **2017**, *17* (5), 2418–2427.

(36) Briggs, N. E. B. B.; Schacht, U.; Raval, V.; McGlone, T.; Sefcik, J.; Florence, A. J. Seeded Crystallization of β-L-Glutamic Acid in a Continuous Oscillatory Baffled Crystallizer. *Org. Process Res. Dev.* **2015**, *19* (12), 1903–1911.

(37) Peña, R.; Oliva, J. A.; Burcham, C. L.; Jarmer, D. J.; Nagy, Z. K. Process Intensification through Continuous Spherical Crystallization Using an Oscillatory Flow Baffled Crystallizer. *Cryst. Growth Des.* **2017**, *17* (9), 4776–4784.

(38) Granberg, R. A.; Rasmuson, Å. C. Solubility of Paracetamol in Pure Solvents. *J. Chem. Eng. Data* **1999**, *44* (6), 1391–1395.

(39) Schöll, J.; Lindenberg, C.; Vicum, L.; Brozio, J.; Mazzotti, M. Precipitation of α L-Glutamic Acid: Determination of Growth Kinetics. *Faraday Discuss.* **2007**, *136*, 247.

(40) Hu, W.; Xie, J.; Chau, H. W.; Si, B. C. Evaluation of Parameter Uncertainties in Nonlinear Regression Using Microsoft Excel Spreadsheet. *Environ. Syst. Res.* **2015**, *4* (1), 4.

(41) Montgomery, D. C. *Design and Analysis of Experiments*, 5th ed.; John Wiley & Sons, Inc.: New York, 2007.

(42) Randolph, A. D.; Larson, M. A. Crystallization Kinetics. In *Theory of Particulate Processes*; Academic Press: New York and London, 1971; pp 101–110.

(43) Nielsen, A. E.; Toft, J. M. Electrolyte Crystal Growth Kinetics. *J. Cryst. Growth* **1984**, *67* (2), 278–288.

(44) Mersmann, A.; Eble, A.; Heyer, C. Crystal Growth. In *Crystallization Technology Handbook*; Mersmann, A., Ed.; Marcel Dekker, Inc: New York, 2001.

(45) Mersmann, A. Design of Crystallizers. In *Crystallization Technology Handbook*; Mersmann, A., Ed.; Marcel Dekker, Inc: New York, 2001; pp 323–392.

(46) Khattab, I. S.; Bandarkar, F.; Fakhree, M. A. A.; Jouyban, A. Density, Viscosity, and Surface Tension of Water+ethanol Mixtures from 293 to 323K. *Korean J. Chem. Eng.* **2012**, *29* (6), 812–817.

(47) Mersmann, A. Appendix. In *Crystallization Technology Handbook*; Mersmann, A., Ed.; Marcel Dekker, Inc: New York.

(48) Stonestreet, P.; Harvey, A. P. A Mixing-Based Design Methodology for Continuous Oscillatory Flow Reactors. *Chem. Eng. Res. Des.* **2002**, *80* (1), 31–44.

Chapter 9 - Continuous Cooling Crystallization in a Planar Oscillatory Flow Crystallizer

9.1 Introduction

The manufacture of most active pharmaceutical ingredients (APIs) involves at least one crystallization step. This step is especially important because it largely defines the final physicochemical properties of the API, including purity, polymorphism, morphology, size, and crystal size distribution (CSD). The size and CSD are particularly crucial because they determine the API dissolution profile and, consequently, its bioavailability, and play a key role in the efficiency of downstream operations, such as filtration, drying and formulation. From a pharmaceutical perspective, small crystals are preferred for faster dissolutions, whereas, from a manufacturing perspective, larger crystals are preferred for efficient downstream processing.[1,2]

In the pharmaceutical industry, batch crystallization is standard practice. The rate at which supersaturation is generated and consumed during the course of batch crystallization defines the final CSD. This is true whether supersaturation is generated by cooling, addition of antisolvent, evaporation of solvent or chemical reaction. In the case of cooling crystallization, the supersaturation profile is controlled by the cooling profile.[3] Linear cooling profiles provide constant cooling rates from the beginning to the end of the crystallization process; concave cooling profiles are similar to natural cooling, with faster cooling rates at the beginning and slower cooling rates at the end of the crystallization process; and convex cooling profiles are the direct opposite of concave cooling profiles, with slower cooling rates at the beginning and faster cooling rates at the end of the crystallization process. Convex cooling profiles maintain the operation at low levels of supersaturation, which minimizes the formation of fines due to excessive nucleation, and are therefore preferred to produce larger mean crystal sizes and narrower CSDs.[4–6]

Some type of fines removal strategy can also be employed to gain control over the CSD. There are basically two main types of fines removal techniques: external and *in situ*. In the first case, a classified stream of slurry containing only fines is removed from the crystallizer, heated to dissolve the fines, and then recycled back to the crystallizer.[7,8] In the second case, the slurry is alternately heated and cooled via temperature cycling, which promotes the dissolution of the fines during the heating cycles, and the growth of the larger crystals during the cooling cycles. *In situ* fines removal techniques do not require additional equipment, which avoids additional capital and operating costs, and are therefore often preferred over external fines removal techniques.

Temperature cycling is commonly implemented on a trial-and-error basis by optimizing the time interval, the temperature range between the cooling and heating cycles, the cooling and heating rates, and the number of

cycles for a target mean crystal size and CSD.[9–11] Alternatively, temperature cycling can also be implemented by using a model-free approach[12–16] or a model-based approach.[17,18] Model-free approaches are closed-loop feedback control strategies that make use of real time measurements provided by process analytical technologies to adjust the operating policies and manage nucleation, crystal growth and dissolution events; whereas model-based approaches are open-loop control strategies that follow the optimal temperature profile, which is obtained by solving a population balance model that adequately describes the crystallization process.

Temperature cycling can also be used to promote de-agglomeration due to the dissolution of the bonds between the crystals during the heating cycles.[13,16,19,20] Agglomeration is usually undesirable because the formation of agglomerates promotes the entrapment of mother liquid and therefore compromises the purity of the final product. Furthermore, the entrapped mother liquor is difficult to remove during washing and drying, which contributes to the caking of crystals during storage. Moreover, irregular agglomerates can generate broad CSDs and induce the formation of a large amount of fines during transport and storage.[21,22]

Temperature cycling is not limited to batch crystallization. Temperature cycling has also been implemented in continuous in a mixed suspension mixed product removal (MSMPR) cascade,[23] in a plug flow crystallizer (PFC),[24] and in slug flow crystallizers (SFC).[25–27] Acevedo *et al*.[23] integrated a dissolution stage for fines removal within a MSMPR cascade for the cooling crystallization of paracetamol; with fines removal, larger particles with a narrower CSD were obtained, but with a significant decrease in yield. Majumder and Nagy[24] simulated the cooling crystallization of potash alum in a PFC; the PFC was conceptually divided into several segments where the temperature of each segment could be controlled independently; some segments were cooled for crystal growth, while others were heated for fines removal; nucleation, crystal growth and dissolution kinetics were incorporated into the population balance model to simulate the process; the simulations showed that the best results in terms of fines removal are achieved when the larger crystals grow faster than the smaller ones and the smaller crystals dissolve faster than the larger ones. Eder *et al*.[25] produced crystals of acetylsalicylic acid by cooling sonocrystallization in a SFC; seeds were produced *in situ* via cooling sonocrystallization, and then a temperature cycling was employed to dissolve the fines and increase the mean crystal size of the final product. Jiang *et al*.[26] produced crystals of L-asparagine monohydrate by cooling crystallization in a SFC; nucleation was induced by mixing hot and cold solutions in coaxial or radial mixers, and then a temperature cycling was employed to increase the mean crystal size, reduce aggregation and improve the overall uniformity of the final product. Besenhard *et al*.[27] produced crystals of D-mannitol by cooling crystallization in a SFC; a suspension with seeds was prepared externally and then fed to the SFC where it was subjected to a temperature cycling; increasing the difference of temperatures between the cooling and heating cycles decreased the number of fines and increased the mean crystal size of the final product.

In this work, paracetamol was crystallized from a 40% (v/v) mixture of ethanol and water in a planar oscillatory flow crystallizer (planar-OFC). In this work, two sets of experiments were performed: continuous crystallization without seeding, and continuous crystallization with seeding and temperature cycling. The main goal was to

investigate the impact and benefits of temperature cycling on the size and CSD of paracetamol. To the best of our knowledge, this is the first time that temperature cycling is employed in an OFC.

9.2 Materials and Methods

9.2.1 Material

Paracetamol (CAS number 103-90-02, min. 99% purity) was supplied by Sigma-Aldrich, ethanol (CAS number 64-17-5, min. 99.5% purity) was supplied by VWR Chemicals, and ultrapure water was obtained from a Millipore ultrapure water system.

9.2.2 Crystallizer

The planar-OFC consists of a plate-like crystallizer with three stacked plates: two polycarbonate plates, one at the base and one at the top, and one aluminum plate coated with Halar® (ethylene-chlorotrifluoroethylene copolymer, ECTFE) or one Teflon® (poly(tetrafluoroethylene), PTFE) plate in the middle – **Figure 9.1 (a)**. The crystallization process takes place in a channel designed with smooth periodic constrictions located between the middle and top plates, and the water of a cooling/heating jacket circulates in a straight channel located between the base and middle plates. The two channels were carved in the middle plate; the top plate seals the crystallization channel and the base plate seals the jacket channel. The crystallization channel has 6 access points (one main inlet, one main outlet and four intermediate inlets/outlets) and comprises a volume of approximately 71 mL (operational volume). The dimensions of each inter-constriction cell are presented in **Figure 9.1 (b)**.

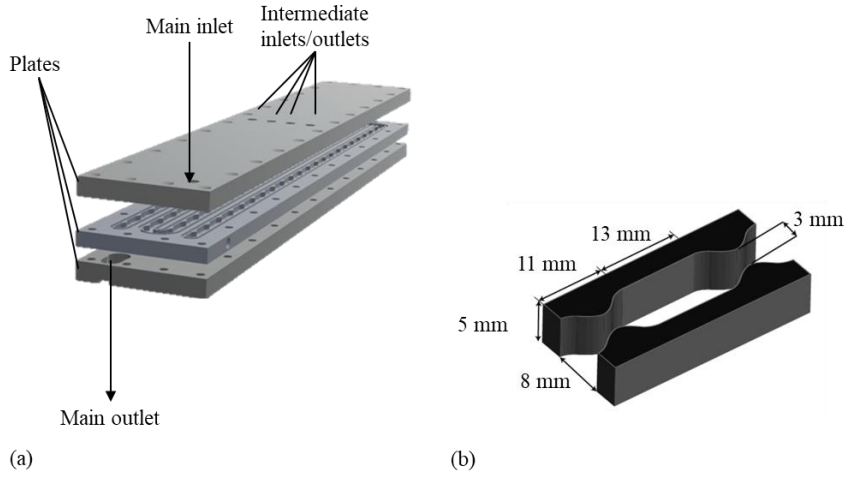


Figure 9.1 – Plate-like planar-OFC. (a) Three stacked plates. (b) Dimensions of each inter-constriction cell.

The continuous crystallizer is formed by two or three planar-OFCs in series. With two planar-OFCs in series, the continuous crystallizer contains an operational volume of 142 mL, and with three planar-OFCs in series, the continuous crystallizer contains an operational volume of 213 mL. The temperature of each planar-OFC is controlled by a cooling/heating bath (Ministat 125, Huber), and the frequency and amplitude of oscillation in the continuous crystallizer is controlled by a linear motor actuating a piston with a 10.3 mm diameter (H01-23x166/80, LinMot).

9.2.3 Continuous Crystallization without Seeding

The experimental set-up for continuous crystallization without seeding with two planar-OFCs in series is presented in **Figure 9.2**. In some runs the middle plate was made of aluminum coated with Halar®, in other runs the middle plate was made of Teflon®.

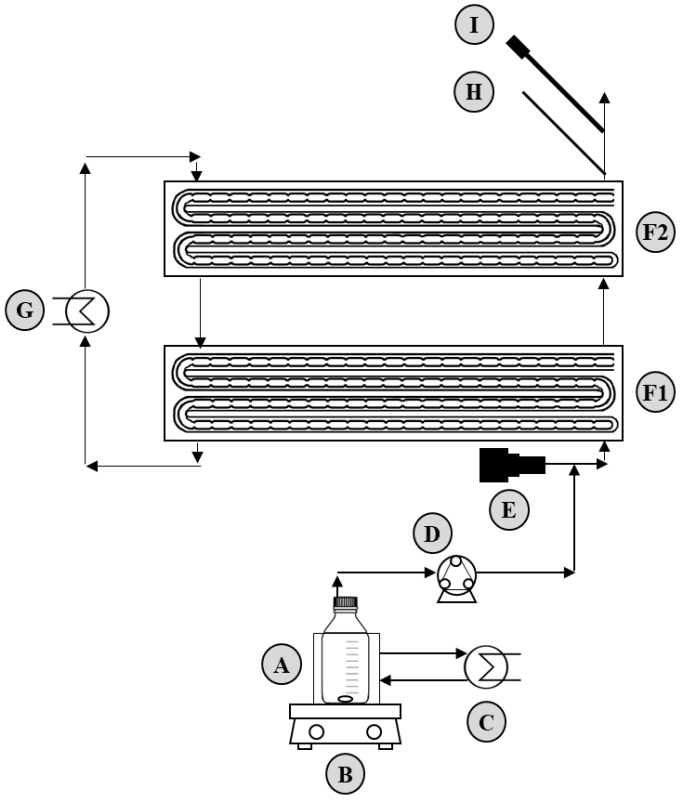


Figure 9.2 – Experimental set-up for continuous crystallization without seeding with two planar-OFCs in series. A – jacketed glass vessel; B – magnetic stirrer; C – cooling/heating bath; D – peristaltic pump; E – linear motor; F1 and F2 – planar-OFCs; G – cooling/heating bath; H – thermocouple; I – ATR-UV/Vis immersion probe.

A solution with a given concentration of paracetamol in a 40 % (v/v) mixture of ethanol and water was prepared in a jacketed glass vessel (Schott glass reactor) with 1 L of maximum capacity. The temperature in the jacket was kept constant by a cooling/heating bath, and stirring was provided by a magnetic stirrer (C-MAG HS 7 digital, IKA). The solution was stirred at 300 rpm and the temperature of the solution, T_i, was kept at 10 °C above its saturation temperature for 1 hour. Then, the temperature of the solution was decreased to 3 °C above its saturation temperature.

First, the continuous crystallizer was thermostated at a given temperature, T_f. Then, a 40% (v/v) mixture of ethanol and water was pumped (BT300-2J, Longer Pump) from a flask to the continuous crystallizer and recirculated back to the flask to eliminate the air bubbles. When the continuous crystallizer was completely free from air bubbles the recirculation was stopped. Then, the solution of paracetamol was pumped from the vessel into the continuous crystallizer at a given flow rate, Q, and the oscillation was activated at a given frequency, f, and amplitude, x_0 (center-to-peak in the straight section). The temperature of the suspension at the outlet of the continuous crystallizer was recorded by a thermocouple connected to a data acquisition system (NI cDAQ-9171, National Instruments), and the absorbance of the solution at the outlet of the continuous crystallizer, Abs, was measured at 249 nm by an attenuated total reflectance (ATR) immersion probe (Katana 6, Hellma) connected to an UV/Vis spectrometer (SPEC RES+ UV/VIS-Sarspec). Samples of the slurry were collected at the outlet of the continuous crystallizer at regular intervals. The samples were filtered and left to dry in an oven at 80 °C overnight. Then, the CSD of each sample was measured by a laser diffraction particle size analyzer (LS230, Beckman Coulter), and images of the crystals were acquired using a stereoscopic zoom microscope (SMZ1500, Nikon) coupled to a video camera (DS-Ri1, Nikon).

This procedure was repeated for different runs. The experimental conditions of each run are presented in **Table 9.1**. In this table, the initial supersaturation ratio, S_i, was calculated as the ratio between the concentration of paracetamol in the vessel and the solubility of paracetamol at T_f.

Table 9.1 – Continuous crystallization without seeding: experimental conditions of each run.

Run	Wall material	f (Hz)	x_0 (mm)	Q (mL min^{-1})	T_i (°C)	C_i (g kg^{-1})	T_f (°C)	S_i
P1	Halar® coating	2	12	29.98	35	139.58	20	1.5
P2	Halar® coating	2	12	14.94	35	139.58	20	1.5
P3	Halar® coating	2	12	7.32	35	139.58	20	1.5
P4	Halar® coating	4	16	29.98	25	98.32	10	1.5
P5	Teflon	4	16	30.02	25	98.32	10	1.5
P6	Teflon	4	16	14.90	25	98.32	10	1.5
P7	Teflon	4	16	14.78	33	131.1	10	2
P8	Teflon	4	16	30.02	33	131.1	10	2
P9	Teflon	4	16	7.60	33	131.1	10	2

9.2.4 Preparation of the Seeds

The experimental setup for the preparation of the seeds is presented in **Figure 9.3**.

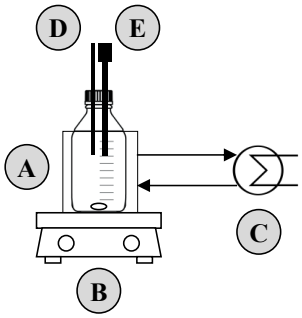


Figure 9.3 – Experimental setup for the preparation of the seeds. A – STC; B – magnetic stirrer; C – cooling/heating bath; D – thermocouple; E – ATR-UV/Vis immersion probe.

The preparation of the seeds involved two steps: the first step was the preparation of a solution of paracetamol in a stirred tank crystallizer (STC), and the second step was the application of a controlled cooling program to induce the crystallization of paracetamol in the STC. The STC consisted of a jacketed glass vessel with 1 L of maximum capacity. The temperature in the jacket was controlled by a cooling/heating bath, and stirring was provided by a magnetic stirrer. The temperature of the solution was recorded by a thermocouple and the absorbance of the solution was measured at 249 nm by an ATR-UV/Vis immersion probe.

A solution with a given concentration of paracetamol in a 40% (v/v) mixture of ethanol and water, C_{STC}, was prepared in the STC. The solution was stirred at 300 rpm and the temperature in the bath, T_b, was manipulated to keep the temperature of the solution, T_{STC}, at 10 °C above its saturation temperature, T_s, for 1 hour. Then, the temperature in the bath was manipulated to cool the solution to 3 °C above its saturation temperature. After that, the temperature in the bath was decreased at a cooling rate, θ, of 0.5 °C min^{-1} to cool the solution from 3 °C above its saturation temperature to the final temperature. At some point, paracetamol crystallized from solution. Approximately 3 h after the start of the controlled cooling program, when the solution reached solubility, a sample of the slurry was filtered, and the seeds were left to dry in an oven at 80 °C overnight. Then, the CSD of the seeds was measured and images of the seeds were acquired as previously described.

Two protocols were employed for the preparation of the seeds: Protocol 1 and Protocol 2. The difference between the two protocols is presented in **Figure 9.4**. Basically, the two protocols followed the same sequence of steps, but, in the case of Protocol 1, the final suspension was saturated at 10 °C, and, in the case of Protocol 2, the final suspension was saturated at 20 °C. The density of seeds in the final suspension was similar in the two protocols (61.51 g of seeds per kg of solution in the case of Protocol 1, and 59.97 g of seeds per kg of solution in the case of Protocol 2). A suspension with seeds was prepared via Protocol 1 or Protocol 2 before each seeded continuous crystallization experiment.

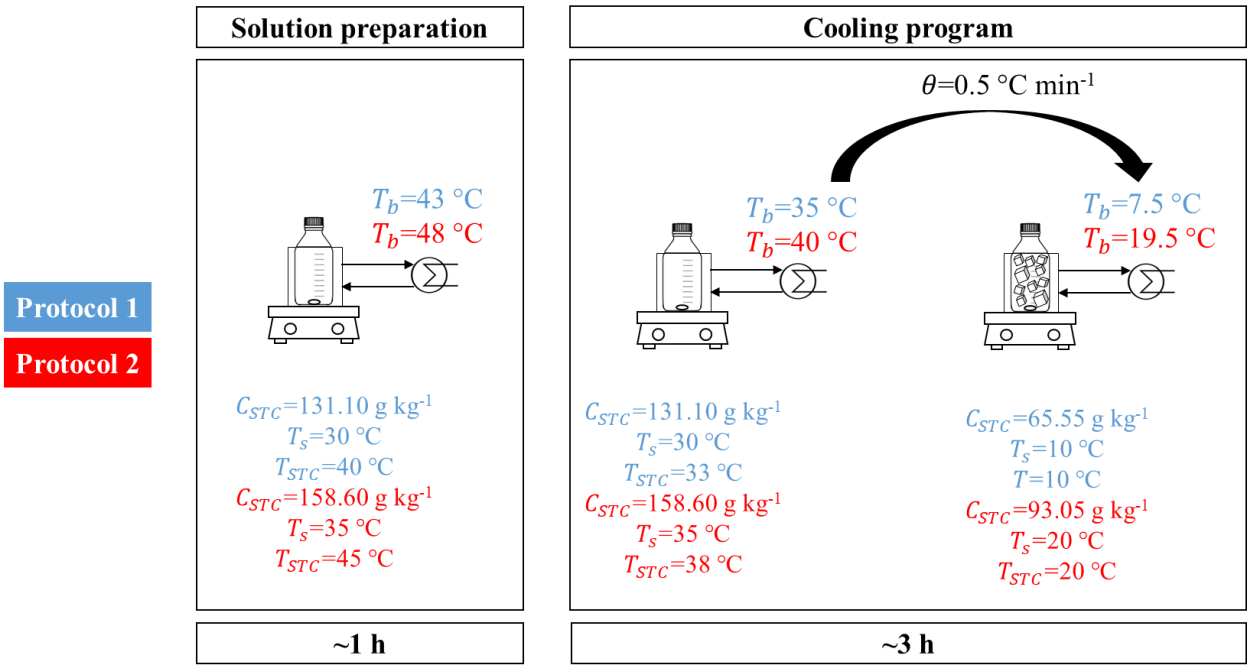


Figure 9.4 – Protocol 1 and Protocol 2 for the preparation of the seeds.

9.2.5 Continuous Crystallization with Seeding and Temperature Cycling

The experimental set-up for continuous crystallization with seeding and temperature cycling with two and three planar-OFCs in series is presented in **Figure 9.5 (a)** and **(b)**, respectively. In this type of experiments, the middle plate was made of aluminum coated with Halar®.

First, a 40% (v/v) mixture of ethanol and water was pumped from a flask to the continuous crystallizer and recirculated back to the flask to eliminate the air bubbles. When the continuous crystallizer was completely free from air bubbles the recirculation was stopped. Then, a suspension with seeds was pumped at Q=7.30 mL min^{-1} from the STC into the hot planar-OFC and the oscillation was activated at f=2 Hz and x_0=12 mm. The temperature of the solution at the outlet of the hot planar-OFC, T_h, was higher than in the STC, T_{STC}, which led to the dissolution of some seeds in the hot planar-OFC. Then, the suspension was injected into the cold planar-OFC. The temperature of the solution at the outlet of the cold planar-OFC, T_c, was lower than at the outlet of the hot planar-OFC, T_h, which led to the growth of the remaining seeds (and eventually also secondary nucleation, agglomeration and crystal breakage) in the cold planar-OFC. In order to increase the duration of the dissolution step in the continuous crystallizer, in some runs, there were two hot planar-OFCs (**Figure 9.5 (b)**) instead of just one (**Figure 9.5 (a)**). The temperature of the solution at the outlet of the cold planar-OFC was recorded by a thermocouple and the absorbance of the solution at the outlet of the cold planar-OFC was measured at 249 nm by an ATR-UV/Vis immersion probe. The supersaturation ratio at the outlet of the cold planar-OFC was calculated as the ratio between the absorbance of the solution and the absorbance of a saturated

solution at T_c. Samples of the slurry were collected at the outlet of the cold planar-OFC at regular intervals. After 4 residence times, a sample was collected at the outlet of the hot planar-OFC (or second hot planar-OFC). The samples were filtered and left to dry in an oven at 80 °C overnight. Then, the CSD of each sample was measured and images of the crystals were acquired as previously described.

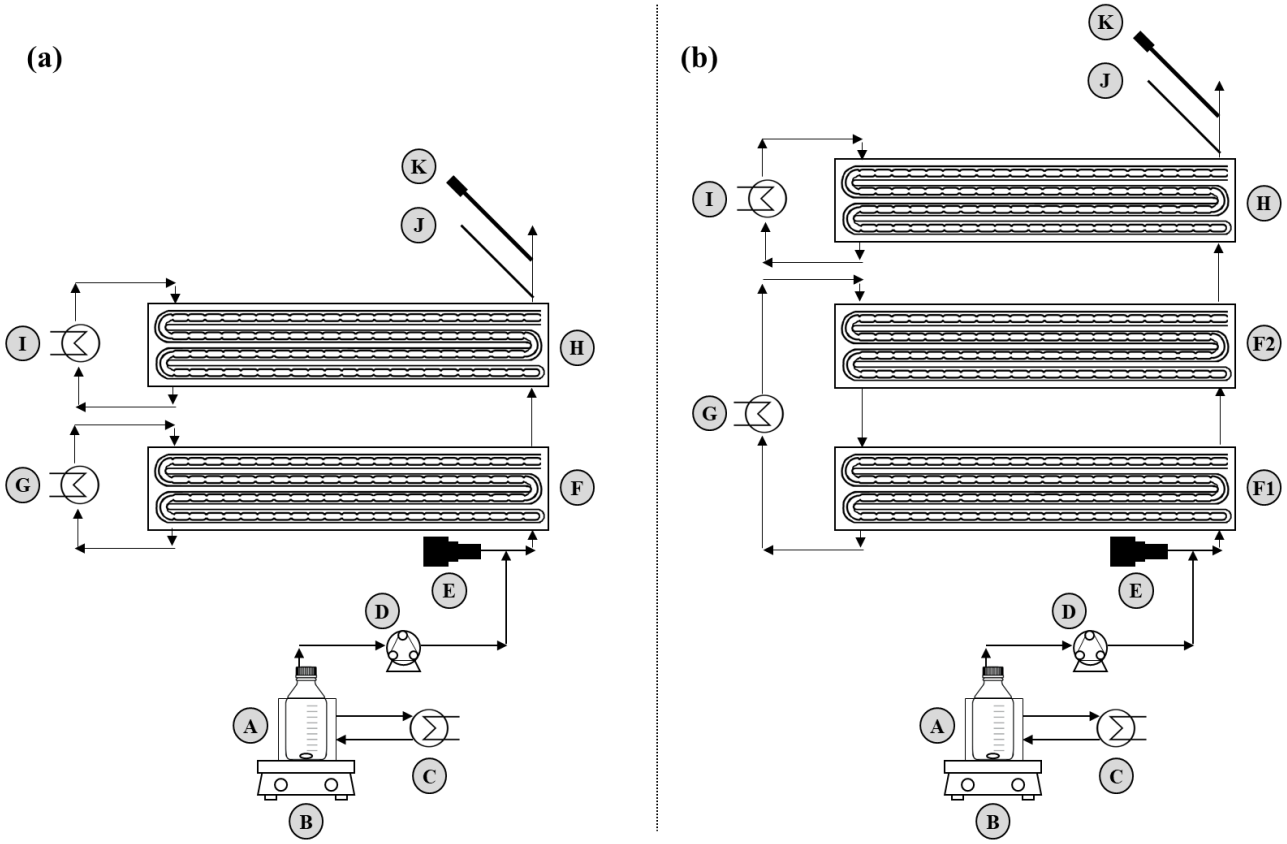


Figure 9.5 – Experimental set-up for continuous crystallization with seeding and temperature cycling with two (a) and three (b) planar-OFCs in series. A – STC; B – magnetic stirrer; C – cooling/heating bath; D – peristaltic pump; E – linear motor; F – hot planar-OFC; F1 – first hot planar-OFC; F2 – second hot planar-OFC; G – cooling/heating bath; H – cold planar-OFC; I – cooling/heating bath; J – thermocouple; K – ATR-UV/Vis immersion probe.

This procedure was repeated for different runs. The experimental conditions of each run are presented in **Table 9.2**. In this table, S_{max} is the maximum possible supersaturation ratio at the inlet of the cold planar-OFC. For example, in the case of Run 2: the concentration of paracetamol at the inlet of the hot planar-OFC is 65.55 g kg^{-1}; the temperature at the outlet of the hot planar-OFC is 13 °C; the solubility of paracetamol at 13 °C is 72.53 g kg^{-1}; therefore, if the solution of paracetamol reached solubility at the outlet of the hot planar-OFC due to the dissolution of seeds, then the concentration of paracetamol at the outlet of the hot planar-OFC would be 72.53 g kg^{-1}; the temperature at the outlet of the cold planar-OFC is 6 °C; the solubility of paracetamol at 6 °C

is 56.70 g kg^{-1}; therefore, the maximum possible supersaturation ratio at the inlet of the cold planar-OFC is S_{max}=72.53/56.70=1.3. The same rationale was used to calculate S_{max} for each run.

Table 9.2 – Continuous crystallization with seeding and temperature cycling: experimental conditions of each run.

Run	T_{STC} (°C)	T_h (°C)	N.º of hot planar-OFCs	S_{max}	T_c (°C)
1	10	10	1	1.2	6
2	10	13	1	1.3	6
3	10	15	1	1.4	6
4	10	17	1	1.5	6
5	10	20	1	1.6	6
6	20	23	1	1.3	16
7	20	26	1	1.4	16
8	20	28	1	1.5	16
9	20	29	1	1.6	16
10	10	13	2	1.3	6
11	10	15	2	1.4	6
12	20	23	2	1.3	16
13	20	26	2	1.4	16

9.3 Results and Discussion

9.3.1 Continuous Crystallization without Seeding

Figure 9.6 presents the evolution of the absorbance, Abs, and temperature, T, and **Figure 9.7** presents the evolution of the volume-based CSD, $f_V(d)$, for each continuous crystallization run without seeding. The absorbance is directly related to the concentration of paracetamol in the mother liquor, but the signal measured by the ATR-UV/Vis probe was not calibrated. During Run P1, there is a peak of absorbance somewhere between the first and second residence times (5-10 min). After this peak, the absorbance decreases substantially due to the nucleation and crystal growth of paracetamol in the continuous crystallizer. However, at some point between the second and the third residence times (10-15 min), the absorbance starts to increase substantially, probably due to the growth of crystals of paracetamol on the surface of the ATR-UV/Vis probe. At the same time, the crystallization channel becomes severely fouled due to the growth of large crystals of paracetamol on the walls of the channel. Ultimately, after only 22 min of operation, the crystallization channel clogs and the operation is shut down.

Since decreasing the flow rate decreases the relative velocity between the crystals that growth on the walls of the crystallization channel and the mother liquor, then decreasing the flow rate should decelerate crystal growth

on the walls. Therefore, the flow rate was decreased from Q=29.98 mL min^{-1} in Run P1, to Q=14.94 mL min^{-1} in Run P2, to Q=7.32 mL min^{-1} in Run P3. Decreasing the flow rate effectively decelerated crystal growth on the walls, which extended the operation time from 22 min in Run P1, to 56 min in Run P2, to 65 min in Run P3, however, this was not enough to avoid fouling and eventually clogging of the crystallization channel. Moreover, the evolution of the CSD and its lack of uniformity during Runs P1, P2 and P3 are clearly indicative of a complex dynamic between nucleation, crystal growth, agglomeration, crystal breakage and fouling. Unfortunately, the flow rate could not be decreased even further because lower flow rates would not be able to drag the crystals along the crystallizer.

Nucleation and crystal growth are favored near the wall of the crystallization channel because the temperature near the wall is lower than the temperature in the bulk, and so the supersaturation near the wall is higher than the supersaturation in the bulk. Therefore, to reduce the gradient of temperatures and supersaturations in the crystallization channel, the oscillation intensity was increased from f=2 Hz and x_0 =12 mm in Run P1 to f=4 Hz and x_0 =16 mm in Run P4. In addition, to reduce the nucleation rate, the temperature was decreased from T_f=20 °C in Run P1 to T_f=10 °C in Run P4. These changes extended the operation time from 22 min in Run P1 to 46 min in Run P4, however, this was still not enough to avoid fouling and eventually clogging of the crystallization channel. Moreover, the evolution of the CSD and its lack of uniformity during Runs P1 and P4 are clearly indicative of non-steady state.

At this point, it was evident that paracetamol has a great affinity with the wall material of the crystallization channel. Lee *et al.*[31] reported that fully fluorinated polymers wet less than partially fluorinated polymers,[31] so, to reduce the contact angle between the solution of paracetamol and the wall material of the crystallization channel, the wall material was changed from Halar® coating (ECTFE, a partially fluorinated polymer) in Run P4 to Teflon® (PTFE, a fully fluorinated polymer) in Run P5. Changing the wall material successfully avoided fouling, but only because paracetamol did not crystallize in the continuous crystallizer. (The large variation of absorbance during Run P5 was due to the presence of air bubbles, which were eventually removed.) This result suggests that heterogeneous nucleation on the walls of the crystallization channel should be the dominant mechanism of nucleation at the beginning of the crystallization process. Therefore, to increase the residence time, t_r, the flow rate was decreased from Q=30.02 mL min^{-1} (t_r ≈5 min) in Run 5 to Q=14.90 mL min^{-1} (t_r ≈10 min) in Run 6. Unfortunately, this was still not enough to have crystallization in the continuous crystallizer. (At the beginning of Run 6, the absorbance was not 0 because there was still some solution of paracetamol in the crystallization channel from the previous run, which was eventually removed as the new solution of paracetamol was pumped into the continuous crystallizer.) Therefore, the initial supersaturation was increased from S_i=1.5 in Run P6 to S_i=2.0 in Run P7. Increasing the initial supersaturation allowed to have crystallization in the crystallization channel, however, clogging could not be prevented. On the one hand, increasing the flow rate from Q=14.78 mL min^{-1} in Run P7 to Q=30.02 mL min^{-1} in Run P8, as expected, did not help. On the other hand, decreasing the flow rate from Q=14.78 mL min^{-1} in Run P7 to Q=7.60 mL min^{-1} in

Run P9 led to an apparent steady state as suggested by the practically constant absorbance and the relatively uniform CSDs, but, clogging still could not be prevented.

Fouling is a common challenge in continuous crystallizers, and the risk is even more imminent when crystallization is triggered by spontaneous nucleation in tubular and channel-type crystallizers such as OFCs. For example, Brown *et al.*[32] had to increase the oscillation intensity to improve the suspension of solids and prevent blockages during the antisolvent crystallization of salicylic acid in an OFC. Similarly, Peña *et al.*[33] had to increase the oscillation intensity and decrease the initial supersaturation to reduce the risk of fouling during the spherical crystallization of benzoic acid in an OFC. Operating within the metastable zone with seeding is the most common strategy to reduce the risk of fouling and clogging in OFCs. For example, Briggs *et al.*[34] studied the cooling crystallization of L-glutamic acid with and without seeding in an OFC; while the unseeded experiments resulted in significant encrustation on the crystallizer walls due to excessive nucleation, the seeded experiments could be operated for more than 10 h without significant fouling (except for one experiment operated at high feed solution concentration and low seed loading). Jiang and Ni[35] studied the reactive seeded cooling crystallization of paracetamol in an OFC; seeding successfully prevented excessive nucleation and subsequent encrustation and/or blockages. Raval *et al.*[36] investigated the seeded cooling crystallization of α-lactose monohydrate and paracetamol in a four-stage cascade of OFCs with moving baffles; no evidence of fouling in the crystallizer or blockage of the transfer lines was observed. Alternatively, additives can also be used to avoid excessive nucleation. For example, Agnew *et al.*[37] investigated the cooling crystallization of paracetamol in a two-stage MSMPR and in an OFC in the presence of metacetamol; the addition of 25% (w/w) of metacetamol avoided fouling in both crystallizers, but decreasing the concentration of metacetamol to 18% (w/w) in the OFC resulted in the eventual blockage of the crystallizer.

Besides causing operational challenges, including blockages and heat transfer issues, fouling can drive the system away from the desired state of control, with implications on critical product attributes and yield. When the crystallizer cannot be operated for extended time without fouling, the advantages of continuous crystallization are severely reduced. Therefore, continuous crystallization with seeding was considered as a more attractive approach for continuous crystallization in a planar-OFC.

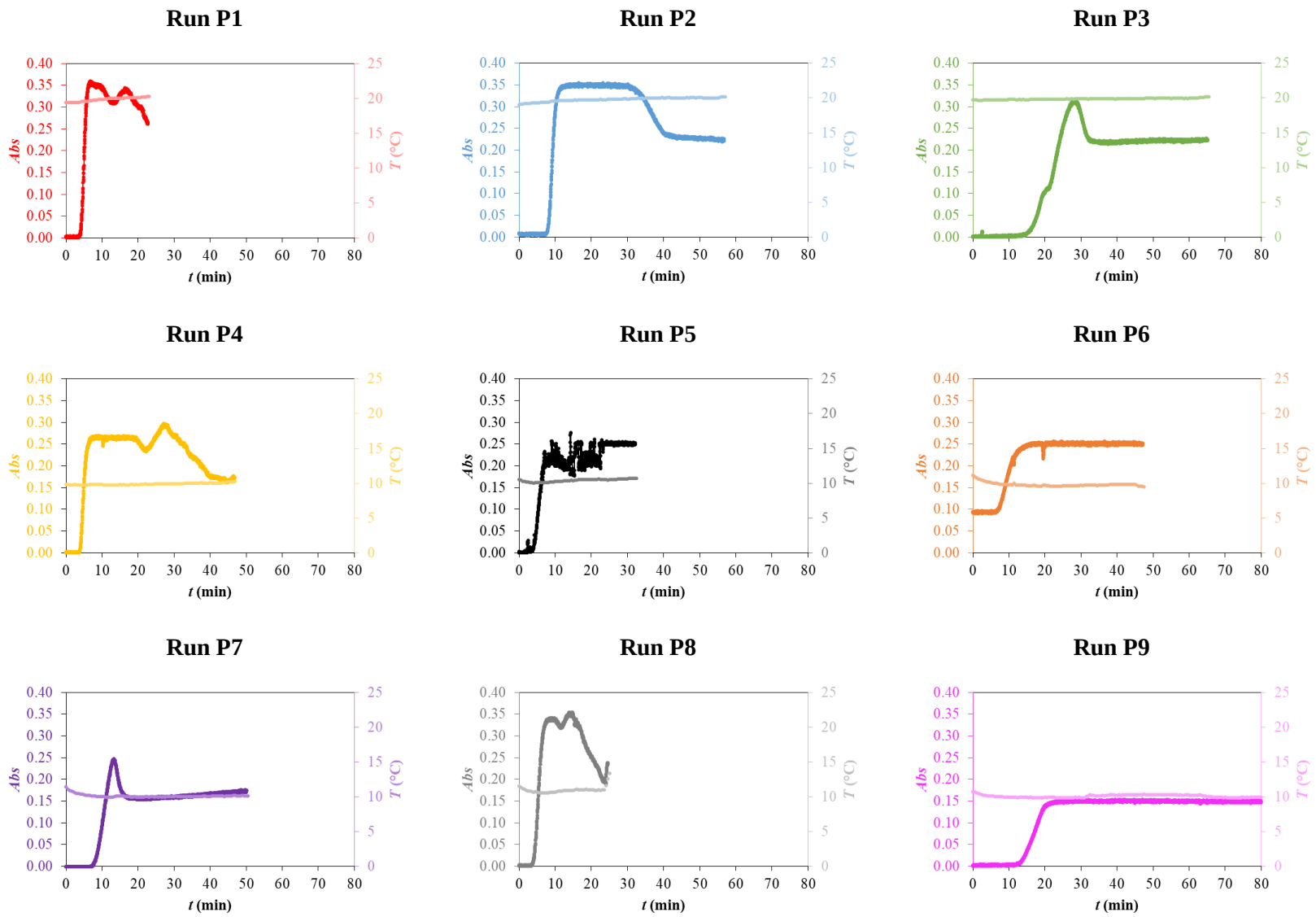


Figure 9.6 – Continuous crystallization without seeding: evolution of absorbance and temperature for each run.

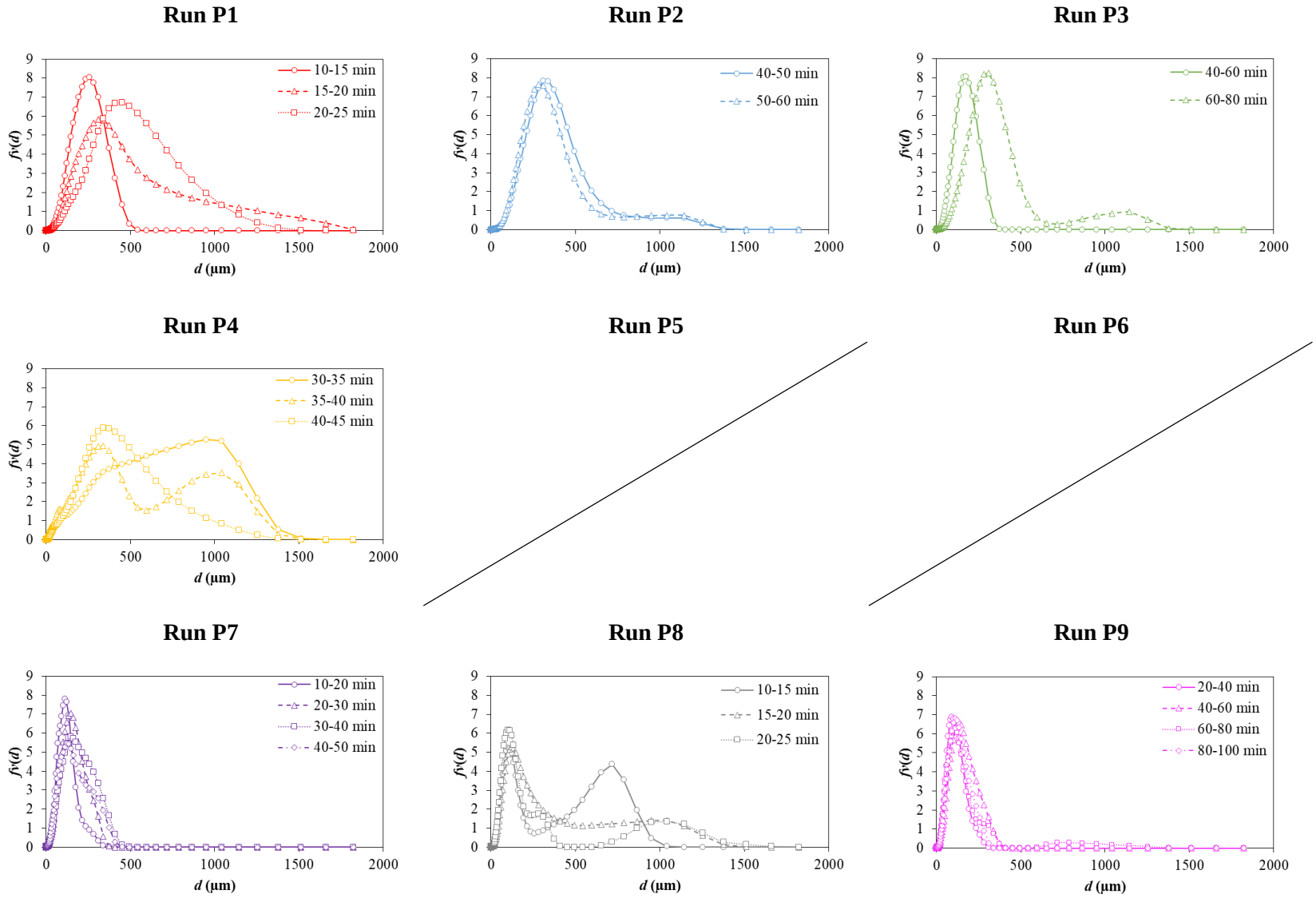


Figure 9.7 – Continuous crystallization without seeding: evolution of the volume-based CSD for each run.

9.3.2 Preparation of the Seeds

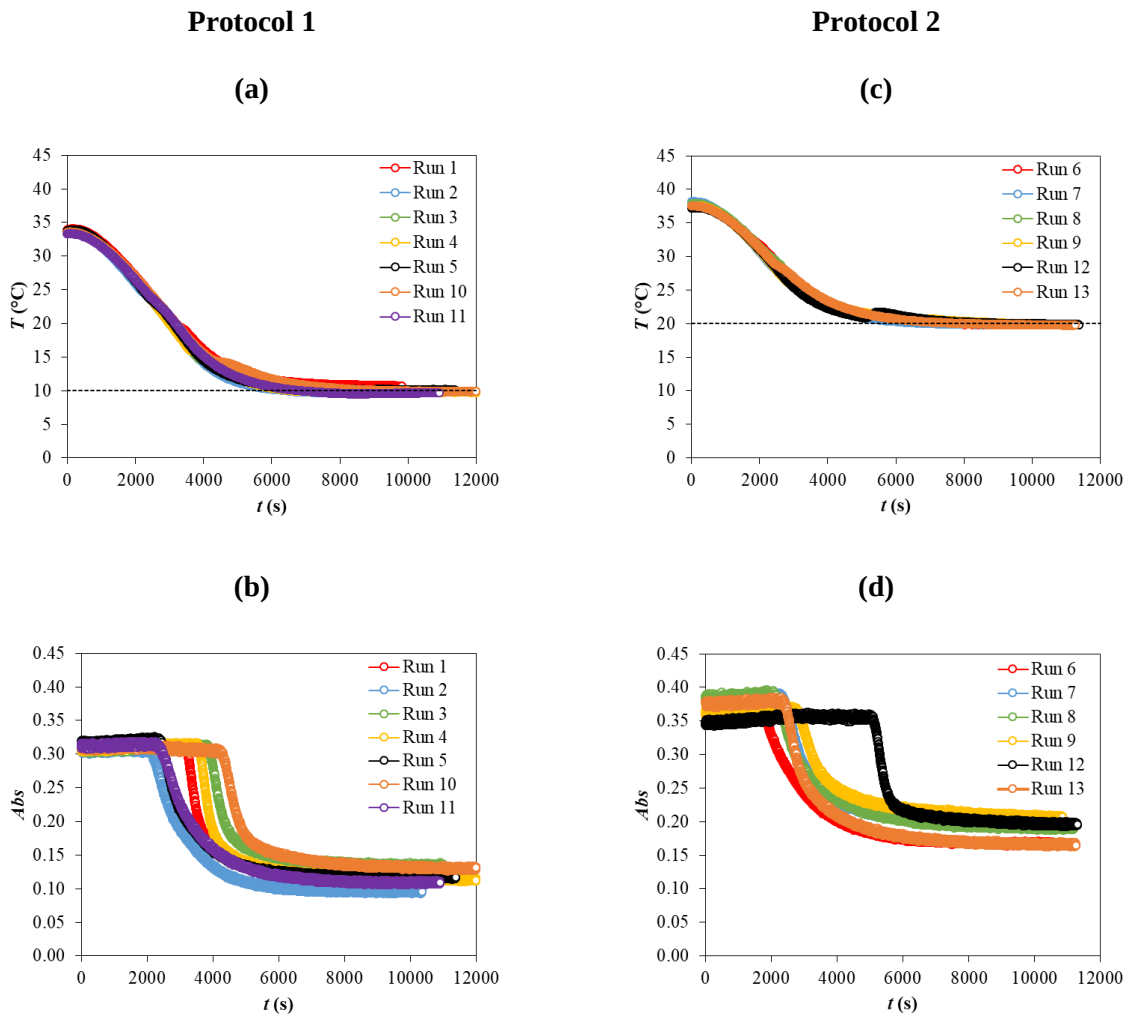


Figure 9.8 – (a) Evolution of temperature and (b) evolution of absorbance during Protocol 1. (c) Evolution of temperature and (d) evolution of absorbance during Protocol 2.

Figure 9.8 (a) and **(c)** present the evolution of the temperature in the STC during the preparation of the seeds according to Protocol 1 and Protocol 2, respectively. These figures show that the evolution of the temperature during the controlled cooling program was identical in all runs. **Figure 9.8 (b)** and **(d)** present the evolution of the absorbance in the STC during the preparation of the seeds according to Protocol 1 and Protocol 2, respectively. These figures show that the onset of nucleation, detected as a sharp decay of absorbance and a slight increase of temperature, occurred sometime after 30 min (1800 s) from the start of the controlled cooling program. It is important to note that, although the absorbance is directly related to the concentration of paracetamol, the signal measured by the ATR-UV/Vis probe was not calibrated. This is the reason why the absorbances at the start and at the end of the controlled cooling program are not the same for all runs, even though the concentrations of paracetamol at the start and at the end are the same for all runs. From our

experience, the signal measured by the ATR-UV/Vis probe is significantly affected by its position, the deposition of solute on its surface, and the temperature. Therefore, the data extracted from the ATR-UV/Vis probe was not used to measure the exact concentration of paracetamol in solution, instead, it was used to insure that the concentration of paracetamol in solution reached steady state, or, in other words, that the concentration of paracetamol in solution reached solubility at the temperature of operation.

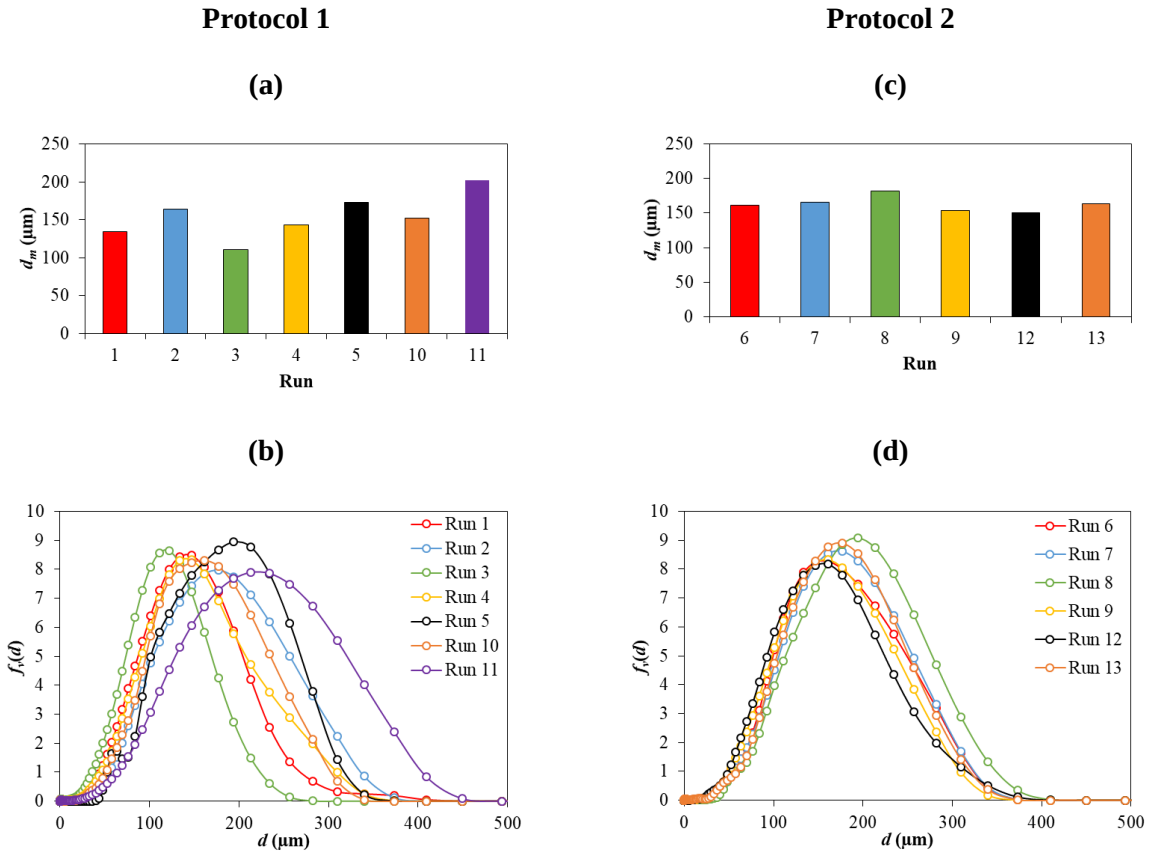


Figure 9.9 – (a) Mean diameter and (b) volume-based CSD of the seeds produced via Protocol 1. (c) Mean diameter and (d) volume-based CSD of the seeds produced via Protocol 2.

Figure 9.9 presents the mean diameter, d_m, and the volume-based CSD of the seeds produced via Protocol 1 and Protocol 2. It is interesting to note that the seeds produced via Protocol 1 display a larger variation in the mean diameter (154±29 µm for the runs following Protocol 1, where 154 µm is the average mean diameter and 29 µm is the standard deviation, and 162±11 µm for the runs following Protocol 2) and CSD width than the seeds produced via Protocol 2. Since nucleation occurs at higher temperatures during Protocol 2 than during Protocol 1, then nucleation should be more intense and should occur over a narrower range of supersaturations during Protocol 2. This could explain why the CSDs of the seeds produced via Protocol 2 are narrower and more reproducible than the CSDs of the seeds produced via Protocol 1. Obviously, this lack of uniformity

between seeds produced in different runs and via different protocols should be taken into consideration when analyzing the results of the following seeded continuous experiments.

9.3.3 Continuous Crystallization with Seeding and Temperature Cycling

Figure 9.10 presents the experimental results of Run 1, including the evolution of the supersaturation ratio, S, and temperature, T, at the outlet of the continuous crystallizer (**Figure 9.10 (a)**), the evolution of the volume-based CSD along the continuous crystallizer (**Figure 9.10 (b)**), images of the seeds (**Figure 9.10 (c)**), images of the crystals after T_h (**Figure 9.10 (d)**) and images of the crystals after T_c (**Figure 9.10 (e)**). The experimental results of the remaining runs are presented in **Figure 9.11-Figure 9.22**. In most runs, the CSD of the seeds is unimodal, however, the images of the seeds show that they consist of several types of particles, including single crystals of different sizes, crystal fragments, and soft and hard agglomerates. The coexistence of distinct hydrodynamic environments within the STC probably explains the formation of the different types of particles.

For Run 1, **Figure 9.10 (a)** and **(b)** show that the temperature, the supersaturation and the CSD at the outlet of the continuous crystallizer remain fairly constant from the first to the fourth residence times. This suggests that Run 1 was at steady state right after the first residence time. For the sake of simplicity, for the remaining runs, **Figure 9.11-Figure 9.22** show only the average CSD at the outlet of the continuous crystallizer, except when it was not constant over time. Run 1 was performed without temperature cycling, *i.e.*, the temperature in the hot planar-OFC was equal to the temperature in the STC ($T_h = T_{STC}$). Therefore, it is not surprising that the original CSD of the seeds has remained practically unchanged after T_h (**Figure 9.10 (b)**) and that the seeds have remained highly agglomerated after T_h and after T_c (**Figure 9.10 (c)**, **(d)** and **(e)**).

In most cases, agglomeration is undesirable because the formation of agglomerates promotes the entrapment of mother liquor and, therefore, compromises the purity of the dried product. In addition, agglomeration can also give rise to broad CSDs and induce the formation of fines during storage and transport.[20,21] Therefore, in the remaining runs, temperature cycling was applied to reduce the amount of agglomerates in the final product.

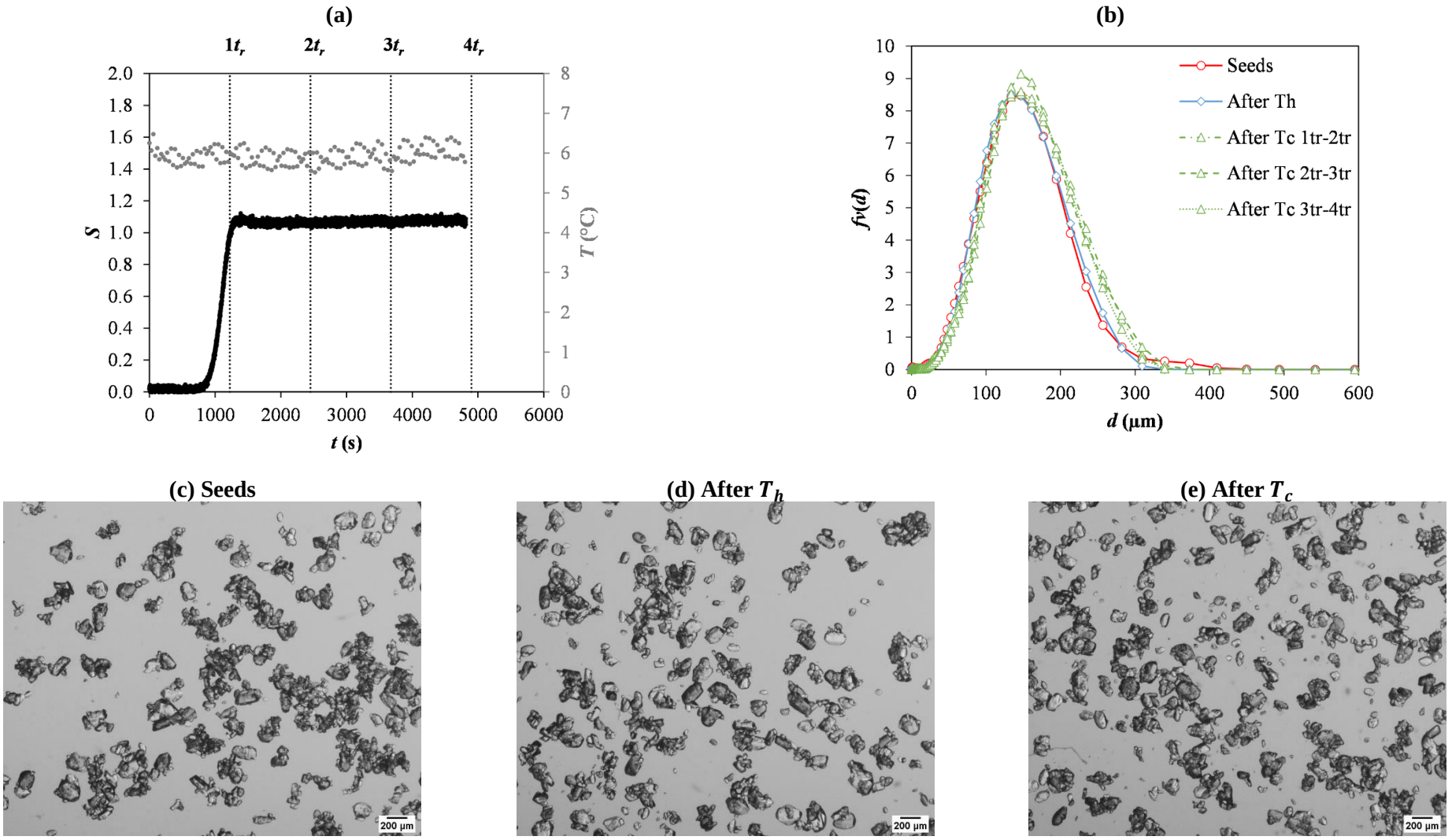


Figure 9.10 – Run 1. (a) Evolution of supersaturation and temperature at the outlet of the continuous crystallizer. (b) Evolution of the volume-based CSD along the continuous crystallizer. (c) Images of the seeds. (d) Images of the crystals after T_h. (e) Images of the crystals after T_c.

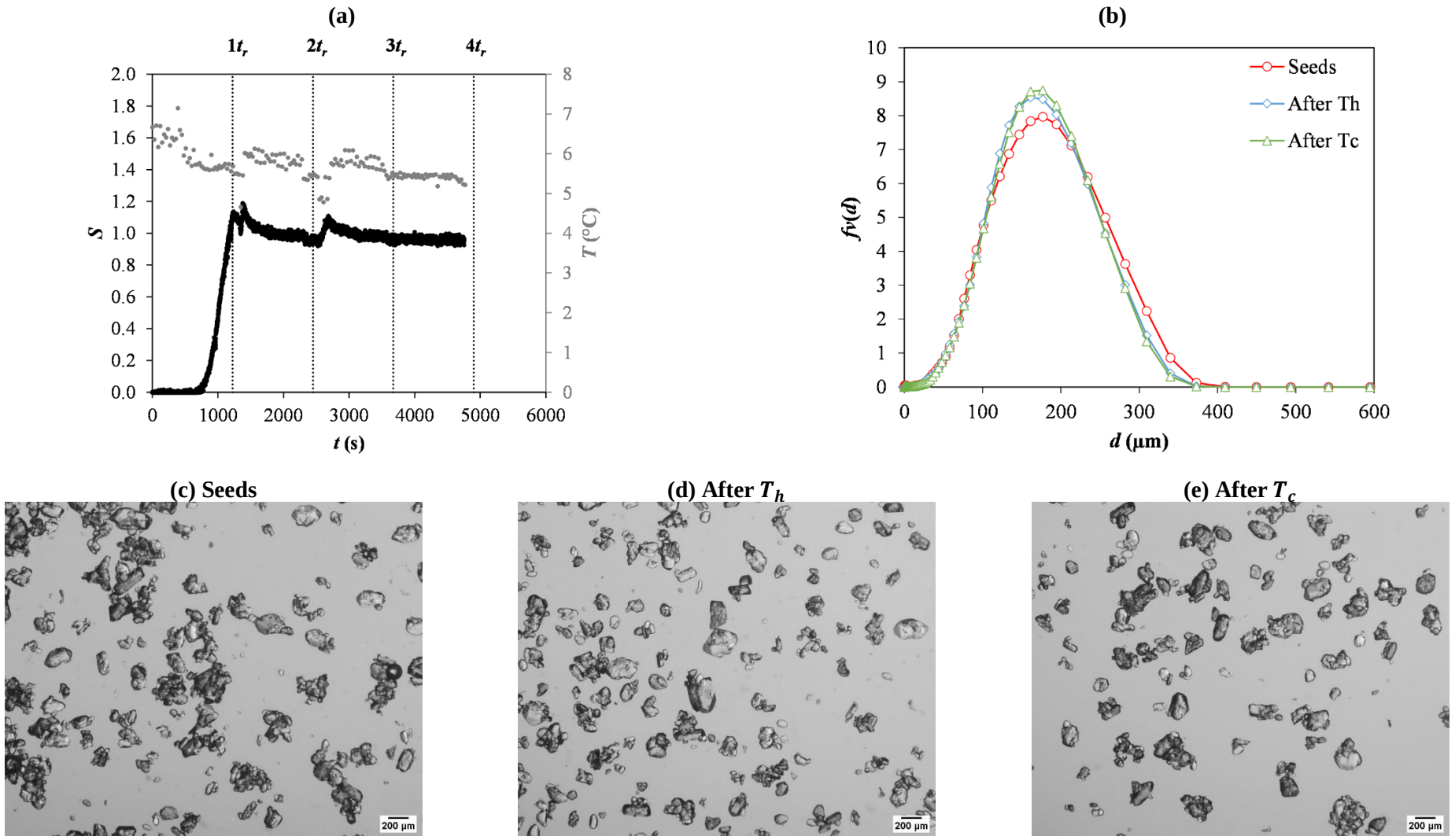


Figure 9.11 – Run 2. (a) Evolution of supersaturation and temperature at the outlet of the continuous crystallizer. (b) Evolution of the volume-based CSD along the continuous crystallizer. (c) Images of the seeds. (d) Images of the crystals after T_h. (e) Images of the crystals after T_c.

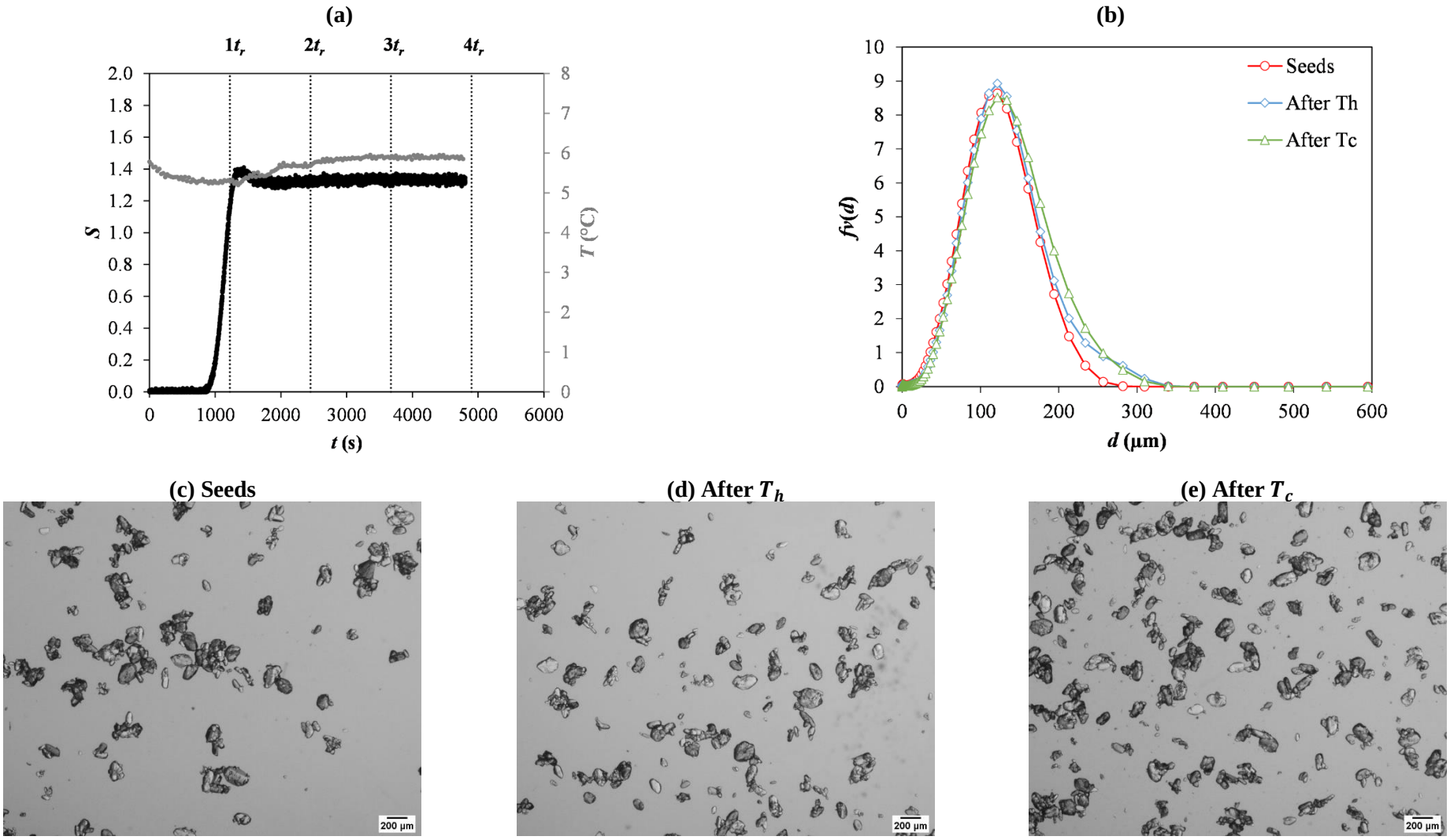


Figure 9.12 – Run 3. (a) Evolution of supersaturation and temperature at the outlet of the continuous crystallizer. (b) Evolution of the volume-based CSD along the continuous crystallizer. (c) Images of the seeds. (d) Images of the crystals after T_h. (e) Images of the crystals after T_c.

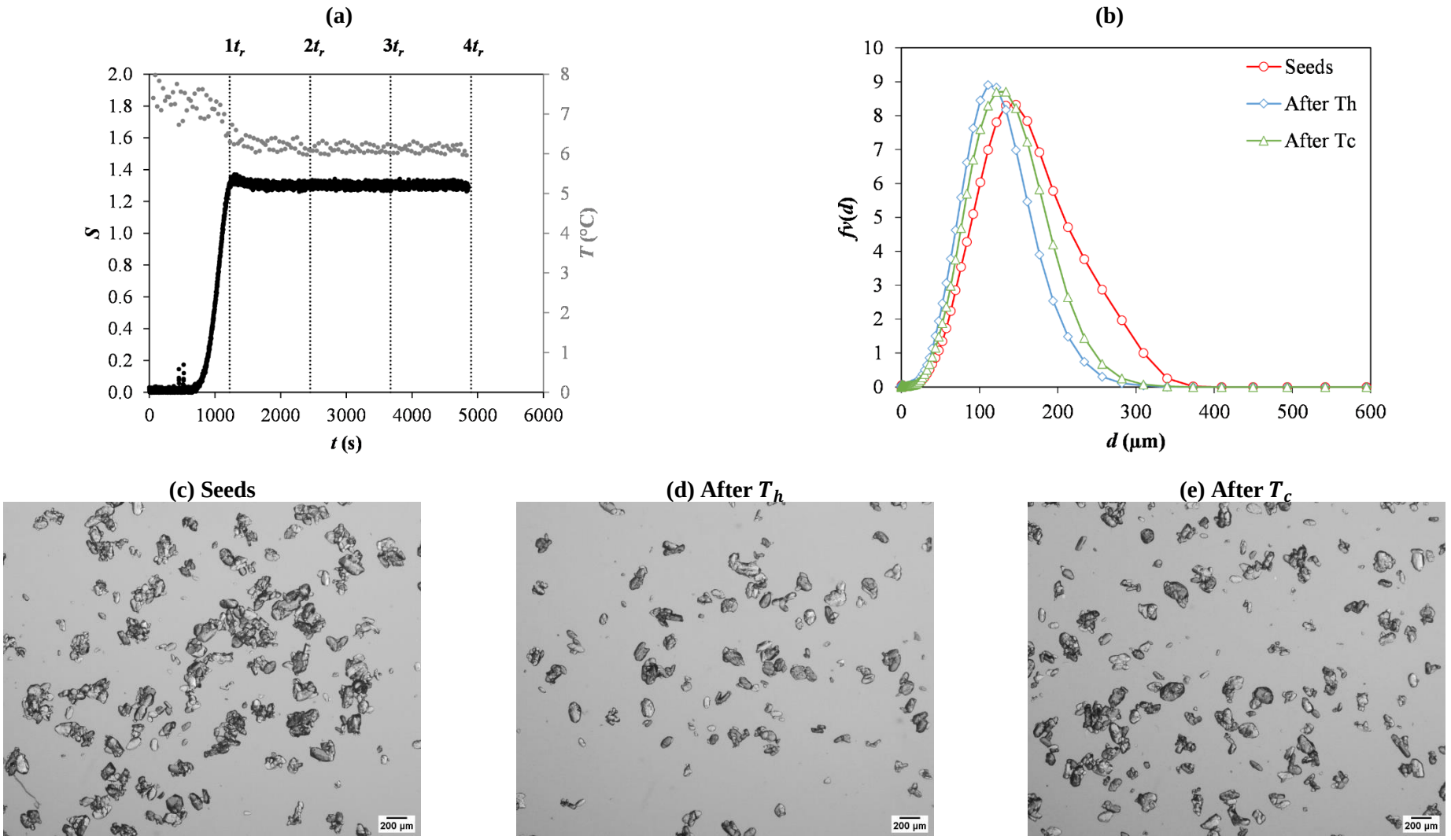


Figure 9.13 – Run 4. (a) Evolution of supersaturation and temperature at the outlet of the continuous crystallizer. (b) Evolution of the volume-based CSD along the continuous crystallizer. (c) Images of the seeds. (d) Images of the crystals after T_h. (e) Images of the crystals after T_c.

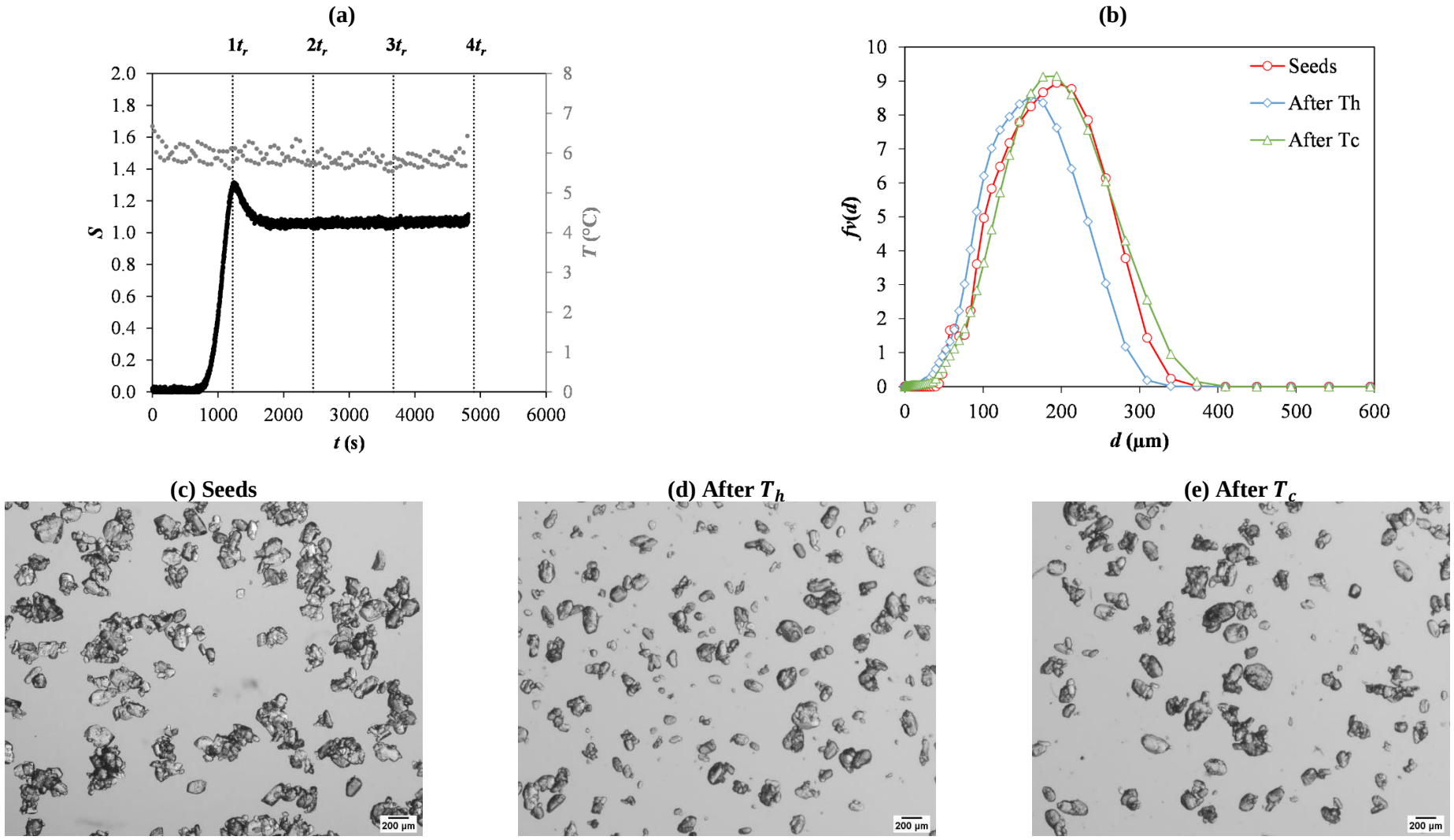


Figure 9.14 – Run 5. (a) Evolution of supersaturation and temperature at the outlet of the continuous crystallizer. (b) Evolution of the volume-based CSD along the continuous crystallizer. (c) Images of the seeds. (d) Images of the crystals after T_h. (e) Images of the crystals after T_c.

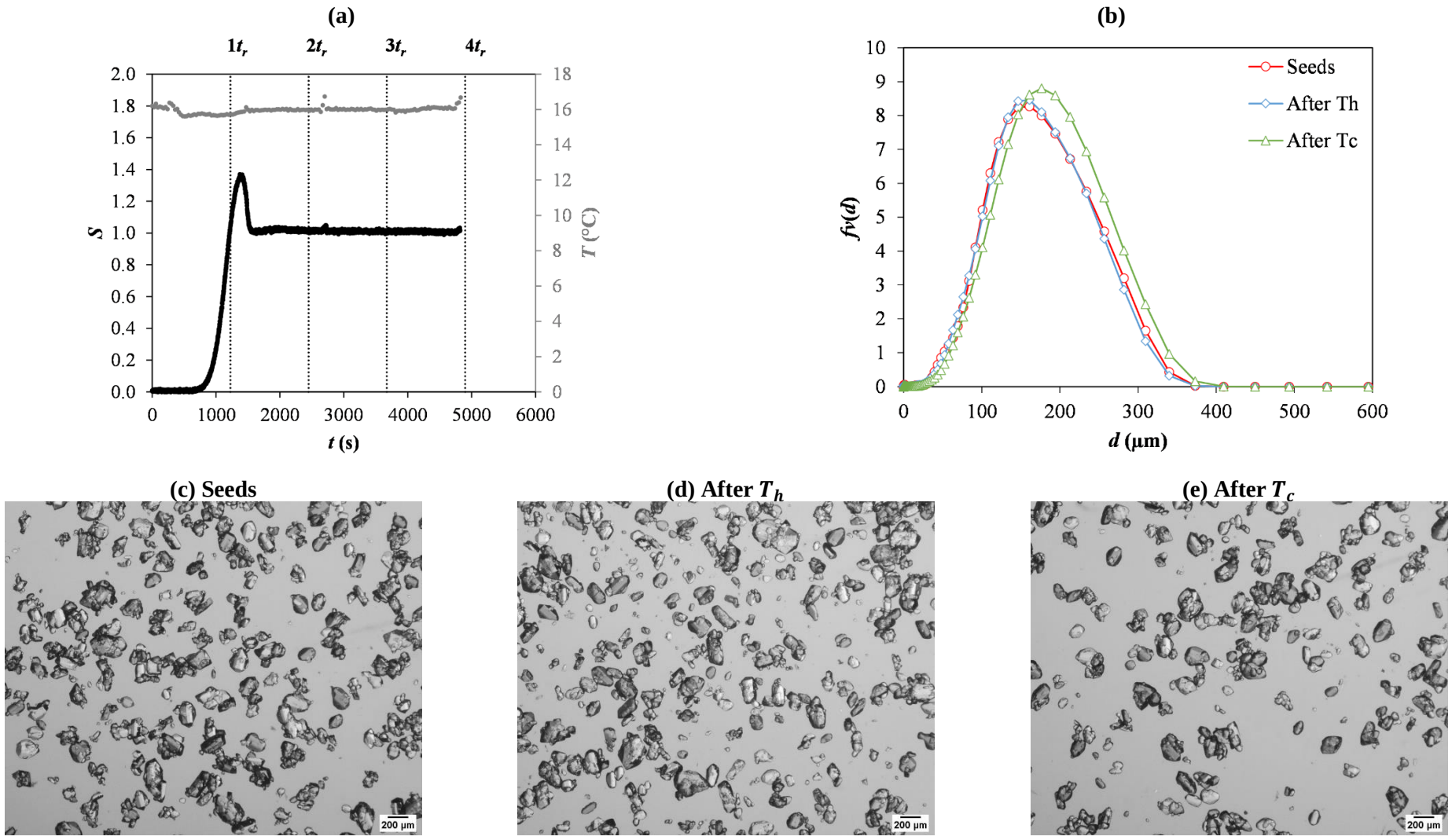


Figure 9.15 – Run 6. (a) Evolution of supersaturation and temperature at the outlet of the continuous crystallizer. (b) Evolution of the volume-based CSD along the continuous crystallizer. (c) Images of the seeds. (d) Images of the crystals after T_h. (e) Images of the crystals after T_c.

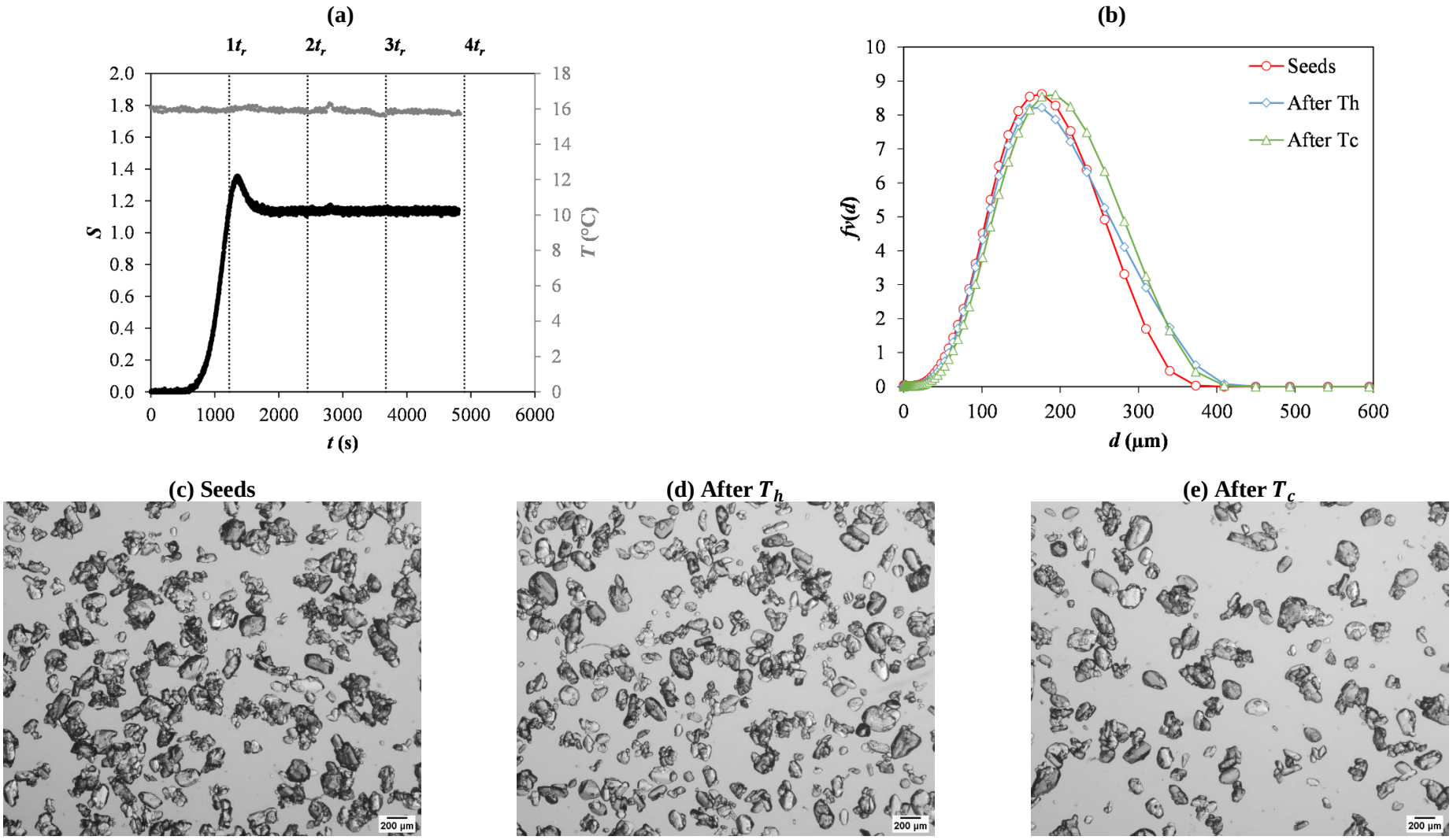


Figure 9.16 – Run 7. (a) Evolution of supersaturation and temperature at the outlet of the continuous crystallizer. (b) Evolution of the volume-based CSD along the continuous crystallizer. (c) Images of the seeds. (d) Images of the crystals after T_h. (e) Images of the crystals after T_c.

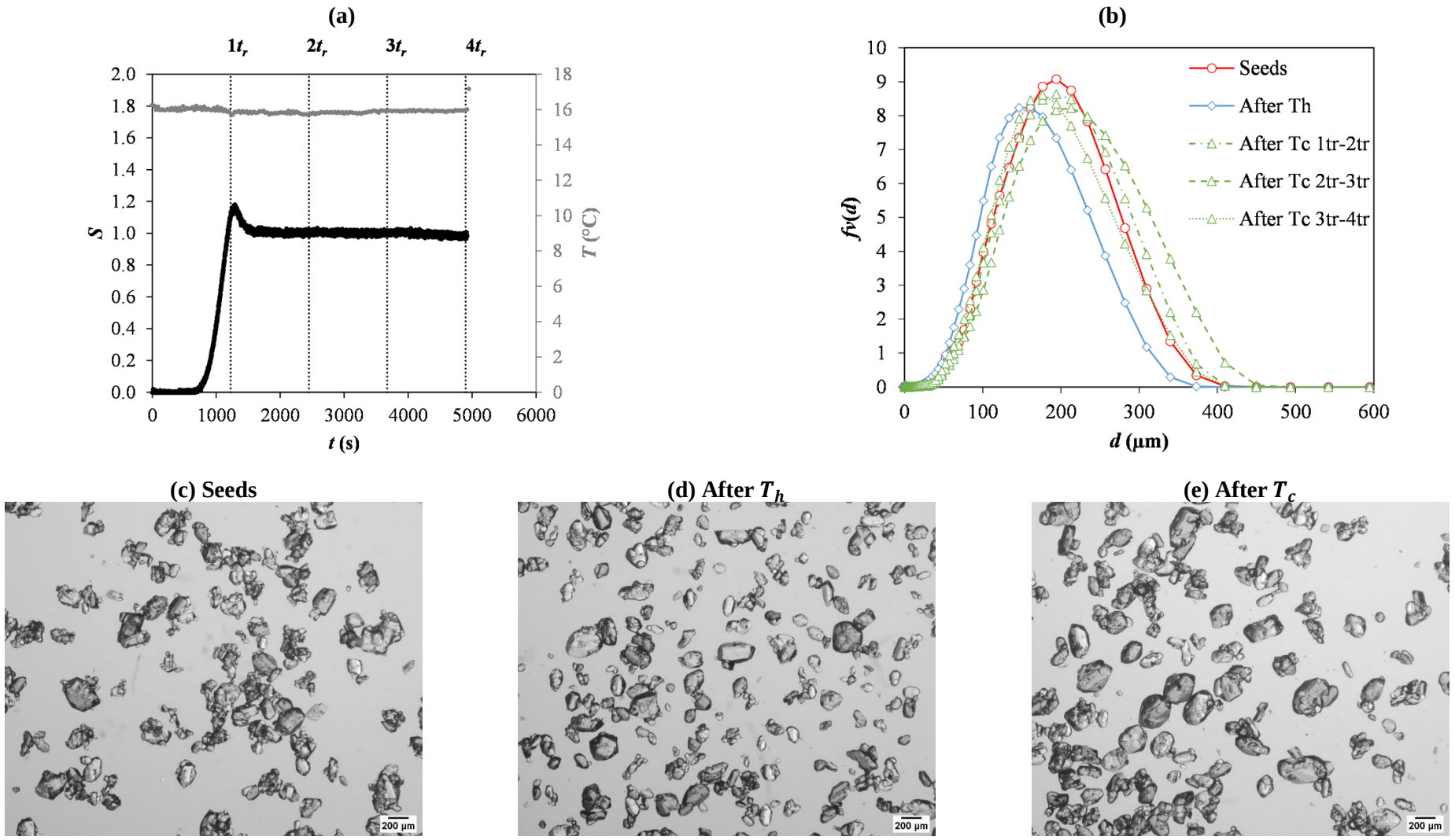


Figure 9.17 – Run 8. (a) Evolution of supersaturation and temperature at the outlet of the continuous crystallizer. (b) Evolution of the volume-based CSD along the continuous crystallizer. (c) Images of the seeds. (d) Images of the crystals after T_h. (e) Images of the crystals after T_c.

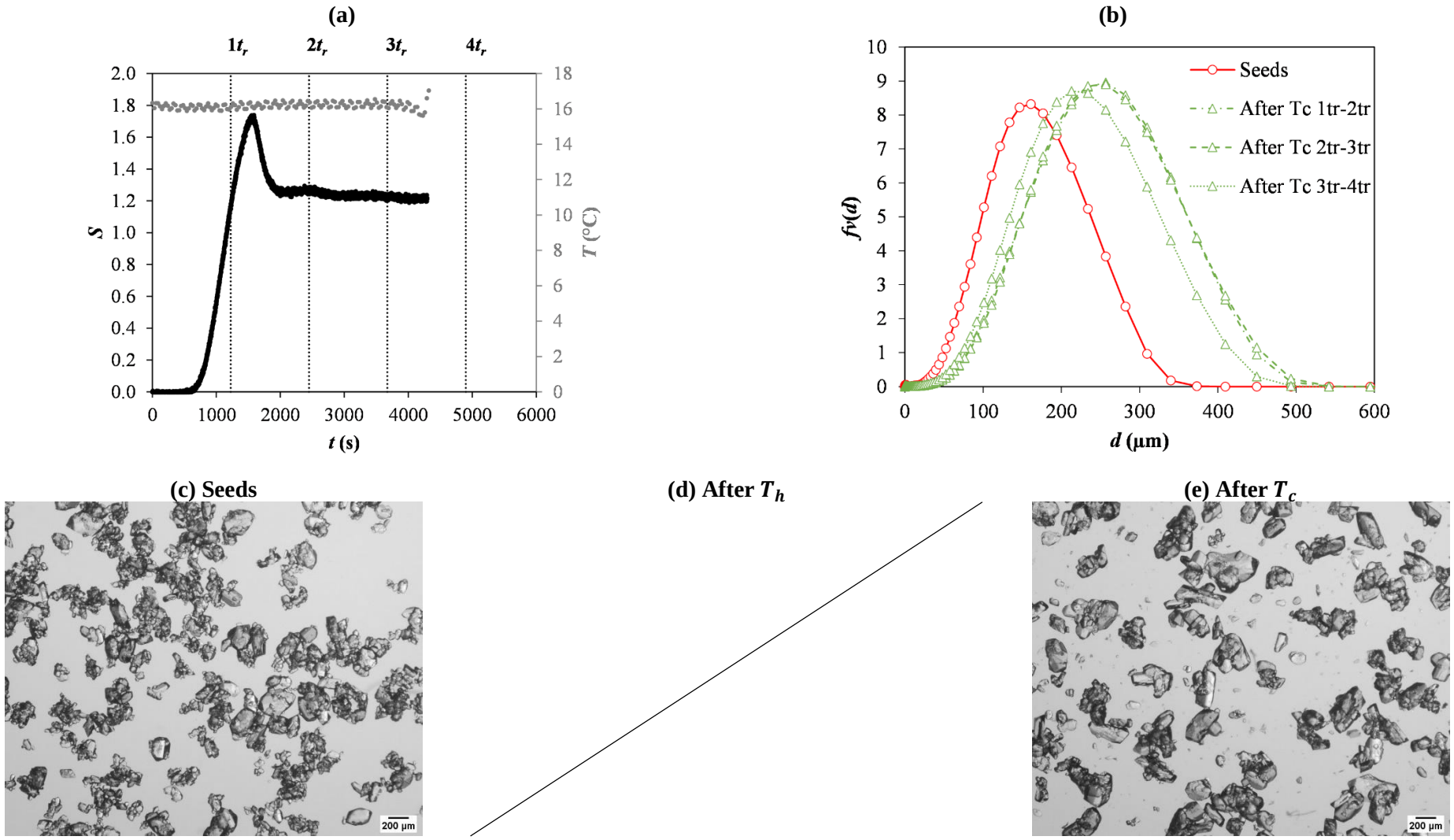


Figure 9.18 – Run 9. (a) Evolution of supersaturation and temperature at the outlet of the continuous crystallizer. (b) Evolution of the volume-based CSD along the continuous crystallizer. (c) Images of the seeds. (d) Images of the crystals after T_h. (e) Images of the crystals after T_c.

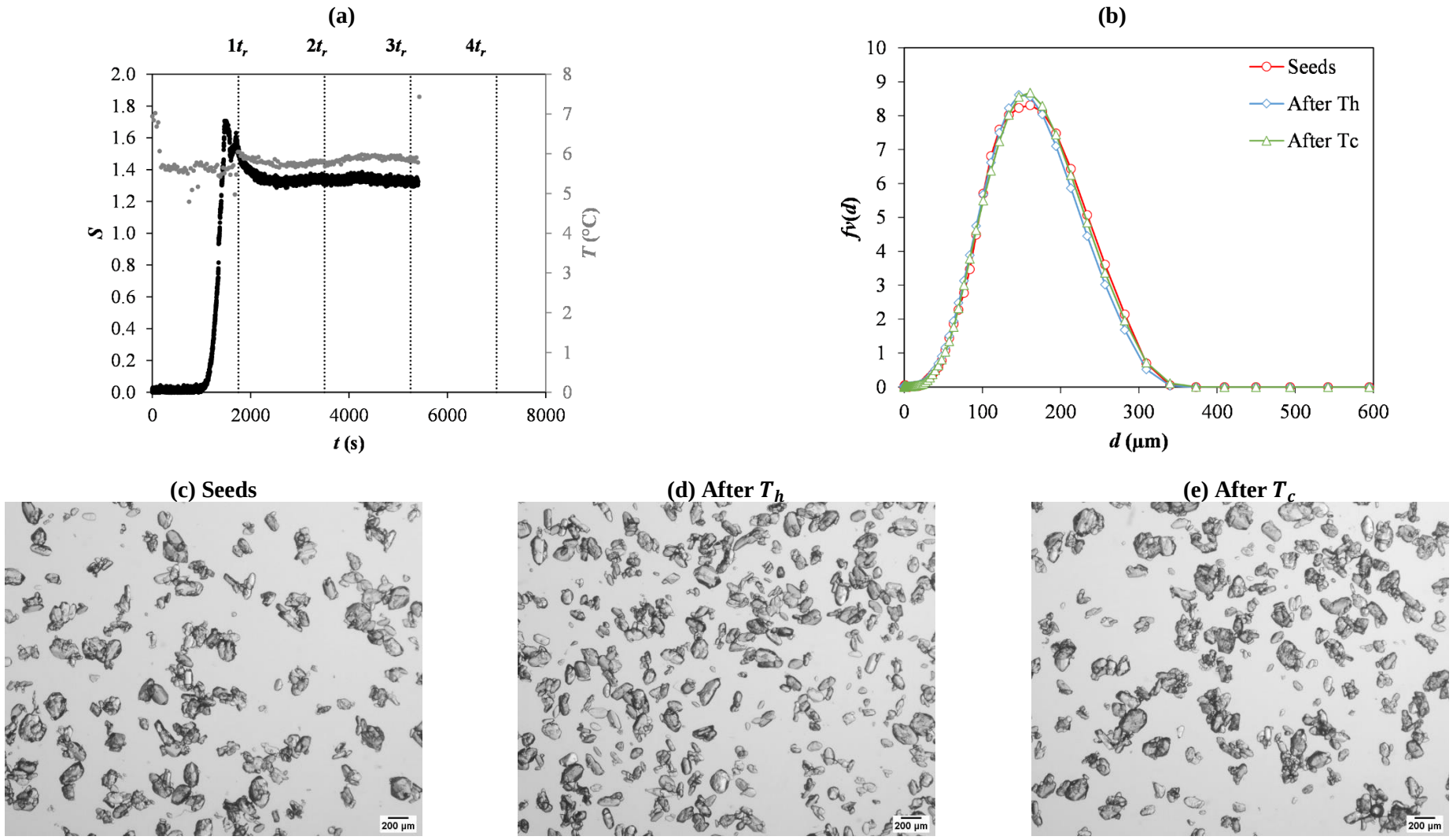


Figure 9.19 – Run 10. (a) Evolution of supersaturation and temperature at the outlet of the continuous crystallizer. (b) Evolution of the volume-based CSD along the continuous crystallizer. (c) Images of the seeds. (d) Images of the crystals after T_h. (e) Images of the crystals after T_c.

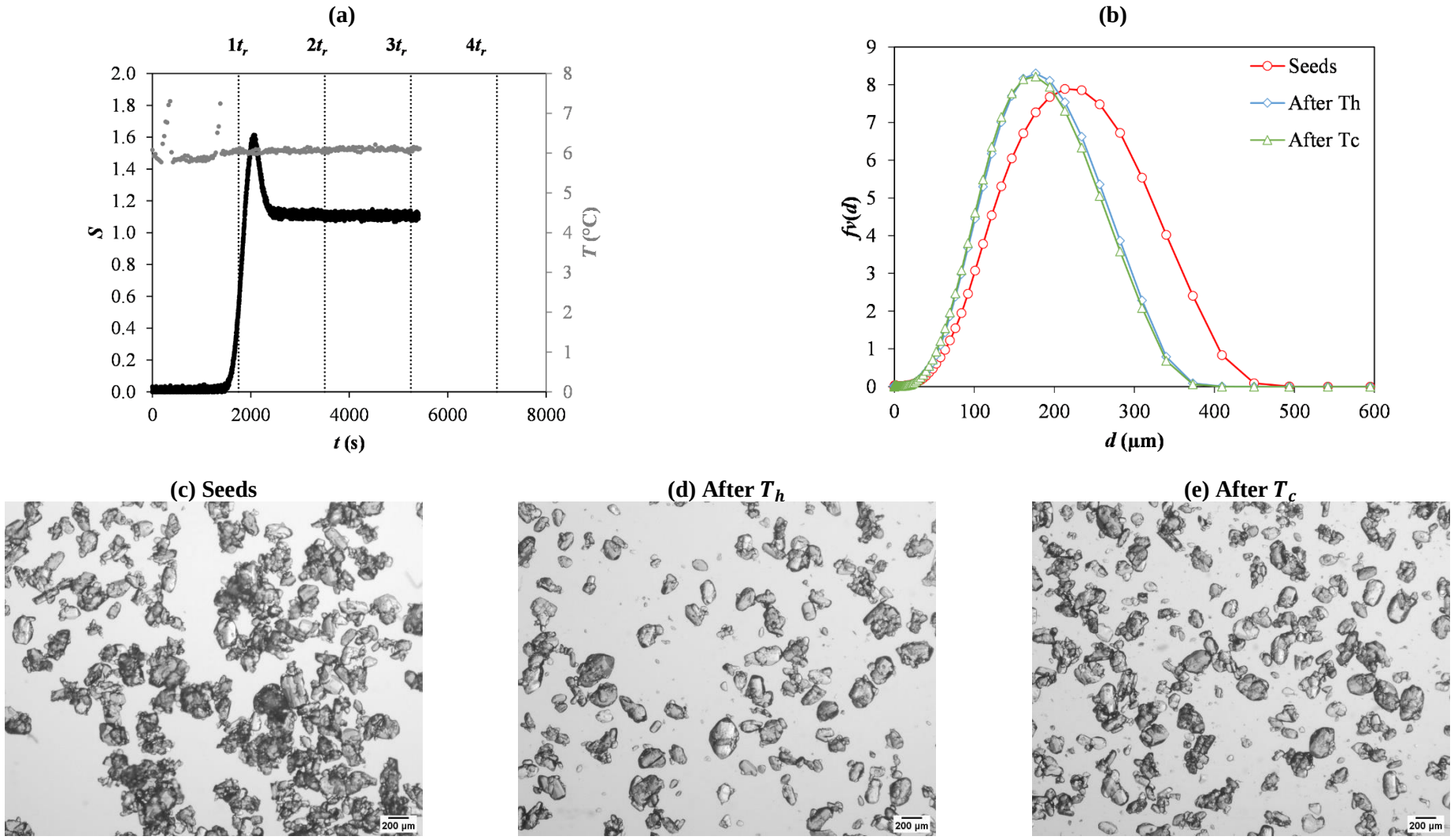


Figure 9.20 – Run 11. (a) Evolution of supersaturation and temperature at the outlet of the continuous crystallizer. (b) Evolution of the volume-based CSD along the continuous crystallizer. (c) Images of the seeds. (d) Images of the crystals after T_h. (e) Images of the crystals after T_c.

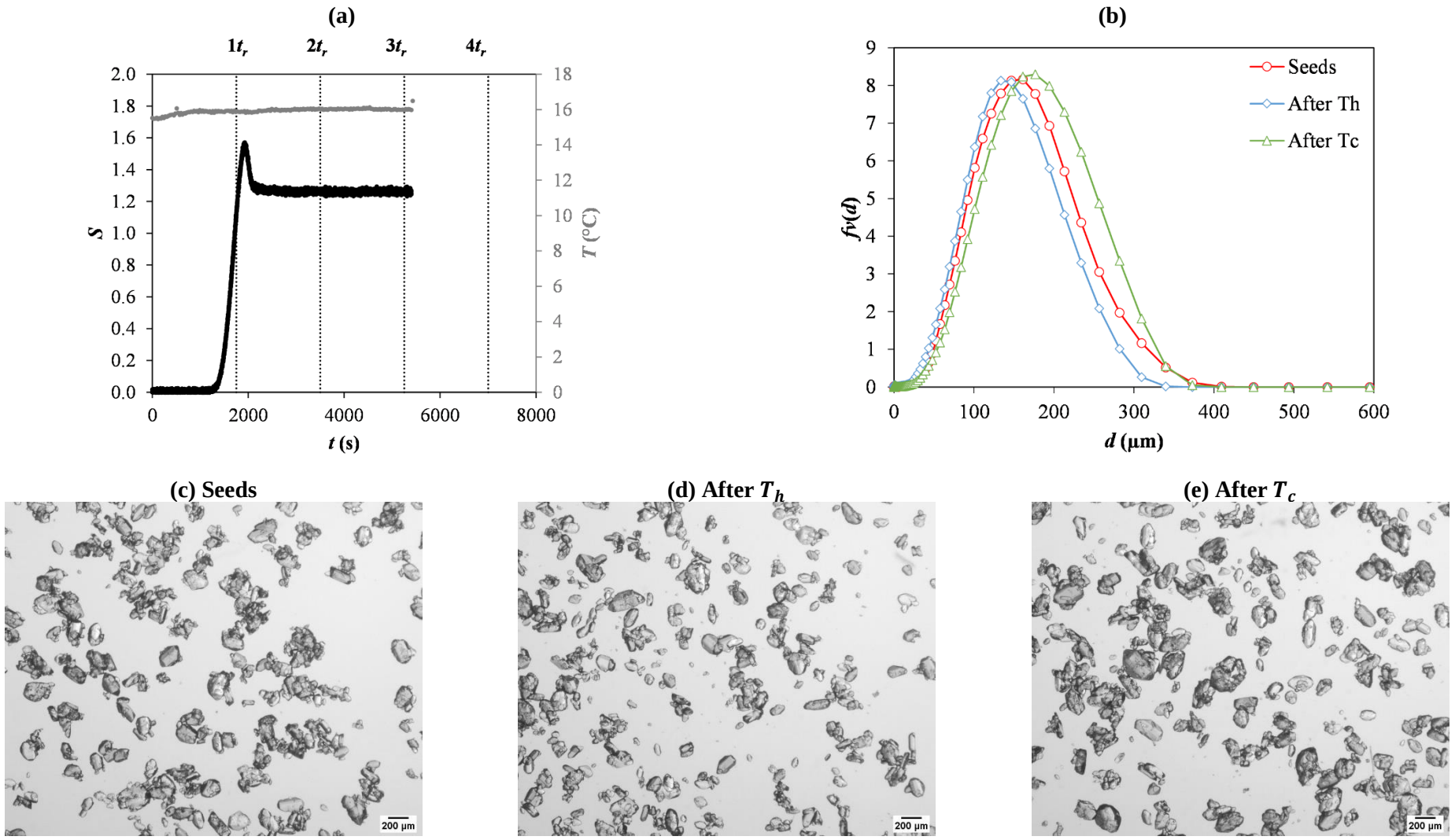


Figure 9.21 – Run 12. (a) Evolution of supersaturation and temperature at the outlet of the continuous crystallizer. (b) Evolution of the volume-based CSD along the continuous crystallizer. (c) Images of the seeds. (d) Images of the crystals after T_h. (e) Images of the crystals after T_c.

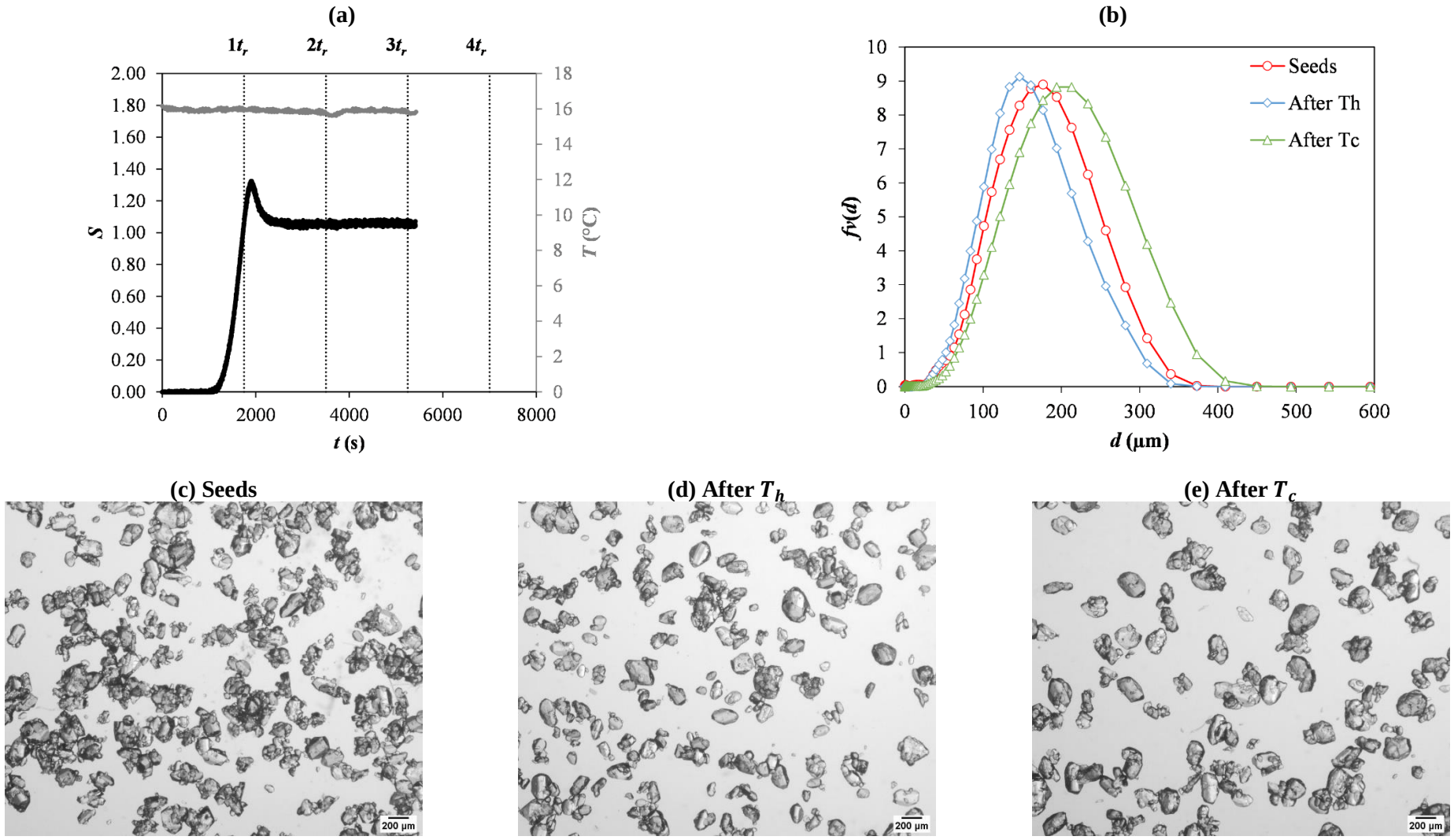


Figure 9.22 – Run 13. (a) Evolution of supersaturation and temperature at the outlet of the continuous crystallizer. (b) Evolution of the volume-based CSD along the continuous crystallizer. (c) Images of the seeds. (d) Images of the crystals after T_h. (e) Images of the crystals after T_c.

Effect of T_h

Runs 2-5 were all performed with T_c=6 °C, while T_h varied from T_h=13 °C in Run 2, to T_h=15 °C in Run 3, to T_h=17 °C in Run 4, to T_h=20 °C in Run 5. **Figure 9.23** presents the mean diameter of the seeds, after T_h and after T_c for Runs 2-5.

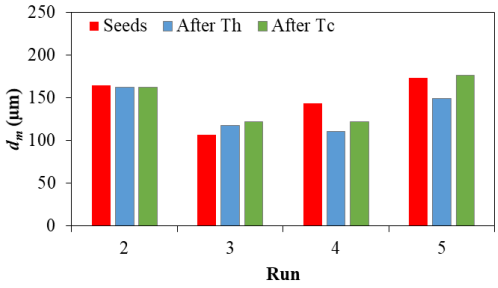


Figure 9.23 – Mean diameter of the seeds, after T_h and after T_c for Runs 2-5 (T_c=6 °C).

In Run 2 (**Figure 9.11**), the temperature cycling did not a cause a significant change in the mean diameter, neither after T_h nor after T_c. (In **Figure 9.11 (a)**, the sharp increase of supersaturation and decrease of temperature after two residence times was due to the presence of air bubbles, which were eventually removed.) However, it is interesting to note that the concentration of paracetamol in solution reached solubility at the outlet of the continuous crystallizer, which indicates that supersaturation had to be consumed either by secondary nucleation or crystal growth in the cold planar-OFC. Since the mean diameter did not change significantly, it is possible that both secondary nucleation and crystal growth coexisted in the cold planar-OFC (as suggested by the presence of smaller and larger crystals in **Figure 9.11 (e)**), with secondary nucleation contributing to decrease the mean diameter and crystal growth contributing to increase the mean diameter in identical proportions.

In Run 3 (**Figure 9.12**), the temperature cycling caused a significant change in the mean diameter. Apparently, after T_h, the mean diameter increased due to the selective dissolution of the smaller particles, which increased the percentage of the larger particles; and, after T_c, the mean diameter increased due to crystal growth.

In Runs 4 and 5 (**Figure 9.13** and **Figure 9.14**, respectively), the temperature cycling caused an even more significant change in the mean diameter. Apparently, after T_h, the mean diameter decreased due to the de-agglomeration of the larger particles, which increased the percentage of smaller particles; and, after T_c, the mean diameter increased due to crystal growth.

The difference of results between Run 3 and Runs 4 and 5 is probably due to the difference in the percentage of agglomerates in the seeds of each run. It seems like the seeds of Runs 4 and 5 had a higher percentage of agglomerates than the seeds of Run 3. Therefore, while the decrease of mean diameter due to the de-

agglomeration of the larger particles counterweighted the increase of mean diameter due to the selective dissolution of the smaller particles in Runs 4 and 5, the opposite happened in Run 3.

Effect of T_c

Runs 6-9 were all performed with T_c=16 °C, while T_h varied from T_h=23 °C in Run 6, to T_h=26 °C in Run 7, to T_h=28 °C in Run 8, to T_h=29 °C in Run 9. **Figure 9.24** presents the mean diameter of the seeds, after T_h and after T_c for Runs 6-9.

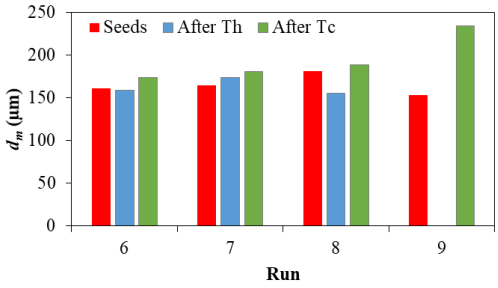


Figure 9.24 – Mean diameter of the seeds, after T_h and after T_c for Runs 6-9 (T_c=16 °C).

In Run 6 (**Figure 9.15**), the temperature cycling did not cause a significant change in the mean diameter after T_h, but it caused a significant change in the mean diameter after T_c. It is interesting to note the difference of results between Run 6 and Run 2, which had the same S_{max}, but different T_c. While the mean diameter remained practically unchanged after T_c in Run 2, it increased more significantly in Run 6. This suggests that while crystal growth and secondary nucleation were equally significant in Run 2, crystal growth was more significant than secondary nucleation in Run 6.

In Run 7 (**Figure 9.16**), the temperature cycling caused a change in the mean diameter after both T_h and T_c. Unlike the previous case, it is interesting to note the similarity of results between Run 7 and Run 3, which had the same S_{max}, but different T_c. In both runs, after T_h, the mean diameter increased due to the selective dissolution of the smaller particles, and after T_c, the mean diameter increased due to crystal growth. However, the steady state supersaturation at the outlet of the continuous crystallizer was lower in Run 7 (S ≅1.1) than in Run 3 (S ≅1.3). A possible explanation for this could be that crystal growth was faster in Run 7, where T_c=16 °C, than in Run 3, where T_c=6 °C.

In Runs 8 and 9 (**Figure 9.17** and **Figure 9.18**, respectively), the steady state was lost due to fouling on the walls of the crystallization channel, which eventually caused the clogging of the continuous crystallizer. This indicates that, in these runs, the supersaturation in the cold planar-OFC was above the metastable limit, which,

as previously demonstrated, should be avoided to prevent uncontrolled nucleation, and also to ensure the maintenance of steady state.

Effect of Residence Time in the Dissolution step

Runs 2 and 10, Runs 3 and 11, Runs 6 and 12, and Runs 7 and 13 were performed with identical operating conditions, however, while there was only one hot planar-OFC in Runs 2, 3, 6 and 7, there were two hot planar-OFCs in series in Runs 10, 11, 12 and 13. **Figure 9.25** presents the mean diameter of the seeds, after T_h and after T_c for Runs 2, 6, 10 and 12 (S_{max}=1.3) and **Figure 9.26** presents the mean diameter of the seeds, after T_h and after T_c for Runs 3, 7, 11 and 13 (S_{max}=1.4).

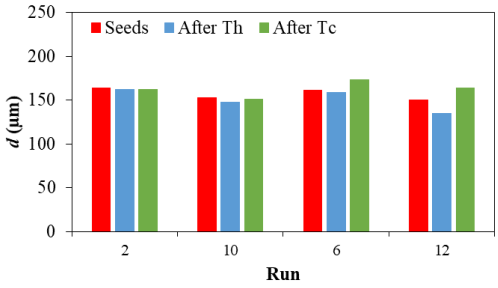


Figure 9.25 – Mean diameter of the seeds, after T_h and after T_c for Runs 2, 6, 10 and 12 (S_{max}=1.3).

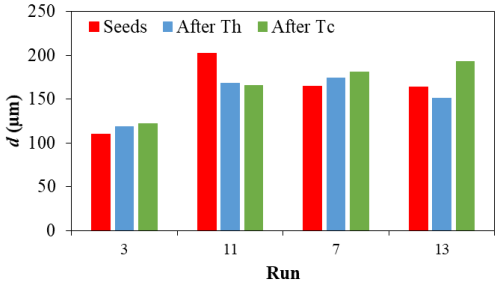


Figure 9.26 – Mean diameter of the seeds, after T_h and after T_c for Runs 3, 7, 11 and 13 (S_{max}=1.4).

Figure 9.25 and **Figure 9.26** show that the mean diameter decreases more with two hot planar-OFCs in series than with only one hot planar-OFC (compare Runs 2 and 10, Runs 3 and 11, Runs 6 and 12, and Runs 7 and 13). This means that, with only one hot planar-OFC, the concentration of paracetamol does not reach solubility after the dissolution step, but it does not necessarily mean that, with two hot planar-OFCs in series, the concentration of paracetamol does reach solubility after the dissolution step. To verify this hypothesis, the concentration of paracetamol after the dissolution step would have to be measured. Finally, **Figure 9.25** and

Figure 9.26 also show that longer residence times in the dissolution step and higher temperatures in the crystal growth step (Runs 12 and 13) are preferred to promote the de-agglomeration of the large particles in the dissolution step and the growth of the single crystals in the crystal growth step.

9.4 Conclusion

The continuous cooling crystallization of paracetamol from a 40% (v/v) mixture of ethanol and water was used as a model system to investigate how temperature cycling in a planar-OFC influences the quality of the final product.

Without seeding, paracetamol has a great tendency to nucleate and grow on the walls of the crystallization channel, which causes severe fouling and, eventually, clogging of the continuous crystallizer. Changing the flow rate, the oscillation intensity, the temperature, and the wall material allows to increase the operation time, but, after some time, fouling is still observed. This means that, without seeding, the continuous crystallizer cannot operate at steady state for a long period of time, and so, primary nucleation should be avoided in the continuous crystallizer. This is true when paracetamol crystallizes in contact with ECTFE and PTFE, but it is not necessarily true when paracetamol crystallizes in contact with other materials. Furthermore, this is also not necessarily true for other compounds, which might have different affinities with different materials.

On the other hand, with seeding, the continuous crystallizer can operate at steady state for long periods of time (at least 4 residence times, the limit time in the present work) without any signs of fouling, and much less of clogging, as long as supersaturation is maintained below the metastable zone limit. However, the quality of the final product largely depends on the quality of the seeds. This means that seeds with a broad CSD, with a significant amount of fines and agglomerates, generate final products of poor uniformity. Therefore, some type of crystal engineering strategy should be used to correct the poor quality of the seeds before they are allowed to grow in the continuous crystallizer.

Temperature cycling can be employed to address this issue. First, the fines are dissolved and the agglomerates are disrupted during the heating steps, and then, the remaining seeds grow during the cooling step. After temperature cycling, the crystals have well-defined shapes, with less fines and agglomerates, which improves the overall uniformity of the final product. Moreover, changing the residence time and the temperature during heating and cooling provides further flexibility to control the mean size and the CSD of the final product.

Notation

Acronyms	
API	Active pharmaceutical ingredient
ATR	Attenuated total reflectance
CSD	Crystal size distribution
ECTFE	Ethylene-chlorotrifluoroethylene copolymer
MSMPR	Mixed suspension mixed product removal
OFC	Oscillatory flow crystallizer
PFC	Plug flow crystallizer
PTFE	Poly(tetrafluoroethylene)
SFC	Slug flow crystallizer
STC	Stirred tank crystallizer

Latin symbols	
Abs	Absorbance
C_{STC}	Concentration in the STC
d	Crystal size
d_m	Mean diameter
f	Frequency of oscillation
$f_V(d)$	Volume-based CSD
Q	Flow rate
S	Supersaturation ratio
S_i	Initial supersaturation ratio
S_{max}	Maximum possible supersaturation ratio at the inlet of the cold planar-OFC
t	Time
T	Temperature
t_r	Residence time
T_b	Temperature in the bath
T_c	Temperature at the outlet of the cold planar-OFC
T_h	Temperature at the outlet of the hot planar-OFC
T_i	Temperature in the vessel
T_{STC}	Temperature in the STC
T_f	Temperature in the planar-OFC
T_s	Saturation temperature
x_0	Center-to-peak amplitude of oscillation

Greek Letters	
θ	Cooling rate

References

(1) Chen, J.; Sarma, B.; Evans, J. M. B.; Myerson, A. S. Pharmaceutical Crystallization. *Cryst. Growth Des.* **2011**, *11* (4), 887–895.

(2) Variankaval, N.; Cote, A. S.; Doherty, M. F. From Form to Function: Crystallization of Active Pharmaceutical Ingredients. *AIChE J.* **2008**, *54* (7), 1682–1688.

(3) Vedantam, S.; Ranade, V. V. Crystallization: Key Thermodynamic, Kinetic and Hydrodynamic Aspects. *Sadhana* **2013**, *38* (6), 1287–1337.

(4) Mullin, J. W.; Nývlt, J. Programmed Cooling of Batch Crystallizers. *Chem. Eng. Sci.* **1971**, *26* (3), 369–377.

(5) Jones, A. G.; Mullin, J. W. Programmed Cooling Crystallization of Potassium Sulphate Solutions. *Chem. Eng. Sci.* **1974**, *29* (1), 105–118.

(6) Xie, W.; Rohani, S.; Phoenix, A. Dynamic Modeling and Operation of a Seeded Batch Cooling Crystallizer. *Chem. Eng. Commun.* **2001**, *187* (1), 229–249.

(7) Jones, A. G.; Chianese, A. Fines Destruction During Batch Crystallization. *Chem. Eng. Commun.* **1987**,

62 (1–6), 5–16.

(8) Zipp, G. L.; Randolph, A. D. Selective Fines Destruction in Batch Crystallization. *Ind. Eng. Chem. Res.* **1989**, *28* (9), 1446–1448.

(9) Carless, J. E.; Foster, A. A. Accelerated Crystal Growth of Sulphathiazole by Temperature Cycling. *J. Pharm. Pharmacol.* **1966**, *18* (11), 697–708.

(10) Kim, S.; Wei, C.; Kiang, S. Crystallization Process Development of an Active Pharmaceutical Ingredient and Particle Engineering via the Use of Ultrasonics and Temperature Cycling. *Org. Process Res. Dev.* **2003**, *7* (6), 997–1001.

(11) Trampuž, M.; Teslić, D.; Likozar, B. Crystallization of Fesoterodine Fumarate Active Pharmaceutical Ingredient: Modelling of Thermodynamic Equilibrium, Nucleation, Growth, Agglomeration and Dissolution Kinetics and Temperature Cycling. *Chem. Eng. Sci.* **2019**, *201*, 97–111.

(12) Abu Bakar, M. R.; Nagy, Z. K.; Rielly, C. D. Seeded Batch Cooling Crystallization with Temperature Cycling for the Control of Size Uniformity and Polymorphic Purity of Sulfathiazole Crystals. *Org. Process Res. Dev.* **2009**, *13* (6), 1343–1356.

(13) Abu Bakar, M. R.; Nagy, Z. K.; Saleemi, A. N.; Rielly, C. D. The Impact of Direct Nucleation Control on Crystal Size Distribution in Pharmaceutical Crystallization Processes. *Cryst. Growth Des.* **2009**, *9* (3), 1378–1384.

(14) Woo, X. Y.; Nagy, Z. K.; Tan, R. B. H.; Braatz, R. D. Adaptive Concentration Control of Cooling and Antisolvent Crystallization with Laser Backscattering Measurement. *Cryst. Growth Des.* **2009**, *9* (1), 182–191.

(15) Saleemi, A.; Rielly, C.; Nagy, Z. K. Automated Direct Nucleation Control for in Situ Dynamic Fines Removal in Batch Cooling Crystallization. *CrystEngComm* **2012**, *14* (6), 2196.

(16) Saleemi, A. N.; Rielly, C. D.; Nagy, Z. K. Comparative Investigation of Supersaturation and Automated Direct Nucleation Control of Crystal Size Distributions Using ATR-UV/Vis Spectroscopy and FBRM. *Cryst. Growth Des.* **2012**, *12* (4), 1792–1807.

(17) Nagy, Z. K.; Aamir, E.; Rielly, C. D. Internal Fines Removal Using Population Balance Model Based Control of Crystal Size Distribution under Dissolution, Growth and Nucleation Mechanisms. *Cryst. Growth Des.* **2011**, *11* (6), 2205–2219.

(18) Nagy, Z. K. Model Based Robust Control Approach for Batch Crystallization Product Design. *Comput.*

Chem. Eng. **2009**, *33* (10), 1685–1691.

(19) Saleemi, A. N.; Steele, G.; Pedge, N. I.; Freeman, A.; Nagy, Z. K. Enhancing Crystalline Properties of a Cardiovascular Active Pharmaceutical Ingredient Using a Process Analytical Technology Based Crystallization Feedback Control Strategy. *Int. J. Pharm.* **2012**, *430* (1–2), 56–64.

(20) Simone, E.; Othman, R.; Vladisavljević, G.; Nagy, Z. Preventing Crystal Agglomeration of Pharmaceutical Crystals Using Temperature Cycling and a Novel Membrane Crystallization Procedure for Seed Crystal Generation. *Pharmaceutics* **2018**, *10* (1), 17.

(21) Ålander, E. M.; Uusi-Penttilä, M. S.; Rasmuson, Å. C. Agglomeration of Paracetamol during Crystallization in Pure and Mixed Solvents. *Ind. Eng. Chem. Res.* **2004**, *43* (2), 629–637.

(22) Yu, Z. Q.; Tan, R. B. H.; Chow, P. S. Effects of Operating Conditions on Agglomeration and Habit of Paracetamol Crystals in Anti-Solvent Crystallization. *J. Cryst. Growth* **2005**, *279* (3–4), 477–488.

(23) Acevedo, D.; Jarmer, D. J.; Burcham, C. L.; Polster, C. S.; Nagy, Z. K. A Continuous Multi-Stage Mixed-Suspension Mixed-Product-Removal Crystallization System with Fines Dissolution. *Chem. Eng. Res. Des.* **2018**, *135*, 112–120.

(24) Majumder, A.; Nagy, Z. K. Fines Removal in a Continuous Plug Flow Crystallizer by Optimal Spatial Temperature Profiles with Controlled Dissolution. *AIChE J.* **2013**, *59* (12), 4582–4594.

(25) Eder, R. J. P.; Schrank, S.; Besenhard, M. O.; Roblegg, E.; Gruber-Woelfler, H.; Khinast, J. G. Continuous Sonocrystallization of Acetylsalicylic Acid (ASA): Control of Crystal Size. *Cryst. Growth Des.* **2012**, *12* (10), 4733–4738.

(26) Jiang, M.; Zhu, Z.; Jimenez, E.; Papageorgiou, C. D.; Waetzig, J.; Hardy, A.; Langston, M.; Braatz, R. D. Continuous-Flow Tubular Crystallization in Slugs Spontaneously Induced by Hydrodynamics. *Cryst. Growth Des.* **2014**, *14* (2), 851–860.

(27) Besenhard, M. O.; Neugebauer, P.; Scheibelhofer, O.; Khinast, J. G. Crystal Engineering in Continuous Plug-Flow Crystallizers. *Cryst. Growth Des.* **2017**, *17* (12), 6432–6444.

(28) McGlone, T.; Briggs, N. E. B.; Clark, C. A.; Brown, C. J.; Sefcik, J.; Florence, A. J. Oscillatory Flow Reactors (OFRs) for Continuous Manufacturing and Crystallization. *Org. Process Res. Dev.* **2015**, *19* (9), 1186–1202.

(29) Cruz, P. C.; Silva, C. R.; Rocha, F. A.; Ferreira, A. M. Mixing Performance of Planar Oscillatory Flow Reactors with Liquid Solutions and Solid Suspensions. *Ind. Eng. Chem. Res.* **2021**, *60* (6), 2663–2676.

(30) Cruz, P.; Silva, C.; Rocha, F.; Ferreira, A. The Axial Dispersion of Liquid Solutions and Solid Suspensions in Planar Oscillatory Flow Crystallizers. *AIChE J.* **2019**, *65* (9), e16683.

(31) Lee, S.; Park, J.-S.; Lee, T. R. The Wettability of Fluoropolymer Surfaces: Influence of Surface Dipoles. *Langmuir* **2008**, *24* (9), 4817–4826.

(32) Brown, C. J.; Adelakun, J. A.; Ni, X.-W. Characterization and Modelling of Antisolvent Crystallization of Salicylic Acid in a Continuous Oscillatory Baffled Crystallizer. *Chem. Eng. Process. Process Intensif.* **2015**, *97*, 180–186.

(33) Peña, R.; Oliva, J. A.; Burcham, C. L.; Jarmer, D. J.; Nagy, Z. K. Process Intensification through Continuous Spherical Crystallization Using an Oscillatory Flow Baffled Crystallizer. *Cryst. Growth Des.* **2017**, *17* (9), 4776–4784.

(34) Briggs, N. E. B. B.; Schacht, U.; Raval, V.; McGlone, T.; Sefcik, J.; Florence, A. J. Seeded Crystallization of β-L-Glutamic Acid in a Continuous Oscillatory Baffled Crystallizer. *Org. Process Res. Dev.* **2015**, *19* (12), 1903–1911.

(35) Jiang, M.; Ni, X.-W. Reactive Crystallization of Paracetamol in a Continuous Oscillatory Baffled Reactor. *Org. Process Res. Dev.* **2019**, *23* (5), 882–890.

(36) Raval, V.; Siddique, H.; Brown, C. J.; Florence, A. J. Development and Characterisation of a Cascade of Moving Baffle Oscillatory Crystallisers (CMBOC). *CrystEngComm* **2020**, *22* (13), 2288–2296.

(37) Agnew, L. R.; McGlone, T.; Wheatcroft, H. P.; Robertson, A.; Parsons, A. R.; Wilson, C. C. Continuous Crystallization of Paracetamol (Acetaminophen) Form II: Selective Access to a Metastable Solid Form. *Cryst. Growth Des.* **2017**, *17* (5), 2418–2427.

This page was intentionally left in blank

Chapter 10 - Continuous Antisolvent Crystallization in a Planar Oscillatory Flow Crystallizer

This chapter is based on: Cruz, P. C.; Rocha, F. A.; Ferreira, A. M. Tailoring the Crystal Size Distribution of an Active Pharmaceutical Ingredient by Continuous Antisolvent Crystallization in a Planar Oscillatory Flow Crystallizer. Chem. Eng. Res. Des. 2021, 175, 115–123.

https://www.sciencedirect.com/science/article/pii/S0263876221003506

10.1 Introduction

The pharmaceutical industry has relied on the development of new drugs for many years, while the investment in innovative technologies has remained on a secondary plan. However, over the past few decades, the increased entry of generic products after patent expiration, the opening of new markets, and the socioeconomic pressure to reduce prices, have been forcing manufacturers to increase the efficiency of their processes. Batch manufacturing has been the preference of the pharmaceutical industry for many years. However, there are several disadvantages associated with batch manufacturing: it lacks flexibility to respond to market growth or shortages; the production costs are usually inflated by high labor costs, excess inventories and significant down time between batches; and, in some cases, there are also serious issues with batch-to-batch variability and scale-up.[1–4] Therefore, this new stimulus for innovation has highlighted the potential of continuous manufacturing to reduce manufacturing costs, including energy consumption, footprint and labor requirements, and to improve capacity, flexibility and quality control.[2,5,6]

The manufacture of active pharmaceutical ingredients (APIs) involves a variety of unit operations, typically a series of reaction stages, followed by the work-up that may include operations such as extraction or concentration steps and, finally, crystallization, filtration, drying and, in many cases, size reduction operations such as milling.[4] The benefits of continuous manufacturing are particularly relevant in the crystallization step, which largely defines the final properties of the product, including purity, polymorphism and morphology. It also offers the possibility to control the crystal size distribution (CSD), which has a direct impact on downstream operations and end-use properties of the product.[7]

Particle formation during crystallization is governed by two primary events: nucleation and crystal growth. In addition, several other secondary events such as agglomeration, breakage, aging and ripening, may also have a significant effect on particle attributes. Apart from nucleation and crystal growth, agglomeration is frequently

the event with the most important effect on the CSD and crystal morphology. Agglomeration comprises the formation of both aggregates and agglomerates. Aggregates are assemblages of particles which are loosely attached to each other, and agglomerates are assemblages of particles rigidly joined together.[8] An aggregate is generated when two or more individual particles collide and adhere, and an agglomerate is generated when a solid bridge is formed between the individual particles of an aggregate that is exposed to high supersaturation for a long period. So, while aggregates can be easily disintegrated, agglomerates require brutal force to break the solid bridges binding the individual particles.[9]

Agglomeration is affected by a variety of factors, some of the most important being supersaturation, particle concentration, particle size and specific power input on the mixture. High supersaturations lead to high nucleation rates, and consequently, to high particle concentrations. In turn, high particle concentrations lead to high collision frequencies, and consequently, to high degrees of agglomeration. In addition, while intermolecular forces suffice to bind very small particles in aggregates, solid bridges are required to bind larger particles. As a consequence, smaller particles agglomerate more easily than larger particles. The effect of the specific power input is more complex, as an increase in specific power input leads to an increase in fluid shear rate, with impact on both agglomeration and disruption rates. As a consequence of the two opposite effects, the agglomeration rate passes through a maximum with increasing fluid shear rate.[9,10]

Agglomeration can be desirable or undesirable depending on the downstream operations and end-use properties of the product. Inclusions of mother liquor and impurities entrapped in agglomerates are undesirable as they compromise purity and contribute for the caking of crystals during storage. Agglomeration also forces a shift in the CSD for larger sizes, which might lead to the intensification of corrective operations, such as increasing the grinding time and/or the energy requirements for grinding, to reduce the impact of larger particles on formulation and bioavailability of the product. Irregularly shaped agglomerates also have the potential to produce more fines during transportation and storage. On the other hand, agglomerates with regular shapes, mostly spherical, can improve the flowability and compaction properties of the product and enhance the separation efficiency in solid-liquid separations, such as filtration.[11–14]

The crystallization equipment can also have an important impact on the final properties of the product. Plug flow crystallizers are especially useful to control the CSD due to their ability to provide narrow residence time distributions.[15,16] This category comprises a great variety of crystallizers, including the oscillatory flow crystallizer (OFC). OFCs have been used for the continuous crystallization of a variety of APIs (aspirin,[18] L-glutamic acid,[19] lactose,[20,21] paracetamol,[22,23] salicylic acid,[24] benzoic acid,[25] and an unspecified API[26]), and also for the continuous cocrystallization of α-lipoic acid:nicotinamide.[27] Cooling crystallizations have been more common,[18–22,26,27] but some antisolvent,[24,25] and reactive[23] crystallizations have also been performed. Additional auxiliary techniques, such as sonication[20] and seeding[19,23,26,27] have also been employed. In several studies, preliminary batch experiments were performed to identify optimal operating conditions and then a linear scale-up strategy was used to transfer the processes from batch to continuous.[20,26,27] Control of mean crystal size and

CSD,[19–21,23,24,26] polymorphism,[19,22] and agglomeration degree[25] has been possible. Furthermore, in some cases, the OFCs required significantly shorter processing times than the traditional batch processes, presumably due to their heat and mass transfer efficiency.[20,26] However, some problems related to the suspension and flowability of solids have been reported. In some cases, the formation of encrustations on the surfaces of the tubes has even lead to loss of control, blockages and, ultimately, process shut-down.[19,22,25] Nevertheless, high oscillation intensities and flow rates have been proved effective in reducing the deposition of solids, and, consequently, the rate of material buildup on the walls of crystallizers. Seeding has also been successfully used to reduce the potential for encrustation due to excessive nucleation. Additionally, it has been suggested that high supersaturations and solids loadings should be avoided so as to prevent clogging and fouling.[19,24,25]

In this work, the planar-OFC was tested for the continuous antisolvent crystallization of an API that is currently produced in a traditional batch process. The main goal was to manipulate the operating conditions to produce small crystals in order to meet very specific formulation requirements and, simultaneously, promote the aggregation of these small crystals in weak aggregates to optimize the filtration operation.

10.2 Materials and Methods

The API, which we are unable to name for commercial reasons, is currently produced by Hovione in an industrial stirred tank crystallizer (STC). A solution of antisolvent, hereinafter solution A, is kept at 10 °C, and a feed solution with a concentration of API higher than 300 g L^{-1}, hereinafter solution B, is kept at 35 °C. Solution B is slowly added to solution A over the course of several hours until the final antisolvent to feed solution ratio V_A/V_B=0.5 is reached. This process has a stoichiometric yield higher than 80% and the product consists of a broad CSD.

The crystallization of this API presents a diversity of factors that makes its adaptation to continuous manufacturing particularly challenging. These factors include the high viscosity and acidity of the mother liquor, and the high particle density of the final product. On the one hand, the acidity of the mother liquor conditioned the selection of the planar-OFC materials, and, on the other hand, the viscosity and density of the suspension conditioned the range of the operating variables.

10.2.1 Calibration Curve

An analytic method was developed to measure the concentration of API in the mother liquor, C. A set of 8 standard solutions of API ranging from 0 to 30 mg L^{-1} were prepared in triplicates at room temperature (~23 °C). The absorbance of each standard solution, Abs, was measured by UV/Vis spectroscopy (SPEC RES+ UV/VIS-

Sarspec) at 270 nm. Then, the linear regression equation was fitted to the experimental data by the method of least squares. The experimental data and the calibration curve are presented in **Figure 10.1**. Further details are provided in **Appendix B**.

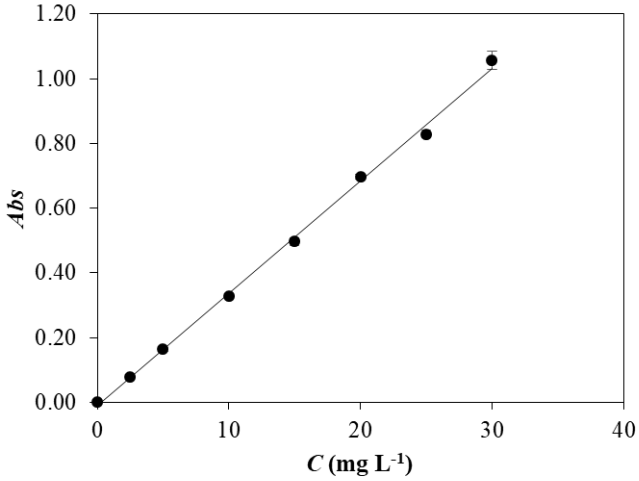


Figure 10.1 – Calibration curve for the absorbance as a function of the concentration of API in the mother liquor at room temperature (~23 °C). The error bars represent the interval between the minimum and maximum values of the three replicates.

10.2.2 Batch Crystallization in a STC

Batch crystallization experiments were performed in small STCs to study the effect of the ratio between the volume of solution A and the volume of solution B, V_A/V_B, on the yield, Y. 10 mL of solution B were added to 3, 5, 10, 20, 30, 40, 50, 60, 70, 80, 90 and 100 mL of solution A in 12 open vessels. The mixtures were stirred by a magnetic bar at 500 rpm for 3 hours. The final product was filtered, washed and left to dry overnight. The mass of crystals was weighted and the yield was calculated. The final concentration of the API in the mother liquor was measured by UV/Vis spectroscopy. Each experiment was replicated three times.

10.2.3 Crystallizer

The planar-OFC consists of a plate-like crystallizer with three stacked plates: two polycarbonate plates, one at the base and one at the top, and one aluminum plate coated with Halar® (ethylene-chlorotrifluoroethylene copolymer, ECTFE) plate in the middle – **Figure 10.2 (a)**. The crystallization process takes place in a channel designed with smooth periodic constrictions located between the middle and top plates, and the water of a cooling/heating jacket circulates in a straight channel located between the base and middle plates. The two channels were carved in the middle plate; the top plate seals the crystallization channel and the base plate seals

the jacket channel. The crystallization channel has 6 access points (one main inlet, one main outlet and four intermediate inlets/outlets) and comprises a volume of approximately 71 mL (operational volume). The dimensions of each inter-constriction cell are presented in **Figure 10.2 (b)**.

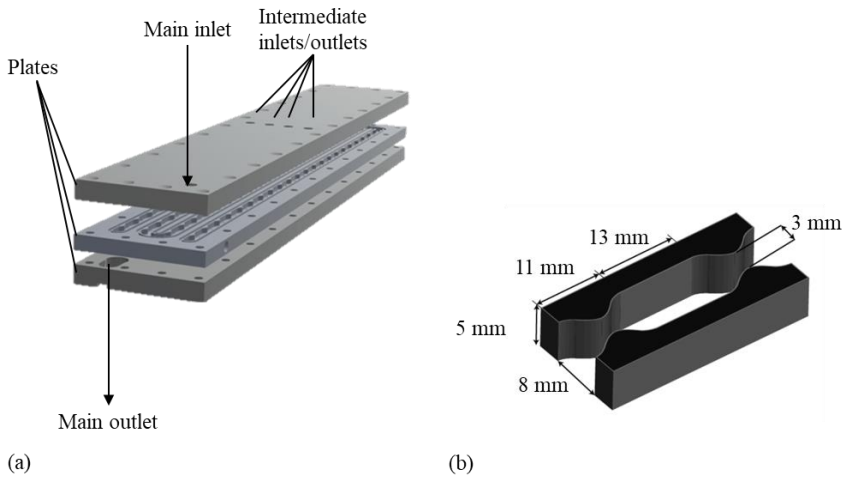


Figure 10.2 – Plate-like planar-OFC. (a) Three stacked plates. (b) Dimensions of each inter-constriction cell.

The crystallizer is formed by one or two planar-OFCs in series. With one planar-OFC, the crystallizer contains an operational volume of 71 mL, and with two planar-OFCs in series, the crystallizer contains an operational volume of 142 mL. The temperature of the crystallizer is controlled by a cooling/heating bath (Ministat 125, Huber), and the frequency and amplitude of oscillation in the crystallizer is controlled by a linear motor actuating a piston with a 10.3 mm diameter (H01-23x166/80, LinMot).

10.2.4 Batch Crystallization in a Planar-OFC

Batch crystallization experiments were performed in a planar-OFC. The experimental set-up is presented in **Figure 10.3**. Solution A was thermostated at 10 °C by a cooling/heating bath and kept under stirring on a magnetic stirrer (C-MAG HS 7 digital, IKA). Solution B was thermostated at 35 °C and kept under stirring on a hotplate magnetic stirrer connected to a PT 1000 temperature sensor. The solutions were transferred by peristaltic pumps (BT300-2J, Longer Pump).

First, the planar-OFC was filled with solution A and thermostated at the desired temperature, T. Then, solutions A and B were injected into an aeration system at the desired flow rates, Q_A and Q_B, respectively. The aeration system comprises a static mixer and an unstirred open vessel. Solutions A and B came into close contact in the static mixer, and then the mixture was discharged into the open vessel. The aeration system eliminated part of a gas that is formed when the two solutions come into contact, which delays nucleation. Q_A and Q_B were

different in different runs to provide different ratios of flow rates, Q_A/Q_B, but the total flow rate, $Q_T = Q_A + Q_B$, was set at 40 mL min^{-1} in all runs. The volume of solution in the open vessel was kept at 20 mL to impose a short residence time of 30 s in the open vessel. Then, the mixture was injected into the planar-OFC close to the piston, which forced solution A out of the crystallizer. When the planar-OFC was completely filled with the mixture, the flow was stopped and the oscillation was activated at the desired frequency, f, and amplitude, x_0.

The final suspension was collected after a given batch time and the product was filtered, washed and left to dry overnight. A sample of dry powder was suspended in a saturated solution of API and kept under sonication for 1 min to disperse the coarse granules that were formed after filtration and drying. Then, the CSD was measured by a laser diffraction particle size analyzer (Coulter LS230), and the volume-based crystal sizes corresponding to the 10th, 50th and 90th percentile of the cumulative CSD, d_{10}, d_{50} and d_{90}, respectively, were determined. The final concentration of the API in the mother liquor was measured by UV/Vis spectroscopy. The morphology of the particles was assessed by scanning electron microscopy (SEM) using a Fei Quanta 400 FEG ESEM/EDAX Pegasus X4M (Eindhoven, The Netherlands) located at the Laboratory for Scanning Electron Microscopy and X-Ray Microanalysis (LMEV) from the Image, Microstructure and Microanalysis Unit (IMICROS) of the Materials Center of the University of Porto (CEMUP). The samples were first mounted on brass stubs using double-faced adhesive carbon tape and then coated in vacuum by a thin layer of gold (electrically conductive).

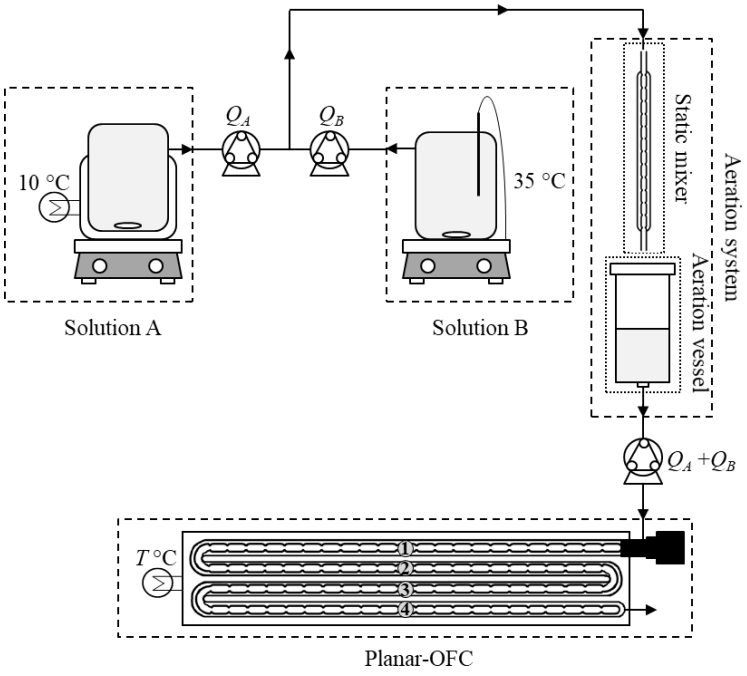


Figure 10.3 – Experimental set-up for batch crystallization in a planar-OFC.

A Plackett-Burman experiment was created in Minitab® to study the effects of T, V_A/V_B, f and x_0 on the CSD. Each factor was studied at two levels: 15 and 25 °C for T, 0.5 and 3 for V_A/V_B, 2 and 6 Hz for f, and 4 and 6 mm for x_0 (4 and 6 mm in the piston, thus 8.3 and 12.5 mm in the straight section of the channel).

10.2.5 Continuous Crystallization in a Planar-OFC

Continuous crystallization experiments were performed in one or two planar-OFCs in series. The experimental set-up is presented in **Figure 10.4**. First, the planar-OFC was filled with solution A and thermostated at the desired temperature. Then, the oscillation was activated at the desired frequency and amplitude. After that, solutions A and B were continuously injected into the planar-OFC close to the piston at the desired flow rates, Q_{A1} and Q_B, respectively. An additional input of solution A was continuously injected into an intermediate inlet of the planar-OFC at the desired flow rate, Q_{A2}. In some experiments A2 was injected into the second intermediate inlet, in other experiments it was injected into the sixth. The total flow rate, $Q_T = Q_{A1} + Q_{A2} + Q_B$, was set at 24 mL min^{-1}.

The suspension was sampled from the main outlet at regular intervals, and the crystals were filtered, washed and left to dry overnight. The CSD of the final product, the final concentration in the mother liquor and the morphology of the particles were assessed as previously described. For practical purposes, it was considered that steady state was reached when the standard deviation of concentration was less than 15% of the mean concentration.

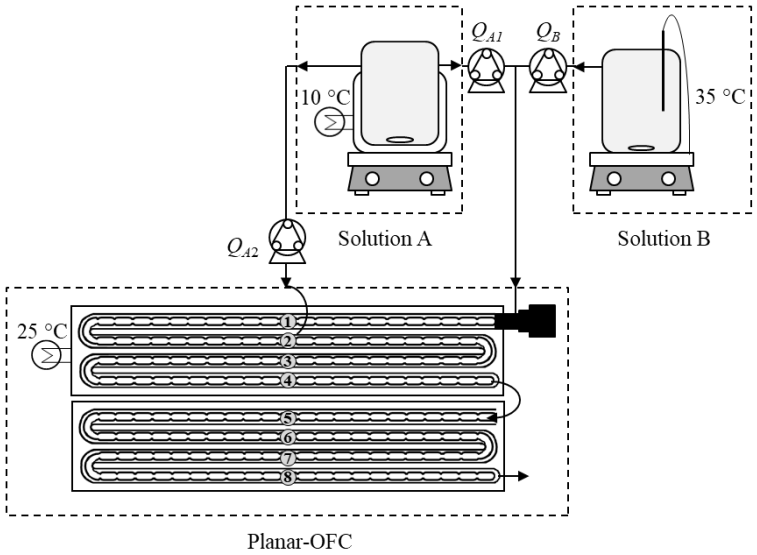


Figure 10.4 – Experimental set-up for continuous crystallization in a planar-OFC.

10.3 Results and Discussion

10.3.1 Batch crystallization in a STC

A set of 12 batch experiments were performed in small STCs to investigate the effect of V_A/V_B on the yield. It was interesting to note that a gas is formed after the addition of solution B (the feed solution) to solution A (the antisolvent). It was also interesting to note that, in this process, unlike most antisolvent crystallization processes, nucleation does not occur immediately after the addition of solution B to solution A. A possible explanation for this could be that the solution only becomes supersaturated as the gas is released.

The initial concentration of API after de addition of solution B to solution A, C_i, and the solubility of the API after the release of the gas, C_s, taken as the final concentration of API in the mother liquor after crystallization, C_f, are plotted as a function of V_A/V_B in **Figure 10.5 (a)**. Both the initial and the final concentration of API in the mother liquor decrease as V_A/V_B increases. The experimental and expected mass of crystallized API, m_{crist}, are plotted as a function of V_A/V_B in **Figure 10.5 (b)**. The expected mass of crystallized API was calculated as $m_{crist} = (C_i - C_f) \times (V_A + V_B)$. The yield, Y, is plotted as a function of V_A/V_B in **Figure 10.5 (c)**. The mass of crystallized API and the yield increase as V_A/V_B increases from 0.3 to 0.5, then they remain practically unchanged as V_A/V_B increases from 0.5 to 3, and finally they decrease as V_A/V_B increases from 3 to 10. This result is a consequence of the different rates at which C_i and C_f decrease as V_A/V_B increases. To be more specific: when V_A/V_B increases from 0.3 to 0.5, C_f decreases more than C_i does, therefore the yield increases; when V_A/V_B increases from 0.5 to 3, C_f and C_i decrease in a similar proportion, therefore the yield remains practically unchanged; when V_A/V_B increases from 3 to 10, C_f decreases less than C_i does, therefore the yield decreases. Finally, the mass of crystallized API per volume of solution, $m_{crist}/(V_A + V_B)$, is plotted as a function of V_A/V_B in **Figure 10.5 (d)**. Clearly, the mass of crystallized API per volume of solution decreases substantially as V_A/V_B increases. Therefore, V_A/V_B=0.5 seems to be optimal to maximize the yield and minimize the consumption of antisolvent. However, V_A/V_B=0.5 might be impractical to operate in continuous, as such a low amount of antisolvent implies that a suspension with high viscosity and high particle density has to be dragged along the crystallization channel. Therefore, it is interesting to have the possibility to increase V_A/V_B from 0.5 up to 3 to improve the flowability of the particles and avoid fouling in the continuous process without compromising the yield. Although this higher consumption of raw material can have negative implications from a commercial point of view, as well as environmental impact, it can be overcome with solvent recycling.

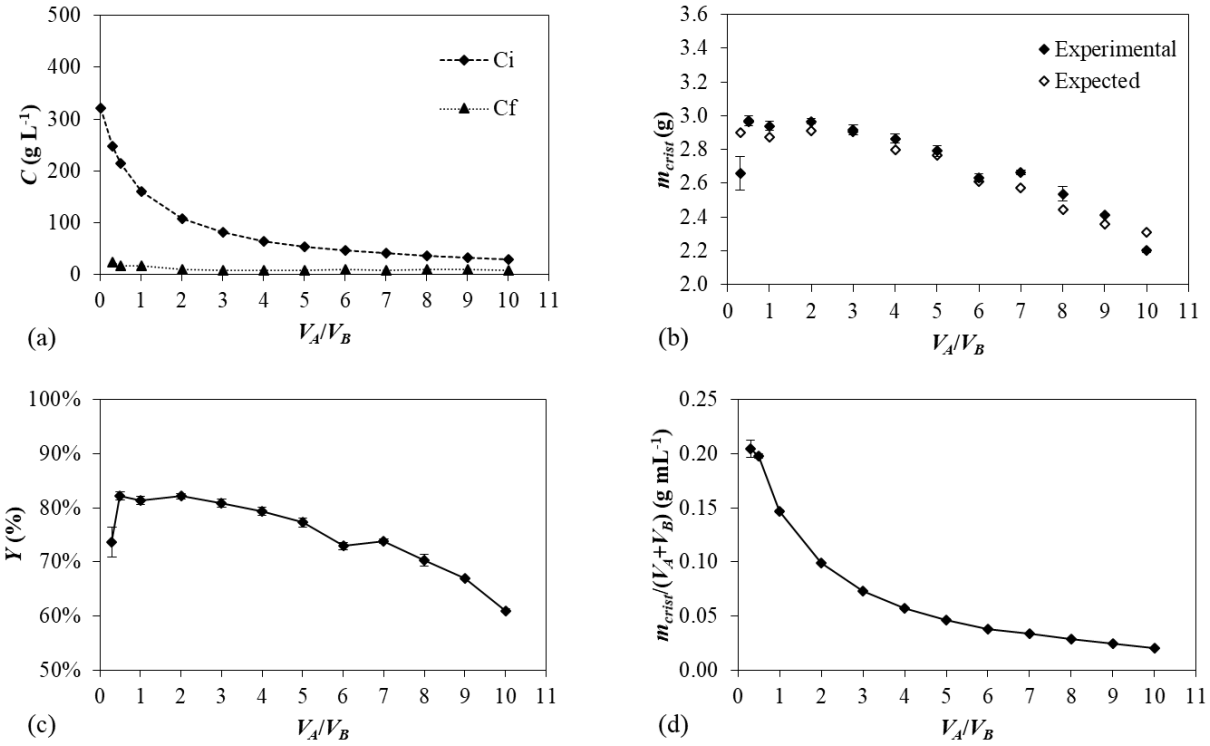


Figure 10.5 – (a) Initial concentration, C_i, and final concentration, C_f, as a function of V_A/V_B. (b) Experimental and expected mass of crystallized API as a function of V_A/V_B. (c) Yield as a function of V_A/V_B. (d) Mass of crystallized API per volume of solution as a function of V_A/V_B. The error bars represent the standard deviation of the three replicates.

10.3.2 Batch crystallization in a planar-OFC

In preliminary experiments, solutions A and B were directly injected into the planar-OFC. However, the nucleation rate was not uniform: crystals appeared first close to the oscillation piston and the outlet, and only then did they appear in the intermediate section of the planar-OFC. On the one hand, the high shear stress region created by the oscillating motion may be responsible for reducing the induction time close to the oscillation piston. On the other hand, the release of gas out of the crystallizer may be responsible for reducing the induction time close to the outlet. The gas is formed when solutions A and B come into contact, and it appears to have an inhibitory effect on nucleation. Therefore, the accumulation of gas in the intermediate section of the planar-OFC may be responsible for increasing the induction time in this section. So, in order to remove part of the gas and promote uniform nucleation rates throughout the planar-OFC, solutions A and B were injected into an aeration system before entering the planar-OFC in the following experiments. The short period of time that the mixture spends in the aeration system (30 s) is enough to allow the release of part of the gas (which reduces the barrier for nucleation in the crystallizer), but is not enough to completely eliminate the gas out of the mixture (which would induce nucleation in the aeration system).

A set of 12 batch experiments (B1-B12) were performed in a planar-OFC to investigate the effects of specific variables associated to this crystallizer. This strategy has been recommended to identify optimal operating conditions with reduced waste of solvents/reagents before conducting the continuous experiments [20,26,27]. The experimental conditions and results obtained in each run after 2 h of residence time are presented in **Table 10.1**.

Table 10.1 – Batch crystallization in a planar-OFC: experimental conditions and results obtained in each run.

Run	f (Hz)	x_0 (mm)	T (°C)	V_A/V_B	d_{10} (µm)	d_{50} (µm)	d_{90} (µm)
B1	2	6	15	0.5	0.81	10.04	24.06
B2	2	6	25	3	0.84	8.49	30.62
B3	6	6	15	3	1.27	16.85	77.57
B4	2	6	25	0.5	1.49	11.46	33.47
B5	6	4	25	0.5	1.71	17.56	37.38
B6	6	4	25	3	1.70	13.29	53.00
B7	6	6	25	0.5	1.06	11.13	29.64
B8	6	6	15	3	0.58	7.41	46.95
B9	2	4	25	3	1.50	12.27	45.85
B10	2	4	15	0.5	1.62	14.88	38.59
B11	2	4	15	3	0.79	7.90	45.10
B12	6	4	15	0.5	1.51	15.03	39.97

Figure 10.6 presents the effects of T, V_A/V_B, f and x_0 on the volume-based CSD, $f_V(d)$, after 2 h of residence time. Three size fractions can be generally identified: the crystal fragments, the single crystals, and the aggregates, in ascending order of size, as illustrated in **Figure 10.7** for Run B2. The aggregates could be easily disintegrated when a sample was slightly pressed between a slide and coverslip, so they must be classified as aggregates and not agglomerates.

Unfortunately, due to their trimodal nature, the CSDs cannot be properly described by d_{10}, d_{50} and d_{90}. Let us take Runs B5 and B7 as an example. **Figure 10.6** shows that the CSD of Run 5 is distinct from the CSD of Run 7, however, **Table 10.1** shows that d_{10}, d_{50} and d_{90} are fairly similar for the two runs (Run 5: d_{10}=1.71 µm, d_{50}=17.56 µm and d_{90}=37.38 µm; Run 7: d_{10}=1.06 µm, d_{50}=11.13 µm and d_{90}=29.64 µm). Therefore, we have based our conclusions on the qualitative effect of T, V_A/V_B, f and x_0 on the complete CSD, in its graphical representation, and not on their quantitative effect on d_{10}, d_{50} and d_{90}.

Figure 10.6 shows that increasing f from 2 to 6 Hz or increasing T from 15 to 25 °C does not have a significant effect on the CSD. However, it also shows that considerably less aggregates are produced when x_0 increases from 4 to 6 mm and V_A/V_B increases from 0.5 to 3. This is probably due to improved particle flowability provided by higher amplitudes, and reduced suspension density provided by higher amounts of antisolvent, both of which reduce the probability of particle collision to form aggregates.

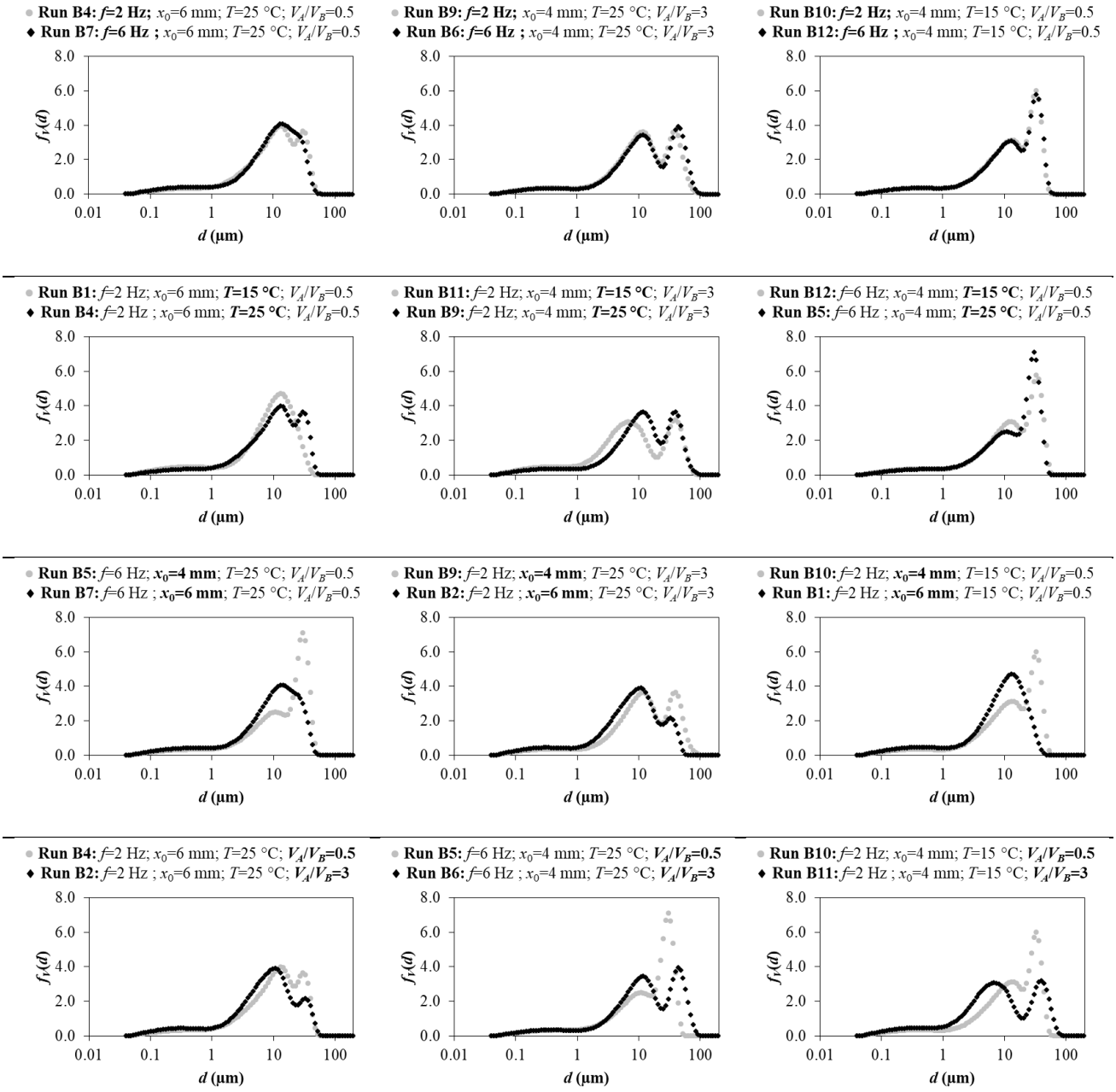


Figure 10.6. Effect of *f*, *T*, x_0 and V_A/V_B on the CSD after 2 h of residence time (from the top to the bottom).

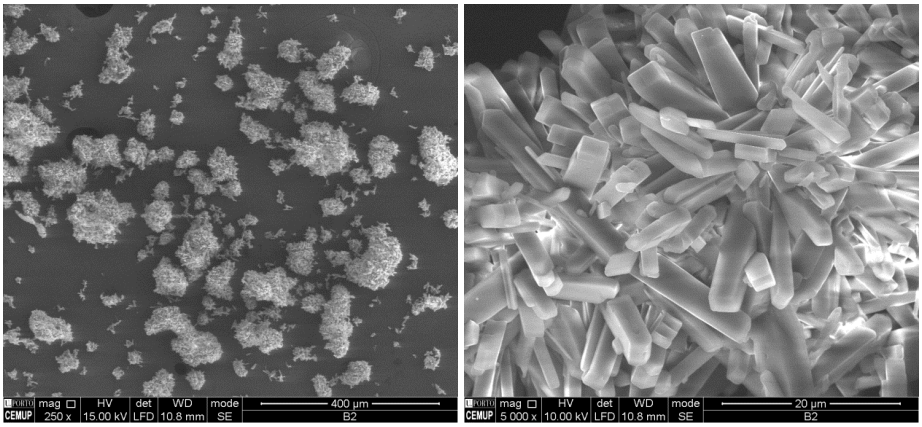


Figure 10.7 – SEM images of the product obtained from Run B2.

10.3.3 Continuous crystallization in a planar-OFC

Preliminary experiments

Preliminary experiments were performed to select a suitable method for the continuous crystallization of the API in a planar-OFC. Several methods were tested, including coupling an STC to a planar-OFC to detach the nucleation and crystal growth steps (Method A), coupling an aeration system to a planar-OFC to remove part of the gas in the aeration system and promote nucleation in the planar-OFC (Method B), and triggering nucleation in the oscillation piston of the planar-OFC (Method C). Controlling the nucleation rate was a major challenge in all methods, but even more so in Method A. Promoting nucleation in the STC and then injecting the suspension into the planar-OFC proved to be unfeasible due to clogging in the tubing between the STC and the planar-OFC. Moving solids in transfer lines was therefore avoided in the other two methods. In Methods B and C, the effect of Q_{A1}/Q_B on nucleation proved to be critical for the viability of the process. In both methods, intense and uncontrolled nucleation, followed by fouling and clogging were observed with Q_{A1}/Q_B>1/3, but full operability was possible with Q_{A1}/Q_B=1/3. So, in methods B and C, the initial ratio of flow rates was defined as Q_{A1}/Q_B=1/3 to promote nucleation under controlled conditions. Although both methods were operable, Method C was chosen to perform the next experiments due to its simplicity compared to Method B.

Optimization of experimental conditions

In relation to f and T, batch experiments in the planar-OFC showed that changing f and T does not have a significant effect on the CSD. Therefore, the optimal levels of f and T for continuous crystallization in the planar-OFC were chosen based on operational aspects. On the one hand, preliminary experiments showed that f should be kept at a low level to reduce the retention time of the gas in the planar-OFC, as low frequencies

avoid the breakage of the gas bubbles into smaller bubbles, which are more prone to be trapped between constrictions.[30] On the other hand, T should be kept at a high level to accelerate the nucleation kinetics, as preliminary experiments showed that increasing the temperature reduces the induction time, possibly due to the release of the gas with an inhibitory effect on nucleation. In relation to x_0, batch experiments in the planar-OFC showed that x_0 should be kept at a low level to promote the formation of aggregates. However, preliminary experiments showed that x_0 should be kept at a high level to improve flowability. As it is extremely important to improve flowability to guarantee the operability of the continuous process, x_0 should be kept at a high level. In relation to Q_A/Q_B, the optimization problem is more complex. Batch experiments in the planar-OFC showed that V_A/V_B should be kept at a low level to promote the formation of aggregates. However, preliminary experiments showed that, on the one hand, Q_A/Q_B should be kept at a low level to promote nucleation under controlled conditions, but, on the other hand, Q_A/Q_B should be kept at a high level to improve flowability in the continuous process. Therefore, stream A should be divided into streams: A1 and A2. A1 and B should be injected directly into the planar-OFC, close to the oscillation piston, at Q_{A1}/Q_B=1/3 to promote nucleation under controlled conditions. Then, A2 should be injected into an intermediate inlet of the planar-OFC to improve flowability. In order to avoid backmixing, the flow rate of A2 should not exceed the combined flow rate of A1 and B ($Q_{A2} \leq Q_{A1} + Q_B$). At the limit, $Q_{A2} = Q_{A1} + Q_B$. Therefore, since $Q_{A1}/Q_B = 1/3 \Leftrightarrow Q_B = 3Q_{A1}$, then $Q_{A2} = Q_{A1} + 3Q_{A1} \Leftrightarrow Q_{A2} = 4Q_{A1}$. So, the final ratio of flow rates can be increased up to $Q_A/Q_B = (Q_{A1} + Q_{A2})/Q_B = (Q_{A1} + 4Q_{A1})/3Q_{A1} = 5/3$. In this way, the planar-OFC is divided into two sections with different antisolvent to feed solution ratios: the nucleation zone, located between the main inlet and the inlet of A2 (where nucleation is dominant, while crystal growth still occurs), and the crystal growth zone, located between the inlet of A2 and the main outlet (where crystal growth is dominant, while nucleation still occurs). Taking all this information into account, a set of 4 continuous experiments (C1-C4) were performed in a planar-OFC with optimized experimental conditions. The experimental conditions of each run are presented in **Table 10.2** and the schematic representation of each run is presented in **Figure 10.8**. The evolution of the concentration of API in the mother liquor and supersaturation ratio, S, at the outlet of the planar-OFC, and the steady state volume-based CSDs obtained from each run are presented in **Figure 10.9**. SEM images of the product obtained from each run are presented in Figure **10.10**.

Table 10.2 – Continuous crystallization in a planar-OFC: experimental conditions of each run.

Run	f (Hz)	x_0 (mm)	T (°C)	Q_T (mL/min)	Q_{A1}/Q_B	Q_A/Q_B	N.º of planar-OFCs in series	Inlet position of A2
C1	2	6	25	24	1/3	0.5	2	2
C2	2	6	25	24	1/3	1.7	2	2
C3	2	6	25	24	1/3	1.7	1	2
C4	2	6	25	24	1/3	1.7	2	6

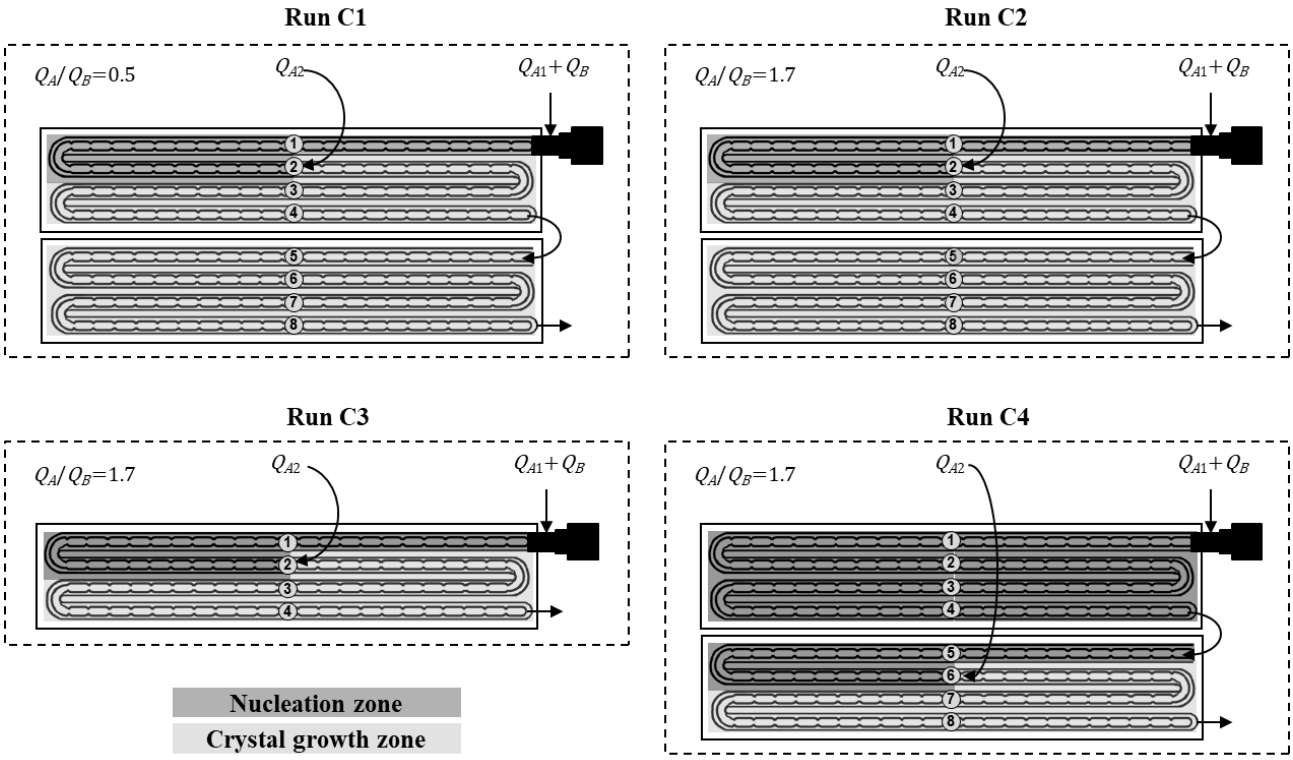


Figure 10.8 – Schematic representation of Runs C1-C4.

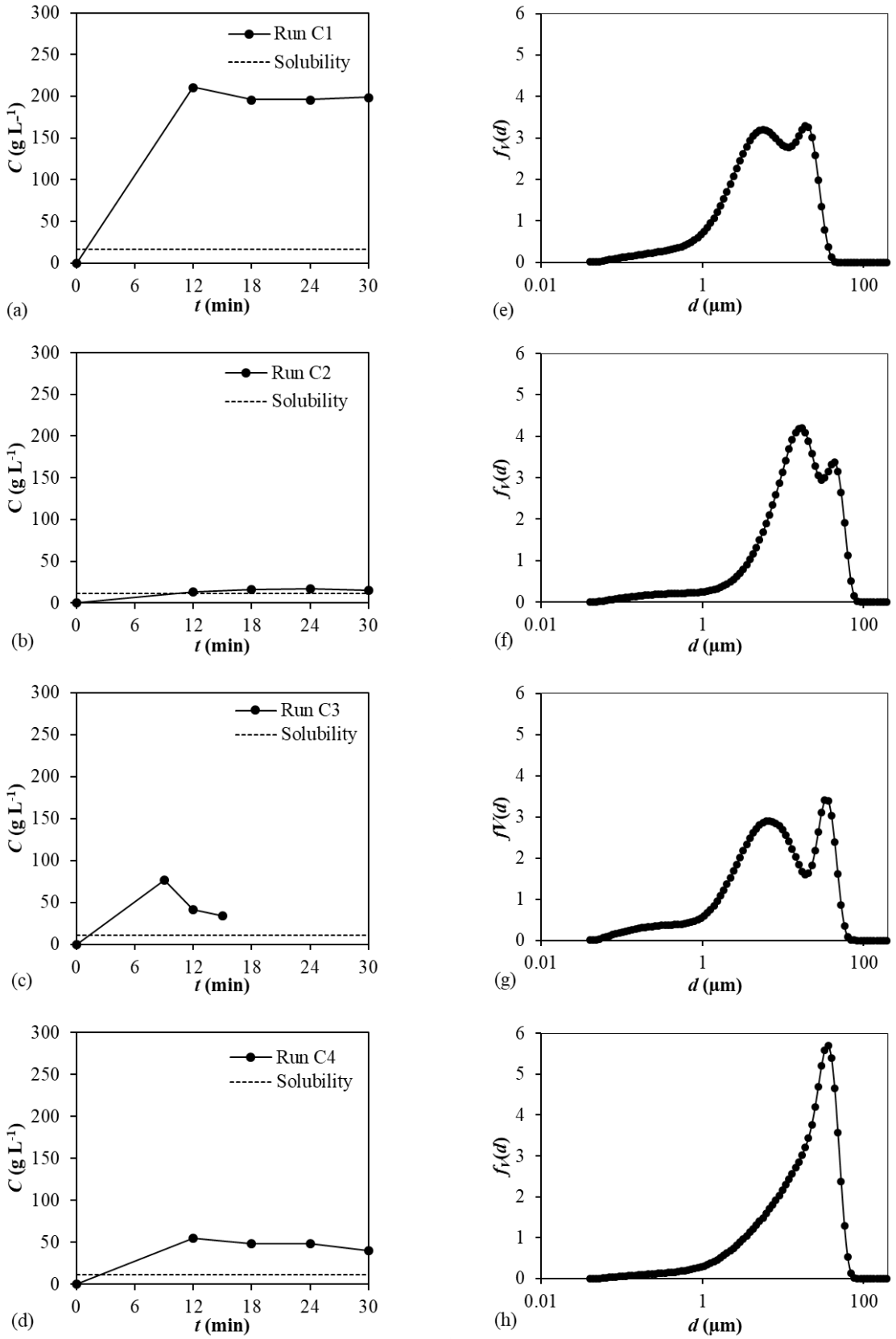


Figure 10.9 – Concentration of API in the mother liquor at the outlet of the planar-OFC over (a) Run C1, (b) Run C2, (c) Run C3, and (d) Run C4. Steady state volume-based CSDs obtained from (e) Run C1, (f) Run C2, (g) Run C3, and (h) Run C4.

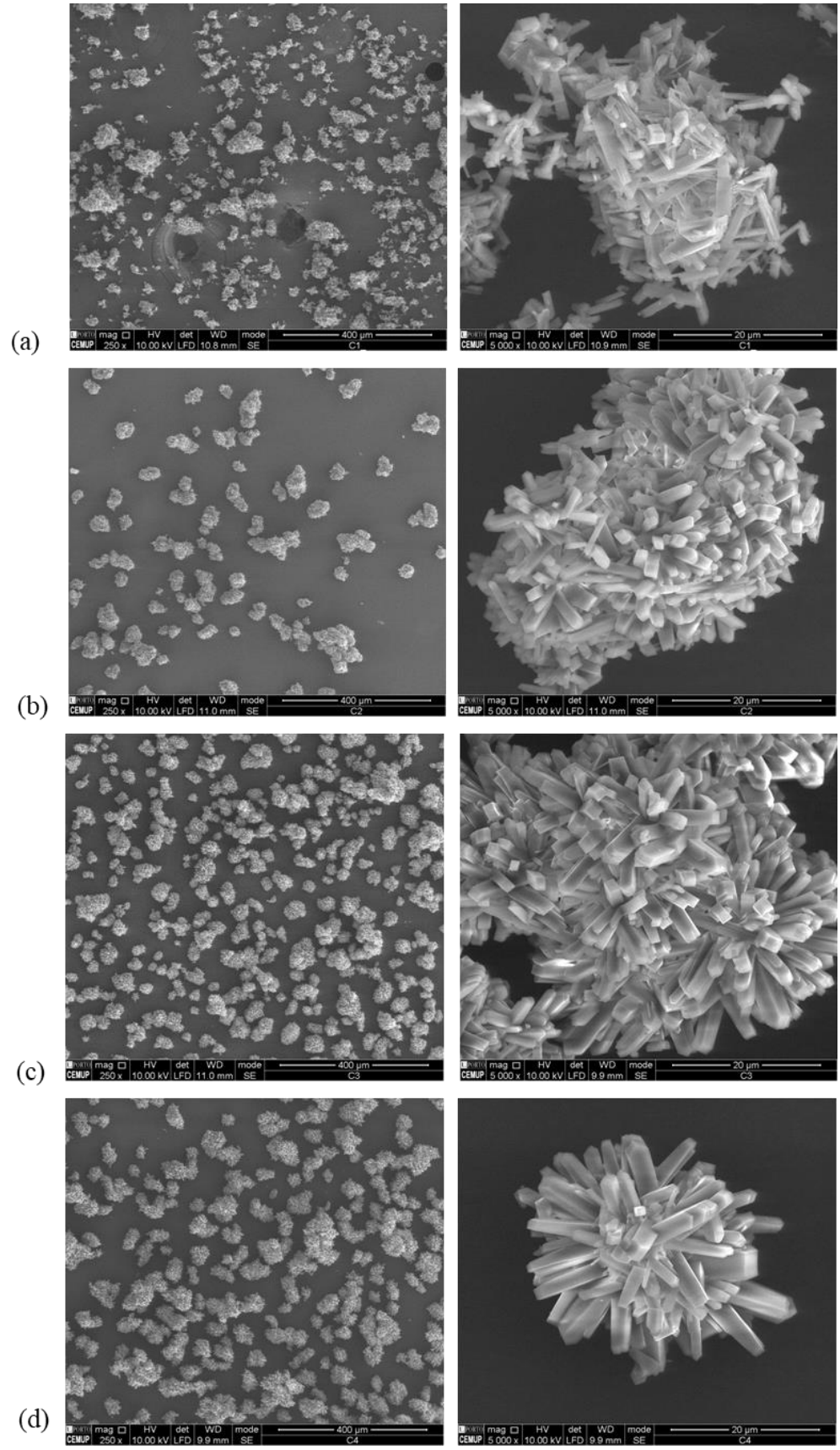


Figure 10.10 – SEM images of the product obtained at steady state from (a) Run 1, (b) Run 2, (c) Run 3, and (d) Run 4.

Effect of Q_{A1}/Q_B

Runs C1 and C2 were performed under the same experimental conditions, except for Q_{A1}/Q_B, with Q_{A1}/Q_B=0.5 in Run C1 and Q_{A1}/Q_B=1.7 in Run C2. **Figure 10.9 (a)** and **(b)** shows that the concentration of API does not vary significantly between 12 and 30 min of operation in both Runs C1 and C2, which indicates that the system operates at steady state at least after 12 min of operation (no sample was analyzed before 12 min). **Figure 10.9 (a)** and **(b)** also shows that the concentration of API practically reaches solubility in Run C2, but not in Run C1, suggesting that a longer residence time would be necessary to achieve solubility in Run C1, which would require more units of planar-OFCs. As to the CSD, **Figure 10.9 (e)** and **(f)** and **Figure 10.10 (a)** and **(b)** show that Run C1 produced smaller single crystals and smaller aggregates than Run C2. This was probably because the mother liquor was not completely desupersatured inside the crystallizer during Run C1, which limited crystal growth. Interestingly, the percentage of aggregates was similar in both runs.

Effect of the Residence Time in the Nucleation Zone

Runs C3 and C4 were performed under the same experimental conditions, except for the residence time in the nucleation zone, which was longer in Run C4 – **Figure 10.8**. **Figure 10.9 (c)** and **(d)** shows that the concentration of API did not reach solubility neither in Run C3 nor in Run C4, but it reached steady state after 12 min of operation in both runs. As to the CSD, **Figure 10.9 (g)** and **(h)** and **Figure 10.10 (c)** and **(d)** show that Run C4 produced a higher percentage of aggregates than Run C3. This could be due to the longer total residence time of Run C4, or due to the longer residence time in the nucleation zone in particular. The results of the following section should clarify this matter.

Effect of the Residence Time in the Crystal Growth Zone

Runs C2 and C3 were performed under the same experimental conditions, except for the residence time in the crystal growth zone, which was longer in Run C2 – **Figure 10.8. Figure 10.9 (b)** and **(c)** shows that the concentration of API reached solubility in Run C2, but not in Run C3, while steady state was reached after 12 min of operation in both runs. As to the CSD, **Figure 10.9 (f)** and **(g)** and **Figure 10.10 (b)** and **(c)** show that Run C2 produced larger single crystals than Run C3, probably as a consequence of the longer residence time in the crystal growth zone of Run C2. Interestingly, the percentage of aggregates was similar in both runs, which supports the hypothesis presented in the previous section that the residence time in the nucleation zone, and not the total residence time, controls the formation of aggregates. This could be due to the combination of high supersaturation, high particle concentration and small crystal sizes in the nucleation zone, which may have promoted the formation of aggregates.

Therefore, the operating conditions of Run C4 should be preferred to produce a highly aggregated product with a narrow CSD. Nevertheless, the residence time should be increased so as to improve the yield. Considering that Run C2 reached solubility with a longer residence time in the crystal growth zone, one more planar-OFC in series in the crystal growth zone should be enough to reach solubility with the operating conditions of Run C4.

The volume-based CSDs obtained from a traditional batch and from Run C4 are compared in **Figure 10.11**. In this figure, a logarithmic scale was not used to highlight the difference in width of the two CSDs. Clearly, the continuous process in the planar-OFC was able to produce smaller particles with a significantly narrower CSD than the traditional batch process in a STC. This was rather expected due the difference in the way the feed solution is added to the antisolvent in the two processes. On the one hand, while the slow addition of feed solution to the antisolvent in the traditional process gives time for the crystals to grow progressively over time, the fast addition of feed solution to the antisolvent in the continuous process induces a strong nucleation which limits crystal growth. On the other hand, while V_A/V_B changes dramatically over time in the traditional process, which leads to a broad CSD, Q_A/Q_B is constant over time in the continuous process, which leads to a narrow CSD.

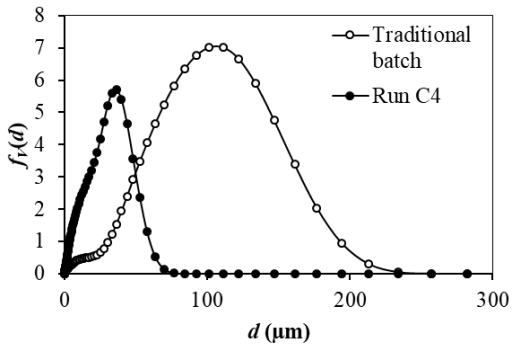


Figure 10.11 – Volume-based CSDs obtained from a traditional batch and from Run C4.

10.4 Conclusion

In this work, a continuous antisolvent crystallization process was implemented in a planar-OFC to produce an API with a narrow CSD. The main purpose was to find an alternative to the traditional batch crystallization process in a large STC, which produces the API with a broad CSD.

Prior to the continuous crystallization experiments, preliminary batch crystallization experiments were performed. It was found that increasing the antisolvent to feed solution ratio can improve flowability without loss of yield. This is very important as improved flowability reduces the potential for fouling and clogging in the planar-OFC. It was also found that a gas, with an inhibitory effect on the nucleation of the API, is formed

when the antisolvent comes into contact with the feed solution. This is not critical in the traditional batch crystallization process that occurs in an open crystallizer, but it cannot be ignored in the planar-OFC. In addition, the continuous crystallization process had to be designed for three phases, and not two as originally thought, which added complexity to the process. With respect to operability, it was found that higher amplitudes of oscillation are preferable to improve flowability, lower frequencies of oscillation are preferable to reduce the retention time of the gas in the crystallizer, and higher temperatures are preferable to promote the nucleation kinetics. As to the antisolvent to feed solution ratio, it should be lower at the beginning to prevent excessive nucleation, and then it should be increased to improve flowability.

In the continuous crystallization experiments, the planar-OFC was divided into two spatially independent sections so as to control the CSD as a function of the residence time in each section. The first section of the crystallizer, where nucleation is dominant, was labeled as nucleation zone, and the second section of the crystallizer, where crystal growth is dominant, was labeled as crystal growth zone. The main goal was to promote the aggregation of small individual crystals in order to improve the separation efficiency of filtration while complying with specific formulation requirements for small crystals. It was found that aggregation can be promoted by increasing the residence time in the nucleation zone due to the combination of high supersaturation, high particle concentration and small crystal sizes in this zone.

Finally, the planar-OFC was able to produce significantly narrower CSDs than the traditional batch crystallization process, thus avoiding reprocessing and/or additional corrective operations. Nevertheless, further studies are still required to optimize the residence time in order to improve the yield.

Notation

Acronyms	
API	Active pharmaceutical ingredient
CSD	Crystal size distribution
ECTFE	Ethylene-chlorotrifluoroethylene copolymer
OFC	Oscillatory flow crystallizer
STC	Stirred tank crystallizer
Latin symbols	
Abs	Absorbance
C	Concentration of API in the mother liquor
C_i	Initial concentration of API in the mother liquor
C_s	Solubility of the API
d	Crystal size
d_{10}, d_{50} and d_{90}	Volume-based crystal size corresponding to the 10th, 50th and 90th percentile of the cumulative CSD, respectively
f	Frequency of oscillation
$f_V(d)$	Volume-based CSD
m_{crist}	Mass of crystallized API
Q_A	Antisolvent flow rate
Q_{A1}	Antisolvent flow rate at A1
Q_{A2}	Antisolvent flow rate at A2
Q_B	Feed solution flow rate
Q_T	Total flow rate
S	Supersaturation ratio
S_i	Initial supersaturation ratio
t	Time
T	Temperature
V_A	Volume of antisolvent
V_B	Volume of feed solution
x_0	Center-to-peak amplitude of oscillation
Y	Yield

References

(1) Crosby, T. Designing For the Future of Continuous Processing. *Pharm. Process.* **2006**, *22* (1).

(2) Plumb, K. Continuous Processing in the Pharmaceutical Industry. *Chem. Eng. Res. Des.* **2005**, *83* (6), 730–738.

(3) Swichtenberg, B. Moving Beyond the Batch. *Pharm. Manuf.* **2008**, *7* (1), 24–26.

(4) Mollan, M. J.; Lodaya, M. Continuous Processing in Pharmaceutical Manufacturing. *Pharmaceutical Manufacturing*. 2004, pp 1–10.

(5) Khinast, J.; Rantanen, J. *Continuous Manufacturing of Pharmaceuticals*; Kleinebudde, P., Ed.; John Wiley & Sons, Ltd: Chichester, UK, 2017.

(6) Manning, R.; Sciacca, R. *Continuous Manufacturing in Pharmaceutical Industry: Economic and Policy Issues*; Bates White Economic Consulting, 2018.

(7) Chen, J.; Sarma, B.; Evans, J. M. B.; Myerson, A. S. Pharmaceutical Crystallization. *Cryst. Growth Des.* **2011**, *11* (4), 887–895.

(8) Nichols, G.; Byard, S.; Bloxham, M. J.; Botterill, J.; Dawson, N. J.; Dennis, A.; Diart, V.; North, N. C.; Sherwood, J. D. A Review of the Terms Agglomerate and Aggregate with a Recommendation for Nomenclature Used in Powder and Particle Characterization. *J. Pharm. Sci.* **2002**, *91* (10), 2103–2109.

(9) Beckmann, W. Agglomeration during Crystallization. In *Crystallization: Basic Concepts and Industrial Applications*; Beckmann, W., Ed.; Wiley-VCH Verlag GmbH & Co. KGaA: Weinheim, Germany, 2013; pp 75–84.

(10) Mersmann, A.; Braun, B. Agglomeration. In *Crystallization Technology Handbook*; Mersmann, A., Ed.; Marcel Dekker, Inc: New York, 2001; pp 235–284.

(11) Ålander, E. M.; Uusi-Penttilä, M. S.; Rasmuson, Å. C. Agglomeration of Paracetamol during Crystallization in Pure and Mixed Solvents. *Ind. Eng. Chem. Res.* **2004**, *43* (2), 629–637.

(12) Simone, E.; Othman, R.; Vladisavljević, G.; Nagy, Z. Preventing Crystal Agglomeration of Pharmaceutical Crystals Using Temperature Cycling and a Novel Membrane Crystallization Procedure for Seed Crystal Generation. *Pharmaceutics* **2018**, *10* (1), 17.

(13) Yu, Z. Q.; Tan, R. B. H.; Chow, P. S. Effects of Operating Conditions on Agglomeration and Habit of Paracetamol Crystals in Anti-Solvent Crystallization. *J. Cryst. Growth* **2005**, *279* (3–4), 477–488.

(14) Pietsch, W. Size Enlargement by Agglomeration. In *Handbook of Powder Science & Technology*; Fayed, M. E., Otten, L., Eds.; Springer US: Boston, MA, 1997; pp 202–377.

(15) Jiang, M.; Braatz, R. D. Designs of Continuous-Flow Pharmaceutical Crystallizers: Developments and Practice. *CrystEngComm* **2019**, *21* (23), 3534–3551.

(16) Zhang, D.; Xu, S.; Du, S.; Wang, J.; Gong, J. Progress of Pharmaceutical Continuous Crystallization. *Engineering* **2017**, *3* (3), 354–364.

(17) McGlone, T.; Briggs, N. E. B.; Clark, C. A.; Brown, C. J.; Sefcik, J.; Florence, A. J. Oscillatory Flow Reactors (OFRs) for Continuous Manufacturing and Crystallization. *Org. Process Res. Dev.* **2015**, *19* (9), 1186–1202.

(18) Caldeira, R.; Ni, X. Evaluation and Establishment of a Cleaning Protocol for the Production of Vanisal Sodium and Aspirin Using a Continuous Oscillatory Baffled Reactor. *Org. Process Res. Dev.* **2009**, *13* (6), 1080–1087.

(19) Briggs, N. E. B. B.; Schacht, U.; Raval, V.; McGlone, T.; Sefcik, J.; Florence, A. J. Seeded Crystallization of β-L-Glutamic Acid in a Continuous Oscillatory Baffled Crystallizer. *Org. Process Res. Dev.* **2015**, *19* (12), 1903–1911.

(20) Siddique, H.; Brown, C. J.; Houson, I.; Florence, A. J. Establishment of a Continuous Sonocrystallization Process for Lactose in an Oscillatory Baffled Crystallizer. *Org. Process Res. Dev.* **2015**, *19* (12), 1871–1881.

(21) Tahir, F.; Krzemieniewska-Nandwani, K.; Mack, J.; Lovett, D.; Siddique, H.; Mabbott, F.; Raval, V.; Houson, I.; Florence, A. Advanced Control of a Continuous Oscillatory Flow Crystalliser. *Control Eng. Pract.* **2017**, *67*, 64–75.

(22) Agnew, L. R.; McGlone, T.; Wheatcroft, H. P.; Robertson, A.; Parsons, A. R.; Wilson, C. C. Continuous Crystallization of Paracetamol (Acetaminophen) Form II: Selective Access to a Metastable Solid Form. *Cryst. Growth Des.* **2017**, *17* (5), 2418–2427.

(23) Jiang, M.; Ni, X.-W. Reactive Crystallization of Paracetamol in a Continuous Oscillatory Baffled Reactor. *Org. Process Res. Dev.* **2019**, *23* (5), 882–890.

(24) Brown, C. J.; Adelakun, J. A.; Ni, X.-W. Characterization and Modelling of Antisolvent Crystallization of Salicylic Acid in a Continuous Oscillatory Baffled Crystallizer. *Chem. Eng. Process. Process Intensif.* **2015**, *97*, 180–186.

(25) Peña, R.; Oliva, J. A.; Burcham, C. L.; Jarmer, D. J.; Nagy, Z. K. Process Intensification through Continuous Spherical Crystallization Using an Oscillatory Flow Baffled Crystallizer. *Cryst. Growth Des.* **2017**, *17* (9), 4776–4784.

(26) Lawton, S.; Steele, G.; Shering, P.; Zhao, L.; Laird, I.; Ni, X.-W. Continuous Crystallization of Pharmaceuticals Using a Continuous Oscillatory Baffled Crystallizer. *Org. Process Res. Dev.* **2009**, *13* (6), 1357–1363.

(27) Zhao, L.; Raval, V.; Briggs, N. E. B.; Bhardwaj, R. M.; McGlone, T.; Oswald, I. D. H.; Florence, A. J. From Discovery to Scale-up: α-Lipoic Acid : Nicotinamide Co-Crystals in a Continuous Oscillatory Baffled Crystalliser. *CrystEngComm* **2014**, *16* (26), 5769–5780.

(28) Ferreira, A.; Rocha, F.; Teixeira, J. A.; Castro, F. Modular Oscillatory Flow Plate Reactor. WO 2017/175207 A1, 2017.

(29) Harvey, A. P.; Mackley, M. R.; Reis, N.; Teixeira, J. A.; Vicente, A. A. The Fluid Mechanics Relating to a Novel Oscillatory Flow Micro Reactor. *4th Eur. Congr. Chem. Eng.* **2003**, 0-6.4-004.

(30) Ferreira, A.; Teixeira, J. A.; Rocha, F. O2 Mass Transfer in an Oscillatory Flow Reactor Provided with Smooth Periodic Constrictions. Individual Characterization of KL and A. *Chem. Eng. J.* **2015**, *262* (15), 499–508.

Chapter 11 - Final Remarks

11.1 Conclusions

This thesis describes how continuous crystallization processes can be implemented in planar oscillatory flow crystallizer (planar-OFCs) to produce active pharmaceutical ingredients (APIs) with narrow crystal size distributions (CSDs). The operating parameters, such as the flow rate, Q, the temperature, T, the frequency of oscillation, f, and the amplitude of oscillation, x_0, and the geometric parameters, such as the cell aspect ratio, L/W, and the ratio of the open constriction area, $\alpha = W_0/W$, were optimized for continuous crystallization in three sets of experiments.

The first set of experiments (**Chapters 4, 5 and 6**), was performed to investigate the influence of operating parameters and geometric parameters on the state of mixing in a planar-OFC. Let us first consider the impact of the operating parameters. The minimum amplitude required to keep all solids in suspension in a planar-OFC decreases as the frequency increases from 1 to 4 Hz, but it increases when the frequency increases from 4 to 8 Hz; apparently, when the frequency is higher than 4 Hz, the vortices do not have time to fully expand and distort before the direction of the flow is reversed; as a result, the minimum amplitude required to keep all solids in suspension significantly increases. Therefore, moderate frequencies, between 3 and 4 Hz, are optimal to keep solids in suspension. Furthermore, when the planar-OFC is operated in batch, both the increase of radial mixing resulting from increasing the frequency and the increase of axial mixing resulting from increasing the amplitude contribute to decrease the mixing time; however, when the planar-OFC is operated in continuous, the increase of radial mixing resulting from increasing the frequency contributes to decrease the axial dispersion, whereas the increase of axial mixing resulting from increasing the amplitude contributes to increase the axial dispersion.

Let us now consider the impact of the geometric parameters. The minimum amplitude required to keep all solids in suspension in a planar-OFC changes as L/W increases from 3.00 to 4.25, and α increases from 0.19 to 0.41; however, increasing L/W has a stronger impact on the suspension of solids than increasing α. In addition, when the planar-OFC is operated in batch, the mixing time decreases as L/W increases and α decreases; however, when the planar-OFC is operated in continuous, the axial dispersion decreases as L/W decreases and α increases.

Moreover, the operating parameters and the geometric parameters can be adjusted so as to minimize the difference between the state of mixing in the liquid phase and in the solid phase. This is important because the crystallization process involves the contact and the migration of molecules between a liquid phase (the supersaturated solution) and a solid phase (the growing crystals).

The second set of experiments (**Chapters 7 and 8**) was performed to investigate the influence of the oscillation conditions on the nucleation and crystal growth kinetics in a planar-OFC. In this second set of experiments, the isothermal crystallization of paracetamol was used as a case study. On the one hand, the oscillation conditions have a significant effect on the nucleation rate: the nucleation rate increases as the amplitude increases at both low and high frequencies; similarly, it also increases as the frequency increases at high amplitudes, but it decreases at low amplitudes. This reflects the same impact that the combination of high frequencies and low amplitudes has on the suspension of solids. Therefore, when a large number of small crystals are desired, high frequencies should be combined with high amplitudes to generate high nucleation rates; whereas, when a small number of large crystals are desired, intermediate to high frequencies should be combined with low amplitudes to generate low nucleation rates. On the other hand, the oscillation conditions have a minor effect on the crystal growth rate. Ultimately, this means that, to gain control over the CSD, one cannot rely on the effect of the oscillation conditions on the crystal growth step alone, but rather on their relative impact on the nucleation and crystal growth steps.

The third set of experiments (**Chapters 9 and 10**), was performed to demonstrate how continuous crystallization processes can be implemented in planar-OFCs. In this third set of experiments, two case studies were investigated: the cooling crystallization of paracetamol, and the antisolvent crystallization of a commercial API. When the solute has a high affinity with the crystallization channel wall material, fouling cannot be avoided due to crystal growth on the surface of the crystallization channel walls. Changing the flow rate, the oscillation intensity, the temperature, and the wall material allows to increase the operation time, but, after some time, fouling cannot not be prevented. In such cases, primary nucleation should be avoided and seeding should be used instead. Furthermore, the planar-OFC can be divided into spatially independent sections with different operating conditions in each section to provide further flexibility to control the mean size and CSD of the final product.

In summary, this thesis demonstrates, that when an API is produced by continuous crystallization in a planar-OFC, the operating parameters and the geometric parameters can be adjusted so as to gain control over the CSD. Ultimately, this allows to reduce manufacturing time and operational costs related to downstream corrective operations.

11.2 Recommendations for Future work

Some recommendations for future work:

- In this thesis, the state of mixing was evaluated in three planar-OFCs with different geometries. This is significant, but provides limit information about the global optimal geometry. Therefore, in the future, more

planar-OFCs with different geometries could be constructed and tested to further improve the state of mixing in the crystallizer.

- In this thesis, the minimum mixing intensity required to keep all solids in suspension in the planar-OFC was determined. In the future, the minimum mixing intensity required to keep all solids uniformly distributed in the planar-OFC could also be determined. This would guarantee that the solids are not only suspended, but also evenly distributed in the planar-OFC, which is important to reduce the concentration gradients and, thus, improve the homogeneity of the suspension inside the crystallizer.
- In this thesis, an ATR-UV/Vis probe was used to monitor the concentration of solute in the mother liquor at a fixed point in the planar-OFC. This is significant, but provides limit information about the supersaturation profile inside the planar-OFC. Therefore, in the future, multiple optic fibers could be used to measure the concentration of solute in the mother liquor at different points in the planar-OFC.
- In this thesis, samples were collected to measure the CSD of the final product offline by laser diffraction. In the future, an image analysis software could be used to measure the CSD of the final product in real-time so as to avoid sample preparation and time delays. In addition, the image analysis software could be used to measure the percentage of agglomerates/aggregates, single crystals and fines in the final product, which would provide further process understanding.
- In this thesis, the capabilities of the planar-OFC were tested for cooling and antisolvent crystallization. In the future, the capabilities of the planar-OFC could also be tested for reactive crystallization. The excellent mixing performance of planar-OFCs could be particularly useful to enhance the homogeneity of the mixture of different reagents.
- In this thesis, the capabilities of the planar-OFC were tested to gain control over the CSD. In the future, the capabilities of the planar-OFC could also be tested to gain control over crystal shape and polymorphism.
- In this thesis, the material of the planar-OFC was changed to reduce the risk of fouling in the crystallization channel. In the future, more planar-OFCs with different materials could be constructed and tested to further reduce the risk of fouling in the crystallization channel.
- In the future, planar-OFCs with different scales could be constructed and tested to establish suitable scale-up rules for planar-OFCs.

This page was intentionally left in blank

Appendix A - Calibration Curves for the Concentration of Paracetamol in a 40% (v/v) Mixture of Ethanol and Water

The linear regression equation, variables and parameters for each calibration curve are presented in **Table A.1**. Five validation parameters were used to validate each calibration curve: linearity, precision, accuracy, limit of detection and limit of quantitation. The methodology used to assess each validation parameter is presented in **Table A.2** and the result for each validation parameter is presented in **Table A.3**.

Table A.1 – Linear regression: equation, variables and parameters.

Linear regression equation: $y = (a \pm ts_a)x + (b + ts_b)$							
Variable	**Definition**						
y	Dependent variable: absorbance (Abs)						
x	Independent variable: concentration of paracetamol (C) in g kg^{-1}						
Parameter	**Definition**	**Value**					
		***T*=10 °C**	***T*=15 °C**	***T*=20 °C**	***T*=25 °C**	***T*=30 °C**	***T*=35 °C**
n	Number of calibration points	6	6	6	6	6	6
a	Slope (kg g^{-1})	0.00236	0.00250	0.00232	0.00249	0.00241	0.00231
b	Intercept	-0.001	0.003	-0.001	0.001	0.002	0.01
t	t-statistic for $n-2$ degrees of freedom	2.7764 with a significance level $\alpha = 0.05$					
s_a	Standard deviation of the slope (kg g^{-1})	0.00003	0.00003	0.00003	0.00004	0.00002	0.00005
s_b	Standard deviation of the intercept	0.002	0.002	0.002	0.004	0.003	0.01
ts_a	Confidence interval of a (kg g^{-1})	0.00009	0.00008	0.00007	0.00012	0.00007	0.00013
ts_b	Confidence interval of b	0.005	0.005	0.007	0.011	0.008	0.02

Table A.2 – Methodology used to assess each validation parameter

Parameter	**Methodology**
Linearity	Linearity was assessed based on the coefficient of determination (R^2) and the statistical significance of a and b. $R^2 > 0.995$ is generally considered as evidence of acceptable linearity. In addition, a should differ statistically and significantly from 0, whilst b should not differ statistically and significantly from 0. Therefore, the t-statistics of a (t_a) should be higher than the critical value ($t_{crit} = 2.7764$) and the t-statistics of b (t_b) should be lower than t_{crit}.
Precision	Precision was assessed based on repeatability. The concentrations of 3 replicates of 3 standard solutions of paracetamol were calculated from the calibration curve. The average coefficient of variation of the three series (CV_{rep}) was calculated to express precision.
Accuracy	Accuracy was assessed based on percent recovery (RE), calculated as the ratio between the concentration obtained from the calibration curve and the actual concentration of a standard solution of paracetamol. The concentrations of 3 replicates of 3 standard solutions of paracetamol were calculated from the calibration curve. The average RE of the three series was calculated to express accuracy.
Limit of detection	LOD was calculated based on s_b and a as LOD $= 3.3s_b/a$.
Limit of quantitation	LOQ was calculated based on s_b and a as LOQ $= 10s_b/a$.

Table A.3 – Result for each validation parameter.

	Result					
Parameter	***T*=10 °C**	***T*=15 °C**	***T*=20 °C**	***T*=25 °C**	***T*=30 °C**	***T*=35 °C**
Linearity	$R^2 = 0.999$	$R^2 = 0.999$	$R^2 = 0.999$	$R^2 = 0.999$	$R^2 = 1.000$	$R^2 = 0.998$
	$t_a = 75.321$	$t_a = 84.318$	$t_a = 87.603$	$t_a = 57.678$	$t_a = 101.011$	$t_a = 47.719$
	$t_b = -0.93$	$t_b = 1.468$	$t_b = -0.247$	$t_b = 0.364$	$t_b = 0.555$	$t_b = 1.048$
Precision	$CV_{rep} = 4\%$	$CV_{rep} = 6\%$	$CV_{rep} = 1\%$	$CV_{rep} = 1\%$	$CV_{rep} = 1\%$	$CV_{rep} = 1\%$
Accuracy	$RE = 100\%$	$RE = 101\%$	$RE = 100\%$	$RE = 100\%$	$RE = 101\%$	$RE = 100\%$
Limit of detection	LOD = 3 g kg^{-1}	LOD = 2 g kg^{-1}	LOD = 3 g kg^{-1}	LOD = 5 g kg^{-1}	LOD = 4 g kg^{-1}	LOD = 8 g kg^{-1}
Limit of quantitation	LOQ = 8 g kg^{-1}	LOQ = 7 g kg^{-1}	LOQ = 11 g kg^{-1}	LOQ = 16 g kg^{-1}	LOQ = 12 g kg^{-1}	LOQ = 25 g kg^{-1}

Appendix B - Calibration Curve for the Concentration of API in the Mother Liquor

The linear regression equation, variables and parameters for the calibration curve are presented in **Table B.1**. Five validation parameters were used to validate the calibration curve: linearity, precision, accuracy, limit of detection and limit of quantitation. The methodology used to assess each validation parameter and respective result is presented in **Table B.2**.

Table B.1 – Linear regression: equation, variables and parameters.

Linear regression equation: $\boldsymbol{y = (a \pm ts_a)x + (b + ts_b)}$		
Variable	**Definition**	
y	Dependent variable: absorbance (Abs)	
x	Independent variable: concentration of API (C) in mg L^{-1}	
Parameter	**Definition**	**Value**
n	Number of calibration points	8
a	Slope (L mg^{-1})	0.035
b	Intercept	-0.01
t	t-statistic for $n-2$ degrees of freedom	2.447 with a significance level $\alpha = 0.05$
s_a	Standard deviation of the slope (L mg^{-1})	0.0006
s_b	Standard deviation of the intecerpt	0.01
ts_a	Confidence interval of a (L mg^{-1})	0.002
ts_b	Confidence interval of b	0.03

Table B.2 – Methodology used to assess each validation parameter and respective result.

Parameter	**Methodology**	**Result**
Linearity	Linearity was assessed based on the coefficient of determination (R^2) and the statistical significance of a and b. $R^2 > 0.995$ is generally considered as evidence of acceptable linearity. In addition, a should differ statistically and significantly from 0, whilst b should not differ statistically and significantly from 0. Therefore, the t-statistics of a (t_a) should be higher than the critical value ($t_{crit} = 2.447$) and the t-statistics of b (t_b) should be lower than t_{crit}.	$R^2 = 0.998$ $t_a = 56.142$ $t_b = -0.976$
Precision	Precision was assessed based on repeatability. The concentrations of 3 replicates of 3 standard solutions of API (5, 15 and 25 mg L^{-1}) were calculated from the calibration curve. The average coefficient of variation of the three series (CV_{rep}) was calculated to express precision.	$CV_{rep} = 5\%$
Accuracy	Accuracy was assessed based on percent recovery (RE), calculated as the ratio between the concentration obtained from the calibration curve and the actual concentration of a standard solution of API. The concentrations of 3 replicates of 3 standard solutions of API (5, 15 and 25 mg L^{-1}) were calculated from the calibration curve. The average RE of the three series was calculated to express accuracy.	$RE = 98\%$
Limit of detection	LOD was calculated based on s_b and a as $\text{LOD} = 3.3s_b/a$.	LOD = 1 mg L^{-1}
Limit of quantitation	LOQ was calculated based on s_b and a as $\text{LOQ} = 10s_b/a$.	LOQ = 3 mg L^{-1}